Thin film batteries for integrated high energy density storage

Jacopo Celè

THESE DE DOCTORAT

NNT : 2023UPASF095

université PARIS-SACLAY

Thin film batteries for integrated high energy density storage

Batteries films minces pour systèmes intégrés à haute densité d'énergie

Thèse de doctorat de l'Université Paris-Saclay

École doctorale n° 571, Sciences Chimiques: Molécules, Matériaux, Instrumentation et Biosystèmes (2MIB)
Spécialité de doctorat : Chimie
Graduate School : GS Chimie. Référent : Faculté des science d'Orsay

Thèse préparée dans l'unité de recherche **Institut de chimie moléculaire et des matériaux d'Orsay (Université Paris-Saclay, CNRS)**
sous la direction de **Sylvain FRANGER**, Professeur,
la co-direction de **Sami OUKASSI**, Ingénieur

Thèse soutenue à Grenoble, le 18 décembre 2023, par

Jacopo CELÈ

Composition du Jury

Membres du jury avec voix délibérative

Philippe LECOEUR Professeur, Université Paris-Saclay	Président
Christel LABERTY-ROBERT Professeure, Université P.Curie UPMC-Paris6	Rapporteur
Jean-Pierre PEREIRA-RAMOS Directeur de recherche, Université Paris Est	Rapporteur
Kun JOONG KIM Docteur, Technische Universität München	Examinateur
François OZANAM Directeur de recherche, CNRS - Ecole Polytechnique	Examinateur
Jesús SANTOS-PENA Maître de conférences, Université Paris-Saclay	Examinateur
Philippe VEREECKEN Professeur, KU-Leuven	Examinateur

université PARIS-SACLAY

ÉCOLE DOCTORALE
Sciences Chimiques : Molécules, Matériaux, Instrumentation et Biosystèmes (2MIB)

Titre : Batteries films minces pour systèmes intégrés à haute densité d'énergie

Mots clés : Matériaux, Batterie, Films minces, Electrochimie

Résumé : Parmi les technologies de rupture, l'Internet des objets (IoT) est la plus populaire. Le concept est né en 1999, et aujourd'hui, c'est toujours un sujet qui mérite d'être discuté.
La vision derrière le mot IoT est un environnement hyper-connecté où chaque pouce de notre monde est peuplé d'innombrables appareils, plus petits qu'une pièce de monnaie : une brume de gouttelettes intelligentes, conçues pour capturer même la plus petite donnée disponible.
Alors que les progrès de la fabrication de semi-conducteurs ont permis de compresser un micro-ordinateur et une station météorologique dans une puce en silicium d'un millimètre carré, l'empreinte d'un dispositif de stockage d'énergie est bloquée dans les années 1990.
La nouvelle génération de batteries à couches minces entièrement solides vise à fournir le dernier bloc fonctionnel à la mise en œuvre de l'IoT. L'élément central pour atteindre la densité d'énergie requise et réduire la taille de l'unité de stockage est l'électrolyte à l'état solide. Grâce à sa stabilité mécanique, il est possible de minimiser l'espacement entre anode et cathode, sans risque de croissance de dendrites et de courts-circuits associés. Néanmoins, la technologie actuelle est limitée par une très mauvaise cyclabilité et la densité de puissance est loin d'être optimale.

Dans le présent travail de thèse, nous avons étudié une micro-batterie à l'état solide à couche mince basée sur une cathode LiCoO2 et un électrolyte solide LiPON dans une configuration sans anode. Le dispositif est réalisé dans une empreinte de 0.5 mm2, avec une épaisseur active inférieure à 50 µm.
Le manuscrit s'ouvre sur une revue bibliographique des batteries tout solide du point de vue de l'appareil, de la fabrication et des matériaux.
Dans le deuxième chapitre, le dispositif est décrit et la caractérisation physico-chimique des différentes couches est rapportée.
Le troisième et principal chapitre traite de l'étude de la perte de capacité intrinsèque des cathodes LiCoO2 en configuration couche mince.
Afin de comprendre la nature physique de cette perte réversible, un modèle physique 1D continu basé sur l'équation de dérive-diffusion et l'équation de Buttler-Volmer a été réalisé.
Le modèle a été résolu au moyen de COMSOL Multiphysics et la perte de capacité a été attribuée à la baisse de la diffusivité du lithium à l'interface cathodique pour un faible état de charge (SOC).
La dépendance de la perte de capacité au courant de décharge a également été extraite, montrant la possibilité de récupérer la capacité théorique à une densité de courant extrêmement faible (<10µAcm-2).
Le modèle a été comparé aux données expérimentales obtenues pour différentes épaisseurs de cathode (5, 10, 20, 30µm LiCoO2). Un bon accord tant du point de vue qualitatif que quantitatif a été obtenu à toutes les épaisseurs de cathode pour les courbes de charge et de décharge à toutes les densités de courant considérées (10µAcm-2-10mAcm-2).
Ensuite, dans le quatrième chapitre, le modèle est vérifié au moyen de 2D dans la diffraction des rayons X synchrotron operando. Le profil de lithium à l'intérieur de l'appareil à différents moments est extrait et comparé à la simulation physique 1D. Encore une fois, un très bon accord est trouvé entre la simulation et les données expérimentales.
Dans la conclusion et la perspective, une solution au niveau de la conception et une solution au niveau de l'appareil sont proposées pour atténuer la perte de capacité du premier cycle à haute densité de courant avec un gain maximum attendu de + 50 % sur la capacité totale.

Title : Thin film batteries for integrated high energy density storage

Keywords : Battery, Electrochemistry, Thin films, Materials

Abstract : Among disruptive technologies, the Internet of Things (*IoT*) is the most popular. The concept was born in 1999, and today it is still a topic worth discussing.
The vision behind the word *IoT* is a hyper-connected environment where each inch of our world is populated by countless devices, smaller than a coin: a mist of intelligent droplets, engineered to catch even the smallest piece of available data.
The IPv6 protocol and the 5G technologies aim to provide the communication infrastructure to manage such a huge amount of data, while cloud computing and machine learning algorithms are developed to process the data lakes, resulting in the aggregation of millions of droplets.
So far, so good, but what about the hardware? While advancements in semiconductor manufacturing have made it possible to compress a microcomputer and a meteorological station into a millimeter-square silicon die, the footprint of an energy storage devices is stuck in the 1990s.
The new generation of all-solid-state thin-film batteries aims to provide the last functional block to the implementation of the IoT. The core element to attain the required energy density and minimize the size of the storage unit is the solid-state electrolyte. Thanks to its mechanical stability, it is possible to reduce the spacing between anode and cathode from hundreds of microns to hundreds of nanometers. Being mechanically rigid, solid electrolyte also prevents the growth of harmful lithium dendrites allowing lithium-metal batteries and improves the safety of the battery concerning short circuit and liquid leakage.
In the present thesis work, we studied a thin-film solid-state micro-battery based on LiCo2 cathode and LiPON solid electrolyte in an anode-free configuration. The device is realized in a 0.5 mm2 footprint, with an active thickness smaller than 50 µm.
The main objective of the thesis was the maximization of the volumetric energy density and the cycle life of the device.
The first chapter deals with the study of the intrinsic capacity loss of LiCoO2 cathodes in thin-film configuration.
In order to understand the physical nature of this reversible loss, a continuous 1D physical model based on the drift-diffusion equation and the Buttler-Volmer equation was realized.
The model was solved by means of COMSOL Multiphysics and the capacity loss was attributed to the drop in lithium diffusivity at the cathode interface for low state-of-charge (SOC).
The capacity loss dependency on the discharge current was also extracted, showing the possibility of recovering the theoretical capacity at an extremely small current density (<10 µAcm-2).
The model was compared with experimental data obtained for different cathode thicknesses (5, 10, 20, 30 µm LiCoO2). Good agreement from both the qualitative and quantitative points of view has been obtained at all cathode thicknesses for both charge and discharge curves at all considered current densities (from 10µAcm-2 to 10 mAcm-2).
A design-level solution and a device-level solution are proposed at the end of the work to mitigate this loss at high current density (for a maximum gain of +50% on the total capacity).
Following, the model is verified by means of 2D in-operando synchrotron X-ray diffraction. Lithium profile inside the device at different times is extracted and compared with the 1D physical simulation. Once again, a very good agreement is found between simulation and experimental data.
As a conclusion, the results are analyzed from a physical point of view in order to identify the main chemical degradation mechanism at the LiCoO2/LiPON interface.

ACKNOWLEDGEMENTS

It is a pleasure to thank my two supervisors, Sylvain Franger and Sami Oukassi, for the opportunity to work on this thesis and their trust. Their encouragement and suggestions all along the path have been of great support. It was their combined expertise that spurred me to encompass such a large spectrum of topics.

This work has been made possible thanks to the effort of the whole micro-battery team of CEA-Leti Grenoble, and in particular of all the people who worked for the realization of the devices, without which all the modeling would have been pure intellectual work. In particular, I thank Jean-Marc Boissel, Jean-Philippe Colonna, and Jouhaiz Rouchou for all their efforts and the cleanroom work during these three years.

For the invaluable opportunity to characterize my devices at the ESRF Grenoble and their support in the data processing, I thank Sandrine Lyonnard, Samuel Tardif, and Quentin Jacquet from the CEA-IRIG STEP laboratory.

For the intellectual and spiritual support, the fruitful discussions and the cheerful company, I would also like to thank Valentin Sallaz, Ngoc-Anh Nguyen, Lara Casiez and Larry Buffle. They not only contributed to the development, progress, and writing of this thesis but also made the time spent a precious memory. Finally, I thank the CEA-Leti for the financial support.

Table of Contents

”This page intentionally left blank.”

anonymous

INTRODUCTION

ABSTRACT

This chapter is an introduction on the general subject of energy storage for implantable and IoT applications.

The first section is entirely dedicated to a review of the energy storage for IoT in order to introduce the background of the thesis and the interest of batteries with respect to other power solution.

The second section is an executive summary of the thesis: what are the scientific goal of the thesis in the context of energy storage, which aspect of thin-film batteries have been studied.

Contents

1. Solid-state Batteries as Integrated Storage Solutions for IoT applications

It was 2013 when Mckinsey *Disruptive technologies* report was first published [1]. Twelve technologies were then chosen according to their economic potential. Over the years, renewed interest has been shown in both the concept of disruption and the there-listed technologies. Periodical reports of the European committee on disruptive technologies (in 2017 [2] and 2021 [3]) have followed the seminal work of Mckinsey. The very same concept of disruption merited its own document in 2020 [4]. In the 2021 EU document, the list of disruptive technologies has been reduced (from 12 to 6) and reviewed (2 new technologies and 3 rebrands). The only one that has kept its name intact since its first baptism in 1999 is *The Internet of Things*. Before delving into the Internet of Things (IoT) technology, it is worth it to define what a disruptive technology should look like and why it is important to invest our time as researchers in one of these fields.

Disruptive technologies

Disruption is defined as a sudden and unexpected phenomenon that impacts human society. In this sense, the coronavirus crisis was a disruptive event. Long-lasting changes in society resulted from it, foremost the increase in the usage of informatics tools in daily working life and the spread of "work-from-home" format. Each change may be small, like the reduction of physical contact during greetings or the vanishing of paper menus, but the overall effect is the reshaping of our way of living. Disruption can be dictated by natural events, like pandemics and earthquakes, or induced by human activity itself, as is the case for new technologies.
The changes that result from disruption are often associated with market growth and opportunities. The word crisis, from the Greek κρίνω (krino), "I decide", indicates a moment in which the consequences of our decisions are amplified and the right choice results in large gain opportunities. While the appearance of natural disruption cannot be anticipated and adaptation follows, when a new technology is introduced, it is possible to be prepared for the subsequent disruption and maximize the positive effect of the crisis. Once technologies with high disruption potential are identified, it is possible to both develop the technology itself and the means to cope and exploit it once deployed. As an example, in 2013, McKinsey pointed to the mobile internet as the first technology with respect to disruption potential. History confirmed this prediction, and just ten years later, the number of new social habits, applications, and job positions related to his technology have already transformed society. Today, the EU list of potentially disruptive technologies comprises: Artificial Intelligence, cloud computing, Internet-of-Things, data sharing, sustainable automotive, and block-chain.

The Internet-of-Things

Since the ancient times, the best way to make reliable predictions has been to be as vague as possible. As once the Apollo's priestess predicted to a king the fall of a kingdom in case of war, without specifying if it was his own or the one of the enemy, predicting the Internet-of-Things (IoT) to be a disruptive technology is kind of a smart guess as long as nobody knows what exactly the IoT is. The various reports on disruptive technologies try to provide us with a vague idea, referring to the Internet-of-Things as an evolution of the Internet. The Internet is a network of personal computers used to share information among humans, while the IoT is a network for objects to exchange information between in order to readily respond to external

variation without any human interaction. To be as poetic as possible, the IoT is defined as a data-driven ecosystem at the interface of the physical world. It is some sort of global-level control system applicable to any aspect of human life: healthcare, agriculture, industry, logistics, and building can all be integrated into a single control loop. We can broadly divide the operation of IoT into sensing, transmission and action [5–7]. But what technical aspects actually differentiate the standard "Internet-of-Humans" from the Internet-of-Things? From the transmission point of view, the first critical aspect is the number of connected devices. At the dawn of the Internet era, the Internet Protocol Version 4 (IPv4) was designed to provide a unique identifier to each computer with a 32-bit address. In the 80s, four billion connected devices were a huge number. Indeed, with some tricks and considering that the entire world population is never connected at the same time, IPv4 is still enough for managing the human connections nowadays. This is not the case if industrial machines, medical devices, buildings, cars or anything else we may think need its own Internet connection. This first issue was addressed by the introduction of Internet Protocol version 6 (IPv6). With its 128-bit address, it is possible to uniquely identify 3.4×10^{38} objects. A number large enough to uniquely point at each atom in the body of each human on earth. A second problem is to guarantee the simultaneous connection of lots of devices in a small area. Lots of us experienced the loss of internet connection in densely crowded areas, like concerts and festivals. This happens because the 3G and 4G communication technologies (that is, the physical infrastructure like antennas and switches) can support a maximum of a few thousand devices per km^2. The next infrastructure, 5G, will be scaled to manage at least 1 million devices on the same surface. In a certain sense, the IoT is already shaping the industry of telecommunications without even existing.
Innovative elaboration strategies are needed to deal with the huge amount of generated data and the technology has developed so far along two parallel axes: centralized elaboration versus distributed elaboration. In the former, the data are transported to large computer clusters in order to be elaborated, the so-called *cloud computing* [8, 9]. The distributed paradigm, called *edge computing* or *fog computing* [6, 10, 11], aims for data elaboration at the collection point or at an intermediate node. Among the various advantages, the edge computing guarantees less latency and higher quality of services (QoS) at the price of lower energy efficiency [11]. Power management is in fact one of the main topics in the design of sensors for the IoT [12–14]. Even if a single device has a low energy consumption, the deployment of billions of them results in an enormous aggregated consumption. For this reason, in the context of IoT sensor powering, energy autonomy by means of energy storing and harvesting is a key topic [15]. The field devoted to the minimization of energy consumption is often called *Green IoT* [7, 16].

Power solutions for IoT

The economic and environmental impact of the energy consumption of IoT devices is already a concern at this early stage of development due to the estimated number of deployed units. The main strategy to optimize and reduce the energy consumption is to equip the sensing node with an autonomous power supply. The core of green IoT is the increase in the on-time of the device, which is the only aspect that can be leveraged to reduce pollution since the production and deployment of the sensors themselves are considered as inevitable [16]. Maximization of power autonomy is also necessary in order to avoid frequent replacements or off-time, which would increase the cost and decrease the quality of services. Power systems are built around three main technologies: batteries, super-capacitors, and energy harvesting [16]. Each technology has its own advantages and drawbacks, and the choice of the right power system mainly depends on the application. For example, in-door and implantable applications will have less

possibility of harvesting energy; hence, the battery solution is more appealing. In general, the main criteria are the availability of a natural source of energy and the power consumption of the device. If there is plenty of energy from the environment, the battery may not be necessary, even if the much larger energy density means more robust operation. Another important aspect is the form factor requirement of certain applications, like implantables and RFID. In these cases, capacitors are a poor choice since the energy density scales badly with size.
As a general consideration, batteries are a good solution when long-term operation is the main requirement, while capacitors tend to outperform in high-power applications. Harvesting, on the other hand, is always a good option to extend autonomy, as long as it can be implemented. Hybrid systems using both capacitors and batteries are state-of-the-art and guarantee both power density and energy density.
Concerning battery solutions, the commercial devices have been developed and optimized for bulky portable applications and do present different problems when integrated into an IoT system. As an example, they come in a large and standard format, the technology is not CMOS-integrable, and the safety is usually too poor to guarantee the minimum quality of service required [13]. In this context, all-solid-state thin-film batteries have emerged as a possible solution to the aforementioned problems. Notwithstanding, this technology has not reached maturity, and intrinsic problems still haunt it. As an example, thin-film batteries present a lower areal capacity, a lower power density and larger capacity fade [14] with respect to the standard batteries, even if the same cathode materials are used. The investigation of the physical origin of the differences between commercial cathodes and thin-film all-solid-state cathodes is the subject of the present work.

2. Contribution and structure of this Thesis

The context in which the present thesis is set is the investigation of the physical principles of cathode materials for batteries, and in particular for thin-film all-solid-state batteries. Even if the materials have been extensively studied in standard electrode configuration, the adoption of new production processes and new cell topologies has resulted in new challenges, and several open questions still hinder the full development of the new generation of batteries. Of utmost importance is the understanding of the intrinsic degradation in performances of cathode materials, and in particular of $LiCoO_2$ when moving from composite to all-electrochemical-active electrodes [17]. As reported in the literature, the latter type of cathode shows a lower performance at high current density and a large capacity loss during the first cycle [18]. Clarifying the physical origin of such differences is the first step in pushing forward the development of this new generation of energy storage devices. All-solid-state batteries are chosen as the test vehicle for the whole analysis, but the results can be generalized to any class of electrodes.
The first of the four chapters composing the present thesis manuscript starts by highlighting the difference between classical cells and thin-film cells. The fabrication process and materials for thin-film are reviewed, along with a first physical description of the system.
The second chapter is dedicated to the physical characterization of the device under test. An important output of this chapter is the validation of various hypotheses exploited in the third chapter to simplify the physical picture and to develop a 1D mathematical model.
The third chapter comprises an extended theoretical section, where all equations are developed from basic thermodynamics. A comparison between classical liquid formulation and solid-state electrochemistry is provided as well. In the second part of the same chapter, the complete physical model is implemented and solved in order to study the lithium diffusion inside the cathode during the charge and discharge processes. The results are used to develop a first hypothesis to explain the behavior of an all-electrochemical active cell with respect to a commercial cell.
In order to verify the modelling results, the fourth chapter is dedicated to the electrical and X-ray diffraction characterization of the device. By means of synchrotron radiation X-ray diffraction, it is possible to resolve the lithium profile along the cathode thickness and directly compare it with the model prediction. Electrical characterization is mainly used to assess and validate the effect of the cathode thickness on the available capacity. First cycle loss and rating performances are satisfactory modeled, and a new comprehensive framework for the analysis of thin-film all-solid-state batteries is established.

Bibliography

Energy Storage for implantable and IoT applications

[1] J. Manyika et al. *Disruptive Technologies: Advances thatWill Transform Life, Business, and the Global Economy*. Tech. rep. McKinsey Global Instit., 2013.

[2] Mira Burri. *Current and Emerging Trends in Disruptive Technologies: Implications for the Present and Future of EU's Trade Policy*. en. Tech. rep. Publications Office of the European Union, 2017.

[3] John Gole et al. *Advanced technologies for industry: AT watch : technology focus on the Internet of Things.* en. Tech. rep. LU: Publications Office of the European Union, 2021.

[4] Philip Boucher et al. *Disruption by technologies: impacts on politics, economics and society : in depth analysis.* en. Tech. rep. LU: Publications Office of the European Union, 2020.

[5] Charith Perera et al. "Context Aware Computing for The Internet of Things: A Survey". en. In: *IEEE Commun. Surv. Tutorials* 16.1 (2014), pp. 414–454. DOI: 10.1109/SURV.2013.042313.00197.

[6] Wei Yu et al. "A Survey on the Edge Computing for the Internet of Things". en. In: *IEEE Access* 6 (2018), pp. 6900–6919. DOI: 10.1109/ACCESS.2017.2778504.

[7] Mahmoud A. Albreem et al. "Green Internet of Things (GIoT): Applications, Practices, Awareness, and Challenges". en. In: *IEEE Access* 9 (2021), pp. 38833–38858. DOI: 10.1109/ACCESS.2021.3061697.

[8] Alessio Botta et al. "Integration of Cloud computing and Internet of Things: A survey". en. In: *Future Generation Computer Systems* 56 (Mar. 2016), pp. 684–700. DOI: 10.1016/j.future.2015.09.021.

[9] Manuel Díaz, Cristian Martín and Bartolomé Rubio. "State-of-the-art, challenges, and open issues in the integration of Internet of things and cloud computing". en. In: *Journal of Network and Computer Applications* 67 (May 2016), pp. 99–117. DOI: 10.1016/j.jnca.2016.01.010.

[10] Najmul Hassan et al. "The Role of Edge Computing in Internet of Things". en. In: *IEEE Commun. Mag.* 56.11 (Nov. 2018), pp. 110–115. DOI: 10.1109/MCOM.2018.1700906.

[11] Hany Atlam, Robert Walters and Gary Wills. "Fog Computing and the Internet of Things: A Review". en. In: *BDCC* 2.2 (Apr. 2018), p. 10. DOI: 10.3390/bdcc2020010.

[12] Guoguang Rong, Yuqiao Zheng and Mohamad Sawan. "Energy Solutions for Wearable Sensors: A Review". en. In: *Sensors* 21.11 (May 2021), p. 3806. DOI: 10.3390/s21113806.

[13] Sourov Roy et al. “Powering Solutions for Biomedical Sensors and Implants Inside the Human Body: A Comprehensive Review on Energy Harvesting Units, Energy Storage, and Wireless Power Transfer Techniques”. en. In: *IEEE Trans. Power Electron.* 37.10 (Oct. 2022), pp. 12237–12263. DOI: 10.1109/TPEL.2022.3164890.

[14] Qiuying Xia et al. “All-Solid-State Thin Film Lithium/Lithium-Ion Microbatteries for Powering the Internet of Things”. en. In: *Advanced Materials* 35.2 (2023), p. 2200538. DOI: 10.1002/adma.202200538.

[15] Arindom Chatterjee et al. “Powering internet-of-things from ambient energy: a review”. en. In: *J. Phys. Energy* 5.2 (Apr. 2023), p. 022001. DOI: 10.1088/2515-7655/acb5e6.

[16] Mohammed H. Alsharif et al. “Green IoT: A Review and Future Research Directions”. en. In: *Symmetry* 15.3 (Mar. 2023), p. 757. DOI: 10.3390/sym15030757.

Contribution of this Thesis

[17] Zhimin Qi and Haiyan Wang. “Advanced Thin Film Cathodes for Lithium Ion Batteries”. en. In: *Research* 2020 (Jan. 2020), pp. 2020/2969510. DOI: 10.34133/2020/2969510.

[18] Chen-Jui Huang et al. “Decoupling the origins of irreversible coulombic efficiency in anode-free lithium metal batteries”. en. In: *Nat Commun* 12.1 (Dec. 2021), p. 1452. DOI: 10.1038/s41467-021-21683-6.

"[..] nos esse quasi nanos gigantium humeris insidentes [...]"

Bernardus Carnotensis

"[..] we are like dwarves sitting on the shoulders of giants [...]"

trad. from **Bernard of Chartres**

CHAPTER I

Review of All-Solid-State Batteries

ABSTRACT

This chapter is dedicated to the review of the main topic concerning All-Solid-State Batteries (ASSBs). No experimental results will be included, only bibliographical ones.

In the first part, the subclass of thin-film solid-state batteries (TFBs) is introduced from an historical point of view as a natural evolution of the slurry electrode. Basic concepts about production and design, as proposed in literature, are reported.

In the second part the main materials for anodes and cathodes are briefly reported. After a bibliographical review of the main materials, the physics behind solid-state electrochemistry is briefly introduced, including how intercalation works and the differences between thin-film configuration and composite electrodes.

The third section is dedicated to solid-state electrolyte physics, with a quick review of the main materials proposed by the literature. The lithium dendrite formation is discussed as well.

The final section is a review of the anode-free configuration and its advantages and drawbacks. A subsection is dedicated to reviewing the plating and stripping of lithium on metal collectors.

Table of Contents

1. All-Solid-State Batteries

1.1 Batteries: a short introduction

I feel it is somehow a tiresome task to introduce a subject to someone already knowledgeable. How many ”introductions” have we skipped without even a glance? It is then not my purpose to simply introduce plain concepts or to build a background of common jargon that I will use for the rest of the book. I will try to add something personal, from my own feelings and understanding, to those same dusty concepts.
Starting from this introduction, I would like to draw from a different perspective the sketch of the battery that we are going to be acquainted with in these pages. At this point, you are expecting me to say that a battery is, as someone said a long time ago, ”omnis divisa in partes tres”. Instead, for now, it will be more than enough to say that a battery is composed of, yes, three parts, but in an A-B-A scheme. I consider superfluous and somehow artificial the distinction between anode and cathode, which, for the moment, we will call, without distinction, electrodes. The electrode is the A element of the unit cell of a battery. I profit here to make a remark about the word ”battery” that I will not thoroughly respect. Indeed, *battery*, which comes from the military term indicating the ensemble of pieces of artillery, should be employed to indicate a multitude of cells, which are the unit ABA element.
The B element, called from now on electrolyte, is similar to the electrode, as inside both ions can diffuse, but it is different as the electrolyte is expected to be an electrical insulator while the electrode a good conductor. It is interesting how, in the literature, the ion conductivity in electrolyte is often referred to as electrical conductivity because, in certain non-blocking configurations (Li/electrolyte/Li), it actually represents the ohmic drop measured when a current is passed through the cell.
If brought into contact, the two electrodes would rearrange the quantity of ions and electrons each one possesses and create a more stable equilibrium. The point of the electrolyte is to avoid this balancing and to keep the system out of equilibrium. The idea is, then, quite simple. If the ion-electron couples residing in the two electrodes have different energies, it will be possible to exploit this difference to produce power. As long as the B element does not allow electrons to pass, each couple is forced to stay in the initial electrode because, due to the quite strong Coulomb attraction, it is not easy to displace charged particles. But if an external bridge is provided for the electrons only, it will be possible to temporarily split the couple and bring them back together at the more energetically favorable electrode. At this point, we can exploit the strong will of the electron, wanting to rejoin its beloved half, to impose a certain toll at the crossing of the bridge. The toll we will be able to impose will be as high as the difference in energy between the starting and ending positions, minus the toll paid by the ions, which need to cross the bridge provided by the electrolyte. Let’s now try to pin some meaningful names to the characters and places of our tale.

Static performance indicators

The moment a cell is assembled, a certain number of properties are expected, which depend solely on the nature of the two electrodes and the electrolyte. That is to say, they do not depend on the specific encounter between the three elements. Even before testing the cell, we will be able to define the theoretical values of such parameters. The total amount of electrons (Q) that we will be able to store in our system will be the minimum between the capacities of the two electrodes. This total capacity is a function of the amount of material that we used in each

electrode and the size of the cell. It is usually more meaningful to somehow normalize this total capacity in order to be able to compare different cells assembled with different materials.
We then have three natural choices for renormalization: over the cell area (A), over the cell volume (V) or over the cell mass (m).

$$Q_A = \frac{Q}{A}$$
$$Q_V = \frac{Q}{V}$$
$$Q_m = \frac{Q}{m}$$

Considering the size of commercial cells, the units of measurement commonly used for the total capacity are the kA h for the automotive market, A h for medium-size batteries (like the lead-acid battery of a car), or mA h for portable devices. This last one is in particular successful in the mobile phone industry for marketing reasons: increasing your phone capacity from 1 to 1.2 A h is for sure less appealing than an increase from 1000 to 1200 mA h.
The normalized unit permits us to bring the different devices to a common scale. The **areal capacity density** Q_A is usually measured in mA h cm^{-2} or in A h m^{-2} (1:10 conversion factor). This normalized unit is particularly interesting in the integrated circuit and sensor markets, where the footprint of the device is an extremely important parameter. Other markets, like cars and portable devices, prefer the **volumetric capacity density** Q_V expressed in A h m^{-3} or A h L^{-1} (which gives more appealing values on the order of hundreds of A h L^{-1} for available technologies). The **gravimetric capacity density** Q_m, measured in mA h g^{-1} or A h kg^{-1} (1:1 conversion factor), is a long-time standard at the industrial level, because it can be easily converted to A h €$^{-1}$. Indeed, knowing the price per kilo of cobalt does not give you much insight on the cost of a 250 A battery using a 1 A h L^{-1} technology. Notwithstanding, this unit of measurement is quite impractical at the research level and should be avoided in scientific publication [1]. The reason for its success is that it tends to boost the performance of lab-scale devices, which are usually very poor in terms of areal or volumetric properties. In terms of gravimetric capacity density, two batteries with different total capacities realized with the same material will appear identical. But, as we discuss dynamic performance, where the size will impact certain parameters, thin cells will seem to outperform thick ones.
As a matter of fact, I would advise against using the gravimetric capacity density because it is such a widespread parameter that it is difficult to make people change their habits. Actually, the correct way of presenting the results is by calculating, when possible, all three parameters. It is sometimes difficult for porous electrodes [2–4] to calculate the areal capacity, but it is better to have a bad estimation than no estimation at all, as long as the calculation procedure is reported.
Recalling our ABA structure, we define **Open Circuit Voltage** (OCV) the difference in energy between the two electrodes; this is once again dependent only on the choice of the two electrodes. This energy difference represents the distance of our system from equilibrium. Of course, as the ion-electron couples move, the systems get closer to equilibrium, and the voltage of the cell is expected to decrease. The toll paid by the electrons and ions is expressed in term of external and internal resistance of the cell. The **external resistance** (R_{ext}) is imposed by the user, while the **internal resistance** (R_{int}) comes from the stack and depends on multiple parameters, among which the nature and size of electrodes and electrolytes, and their capacity to conduct ions and electrons. It is, in particular, a measurement of the ionic conductivity of the electrolyte. Another parameter, with the unit of resistance, is the electrolyte electronic conductivity, contributing to the self-discharge of the cell (R_{self}). We said that the electrolyte should be electronically insulating, but of course its resistance will not be infinity. This resistance represents an unwanted path

for the ion-electron couples. Through this resistance, the couples can move without crossing the external resistance, thereby removing the possibility for us to exploit the electrons to produce power.
Most of the aforementioned parameters will change as a function of the temperature and the **State Of Charge** (SOC) of the battery. The latter is the percentage of the total capacity Q stored in the cell at a given moment.

Dynamic performance indicator

As the cell is assembled, a new set of indicators needs to be studied, in order to assess the performance of the cell when actually used. When referring to the dynamic performance of a cell, we are implicitly assuming that a current flows in order to charge or discharge it. The question that we want to answer by using dynamic indicators is how the static indicator evolves with this current. In particular, we already expect the voltage of the battery to change as an effect of R_{int}, which will decrease the actually available voltage difference by an amount equal to the product of the current and the internal resistance. But what about the variation of the internal resistance with the imposed current? As we will see later, the internal resistance provided for a device is indeed the static internal resistance, which can increase by orders of magnitude as a function of the state of charge and the drawn current.
We can summarize all the variation taking place at different current density by measuring the percentage of the theoretical capacity the cell is able to provide at any current rate, both in charge and discharge. It is particularly important to measure the charge and discharge indicators separately because the system may not be symmetric: e.g., fast charge, slow discharge. This kind of indicator is called a ragone or ragone-like plot, and it is usually a low-pass shape [5, 6]: only at low current is it possible to charge or discharge the theoretical capacity of the cell.
Another parameter linked to the current density is the so-called **critical current density** (I_c) [7]. This current represents the maximum current the electrolyte can sustain before shorting out due to dielectric breakdown or dendrite formation.
A last parameter that depends on the current is the heat dissipation of the cell, which is again a function of the internal resistance.
As for the static indicators, the dynamic indicators usually strongly depend on operating temperature.

Cyclic performance indicator

The last class of indicators is linked to the cycling of a cell. So far, we have assembled it and analyzed how it behaves when we try to charge and discharge it at different currents, but what about the evolution of performance after a certain number of cycles? During cycling, different degradation mechanisms may lead to a loss in initial performance. Of great importance is the evolution of the internal resistance, which can vary due to the degradation of the electrolyte and the interface contact between different components. Linked, but not exclusively, with the increase in internal resistance is the loss of available capacity, expressed in terms of the ratio between the initial capacity charged or discharged at a certain current and its value after a certain number of cycles. It has to be noted that, usually in scientific publications, a great deal of importance is attached to the **coulombic efficiency**. This indicator is calculated as the ratio between the charge and discharge capacities at each cycle. That is to say, the ability of the cell to give you back what you initially charged. The main flaw of this indicator is that it will not take into account the loss during the charge. It may be possible to recover the full charge capacity,

but if the charge capacity decreases during cycling, the battery is still degrading. Actually, the behavior of those indicators is strongly dependent on the charge and discharge protocol used to test the cell.
Linked with the cycling stability is another parameter called *electrochemical stability window*. It represents the maximum and minimum voltages that can be imposed on a cell before the electrodes or the electrolyte start decomposing. It is usually given with reference to lithium metal but is indeed specific to each cell, and it has to be evaluated for each couple of materials (electrode/electrolyte).

Electrode suites

As already mentioned, during charge and discharge, the ion-electron couples move back and forth between the two electrodes. It implies that the moles of ion-electron couples stored in the electrode material change over time, at the electrode will have a different average stoichiometry at any different point of the charge-discharge process. The electrode actually withstands a chemical transformation, and according to the particular mechanism that drives this reaction, electrodes can be divided into four suites: insertion, conversion, alloying, and plating [8–10]. Following is an example for each of the four reactions.

$$Mg^{2+} + 2\,e^- + Mg_xMnO_2 \rightleftharpoons Mg_{x+dx}MnO_2 \qquad \text{(Intercalation) } \clubsuit$$
$$Mg^{2+} + 2\,e^- + MnO_2 \rightleftharpoons MgO + MnO \qquad \text{(Conversion) } \diamondsuit$$
$$Sn + x\,Li^+ + xe^- \rightleftharpoons Li_xSn \qquad \text{(Alloying) } \spadesuit$$
$$Li^+ + e^- \rightleftharpoons Li \qquad \text{(Plating) } \heartsuit$$

In an ideal insertion reaction, the electrode is characterized by a stable structure that does not change chemically during the charge-discharge process. This structure possesses channels (1D), planes (2D) or a complex matrix (3D), in which ions can move freely. In the case of 2D insertion, the reaction is usually called *intercalation*. The insertion reaction has the advantage of providing stable interfaces due to the absence of chemical modification at the electrode. This is the suite of electrodes with the lowest volumetric capacity density.
The *conversion* electrode relies on strong changes in the nature of its components. That is to say, for each electron-ion couple that is removed (or added) from the electrode, new chemical substances are created. This suite of electrodes, relying on chemical change, possesses a high capacity density, but usually at the price of a low electronic conductivity of one of the products of the conversion reaction. Moreover, the chemical change in the nature of the electrode can lead to instability at the electrode/electrolyte interface.
The first two suites are characterized by a predominance of covalent or ionic compounds, while alloying and plating rely mainly on metal bonds. The alloying reaction consists of the creation of an alloy between the electrode metal and the ions. Because the chemical nature of the electrode is not changed, good interface stability is expected. At the same time, it is usually possible to create a lithium-rich alloy, meaning a lot of moles of lithium can be added to the initial electrode, resulting in an extremely high capacity. The price of such good performance is the mechanical stress due to the large volume expansion of lithium-rich alloys. The volume expansion can be as high as quadrupling the initial electrode volume, leading to the mechanical pulverization of the electrode.
The last suite is indeed quite similar to the alloying; it is in fact the ”self-alloying” of ions in an electrode of the same material. The big difference between the alloying and the plating is the

absence of any chemical modification. While during alloying, different phases are usually created when the ratio between the base electrode metal and the inserted metal varies; during plating, the ions are plated on themselves, and the only phase present is the pure metal. As for the alloying, high capacity and high stability are expected during cycling. The problem with, for example, pure metal lithium is the intrinsic reactivity of lithium with air and almost all electrolytes. Moreover, the plating may not be homogeneous enough, leading to the formation of complex 3D structures (called *dendrites*), which may, with time, grow inside the electrolyte and eventually short the two electrodes.
All suites have their advantages and drawbacks. In general, the insertion/intercalation electrode is the preferred one when rechargeable batteries are concerned, for their superior stability, while non-rechargeable primary batteries usually rely on more energy-rich electrodes, like conversion and alloying.

Electrolyte suites

For a matter of symmetry and a bit of luck, it is possible to divide the electrolytes into four suites as well: liquid electrolyte, polymer electrolyte, solid electrolyte, and composite electrolyte [11–18]. For electrolytes, it is the physical process behind ion diffusion that helps us group the material into four groups. The details, as for the electrode, will be discussed in the following sections. Notwithstanding, it is possible to imagine directly from the nomenclature that the difference between liquid and polymer electrolytes resides in the medium in which ion diffusion takes place. Solid electrolytes and composite electrolytes are usually associated, but indeed, from the point of view of the ions' conduction, a major difference can be highlighted. Solid or thin-film electrolytes are characterized by a single, solid framework for ion diffusion. They are quite close to electrodes and, together with liquid and polymer, can be grouped in the super-class of homogeneous electrolytes, that is to say, electrolytes composed of a single homogeneous phase. On the other hand, composite electrolyte is an umbrella term, comprising all possible mixtures of the three previous electrolytes and other materials [13–15, 17]. Composite electrolytes possess a mixed conductivity, which may be, for example, polymeric-liquid or polymeric-solid. The terms come from the classical electrode fabrication process, which we will address in the following lines.
In terms of ionic conductivity, which influences the internal resistance, the solid and liquid electrolytes are quite close, with the solid electrolyte outperforming the liquid ones by one order of magnitude at best [19]. Polymer electrolytes suffer from a low ionic conductivity ($< 10^{-6}$ S cm^{-2}) but, being solid, can be cast as a very thin layer, reducing the overall gap [11, 18, 20]. As with the polymer, the solid electrolyte can be realized as thin films, but the result is a fragile structure incompatible with the roll-to-roll process. It is interesting to observe that any suite shares a property with another one, while this same property is absent in the third class: two are good conductors and one is not; two are compatible with the roll-to-roll and one is not. Another intersection of this kind is the adhesion between electrode and electrolyte. In order to exchange ions between the two components, a good mechanical contact has to be realized at the interface. This is straightforward in the case of liquids and polymers, which can easily accommodate the roughness of the electrode, but is hardly accomplished for solid electrolytes. So far, I left apart the fourth suite, the composite electrolyte, but the idea behind it is to mix the three other suites in order to obtain the "perfect" electrolyte. Instead, composite electrolytes end up being haunted by the flaws of the other three. They are indeed quite bulky when realized with solid electrolytes due to the fragility of the solid part, and they cannot form a good interface with the electrode. When realized as a mixture of liquid and polymer, they are as safe as the liquid ones

but slightly less conductive and do not offer any resistance to the growth of dendrites.

1.2 A historical perspective on all-solid-state batteries development

Even if the different suites of electrodes and electrolytes were discovered more or less in parallel (e.g., polymer electrolyte, $LiCoO_2$ and LiPON were introduced in the '78 [19], '80 [21] and '83 [22, 23] respectively), the development of each, in particular in the field of electrolyte, was delayed in time.
The first technologies to be introduced in non-rechargeable batteries were based on conversion mechanism. In the 90's with the spread of portable devices, rechargeable batteries were introduced, along with insertion materials that proved to be the best choice in terms of cycling stability. All along, the electrolyte was a liquid one, and a porous membrane soaked in it was used to mechanically separate the two electrodes.
With the consolidation of the technology, the production process crystallized into the well-known roll-to-roll method [24]. This method is quite flexible due to the possibility of synthesizing and assembling each component separately. The two electrodes are realized as a mixture of particles of an active material (one of the four suites of electrodes), a binder to keep them together, and a conductive filler to ensure high electronic conductivity. From which the name *composite* electrode comes. Reused, as a matter of similarity, for electrolytes.

Limitation of commercial batteries

While battery production stabilized, the electronic and device fields expanded at an unexpected rate. The battery developed in the '90s was not enough. Two were the axes of forced development imposed by the surrounding technological landscape: medium-large scale, cheap cells for automotive and stationary storage, and tiny and performing cells for monolithic integration with ICs and MEMS [25]. As soon as the commercial battery started evolving to respond to new technological needs, various limitations of the roll-to-roll liquid technologies manifested.
In the beginning, in the hope of preserving the production process, the research focused on the development of more energetic electrodes. In particular, the possibility of using a plating anode was an appealing possibility, but a well-known limitation was hindering it. As already pointed out, plating electrodes suffer from the formation of so-called dendrites, which lead to the short circuit of the cell. As a consequence, strong heat dissipation may trigger the combustion of the liquid electrolyte . The liquid electrolyte is, of course, intrinsically dangerous (flammable and polluting) due to the possible leakage in the event of a piercing of the cell. But this is for sure a marketing issue, as gas is as flammable and polluting as any liquid electrolyte. Anyway, dendrite formation was a real issue, in particular because, as explained in more detail later, the formation of dendrites is strongly influenced by the current density. The switch to larger and more power-demanding applications, from personal computers to electric vehicles, increased awareness about the problem. Still, a metal lithium anode was a quick and efficient way of increasing the capacity of the cell, so the forgotten technologies of polymer and solid electrolyte were resurrected as a possible solution to the dendrite issue. At this point in the history of batteries, the belief was that a solid layer between the two electrodes could have prevented the growth of lithium dendrites due to its intrinsic mechanical stability.
Solid-state electrolyte was also regarded as an interesting solution to another problem linked with liquid electrolyte: electrochemical stability and electronic resistivity of solid and polymer electrolyte are higher than that of liquid electrolyte, limiting the self-discharge and the current

leakage of the cell. This is of course a major problem in electric vehicles because an unexpected dead battery in a car at the moment of departure is a greater issue than a dead computer when you need to send an email (which anyway needs a very limited amount of capacity to properly satisfy the user demand).
The last issue with roll-to-roll liquid cells is the size at which the device can be realized. The production process is intrinsically a bulk process, and batteries of comparable size to an integrated circuit are extremely hard to manufacture. The need for such small batteries has started increasing in the last few years thanks to the internet-of-things revolution.

The development of the all-solid-state battery

Now that the root causes and needs that foster its development are known, it is possible for us to venture along the historical development of the *all-solid-state* cell. Its historical development was determined by two opposite forces: the need to provide more performing and safer cells, which pushed for innovation in the field, and the conservative force of industrial continuity, which pulled in the direction of the preservation of certain design principles compatible with the roll-to-roll process.
As mentioned before, solid and polymer electrolytes were available and known for some decades, but their intrinsic limitations on one side and the excellent performance of the liquid electrolyte on the other slowed down further development [26]. Curiously enough, polymers and solid electrolytes are somehow complementary in terms of performance. Summarizing what was exposed in the previous section, I will at the same time try to be more quantitative. In particular, we have to recall that the main goal of the development of new technologies was to increase available capacity. More precisely, the increase in volumetric and gravimetric energy density in the case of medium and large storage. This was the original force that spurned the development of solid-state batteries, and so we have to keep it in mind to understand the history of this technology. In Figure 1.1 the thickness of different components for each technology is reported for a cell with the same total areal capacity density. The value are collected from bibliographical sources [1, 27]. Compared to the electrolyte suites introduction, I decided to replace *solid electrolyte* with *thin-film* because bulky homogeneous solid electrolytes have never been commercialized due to the extremely high interface resistance. Let's leave thin-film out of the picture for the moment and focus on the first three technologies, which were developed to respond to large-scale format demand. In terms of electrodes and the current collector (the metal layer that is actually connected to the external device), no difference in the three technologies is visible. We started by saying that polymers and composites were introduced to avoid dendrite formation and enable the lithium metal anode (thereby decreasing the total volume of the battery). Notwithstanding, none of them allow for suppressing the dendrite growth at the demanded current density. Moreover, the composite electrodes, to be manufactured in the roll-to-roll configuration [17, 28], end up decreasing the volumetric capacity, which is indeed the opposite of the expected results. No need to say that no composite electrolyte have even been commercialized [13, 20]. Polymer electrolytes, at least, result in a small decrease in the total volume. The problem of low conductivity was solved by using a low-molecular-weight polymer (gel-polymer electrolyte), which is much closer to a liquid than a solid electrolyte. Those batteries have been commercialized not as a solution for dendrites but as an improvement of the classical cell.
The battle for large-scale battery technology is still raging today, but it is eventually time for us to change fields and focus on the second axis of development, which is the one addressed in the rest of my work.
The other battleground is, as anticipated, the miniaturization of the cell in order to be integrated

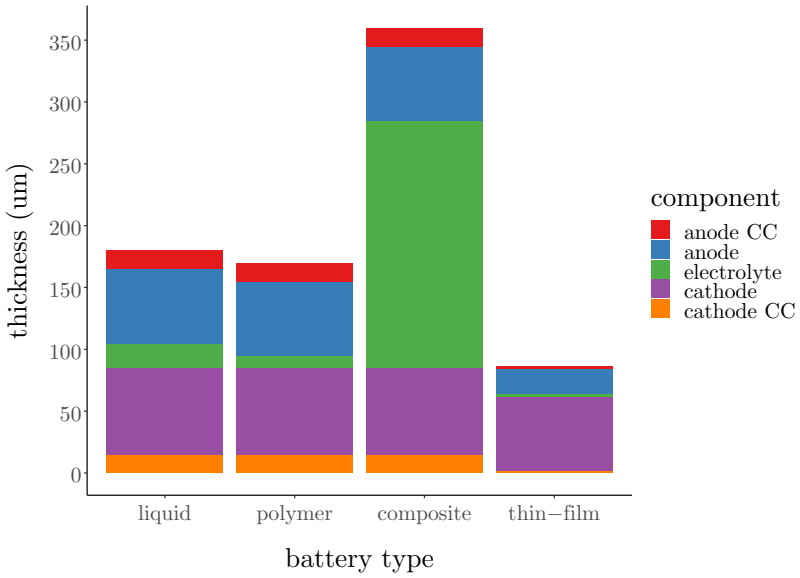

Figure 1.1: Typical thickness for a $4\,\mathrm{mA\,h\,cm^{-2}}$ cell realized with different technologies as reported in the literature [1, 27]. Thin-film gain is due to lithium metal anode and very thin glassy solid electrolyte.

with circuits and sensors. In this field, the roll-to-roll process is such an impediment that a completely new production process is required, enabling a custom form factor down to a few hundreds of micrometers. The obvious solution was to adopt the same production process as the ICs industry: In the thin-film battery, the layers are fabricated one over the other instead of assembled. This solution enables a good solid-solid interface by construction and revives the solid-electrolyte. Moreover, thin-film solid electrolytes can prevent the growth of dendrites and enable the lithium-metal electrode. Another advantage of thin-film, which is usually overlooked, is the size of the current collectors. In the roll-to-roll process, current collectors are used as deposition substrates and hence must be mechanically stable (around $15\,\mu\mathrm{m}$ thick). In thin-film technology, the battery is fabricated directly on the ICs substrate, and the thickness of the current collectors can be reduced to a few microns. It is the combined reduction of the anode and current collector, together with the minimization of the electrolyte thickness, that determines the final gain in volumetric capacity of the thin-film technologies. In the end, both safety and capacity are increased, but the price is a different process that is not scaled and is more expensive (x1000 for today's commercial thin-film batteries). Notwithstanding, some applications require a very high standard of safety and miniaturization (IoT, medical, drones, and space applications), for which thin-film batteries are a viable option. Moreover, the price is expected to fall with the mass production of such devices.

1.3 Fabrication process for TFBs

Before proceeding with a thin-film-oriented review of electrode and electrolyte materials, it may be a good time for a quick revision of the main production process for thin films. The topic is of interest not only to provide a framework for the critical evaluation of the literature on materials but also as a reminder of the fact that the production process of thin-film batteries is far from fixed. Keeping in mind alternative routes for synthesis is an advantage when trying to industrialize a new cell technology.
Thin-films process differs from the roll-to-roll process in that it has the capability of patterning

the thin-film at the same time the materials are deposited.I will first present the techniques to deposit thin films, followed by the methods employed to pattern these same thin films. Detailed information can be found in the excellent text of Wolf and Tauber [29] which I found enlightening on classic ICs processing. New and more chemically oriented techniques are scattered around in specialist texts, which are more or less equivalent [30, 31]. Various authors focus on all-solid-state thin-film batteries' fabrication. I mainly based my discussion on their works [26, 32, 33]. Being mainly comparative studies, I avoided quoting the same few papers again and again, and if no additional references are reported, please refer to the aforementioned sources.

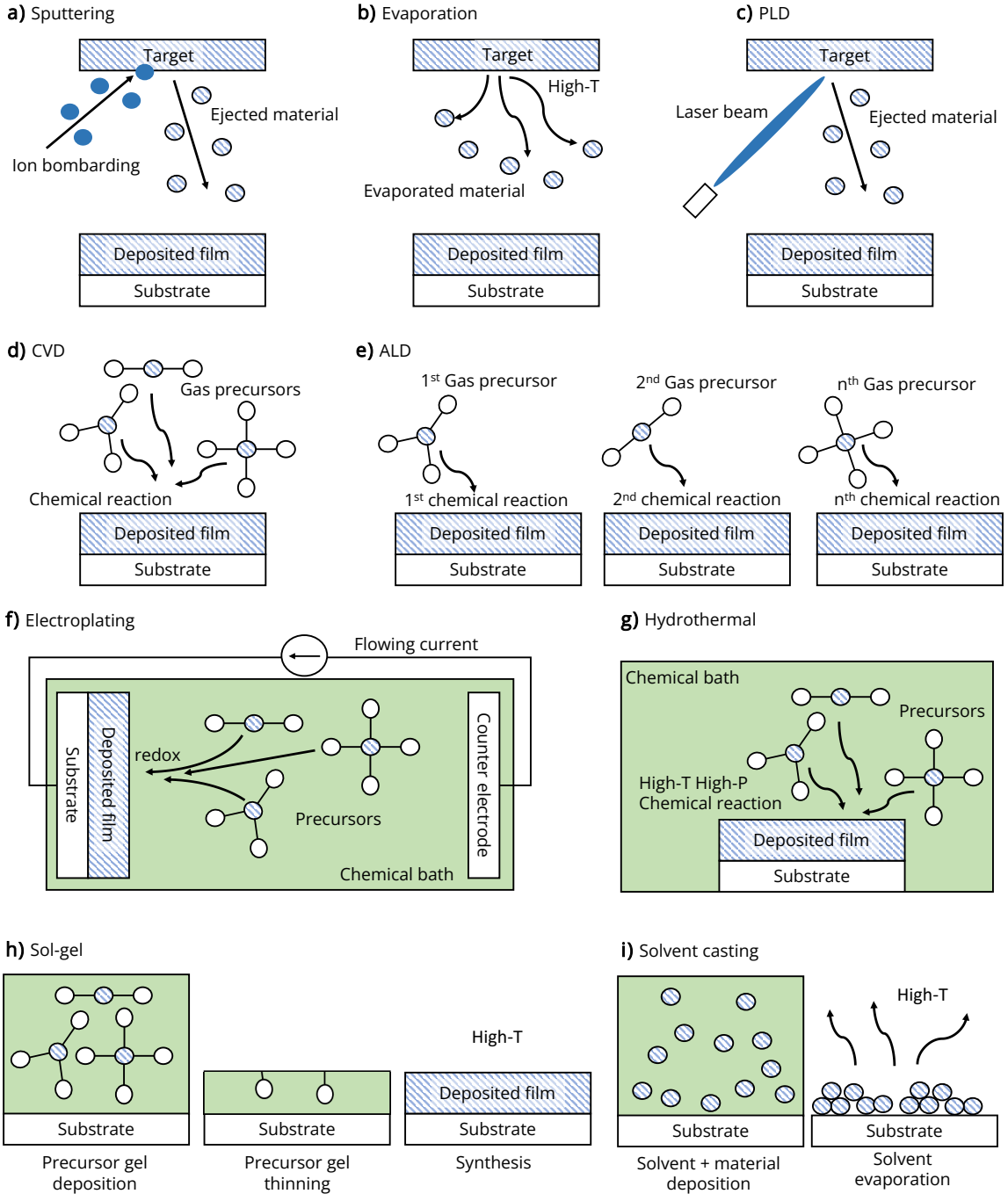

Figure 1.2: Thin films deposition techniques.

Sputtering

Sputtering is probably the most common technique for the deposition of thin films, it is part of the physical vapour deposition (PVD) family. The sputtering process consists of bombarding a target material with high-energy atoms (plasma) in order to physically dislodge its atoms. The ejected atoms will travel all around the deposition chamber and eventually deposit on the deposition substrate (Figure 1.2a). This technique permits fine control of both the stoichiometry and the thickness of the final film. Employing the right variation (DC, RF, RF-magneton sputtering), it is possible to deposit virtually any inorganic material, both conductive and insulating. Of course, the material has to withstand the ion bombardment and redeposit in the right chemical form. Polymer chains are particularly sensitive to sputtering conditions. The process is also prone to impurity inclusion. This can be an advantage, as in the case of LiPON electrolyte, where the nitrogen content is introduced by impurity doping during PVD. A final remark concerns the sputtering equipment, which is expensive, and the low deposition rate. These two factors combine to determine the high price of the final product.

Evaporation

Another important PVD technique is evaporation. It is based on the thermal evaporation of material in a vacuum chamber (Figure 1.2b). This technique has been exploited in the thin-film domain to deposit mainly lithium anodes. Many metals can be deposited at a very fast rate by this technique, and even if the evaporation temperature is high, the atoms impinging on the substrate usually have lower energy compared to the sputtering technique. Nevertheless, the control over film thickness is lower than in the case of sputtering, and it is also difficult to ensure a proper stoichiometry for the final compound due to the different decomposition and evaporation routes of the initial target. The technique is in fact limited to the deposition of pure metal layers, which indeed results in high purity due to the vacuum environment.

Pulsed Laser Deposition (PLD)

Pulsed laser deposition (PLD) can be viewed as a particular case of evaporation, where the material is vaporized by means of a high-energy laser pulse (Figure 1.2c). As for evaporation, the process takes place in a high-vacuum chamber. The method is appealing from the point of view of lab-scale research due to the fine control on the final stoichiometry, fast deposition rate, low cost, and ease of implementation. As for sputtering, the quality of the final film depends on the initial quality of the target, which can be synthesized with the preferred method. However, it is difficult to scale to industrial production, and for the moment, it is not competitive with respect to sputtering.

Chemical Vapour Deposition (CVD)

Chemical vapor deposition (CVD) is the chemical counterpart of PVD. While in PVD the material is deposited from a solid target with the same stoichiometry as the final film, in CVD the precursors are introduced in the deposition chamber in gas form. The gaseous precursors react at the film surface, and the solid products are deposited (Figure 1.2d). A fine control over the final composition and the thickness of the film is achieved with this technique. One of the limitations is the necessity to develop a chemical route for the synthesis of the thin film starting from gaseous

precursors. Sputtering has the advantage of being mainly a deposition technique, while the synthesis can be performed in an already established way. This is probably the main reason for the limited use of this technique. The deposition and the equipment are cheaper than sputtering.

Atomic Layer Deposition (ALD)

All the preceding techniques can be employed to deposit a film of thickness ranging from one hundred nanometers to a few hundreds of micrometers. This is, of course, more than enough control for the electrode layer, which has to be thick (tens of microns) in order to have a high energy density. On the other side, the electrolyte, as long as electronically insulating, can be reduced to a few tenths of nanometers. In order to achieve such results, atomic layer deposition (ALD) has to be employed [33, 34]. Conceptually, ALD is a carefully tuned CVD where the deposition process is controlled at the atomic level. ALD is based on the concept of cycles. Each cycle is composed of several steps, during which the deposition chamber is filled with a precursor and then emptied before the next precursor is injected (Figure 1.2e). The new precursor reacts chemically with the previous one, and the final result, if properly tuned, is the deposition of a single atomic layer per cycle. The technique is extremely costly to develop for new materials due to the necessity of designing the chemical cycle. The technique is nevertheless useful when high aspect ratio features have to be covered, like in 3D battery design.

Electrodeposition

Another technique that enables extremely fine control of the deposition thickness is electrodeposition [35]. Electrodeposition exploits the very same working principle as a battery: two electrodes are immersed in an electrolytic solution that contains the precursors of the final film. The redox reaction that leads to the deposition of the desired thin film is controlled by potential and current pulses (Figure 1.2f). The amount of deposited material is controlled by the current passed through the electrodes, while temperature, pH, voltage, and solution composition can be used to control the stoichiometry and even the crystal phase and orientation of the deposited film. Of particular interest is the process developed by Xerion for $LiCoO_2$ which produces already crystallized LCO at different orientations according to the experimental condition [36].
If properly controlled, electrodeposition can almost reach the precision of ALD and, at the same time, is usually much faster and more flexible. As for ALD, a great deal of effort is required each time the material is changed to design the deposition. The technique can be employed to deposit conductive film only.
In the case of hot electrolyte solutions, the technique is also called molten salt electrodeposition, which is indeed a synonym. Instead, it should not be confused with electrophoresis [37], which has a similar setup, but the material is synthesized before deposition and dispersed to form a colloidal solution. It is the drag force of the solution, created by means of an applied electric field, that displaces and deposits the material without any redox reaction.

Hydrothermal

The last three deposition techniques to be presented are inherited from chemical synthesis and adapted to thin-film processing. The first one is hydrothermal synthesis [38]. This synthesis is inspired by the geological formation of crystals, which takes place at monstrous pressure. In particular, it is possible to make a trade-off between the temperature and the pressure of synthesis, as known from the renowned phase diagrams. During hydrothermal synthesis, a high

pressure is created inside a sealed container by means of a gas, usually water (Figure 1.2g). The principle is the same as that of pressure cooking. This route enables the synthesis at a lower temperature and, hence, at a lower cost compared to standard solid-state synthesis. The thin-film version of hydrothermal synthesis consists of placing the deposition substrate inside the sealed vessel.
This technique can be combined with electrodeposition for fine control over the deposition process. The films created by this technique are of high quality, and the process is cheap. The main drawback is the low deposition rate and the harsh conditions to which the substrate is exposed; it cannot be employed at the back-end of an ICs processing.

sol-gel

Sol-gel is both a synthesis and a deposition technique [39, 40]. It consists of mixing the precursors of the desired material in a solvent, which is then partially dried to form a gel. The advantage of a gel with high viscosity is the possibility of controlling the thickness of the film by mechanically thinning the gel before complete evaporation of the solvent (Figure 1.2h). It is especially used to synthesize oxide for electrode materials in a simple and cheap way. It is a low-temperature synthesis, which makes it highly compatible with polymers. Notwithstanding, it suffers from poor control over the morphology and thickness of the film and shows no substantial advantages with respect to other techniques in terms of the films quality.

Solvent casting

Solvent casting is a deposition technique only, used mainly for polymer electrolytes [41–43]. It is indeed quite similar to sol-gel in terms of processing. The main difference is that the material is synthesized and then dispersed into a solvent (Figure 1.2i). This is the same difference that exists between electrodeposition and electrophoresis. It suffers from the same limitations, in terms of film quality, as the sol-gel method. Once again, the main advantages are the cost, low temperature, and simplicity.

Patterning

Once the film is deposited, in order to obtain a sub-millimeter-sized battery, it has to be patterned with the desired shape. To achieve this result, it should be possible to somehow remove the deposited film. This is accomplished by means of different etching processes inherited from ICs manufacturing.
The broad term *patterning* refers to a two-step process. In order to pattern a film, two ingredients are required: a way to remove the film and a way not to remove it in selected zones. The latter is accomplished by means of photolithography. First, a sacrificial mask layer is superimposed on the deposited layer. The final pattern is transferred from a master mask to the sacrificial layer by means of light (UV or X-ray), and the sacrificial layer is developed much like a photograph (Figure 1.3 textbfa and textbfb). The part of the film covered by the sacrificial layer will be protected during the etching step.

Wet etching

The fastest way to remove a material is by means of wet chemical etching. That is to say, by using a solution of acid or base that can dissolve the material. Wet etching is not only fast but

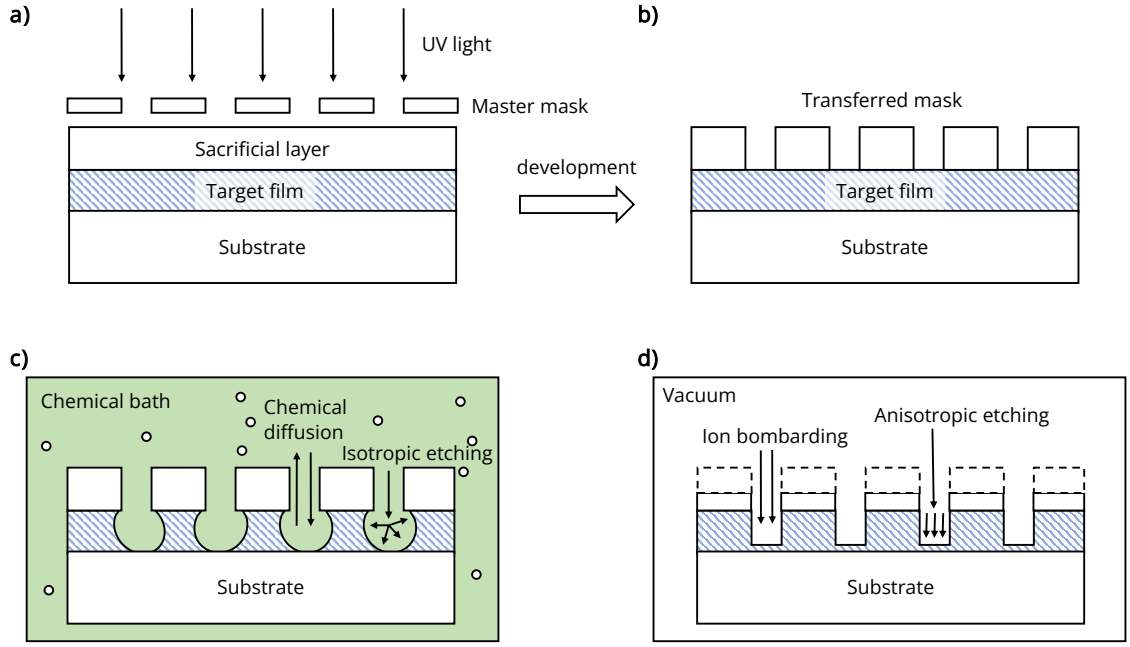

Figure 1.3: Patterning of a thin film: a) transfer of the master pattern on the sacrificial layer; b) developmenet of the transfered pattern; c) wet ecthing; d) dry etching.

also selective. The selectivity of a certain etching solution is defined as the ratio between the dissolution of the target material and the sacrificial layer or other materials already deposited. As a matter of example, if an electrode material is deposited on a silicon wafer, a selective wet etching will dissolve the electrode material but not the silicon or the protective mask (or at least dissolve them very slowly).
As for the deposition techniques like CVD, ALD, and electrodeposition, wet etching is very efficient and targets a specific material, implying the necessity to develop a different solution for each material. One main issue with wet etching is the isotropy of the process, which makes it hard to realize high aspect ratio features (Figure 1.3 **c**). The process is also polluting due to the large volumes of strong acids and bases employed. The development of less polluting wet etching is a concern for battery recycling too. Indeed, having a selective and environmentally friendly way to remove each layer of a battery is the best way to recycle. As an example, the dissolution of LiCoO2 by means of a low-T deep eutectic solvent [44].

Dry etching

The general purpose counterpart of wet etching is dry etching. As wet etching is the counterpart of CVD deposition, dry etching is the counterpart of sputtering. Dry etching is indeed based on the very same principle: the mechanical ablation of a material by means of highly energetic plasma (Figure 1.3 **d**). Dry etching tends to be less selective, even if chemically assisted variations like *reactive ion etching* (RIE) can add the necessary selectivity to the process. In general, the greatest advantages of this technique are its flexibility (there is no need to develop the process from scratch for different materials), its high precision and its anisotropy. This last point comes from the control of the impinging direction of the plasma, which enables the high aspect ratio feature. A drawback is usually the poor selectivity with respect to the sacrificial layer, which, for high aspect ratio features, needs to be thick enough to resist until the end of the etching.

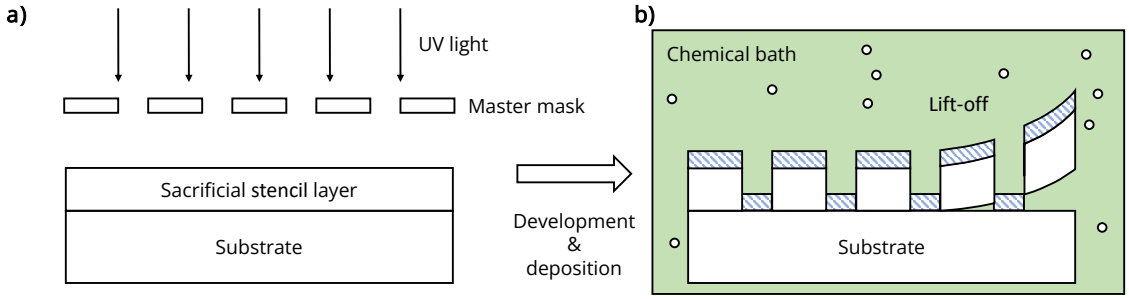

Figure 1.4: Patterning of a thin film by lift-off: a) transfer of the master pattern on the sacrificial layer; b) deposition of the target film and lift-off in a chemical bath.

Lift-off

The last removal process here presented is *lift-off*. This process is composed of the same steps as wet etching but in a different order. The sacrificial layer (called *stencil layer*) is the first one to be deposited, and the mask design is transferred (Figure 1.4 **a**). Then the target film is deposited onto the sacrificial layer. As long as a break is ensured between the film deposited on the top and on the bottom of the sacrificial layer, when the stencil layer is lifted off (dissolved), the pattern will be transferred to the target film (Figure 1.4 **b**). Lift-off is characterized by almost zero residual of the target layer and good step coverage (proper coverage and patterning of sloped side walls). This technique's main drawback resides in the compatibility between the stencil layer and the deposition of the target layer, which is hard to ensure.

1.4 Design considerations

So far, different processes for depositing and patterning thin films have been reviewed, but what about the different topologies and designs we can realize a battery with?
I will start by presenting the different designs of a single cell and then switch to the design of a battery of cells. Cell design can be divided into lateral and vertical cell stacks, with 2D and 3D variants for each of the two [45].

2D and 3D lateral cell

Designs are differentiated according to the relative position of the electrodes with respect to the deposition substrate. Lateral stacking is achieved when both electrodes are deposited on the deposition substrate (Figure 1.5 **a**). This design enables the deposition of the two electrodes before the deposition of the electrolyte. This is the greatest advantage of lateral stacking. The electrode may be made of crystalline material, and the deposition technique and heating treatment usually require high temperatures. The reverse is true of the electrolyte, which has to be manufactured at low temperatures and is not always stable at high temperatures. The lateral stacking is more flexible in the choice of electrode material because the thermal budget of the electrolyte does not impact the deposition of the two. Another interesting feature is the direction of the ion's motion. The ions move parallel to the substrate, meaning that an increase in the thickness of the electrode does not impact the diffusion length and results in an increase in capacity without loss of dynamic performance. The main drawback is that it is much more difficult to make thin electrolytes. The gap between the two electrodes will dictate the thick-

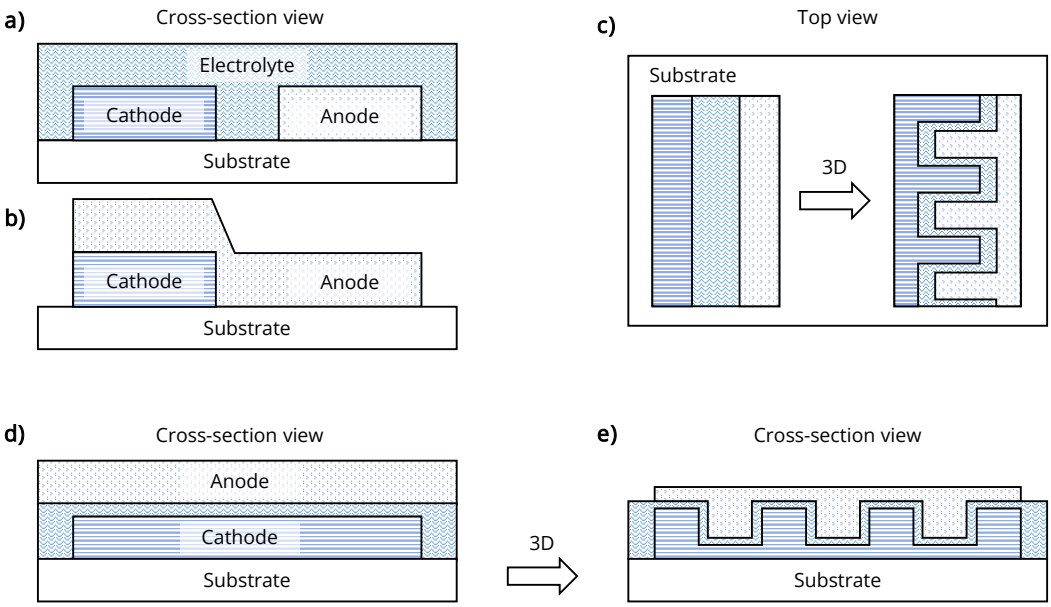

Figure 1.5: Different design of a thin-film cell: a) 2D lateral design; b) impact of the first deposited electrode on the patterning of the second electrode in 2D lateral design; c) from 2D to 3D lateral design (top view); d) 2D vertical design; e) 3D vertical design.

ness of the electrolyte. Not only is it necessary to master the etching and patterning of the two electrodes and ensure a fine alignment, but also the topography induced by the first electrode already deposited on the second one will introduce additional challenges in the manufacturing process (Figure 1.5 **b**).
The lateral design can be converted into the 3D lateral design with minimum effort once the 2D production process is mastered. The 3D design consists of an interdigitated array of anodes and cathodes (Figure 1.5 **c**), which aims to increase the interface between the two electrodes. Because dynamic performance is impacted by the effective interface between electrodes, the 3D design will maximize the current density supported by the cell.

2D and 3D vertical cell

In the case of vertical design, the two electrodes are not deposited onto the substrate but one over the other, much like the roll-to-roll process with the electrolyte sandwiched between the two (Figure 1.5 **d**). In a vertical cell, the material deposition order is unique, and the only choice is which of the two electrodes deposits as the first layer. The production process of vertical cells is more constrained in terms of thermal budget and process compatibility. The first electrode to be deposited is usually the cathode, because cathode materials are almost exclusively crystalline, which requires high deposition or annealing temperatures. The great advantage of this design is the possibility of squeezing the electrolyte down to a few nanometers without much effort from the point of view of the process.
In contrast to lateral design, in vertical design, the ions flow perpendicular to the deposition substrate, and the thickness of the electrode does impact the dynamic properties of the cell. Being complementary to lateral design, the conversion to 3D structure is not as straightforward as in the former scenario. The interdigitated array extends vertically (Figure 1.5 **e**), and its man-

ufacturing implies the mastering of high aspect ratio tranches inside the first electrode. This requires extra development effort compared to the 2D vertical design. As for the lateral 3D design, the aim is to maximize the effective area between electrodes and increase the dynamic performance. In order to fully exploit thick electrodes in the vertical cell, due to the diffusion limitation imposed by the electrode thickness itself, the 3D design is a viable solution. That is to say, we expect much more benefits when switching from 2D to 3D design in vertical cells than in lateral cells.

Cell stacking

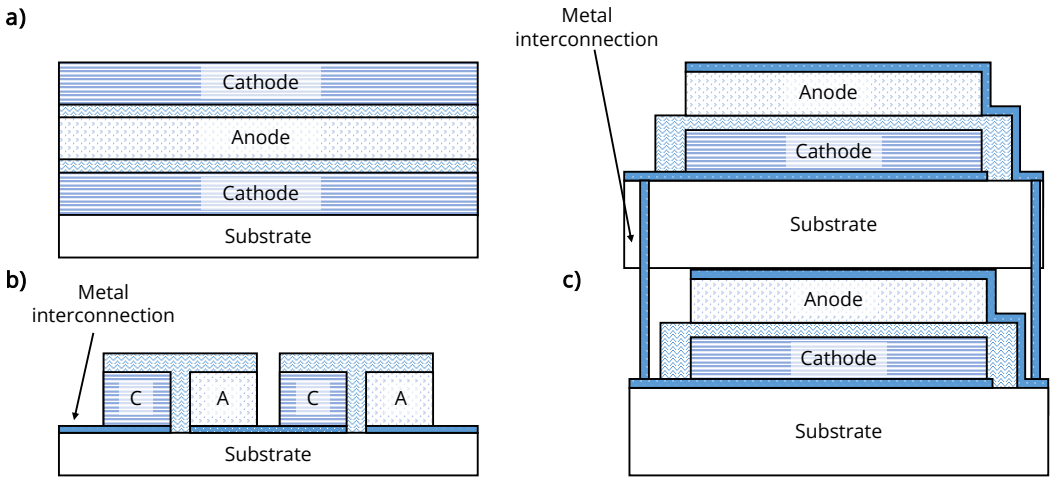

Figure 1.6: Stacking of thin-film batteries: a) vertical monolithic stacking (parallel connection); b) lateral monolithic stacking (series connection); c) die-level stacking (parallel connection).

Single cell optimization can increase the capacity density and the dynamic performance of the final device. However, maximum capacity is limited by the maximum achievable electrode size, and the total voltage is fixed by the choice of electrodes. To gain in total capacity (parallel connection) and to be able to increase the voltage of the final battery (serial connection), it is important to stack multiple cells. The standard roll-to-roll process relies on the flexibility of the cell to *wind* and stack multiple cells in a single package [46, 47]. For thin-film manufacturing, this is not an option due to the mechanical rigidity of the device and substrate. Two solutions are usually adopted: monolithic stacking [48] and die-level stacking [49]. In monolithic stacking, the different cells of the stack share the same substrate. Stacking can be lateral or vertical. Vertical stacking (Figure 1.6 **a**) on the same substrate is particularly hard due to the necessity to deposit the electrodes and electrolytes multiple times, which, as already pointed out, are not always compatible with each other in terms of processing. Lateral stacking is quite straightforward, and it relies on the patterning of metal connections (Figure 1.6 **b**). The great advantage of monolithic stacking is the minimization of the *overhead* by substrate sharing, that is to say, the minimization of the volume not used to store energy and the maximization of volumetric and gravimetric capacity density.
Die-level stacking is realized on the finished device via through-substrate connections(Figure 1.6 **c**), wire bonding, or stud bumping. The process is much more flexible with respect to monolithic stacking and is easy to realize. In particular, the final capacity and voltage of the battery can be tailored at the end of the line without any split in the main fabrication process. The drawback is

the addition of an extra substrate layer for each cell to be stacked, resulting in a lower volumetric capacity density than monolithic stacking.

2. Intercalation Materials for Thin-film Cathodes

So far, we have dealt with the electrochemical cell as a device, with few details on the physics behind ion diffusion in electrodes and electrolytes. These two are the topics of the present and following sections, together with a review of the main materials for thin-film batteries. Physical comprehension relies on my understanding and few good texts on solid-state electrochemistry. In order to avoid quoting the very same work again and again, I will propose here the essential bibliography and add, along the way, more specific references. In particular, for the bulk thermodynamics of electrodes, I will refer mainly to the work of McKinnon [19, 50, 51]. Diffusion and phase transition are integrated with the text of Yoo [52]. Concerning solid-solid interface reactions and the differences between electron-transfer and ion-transfer reactions, I will rely on the text of Bockris [53, 54] and Schmickler [55].

2.1 Physics of electrodes

In this section, we are interested in gaining some insight into the physical processes taking place inside the electrode and at the electrode/electrolyte interface during the charge-discharge of an electrochemical cell. This way, it will be possible to obtain a more concrete understanding of most of the static and dynamic performance indicators reported at the beginning of the chapter. Thin-film batteries mainly rely on insertion and alloying, so I will restrict the theoretical part to those two types of electrodes. Moreover, the two rely on very similar physical mechanisms for both the variation of electrochemical potential and diffusion of ions inside the electrode.

Thermodynamics for insertion and alloying electrodes

The thermodynamics of electrodes refers to the study of their thermodynamic properties at equilibrium. This is of interest because electrode voltage is defined by those same thermodynamic properties. It is in fact possible to link the measured electrochemical potential at equilibrium versus lithium, called open circuit voltage (OCV), to the change in Gibbs free energy of the system:

$$\Delta G = -nF\Delta V_{\mathrm{Li/Li^+}} \tag{1.1}$$

For example, a silicon alloying anode at the compositions $Li_{22}Si_5$ and $400\,^{\circ}C$ shows an OCV of 48 mV while at the composition Li_2Si the OCV increased up to 336 mV [56–58]. Conceptually, this is the change in Gibbs free energy between a pure lithium system and a lithium-silicon alloy. It represents the energy to be provided to mix a certain amount of silicon into pure lithium. The more silicon added, the greater the energy to be provided. It may be counter-intuitive to think of silicon as the atom to be added instead of lithium, which is actually introduced in the anode. Notwithstanding, looking from the perspective of the lithium reference makes it straightforward to interpret the values and tendency of the change in Gibbs free energy.
But what about the continuous variation of the electrode potential with the lithium content? If the electrode can form a solid solution with the lithium (the system can be at thermodynamic equilibrium for a range of values and not only for certain stoichiometries), we would need the value of the change in Gibbs free energy for the whole range.

Let's start with a very simple system. An electrode with N sites available for intercalation. If a site is occupied by an atom, the system gains E_0 energy. Assuming no interaction between intercalated atoms, the total energy (E) added to the system is nE_0, with n the number of intercalated atoms ($x = \frac{n}{N}$ is the intercalation fraction). Gibbs free energy can be written as:

$$G = E - TS \tag{1.2}$$

Where S is the entropy of the system, which for a non-interacting system of n atoms distributed over N sites is:

$$S = k \ln \left(\frac{N!}{n!(N-n)!} \right) \tag{1.3}$$

Where k is the Boltzmann constant. Recalling that 1.1 refers to a change in energy with respect to the mobile atom concentration, we can rewrite, in differential form, and combine 1.2 and 1.3:

$$\frac{\partial G}{\partial n}_{T,V} = E_0 + k \ln \left(\frac{n/N}{1 - n/N} \right) = E_0 + k \ln \left(\frac{x}{1-x} \right) = -nF\Delta V_{\mathrm{Li/Li^+}} \tag{1.4}$$

The first term is called chemical potential $\mu = \frac{\partial G}{\partial n}_{T,V}$. Experimentally, it is enough to one single measure of the change in Gibbs free energy for $x = 0.5$ for which the logarithms vanish, to get the unknown value E_0 and determine the whole voltage profile. For such a simple system, the voltage variation with respect to the intercalation fraction will resemble figure 1.7a. Even at this level of approximation, we can gain some insight on the expected behavior of a cell; in particular, equation 1.4 predicts an infinite increase or decrease in Gibbs free energy if the system is totally filled or emptied. This behavior is determined by entropy and can be understood as follows: if we imagine the voltage as the effort (time and energy) to insert or remove atoms, the last atom will require a big effort to be found. Gibbs free energy accounts also for the effort to find the atom, not only for the energy required to displace it once we find it.

The solution can be extended to more than a single type of intercalation site. For example, we can imagine an electrode having two kinds of sites: N_0 sites with energy E_0 and N_1 with energy $E_1 > E_0$. Intuitively, the atoms will occupy the sites at lower energy first. Let's define x_0 and x_1 the intercalation fractions for each type of site. At equilibrium, the potentials of particles in the first and second sites will be equal:

$$\mu = \frac{\partial G}{\partial n}_{T,V} = E_0 + k \ln \left(\frac{x_0}{N_0/N - x_0} \right) = E_1 + k \ln \left(\frac{x_1}{N_1/N - x_1} \right) \tag{1.5}$$

Where $N = N_0 + N_1$ is the total number of available sites. Inverting equation 1.5 and imposing $x = x_0 + x_1$ the total amount of inserted atoms, we get:

$$x = x_0 + x_1 = \frac{N_0/N}{1 + e^{(E_0 - \mu)/kT}} + \frac{N_1/N}{1 + e^{(E_1 - \mu)/kT}} \tag{1.6}$$

In figure 1.7b the resulting shape of the electrode voltage is shown. As imagined, the atoms first occupy the site at E_0 stabilizing the potential, and when the lower energy sites are almost over, the potential experiences a step to E_1. Each step in the curve indicated sites at different energies.

From this point on, the theory can be made as complex as desired by introducing ion-ion interaction and ion-matrix interaction. This permits the inclusion of phase transition mechanisms, clustering, and electrode volume expansion in the final expression of the OCV. As an example, in figure 1.7c, the predicted voltage profile is shown during a phase transition taking place when the intermediate stoichiometry between the two phases is not thermodynamically stable. The shown voltage plateau is the signature of two-phase regions.

As far as it concerns us, this introduction is enough to help us understand the voltage profile in the review section, and I won't fill more pages with thermodynamic equations. Let's instead switch to the ion and electron diffusion inside the electrode, that is, to the electrode dynamics.

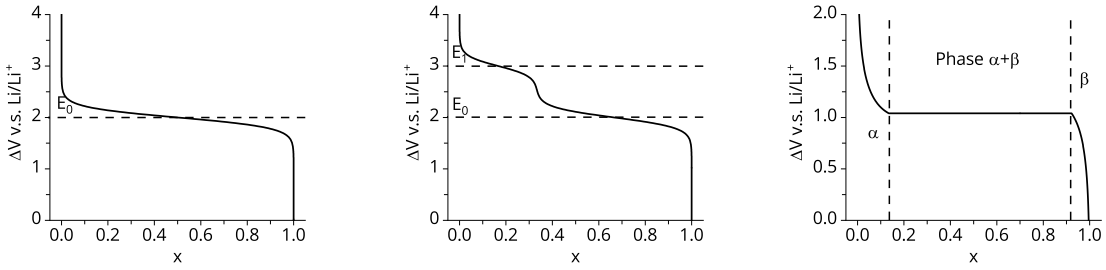

(a) Simulated voltage profile for a single energy sites($E_0 = 2$ V) according to eq. (1.4).

(b) Simulated voltage profile for two energy sites (N sites at $E_0 = 2$ V and $2N$ sites at $E_1 = 3$ V) according to eq. (1.5).

(c) Simulated voltage profile for a system exibiting phase transition. Phase α is thermodynamically stable for $0 \leq x \leq 0.1$ and phase β for $0.9 \leq x \leq 1$

Figure 1.7: Simulated voltage profiles for prototype intercalation systems.

Ion diffusion in solids

So far, we have considered an electrode at thermodynamic equilibrium for different concentrations of intercalated atoms, but what about the dynamics of intercalation? This question is of particular interest because when a cell is actually charged and discharged, the distribution of ions along the electrode thickness may substantially differ from the equilibrium concentration. In particular, a concentration gradient of diffusion species can build up.
Diffusion of atomic species in a solid framework is a well-established subject, and comprehension relies on the concept of lattice defects. Both intercalation and alloying electrodes tend to be crystalline or polycrystalline materials in which the atoms are arranged in an organized way. In an ideal crystal, every site is occupied by an atom, and diffusion is almost impossible. Luckily, real crystals at temperatures above 0 K show different types of imperfections, which can be exploited by atoms to move around. The kinds of defects we are interested in are vacancy defects and interstitial defects. A vacancy is a crystal site that should be occupied in the ideal structure, but is instead empty. The reverse is an interstitial atom, which resides in a position that should be empty in the ideal lattice (Figure 1.8)

In order for a defect to form, an atom from the crystal lattice has to overcome the energy that binds. It can then jump into an interstitial position and create a vacancy and an interstitial defect. In the case of non-interacting particles, the Gibbs distribution describes the mean number of atoms $\bar{n}_k$ with a certain energy ϵ_k as:

$$\bar{n}_k = ae^{-\epsilon_k/kT} \tag{1.7}$$

Where a is the normalization constant for $\sum \bar{n}_k = N$, with N the number of atoms in the crystal. If ΔG_V is the vacancy energy formation to be overcome, the mean number of vacancies at equilibrium ($\bar{N}_V$) is proportional to the number of atoms with enough energy to overcome the lattice force:

$$\bar{N}_V = \int_{\Delta G_V}^{\infty} d\epsilon \cdot ae^{-\epsilon/kT} = kTae^{-\Delta G_V/kT} = N_0 e^{-\Delta G_V/kT} \tag{1.8}$$

I took the time to review the derivation of this simple distribution, called the Boltzmann distribution, and its main hypothesis because most of the phenomena that we are going to address can be described by the same statistics.
Back to business: the presence of such defects enables the atoms to diffuse. In particular, once

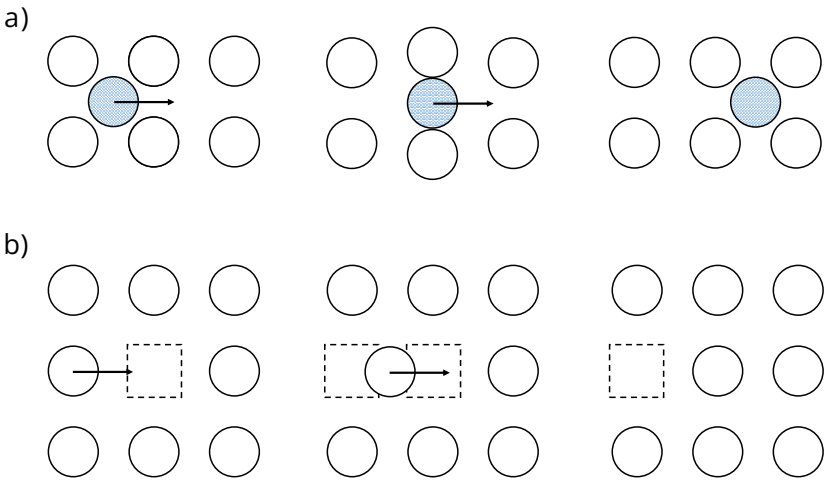

Figure 1.8: Defects diffusion in crystal lattice: a) Interstitial atom in blue; during the jump it needs to displace the surrounding atoms b) Vacancy defects; near-neighbours atoms can jump into the empty site and displace the vacancy.

the couple of vacancy/interstitial-atom is formed, the two, as long as they're not interacting (e.g., electrically neutral), will diffuse independently. A vacancy will move when an atom in a lattice position near the vacancy jumps into it. So the atom needs to have enough energy to overcome the energy barrier that keeps it at its position and move to the new position. Defining ΔG_b the height of the energy barrier, we can use again the Gibbs and Boltzmann statistic to estimate the probability for an atom to jump into the vacancy. The final jump probability will be the product of two probabilities: the probability for an atom to have enough energy to move and the probability for a vacancy to be near the atom for him to jump into it.

$$\text{probability to jump} \propto e^{-\Delta G_V/kT} e^{-\Delta G_b/kT} \tag{1.9}$$

The very same reasoning applies to the jump of an interstitial atom. The only difference, which is conceptual, is that the second energy distribution to be introduced is the energy of the interstitial atom, which needs to make its way across the lattice, and not that of the atoms in the lattice.
In a regular crystal, we can make the assumption that each atom will be able to move one site per successful jump and equal the unit displacement to the lattice parameter a_O. If v_0 is the number of trial jumps of each atom in unit time (jumps/seconds), we can define the mean square displacement (D) in unit time as:

$$D = a_0^2 \nu_0 e^{-\Delta G_V/kT} e^{-\Delta G_b/kT} \tag{1.10}$$

D is referred to as **self-diffusion coefficient** and is expressed in m s^{-2}. Self-diffusion in the absence of any external force can be measured by means of isotopes called *tracers*. The extracted value for isotope diffusion is called **tracer diffusion coefficient** (D^*). Its value is lower than the actual self-diffusion coefficient due to correlation effects, which I will not treat here. For further details, see [52].
So far, we have considered the diffusion of atoms in a crystal at thermodynamic equilibrium. That is to say, temperature, concentration, chemical potential, and electric field are constants inside the crystal. Even in this condition, atoms are allowed to roam around. However, as mentioned at the beginning, we are interested in the diffusion inside the electrode during charge and discharge, that is to say, in non-equilibrium conditions. During charge, an electric field is applied,

and the displacement of atoms between the two electrodes will cause a gradient of electric and chemical potential inside each electrode. Of particular interest is the case of a chemical gradient that is linked to the flux of atoms (J) by:

$$J = -c\frac{D}{kT}\frac{\partial \mu}{\partial x} \tag{1.11}$$

Where c is the concentration of diffusing atoms. The gradient of chemical potential is not easily measurable, and the equation is rewritten as a function of the concentration gradient:

$$J = -c\frac{D}{kT}\frac{\partial \mu}{\partial c}\frac{\partial c}{\partial x} = -\frac{D}{kT}\frac{\partial \mu}{\partial \ln c}\frac{\partial c}{\partial x} \tag{1.12}$$

From this equation, the **chemical diffusion coefficient** ($\tilde{D}$) is defined as:

$$\tilde{D} = \frac{D}{kT}\frac{\partial \mu}{\partial \ln c} \tag{1.13}$$

The derivative of the chemical potential with respect to the concentration is calculated via the electrode voltage evolution with the intercalation fraction by means of eq. 1.1 and 1.5. The derivative of the electrode voltage acts as an enhancement or suppression factor for diffusion and may dominate the behavior of the cell. In the next section, comparing real cases of chemical diffusion coefficients, we will see how they are strongly correlated to the electrode potential through the enhancement factor.
We assumed the lattice defects to be thermally generated when we derive the dependency of the defect concentration with respect to temperature. In insertion materials, defects are also generated each time an atom is extracted from the matrix. The number of defects thermally generated is usually much lower than the defects generated by insertion/extraction, and the defect density is constant and equal to one minus the intercalation fraction.

Electron conduction in solids

As important as the ionic conductivity is the electron conductivity in the electrode. As we will see in the next section, in order for an atom to be intercalated or alloyed, an available electronic state is needed. An electron also needs to be able to flow between the two electrodes in order to maintain the charge balance and sustain the reactions at the two electrode/electrolyte interfaces (Figure 1.9a). Dynamic limitation may result from both poor ionic and poor electronic conductivity in the electrode; hence, it is important to quickly review the main concept behind electron conductivity and the relation between electrons and ion conduction.
In a solid, most of the electrons are strongly bound to a single atom and cannot freely move around. The electrons are distributed in multiple electronic shells surrounding the nucleus of the atom. Different shells have different average distances from the nucleus, and the further away they are, the lower the binding force between the electrons and the nucleus. Because each shell can be occupied by a finite number of electrons, the shells are filled from the closest to the farthest away. In a solid, the outermost electrons participate in the creation of a chemical bond between different atoms. In metal, those electrons do not interact exclusively with their original atom, and their wave function extends to the entire solid. It is indeed more correct to imagine an electron with an infinite ”shape” covering the whole solid, instead of a point charge moving around. In semiconductors and insulators, those broad electron states (conduction electrons) are empty at 0 K and all electrons are localized around one or a few atoms, so no electron conduction is possible. As for ion conduction, we are saved by this imperfect world where no ideal crystals or 0 K exists. Indeed, the very same defects mentioned in ion conduction,

have an impact on electron conduction in metals and non-metals. An ideal metal would have infinite conductivity, but the presence of defects in the crystal lattice reduces the conductivity to a finite value. Because the quantity of defects is impacted by the temperature according to the Boltzmann distribution, the higher the temperature, the higher the number of defects and the lower the conductivity. The metal shows a slowing decay in conductivity as a function of temperature. That means that for an alloying electrode, the temperature increase will increase the ion conductivity but decrease the electronic conductivity. Luckily, the increase in ion conductivity is much faster, and higher temperatures are beneficial in terms of electrode performance.
In non-metals, conductivity is not determined by the presence of defects. Indeed, non-metals lack conduction electrons, and the presence of defects does not change this fact. Notwithstanding, the Boltzmann statistics will come again to our rescue. The broad electronic state shells exists, but at $0\,\mathrm{K}$ no electron lives there. A non-metal can be described in terms of the energy between the highest bound electronic state and the first diffuse electronic state; this energy is called **band gap** (E_g). At a finite temperature, the electrons will possess some extra energy, and according to Boltzmann, some of them will be able to escape from the bound state and become conduction electrons. This way, an electronic defect is formed, leaving a hole, similar to the formation of an atomic vacancy in the lattice. The band gap is the energy value to be considered in the Boltzmann distribution to determine the concentration of free electrons available for conduction. The difference between a semiconductor and an insulator is relative: a semiconductor is a material with a small enough band gap to have a non-negligible conduction at room temperature. We can see how negligible and room temperature are points of view that have significance for humans but not much for physics. In contrast to metals, non-metals will have an electronic conductivity that increases with temperature, as the ions' conductivity does. An important fact not to be underestimated is the electron-neutrality hypothesis made when discussing ion diffusion. If electrons are strongly bound to lattice atoms, the energy required to create and diffuse mobile atoms may be strongly impacted. In the material review, we will encounter materials in which electronic conductivity strongly impacts solid diffusion due to the coupling of electron and atom motion.

Ion-transfer and electron-transfer reaction

We have analyzed the bulk phenomena taking place in an electrode, but the core of the electrode's working principle is the interface where ions-electron couples are split and united (Figure 1.9a). The physics of the interface is strongly dependent on the electrolyte. However, we can introduce a few general elements to complete the picture from the electrode point of view. A more detailed treatment of the subject will be carried out in the electrolyte and modeling sections.
My main objective is to clarify the difference at the reaction interface between the two most common electrodes: insertion and alloying. The interface physics is indeed a main element of difference between the two; even if the final equations are almost identical for the two cases, their significance is different.
Let's start with the alloying electrode and electron-transfer reaction. The theory of electrified interfaces was developed for this kind of reaction and later adapted to the ion-transfer one. In an electron transfer reaction, as the name suggests, the species that cross the electrode/electrolyte interface are the electrons. As shown in Figure 1.9b, the first step is the diffusion of ions close enough to the electrode surface. The interface electrons have a wave function that extends beyond the last row of atoms. The density of electrons decays exponentially with the distance to the surface, but is never zero. If the ions are close enough to permit electron tunneling through

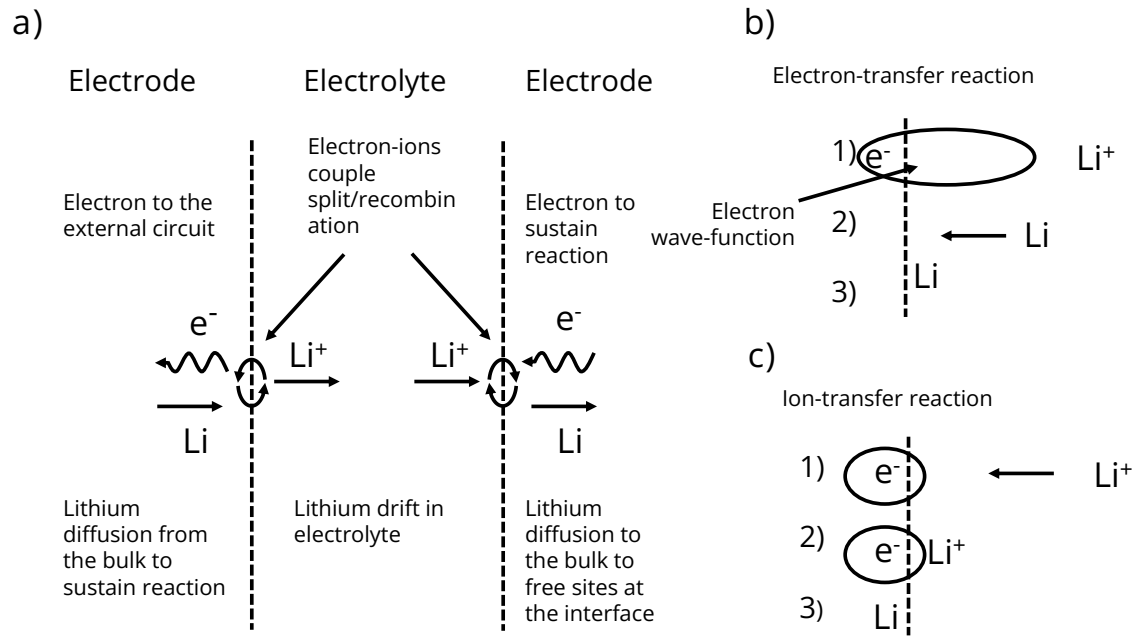

Figure 1.9: a) Schematic of the electrons-ions path during cell charge/discharge; b) electron-ions recombination detail for electron-transfer reaction; c) electron-ions recombination detail for ion-transfer reaction.

the electrolyte, the ion-electron couple can reunite near the interface on the solution side. A neutral atom is formed, and it diffuses to the interface and becomes part of the metal electrode. In the case of intercalation electrodes, instead, the ions cross the electrode/electrolyte interface and not the electrons. In Figure 1.9c the schematic representation of such an ion-transfer reaction is shown. First, the charged ions have to diffuse near the surface, and it is during the process of crossing the electrode interface that their charge is neutralized by an electron. From the point of view of electrons, this kind of process is less energetic, because it does not require electron tunneling. It is interesting to note how the growth of dendrites at a graphite electrode can be interpreted as a change from an ion-transfer to an electron-transfer reaction. This happens when lithium ions are consumed too quickly at the interface. The ion-transfer reaction requires ions to be really close to the interface. If the interface is totally depleted, more energetic electrons are created by polarization, enabling electron-transfer reactions and lithium metal plating at the electrode interface.

2.2 Cathode materials

Equipped with an essential toolbox of physical concepts, we are ready to delve into the bibliographical review of electrode materials. I decided at this point to follow the classical division of anode and cathode materials. It should be clear at this point that this division is artificial and is usually realized on the basis of the electrode potential with respect to the lithium reference. In particular, electrodes with a potential below $2\,\mathrm{V}$ are considered anodes, while the rest are addressed as cathodes. V_2O_5 is a peculiar case; this material lies at the border, and it is sometimes referred to as cathode and sometimes as anode. I decided to list it in the cathode section because of its physical similarities with other metal oxides. Even if the division has no real physical meaning, it is useful to notice how anodes for thin-film batteries are mostly alloying electrodes

with large volume expansion during charge-discharge. Cathode materials, instead, are exclusively insertion electrodes. A summary of the main cathode for thin-film batteries is proposed in table 1.1 together with their performance indicators.

Cathode	**OCV** (V)	Q_V (mA h cm^{-3})	ρ (g cm^{-3})	Q_m (mA h g^{-1})	σ_{el}^{-1} (Ω cm)	$\tilde{D}$ (m^2 s^{-1})	**dim**
$LiCoO_2$	3.9 to 4.3	710	5.1	140	10^3 to 10^6	10^{-14}	2D
$LiFePO_4$	3.4 to 3.5	610	3.6	170	10^9	10^{-18}	1D
$LiMn_2O_4$	3.5 to 4.5	615	4.1	150	10^3	10^{-15}	3D
$LiNiO_2$	3.9 to 4.3	670	4.8	140	10	10^{-14}	2D
$Li_xV_3O_8$	2.5 to 3.8	850	3.5	200 to 300	10^6	10^{-13}	2D
LiV_2O_5	2 to 3.5	660	3.3	200	10^3	10^{-18}	1D
Li_xMoO_3	2 to 3.5	1300	4.7	280	10^3 to 10^6	10^{-15}	2D

Table 1.1: Properties of popular cathode materials at RT. From left to right: minimum and maximum voltage; theoretical gravimetric capacity density; theoretical cathode density; theoretical volumetric capacity density; average electron conductivity; average chemical diffusion coefficient; dimension of the diffusion path. Sources are provided at each section. For a general reference see Park et al. [59].

$LiCoO_2$ *(LCO)*

Let's start this review with the most popular cathode. $LiCoO_2$ is the overall best cathode in terms of power density. It's a dense oxide with excellent capacity density and high voltage. Its main drawbacks are its high cost, scarcity, and toxicity. Its crystal structure is reported in Figure 1.10a. Lithium planes, in green, are separated by cobalt oxide planes. Lithium diffusion takes place in the 2D planes thanks to lithium vacancies generated during the extraction and insertion of lithium. LCO experiences two main phase transitions [60]. The first determines a broad voltage plateau between $x = 1$ to 0.7 (Figure 1.10b). The two phases are both hexagonal but have different lattice parameters. The most important change between the two is the electron band gap. The first hexagonal phase has a large band gap (2.7 eV) and is a semiconductor, while the second one, with a very narrow energy gap, is almost metallic [61–64]. As reported in table 1.1, the electronic resistance varies up to three orders of magnitude between the two phases. The second phase transition around $x = 0.5$ is harder to spot, but a small bump in the voltage is visible. This is an order disorder phase transition with almost no change in the crystal lattice parameters and involves a rearrangement in the lithium position.

As anticipated, the chemical diffusion coefficient variation as a function of the intercalation fraction (Figure 1.10c) is strongly impacted by the derivative of the electrode potential. The drop experienced for $x > 0.7$ is indeed linked to the phase transition plateau, where the derivative is almost zero. Moreover, the drop in electronic conductivity changes the diffusion mechanisms: ions and electrons are no longer able to travel as neutral particles, and diffusion is strongly impacted. Interaction between ions and electrons is not treated in the present work; for some hints on the subject, refer to [52, 65].

$LiCoO_2$ can be deposited as a thin film with different processes. The preferred one is sputtering followed by high-temperature annealing, which ensures a high-quality film in terms of density and crystallinity. A main issue with sputtering is the generation of large defects when depositing film thicker than a few µm [68]. Other deposition methods are proposed in the literature, comprising PLD and hydrothermal [69, 70], which have however major limitations in process scalability. ALD and electrodeposition [36, 71] ensure much higher control on the film morphol-

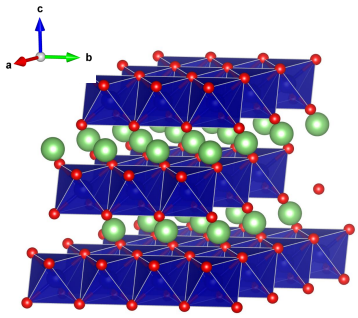

(a) $LiCoO_2$ crystal structure, lithium in green

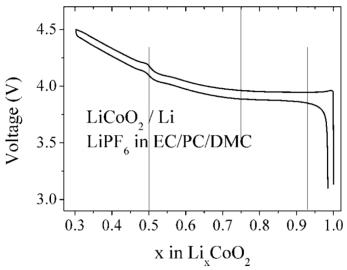

(b) Voltage variation as a function of the intercalation fraction (reproduced with permission from [66])

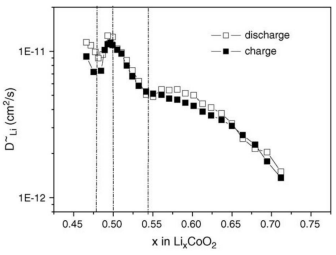

(c) Diffusion coefficient variation as a function of the intercalation fraction (reproduced with permission from [67])

Figure 1.10: $LiCoO_2$ summary

ogy, but the latter is clearly superior when micrometer-size film has to be deposited due to its high deposition rate.

$LiFePO_4$ *(LFP)*

Lithium iron phosphate (LFP) is another popular electrode material. Ion conduction is supported by 1D channels crossing the crystal matrix (Figure 1.11a). It is the cheap and environmentally friendly counterpart of LCO. Comparing static performance, only $LiFePO_4$ is a perfect cathode material. Its volumetric and gravimetric capacities are quite close to those of the LCO. It also possesses a flat voltage plateau at 3.4 V (Figure 1.11b), constituting a very stable voltage source. As one can expect from the theoretical introduction, the flat voltage plateau is the signature of a phase transition. Actually, the only two stable phases are $LiFePO_4$ and $FePO_4$. Unfortunately, this is not good news in terms of dynamic performances. We pointed out how the diffusion inside the electrode relies on concentration and a chemical gradient. But if the intermediate phases are highly energetic and difficult to form, it implies that it is quite hard to build a concentration gradient. This results in a very poor chemical diffusion coefficient compared to LCO. We showed how the diffusion coefficient of cobalt oxide was suppressed during the phase transition due to the flat profile of the voltage. In the case of iron phosphate, the voltage is on a unique plateau, and the chemical diffusion coefficient is suppressed at all stoichiometries (Figure 1.11c). That is the price to pay for an ideal flat voltage.
As for the case of LCO, the phase transition impacts the band gap, but unfortunately, neither of the two phases is conductive. The lithium-rich phase has an enormous 6 eV band gap and is basically an insulator. The second phase with half the band gap (3.2 eV) is still a poor electron-conducting semiconductor [72]. As suggested for LCO, poor electron mobility is strongly correlated with poor chemical ion diffusion due to interaction between ion-electron couples.
Even with such poor dynamic performance, LFP is still an interesting option due to its low cost. It can be deposited as a thin film by PLD, sputtering, ALD, and electrodeposition [73–77].

$LiMn_2O_4$

Another popular oxide among cathodes is the spinel lithium manganese oxide $LiMn_2O_4$. As LFP, this cathode is interesting from a commercial point of view due to its cheap precursors. Another

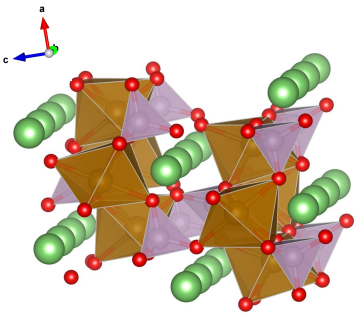

(a) $LiFePO_4$ crystal structure, lithium in green

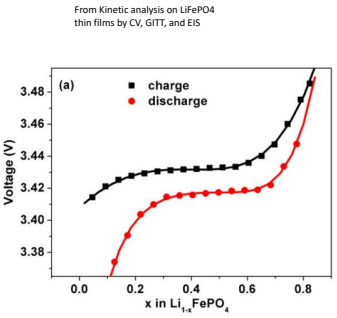

(b) Voltage variation as a function of the intercalation fraction (reproduced with permission from [73])

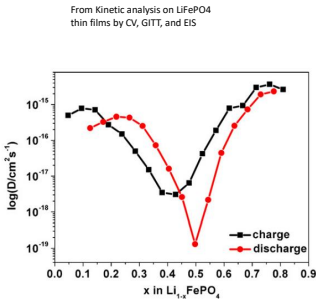

(c) Diffusion coefficient variation as a function of the intercalation fraction (reproduced with permission from [73])

Figure 1.11: $LiFePO_4$ summary

appealing feature is its 3D ion conduction mechanism. This is particularly relevant information for thin films. During the deposition of crystalline thin films, the crystal grains tend to align in a preferential direction. For 1D and 2D materials, this may represent a problem if the diffusion channels are not oriented in the direction of the electrode/electrolyte interface. A 3D material is more flexible in thin-film design because no preferential orientation is needed to ensure lithium diffusion in the right direction.

In terms of static performance, manganese oxide is quite close to LCO and LFP (Table 1.1). The voltage curve (in purple in Figure 1.12b) of this oxide shows multiple interesting features. The central portion ($1 \leq x \leq 0.6$ Figure 1.12b) is close to the ideal shape traced in Figure 1.7a. This is due to the excellent stability of the crystal and its good electronic conductivity. Both hypothesis of constant energy for the insertion sites and non-interaction between inserted atoms are respected. The second half is a phase transition plateau similar to that of LFP. The phase forming at poor lithium content is characterized by a small increase in lattice parameters [78, 79]. In this region, only the two phases $Li_{0.6}Mn_2O_4$ and $Li_{0.3}Mn_2O_4$ are stable. If extraction proceeds further, a second ideal zone is expected up to MnO_2 formation [80]. The third feature is a low-voltage phase transition plateau, which corresponds to the formation of a tetragonal phase Characterized by a distortion of the MnO_6-octahedra (in purple in Figure 1.12a) . This phase cannot be converted back to $LiMn_2O_4$ and is not exploited during reversible cycling [81, 82]. This electrode possesses a fairly constant ion diffusivity, as reported in Figure 1.12c. The reported value for electronic conduction in literature varies largely, even if most authors agree on a high value around $1 \times 10^3\,\Omega\,$cm. Notwithstanding, the implementation of this electrode in a thin-film configuration has not been particularly successful so far. Even a cathode of a few hundreds of nanometers seems to be unable to sustain a current density as high as LCO [83–86]. This can be explained by the lower ion diffusivity [86]. Due to its inferior volumetric capacity density, manganese cathode has to be fabricated in thicker film with respect to LCO to obtain the same total area capacity. This will couple negatively with the lower diffusion coefficient, degrading even more the dynamic performance. $LiMn_2O_4$ is comparable to cobalt oxide when the cycling stability is compared (number of cycles before $20\,\%$ capacity loss). For applications with a lower constraint over occupied volume and required current rating, manganese can be a viable choice from an economical and environmental point of view.

$LiMn_2O_4$ has been fabricated as thin-film with all common techniques, including CVD, sputtering, PLD, ALD, sol-gel, and electrodeposition [80, 82, 85–88]. The reported deposition rate for

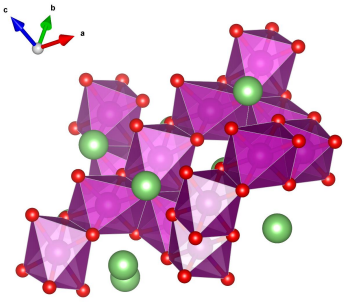

(a) $LiMn_2O_4$ crystal structure, lithium in green

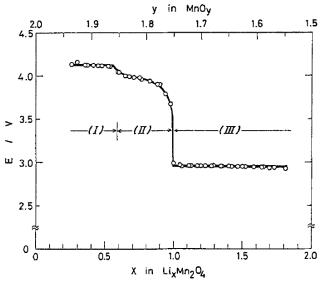

(b) Voltage variation as a function of the intercalation fraction (reproduced with permission from [78])

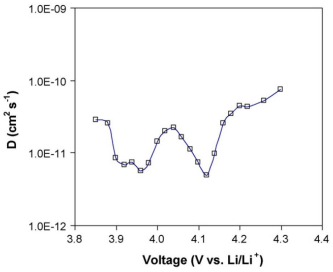

(c) Diffusion coefficient variation as a function of the intercalation fraction (reproduced with permission from [80])

Figure 1.12: $LiMn_2O_4$ summary

sputtered $LiMn_2O_4$ ($1\,\mathrm{nm\,min^{-1}}$ [82, 89, 90]) seems to be much lower than for LCO ($10\,\mathrm{nm\,s^{-1}}$ [91]), which may be another reason for the poor success of this electrode.

$LiNiO_2$

Nickel oxide is the fourth high-voltage cathode in this review. It is a 2D-layered oxide (Figure 1.13a) of the same family of LCO. $LiNiO_2$ is a highly performing material in terms of both static and dynamic performance. It has a high capacity density, a high voltage, and good conduction of both ions and electrons (metal). During lithium insertion and extraction, the crystal structure changes multiple times, as reported in Figure 1.13b. Due to multiple phase transitions, the curve is far from ideal. It is still possible to identify the voltage plateau linked to the two-phase region between phases H1 and M ($0.8 \leq x \leq 0.7$) and between phases H2 and H3 ($0.25 \leq x \leq 0.1$). As expected, the effect of the phase transition plateau is visible also in the variation of the chemical diffusion coefficient reported in Figure 1.13c.
Such electrodes suffer from two related problems: off-stoichiometry synthesis and poor cycling performances. The synthesis is reported to be very difficult, and small variations in the process produce impurities and imperfections [92, 93]. This is the main reason behind the huge variation in terms of voltage curve and performance in literature. Compared to cobalt oxide, nickel is reported to be far less stable, and nickel atoms can easily take the place of lithium, blocking the diffusion path in non-stoichiometric compounds [94] . A remark on the whole point is that no systematic study on the difficulties of synthesis has been performed for thin-film. As a matter of fact, complete studies were performed in 1985 and 1990 [95, 96] and quoted as proof of difficult synthesis until today. This is one of those cases in which the literature seems to quote an infinite number of sources without anyone actually performing the experiment. For the sake of my personal amusement and in order to dissolve any accusation of superficiality, I will report the full quoting path of the last 30 years. The story begins, or even better, ends, in 2022 with Rao et al. [93]. In this work, the word "proverbial" is used to describe the allegedly difficult synthesis of $LiNiO_2$. Apparently, such a proverbial fact does not need any reference. Anyway, looking closer at the first quote, we can easily deduce where the *proverbiality* comes from: in the recent review of Bianchini et al. [97] we found a less vigorous but still solid "strongly prone" (to off-stoichiometry). We are hence referred to the work of Lai et al. of 2009 [98] and the old but gold work of J.R. Dahn et al. dating back to 1990 [94]. The latter does not seem to be particularly

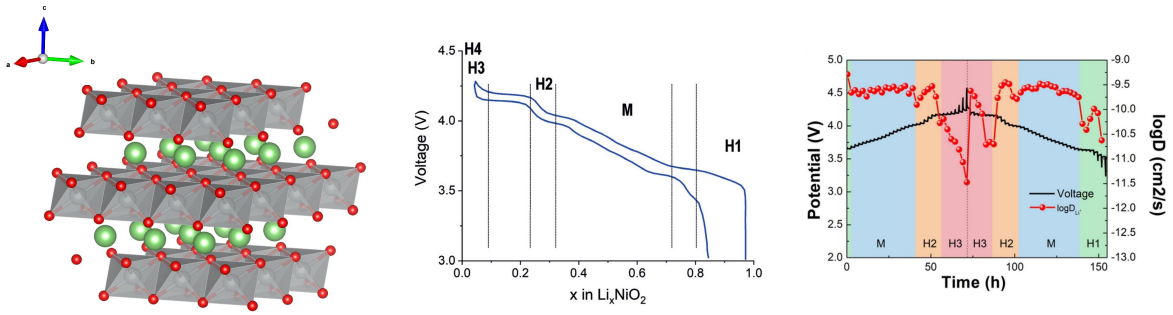

(a) $LiNiO_2$ crystal structure, lithium in green

(b) Voltage variation as a function of the intercalation fraction (reproduced with permission from [97])

(c) Diffusion coefficient variation as a function of the intercalation fraction (reproduced with permission from [93])

Figure 1.13: $LiNiO_2$ summary

certain of the difficulty of synthesis, but highlights the variety of experimental results and different stoichiometric compounds reported in the literature. The former is another piece of our infinite bibliographical puzzle. In Lai et al. the opinion has already turned to a mild "tendency" and, for any doubts, invites us to refer to two sources. The first is the work of Li et al. of 2007 [99], which eventually, after a laconic "very difficult to synthesize," points us in the direction of an actual work on synthesis carried out by Morales et al. in 1990 [96]. The second is the work of Bianchi et al. of 2001 [100] which indeed proposes a reliable method to obtain stoichiometric and reproducible $LiNiO_2$. It is true that in the introduction, Bianchi et al. suggest that it "appears to be difficult", but just compared to the LCO, not in general. Anyway, we can agree that reliable works on solid-state powder synthesis dating back 30–40 years are not enough to prove anything concerning the difficulties of processing thin-films.
It is, however, true that off-stoichiometry electrodes show poor stability during cycling [100, 101]. At the same time, for the stoichiometry cathode, the poor cyclability seems to strongly correlate with the last phase transition (H3-H4) [93]. At this stage, the crystal lattice experiences a larger volume expansion, which results in cracks and contact loss [93, 97]. If properly cycled nickel oxide is stable [102, 103] and the actual implementation in thin-film cathode does not seem to really disqualify it with respect to LCO [104].
Fabrication processes are available for ALD, sputtering, hydrothermal, and electrodeposition [98, 104–106]. In commercial cathodes, it is common to mix cobalt, nickel, and manganese (NMC electrodes) in order to decrease the price of the electrode without major loss of performance. This approach can also be implemented for thin-film solid-state batteries [107, 108]. The results are electrodes with a capacity density even higher than LCO but much lower electronic conductivity, limiting their rate performance [109].

LiV_3O_8

Vanadium oxide can be used as an electrode in two different stoichiometries and crystal structures: LiV_3O_8 and LiV_2O_5. The two are quite close to each other with respect to the voltage profile, which is a bit lower than other oxides presented so far (Figure 1.14a and 1.15a). Apart from that, the two are very different and complementary in their properties. Let's start with LiV_3O_8. This compound crystallizes in a layer structure with a 2D diffusion plane for lithium ions (Figure 1.14b). In contrast to other oxides seen so far, lithium trivanadate is charged by inserting

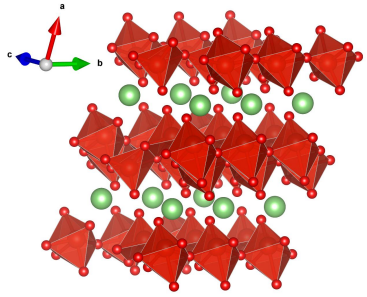

(a) LiV_3O_8 crystal structure, lithium in green

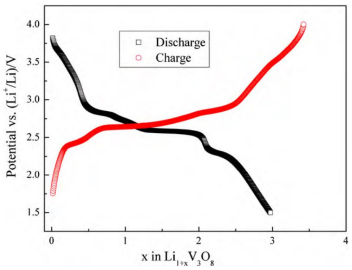

(b) Voltage variation as a function of the intercalation fraction (reproduced with permission from [118])

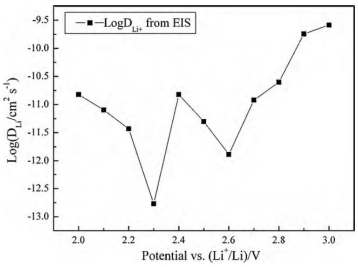

(c) Diffusion coefficient variation as a function of the intercalation fraction (reproduced with permission from [118])

Figure 1.14: LiV_3O_8 summary

more lithium. In fact, this electrode can accommodate up to 5 lithium atoms per formula unit, $Li_{1+x}V_3O_8$ ($0 \leq x \leq 4$). This gives rise to a complex voltage profile with bumps and plateaus, as reported in Figure 1.14b. Moreover, the degree of crystallinity strongly impacts the intercalation energy sites and their availability. Low-crystalline LiV_3O_8 has a totally flat profile [110, 111]. Available energy density is impacted as well, and reported values in the literature can vary between 100 to 400mA h g^{-1}[110, 112]. From a theoretical point of view, the lithium intercalation is expected to take place in three different regimes [113]. The first is a single-phase intercalation for $0 \leq x \leq 1$. Followed by a phase transition plateau in the range $1 \leq x \leq 3$, which is partially visible in the major part of the reported curves. The final part is another single-phase region for $3 \leq x \leq 4.5$. The final phase has a much lower chemical diffusion coefficient (Figure 1.14c), and at room temperature it cannot be fully exploited [114, 115]. The size itself of the plateau is influenced by the dynamics of the second phase. moreover, degree of crystallinity, crystal orientation, and current density can all impact the measured voltage profile [112, 116, 117] leading to large variations with respect to the expected profile.
Dynamic limitation, linked to both low ionic and electronic conduction, is the main drawback of this electrode. RF sputtered thin-film configurations are reported to be able to insert up to 5 lithium atoms [118] but only at a minuscule current density (10 µA cm^{-1}) for a film of a few hundred nanometers, limiting the practical application of this electrode.

LiV_2O_5

The second oxide based on vanadium is alternatively used as an anode or cathode due to its intermediate voltage (Figure 1.15b). This is, of course, a negative because it means that it is both a low-voltage cathode and a high-voltage anode, resulting in poor power density in the full cell. Concerning the voltage curve, two plateaus are visible, corresponding to a two-phase region for intercalation fraction in the range $0.1 \leq x \leq 0.35$ and $0.5 \leq x \leq 0.9$ for a total of three different phases. The material, as for the previous vanadium oxide, can be deposited at different degrees of crystallinity, with a smoothing effect on the voltage curve [119]. The same smoothing appears as soon as the current rate increases. This is a sign of low ion diffusion, which results in poor rating performances [119–121]. The one-dimensional conducting path of the crystallized structure, as for LFP, makes the ion diffusion anisotropic and sluggish. On the other hand, LiV_2O_5 shows very good electron conduction, which results in a low ohmic drop (the initial

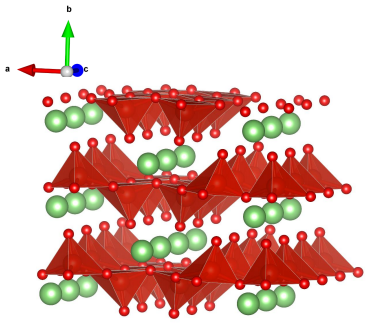

(a) LiV_2O_5 crystal structure, lithium in green

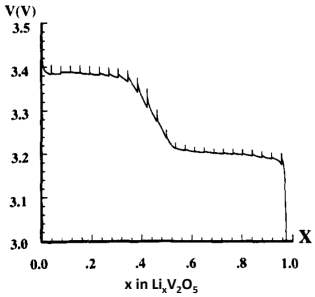

(b) Voltage variation as a function of the intercalation fraction (reproduced with permission from [127])

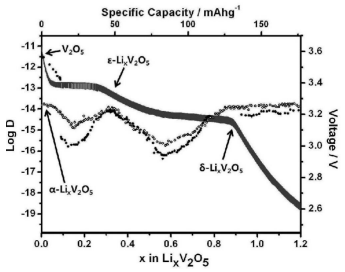

(c) Diffusion coefficient variation as a function of the intercalation fraction (reproduced with permission from [128])

Figure 1.15: LiV_2O_5 summary

voltage is constant at different current rates) [121]. The low dynamic performance is the main reason for the poor success of this material. Notwithstanding, a large amount of research has been conducted, in particular in the domain of thin-film batteries. This cathode is attractive due to a low-temperature synthesis of both amorphous and crystalline phases; the latter does not require a very high temperature step ($<300\,°C$) to be crystallized. Low-temperature deposition is reported for ALD, sputtering, CVD and PLD [119, 120, 122–125]. This improves the compatibility of the electrode, which is popular in the ALD configuration for 3D vertical stack [121, 126]. In sub-100-nanometers films, the low diffusion coefficient has less impact on the overall dynamic performance.

Li_xMoO_3

The last positive electrode I will present is molybdenum oxide Li_xMoO_3. The material can be crystallized in different phases, but the most studied and easily synthesized are as $\alpha - MoO_3$ (orthorhombic in Figure 1.16a) and $\beta - MoO_3$ (monoclinic). The α phase is the most commonly used as electrode material. It possesses a quite regular voltage profile. In liquid electrolyte, this electrode performs poorly in terms of cycling and presents an irreversible reaction at the beginning of the charge, which leads to poor cyclability. This is not the case in thin-film solid-state cells [129]. This irreversible reaction is characterized by a voltage plateau in the range $0 \leq x \leq 0.25$ and is explained by the intercalation of liquid solvent inside the electrode [130]. Literature results must then be critically analyzed in order to predict the performance in a thin-film configuration. In particular, different studies on PVD, ALD or CVD-deposited thin-film rely on liquid electrolyte for the electrochemical characterization and are hence not fully reliable [131–133]. This is a general warning valid for the whole literature when dynamic and cycling performance has to be deduced from previous works.
For both liquid and solid electrolytes, the reaction can be described as a first solid-solution for $0 \leq x \leq 0.5$ a two phase region ($0.5 \leq x \leq 1$) and a second solid solution in the range $1 \leq x \leq 1.6$ [132].

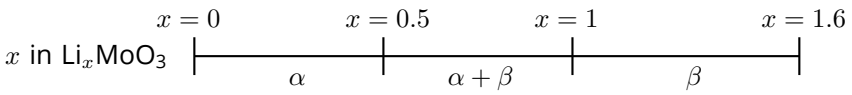

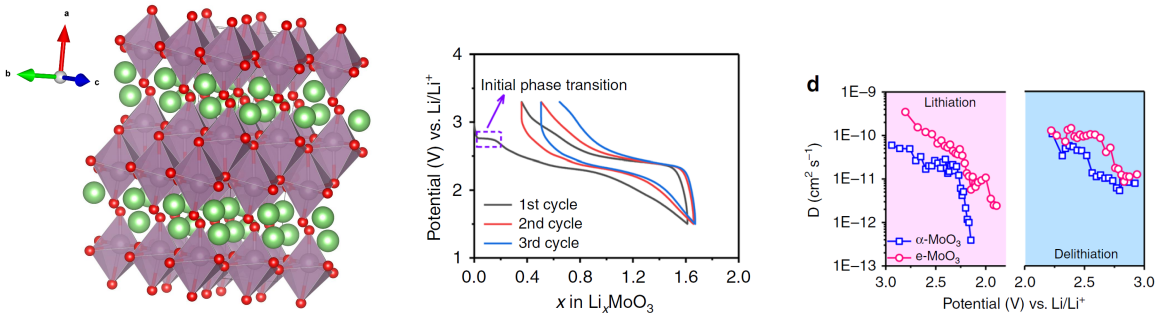

(a) $LiMoO_3$ crystal structure, lithium in green

(b) Voltage variation as a function of the intercalation fraction (reproduced with permission from [140])

(c) Diffusion coefficient variation as a function of the intercalation fraction (reproduced with permission from [140])

Figure 1.16: $LiMoO_3$ summary

A clarification on the results of Self et al. for all-solid state cells [129] is needed. During the first discharge, the thin-film cell experiences a $25\,\%$ loss. Which is even higher than $15\,\%$ loss linked to irreversible reactions in liquid electrolytes. Two points are important. First, the liquid loss is not limited to the first cycle and grows to $40\,\%$ by cycles twenty. Second, the thin-film cell voltage is cut before complete de-intercalation. This is clearly visible from both the different shape of the voltage at the end of the discharge and by analyzing the current in the cyclic-voltametry at $2\,\mathrm{V}$ in the oxidation cycle. Even if the reaction peaks are at the same position, thin-film have worse conduction and broader features. In fact, the first cycle loss is artificial and linked to the discharge protocol, which stops the discharge too early. The drop in diffusion coefficient in the lithium poor phase (Figure 1.16c) is another indicator of its poor ionic conduction. In general, this electrode suffers from non-optimal ionic conduction at all stoichiometry and even worse electronic conductivity, resulting in poor dynamic performance [134, 135]. Notwithstanding, the concern of poor cyclability, typically observed in liquid configuration, should be revisited for thin-film solid-state cells [135].
A broad range of processes are available for deposition, comprising ALD, PLD, sputtering, electrodeposition, and CVD [132, 133, 135–139].

Conclusion on cathode materials for TFBs

In conclusion, it is possible to affirm that among the available cathode materials at the present time, LCO is overall the most performing one [141]. Some materials may outperform it in some aspects, but the price is usually a strong reduction in other indicators. Unless a strong constraint from the final application is present, cobalt oxide is the best choice for small and highly performing thin-film batteries. Notwithstanding, not all materials have been properly implemented in a thin-film, all-solid-state configuration and some of the conclusions in the literature are based exclusively on liquid-electrolyte cells. Among others, the assessment of the cycling stability with respect to the solid-electrolyte interface and a complete study of the effect of the thin-film configuration on the rating performances should be properly investigated for all materials before drawing any hard conclusions.

2.3 Anode materials

The review of anode material is going to conclude this section on electrode materials. I already mentioned that anode materials are mostly based on alloying mechanism. Exceptions are the intercalation in TiO_2 and plating on lithium metal. The final section of the present chapter is entirely devoted to anode-free configuration, which is a special case of lithium plating anode, so I will not spend too much time on it at present. The only observation concern the volumetric expansion of lithium anode and anode-free configuration. Being a plating electrode, it is not totally correct to talk about volume expansion because the anode itself does not expand. It simply increases in thickness, and the volume expansion depends on the initial thickness of lithium and the capacity of the cathode. In an anode-free configuration, the lithium anode is absent at the beginning, hence it would have an infinite expansion (initial volume is zero) between charge and discharge states. In the summary table (table 1.2) I filled the data for an anode containing (before charge) exactly the amount of lithium to be charged, which means a doubling in the final thickness between charge and discharge.

Another remark on the same tone is the calculation of the volumetric and gravimetric capacity

Anode	**OCV** (V)	Q_V (mA h cm^{-3})	ρ (g cm^{-3})	Q_m (mA h g^{-1})	σ_{el}^{-1} (Ω cm)	$\tilde{D}$ (m^2 s^{-1})	**ΔV** (%)
Li	0	2100	0.53	3900	10^{-7}	10^{-12}	100
Al	0.2 to 0.4	2700	2.7 to 1.8	1000	10^{-7}	10^{-14}	95
In	0 to 0.6	7300	7.3	1000	10^{-7}	10^{-11}	50
In_2O_3	0 to 1.7	7200	7.2	1000	10^{-2} to 10^{5}	-	50
Sn	0.3 to 0.8	7300	7.3 to 2.6	1000	10^{-7}	10^{-16} to 10^{-14}	250
SnO_2	0.2 to 1.2	3500	7.0 to 2.6	500	10^{-3}	-	200
Sn_3N_4	0.2 to 1.2	5800	7.2 to 2.6	800	10^{-2}	-	200
Si	0 to 1	6700	2.3	4200	10^{5}	10^{-14}	350
TiO_2	1.4 to 2	1300	4.3	300	10^{-8} to 10^{-6}	10^{-18}	3

Table 1.2: Properties of popular anode materials at RT. From left to right: minimum and maximum voltage; theoretical gravimetric capacity density; theoretical density; theoretical volumetric capacity density; average electron conductivity; average chemical diffusion coefficient; volume expansion calculated as ratio between initial volume V_0 and final volume V. Sources are provided at each section.

densities. Almost everybody in the literature will report the volumetric and gravimetric energy density at the minimum volume. That is, they will divide the stored capacity by the volume before storage. In the summary table, I reported the boosted values to be coherent with the literature, but at the same time, changes in density are also available to calculate the real volumetric capacity at maximum volume. Because anode with the highest volumetric energy density possess also the highest volume expansion, the two will compensate and reduce the actual differences between materials.

Al

Aluminum alloying with lithium is a well-known phenomenon. Before delving into it, I will detour for a brief excursus. In commercial batteries, the anode current collector is usually made of copper and the cathode of aluminum. Copper is far more expensive, and in fact, it is chosen solely to avoid unwanted lithium alloying in the anode current collector. Ion diffusion in metal is an even more serious issue in thin-film due to the direct synthesis of electrodes on substrates,

which are usually metals or the silicon wafer itself.
Binary alloy electrodes are particularly convenient to treat through phase diagrams. Today, we have high-quality phase diagrams of all lithium alloys, which can help us to precisely describe the voltage variation and the expected dynamics during charge and discharge. In Figure 1.17aa the latest phase diagram of Al-Li systems is shown down to $100\,^{\circ}$C. A total of four phases are thermodynamically stable: AlLi, Al_2Li_3, $AlLi_{2-x}$, and Al_4Li_9. The first and third phases form solid solutions in the range of $0.49 \leq x \leq 0.51$ and $0.64 \leq x \leq 0.66$. The other two are line compounds, stable in a narrow stoichiometric range. From the Gibbs free energy of each phase, it is possible to predict the theoretical voltage of each one vs. lithium metal. In the same order, the four phases are expected at 300 mV ,90 mV ,10 mV, and 4 mV [142]. We can try, from this knowledge, to explain the typical voltage profile for an aluminum electrode, as reported in Figure 1.17ab. At the very beginning, no lithium is present in the system, hence the variation of the Gibbs free energy is theoretically infinite. The actual, finite potential, measured as soon as the alloying of lithium begins, strongly depends on the electrode surface. The presence of residual oxide or other impurities may change its value [142, 143]. Once the nucleation of the new crystal phase ($\beta -$ AlLi) is completed, the voltage stabilizes, and the phase transition can continue undisturbed at 300 mV. As soon as the first phase transition is over, the system is supposed to start the conversion to the second phase Al_2Li_3. This phase is a line compound, and, as already pointed out in the introduction, line compounds are difficult to exploit because they readily tend to transform due to the dynamic lithium gradient. Indeed, no plateau in the predicted range of $1 \leq x \leq 1.5$ is visible at room temperature. However, at higher temperatures, it is possible to recover this second phase [142]. The following phase should be accessible, but its voltage is already very close to zero (10 mV) and the cell polarization plus the lithium gradient, do not permit but an extra 0.1 intercalation fraction before crossing the 0 V limit. The discharge is characterized by a quick inflection before stabilizing back to the AlLi plateau. The full capacity cannot be recovered in the particular case reported in Figure 1.17ab because the systems experience cracking due to volume expansion. Mechanical stress is a common feature of alloying electrodes, and aluminum, with a doubling of the total volume during the first plateau, is no exception. Deposition and patterning of aluminum is a mastered art due to its extensive use in ICs manufacturing. For any details, refer to Wolf and Tauber [29] where an entire chapter is dedicated to the subject. Sputtered and evaporated aluminum anodes in thin film configuration with acceptable static performance are reported in literature [144, 145].

In *and* In_2O_3

The second binary system we are going to analyze is indium-lithium. The phase diagram of this system is reported in Figure 1.17ba. The phases involved during charge and discharge are InLi,In_4Li_5,In_2Li_3, $InLi_2$. With voltage plateaus at 620 mV, 340 mV,120 mV, and <50 mV. The last phase, with such low voltage, is found at higher temperatures only, where the solubility range and its voltage are increased [149]. In general, the majority of alloying takes place in the first phase at 620 mV (see Figure 1.17bc). Restricting the operation of the anode to this zone reduces the available capacity but also limits the volume expansion to "only" 50 % [150]. Indium is generally accepted as a fast lithium conductor, but no systematic studies at room temperature are available [147, 149].
In literature, In_2O_3 is proposed as an anode material as well, but a closer look at the chemical intercalation process will make it clear that it is equivalent to an indium anode. Indeed, as soon as the charge begins, a conversion reaction will transform the indium oxide into lithium oxide and metal indium. Once the metallic indium is formed, the alloying between indium and lithium

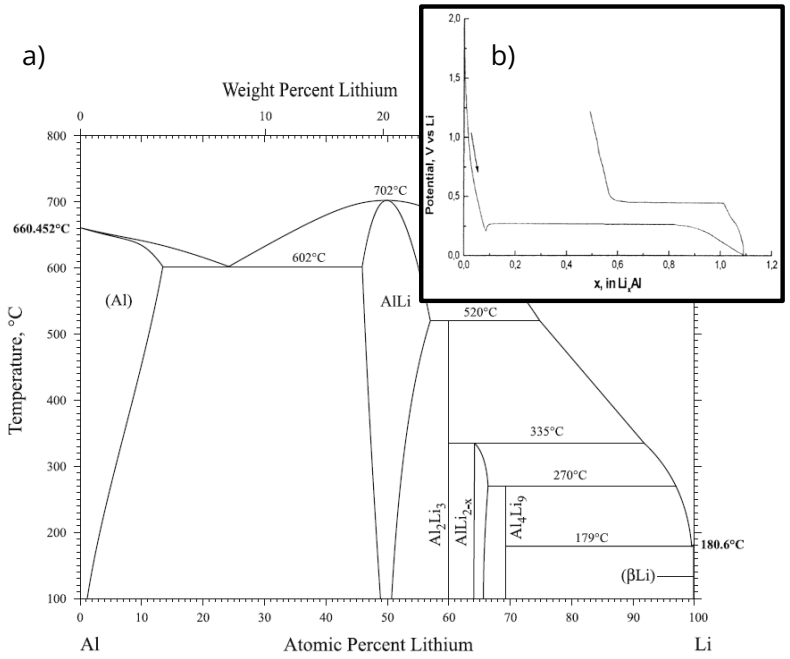

(a) a) Al−Li system phase diagram (reproduced with permission from [146]); b) Voltage variation as a function of the intercalation fraction (reproduced with permission from [143])

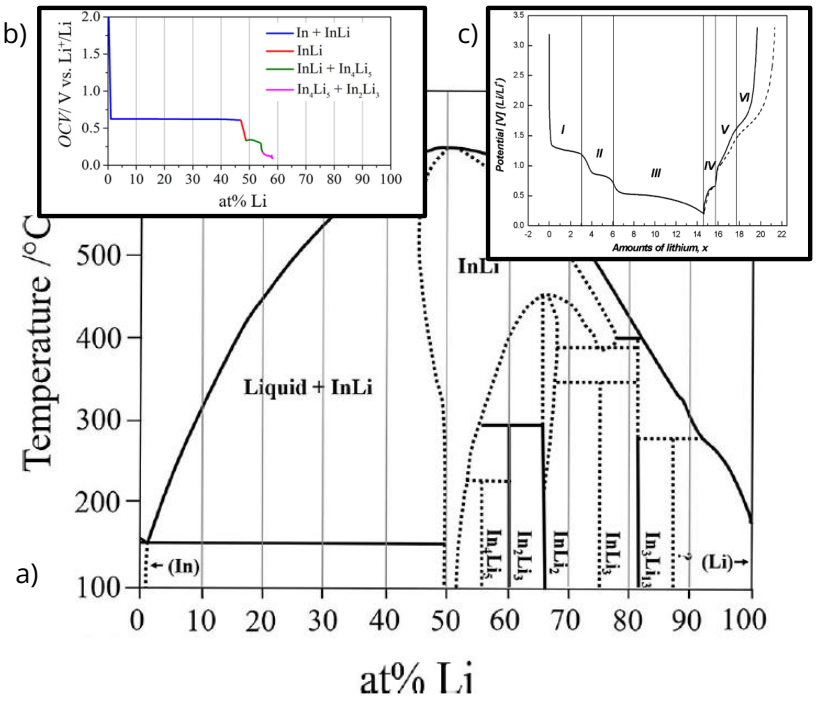

(b) a) In−Li system phase diagram (reproduced with permission from [147]); b) Voltage variation as a function of the intercalation fraction (reproduced with permission from [147]); c) Voltage variation as a function of the intercalation fraction for In_2O_3 (reproduced with permission from [148])

Figure 1.17

takes place [151]

$$\mathrm{In_2O_3} + 6\,\mathrm{Li^+} + 6\,\mathrm{e^-} \longrightarrow 2\,\mathrm{In} + 3\,\mathrm{Li_2O}$$
$$\mathrm{In} + x\,\mathrm{Li^+} + x\mathrm{e^-} \rightleftharpoons \mathrm{InLi}_x$$

An example of the resulting voltage is reported in figure 1.17bc. Zones I and II correspond to the lithium oxide formation, while the third plateau at around 600 mV corresponds to the InLi phase formation. The discharge profile suggests a partial reversibility of the conversion reaction, but no agreement on the subject has been reached yet [152]. Indium can be easily deposited by sputtering, evaporation, PLD, and electrodeposition [148, 152]. The main drawback of indium is its very high cost, which hinders its adoption in a large-volume markets.

Sn,SnO_2 *and* Sn_3N_4

The popular and cheap counterpart of indium is tin. This system has been widely studied and characterized since the 1980s. Up-to-date phase diagram of the tin-lithium system is reported in Figure 1.18aa. All phases up to $Li_{17}Sn4$ can be exploited during intercalation [159]. The voltage plateaus, as shown in Figure 1.18ac, ranges from 0.38 mV to 0.66 mV at room temperature [160]. The formation of lithium-rich phases is followed by a large volume expansion. At the beginning of the last solid solution domain in the range $0.8 \leq x \leq 1$ of lithium molar percent, the volume expansion is 250 %. Further intercalation is possible, but >400 % volume expansion is reached. In figure 1.18ab the volume expansion as a function of the quantity of intercalated lithium is reported. The shape is a quite flat parabola. At this point, a quick remark about the link between voltage and thermodynamic properties is necessary. In the theoretical section, we expressed the voltage versus lithium in terms of the Gibbs free energy of formation. One main hypothesis of the derivation of that equation and of the whole ion diffusion discussion is constant volume. In cathode, the mean volume expansion is in the order of 1 to 3% and the hypothesis can be considered satisfied. Of course, in anode, the volume expansion cannot be disregarded anymore. In particular, the new expression for the electrode voltage at constant pressure and temperature reads:

$$\mu = \frac{\partial G}{\partial n}_{P,V} = \frac{dE}{dn} - T\frac{dS}{dn} + P\frac{dV}{dn} \tag{1.14}$$

This is not a real issue from our point of view, as long as the relationship between potential and concentration is available. But it will not be possible anymore to straightforwardly calculate the Gibbs free energy from the OCV. On the other hand, it will make it much more difficult to treat the system from a dynamic point of view and to extract the chemical diffusion coefficient. From the point of view of cycling performance, this electrode shows low stability due to mechanical stress and cracking [25]. As for indium, other tin compounds are used in the literature as electrodes: SnO_2 and Sn_3N_4. Those two electrodes are closely related to the pure metal one. The conversion reaction (Figure 1.18ba) creates, as in the case of indium, lithium oxide and nitride, and further lithium alloying takes place in the metal tin. The whole process is described according to the following reactions [156, 161, 162]:

$$\mathrm{SnO_2} + 4\,\mathrm{Li^+} + 4\,\mathrm{e^-} \longrightarrow \mathrm{Sn} + 2\,\mathrm{Li_2O}$$
$$\mathrm{Sn} + x\,\mathrm{Li^+} + x\mathrm{e^-} \rightleftharpoons \mathrm{Li}_x\mathrm{Sn}$$

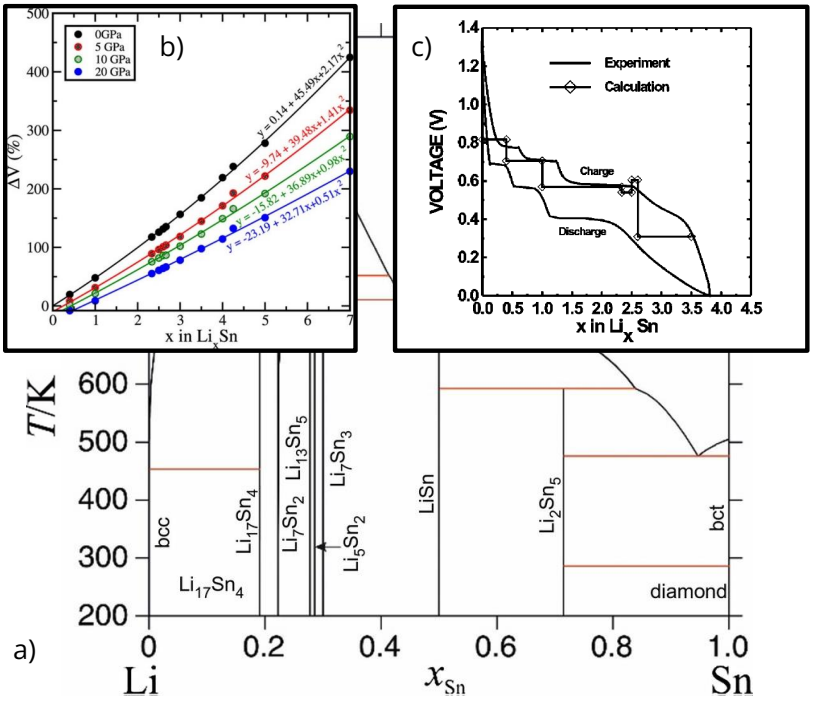

(a) a) Sn−Li system phase diagram (reproduced with permission from [153]); b) Volume variation as a function of the intercalation fraction (reproduced with permission from [154]); c) Voltage variation as a function of the intercalation fraction (reproduced with permission from [155])

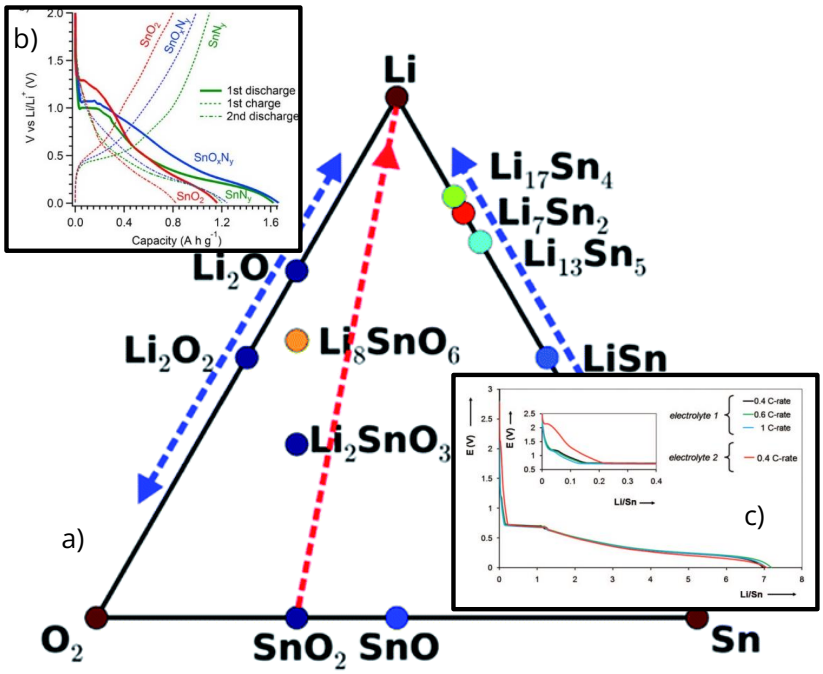

(b) a) Sn−Li Sn−Li−O system phase diagram (reproduced with permission from [156]); b) Voltage variation for different Tin systems (reproduced with permission from [157]); c) Voltage variation as a function of the intercalation fraction for Sn_3N_4 (reproduced with permission from [158])

Figure 1.18

and

$$\mathrm{Sn_3N_4} + 4\,\mathrm{Li^+} + 4\,\mathrm{e^-} \longrightarrow 3\,\mathrm{Sn} + 4\,\mathrm{LiN}$$
$$\mathrm{Sn} + x\,\mathrm{Li^+} + x\mathrm{e^-} \rightleftharpoons \mathrm{Li}_x\mathrm{Sn}$$

The close relationship between pure tin, tin oxide, and tin nitride in terms of lithium storage mechanisms is confirmed by the voltage profile. As reported in Figure 1.18bb and 1.18bc, all compounds have similar OCV. The different plateaus of tin are not quite visible due to the poor crystallinity of the converted metal. However, the oxide and nitride electrodes are reported to be much more stable during cycling with respect to the tin anode [161, 163]. The superior cycling performance can be understood in terms of the additional conversion phase. With respect to pure tin metal, in oxide and nitride electrodes, the tin domains are surrounded by an electrochemically inactive phase of Li_2O or LiN. The volume expansion during lithium intercalation is then buffered by the extra phase, which is at the same time a high electron and ion conductor. In the end, it is like embedding tin nanoparticles in a matrix.
All three materials can be deposited as thin films by evaporation, sputtering, CVD, ALD, and electrodeposition [25, 157, 158, 161, 163–167].

Si

We already anticipated the possibility of alloy formation between lithium and silicon, which may be a problem during thin-film fabrication. The same alloying reaction can, of course, be exploited to build an electrode from silicon. The lithium-silicon phase diagram is reported in Figure 1.19a. Starting from pure silicon on the right, the first alloy is LiSi followed by Li_7Si_3,$Li_{12}Si_7$,$Li_{13}Si_4$, and $Li_{17}Si_4$. The progressive insertion of lithium leads to a huge volume expansion, up to $300\,\%$ for the final phase. As for tin, the volume increase is approximately parabolic (Figure 1.19b). Crystalline silicon and amorphous silicon can both intercalate lithium, but the dynamics differ. In particular, crystalline silicon strongly opposes initial alloying. This results in a high potential drop with respect to the predicted plateau for the first phase. According to the literature, at the electrode/electrolyte interface, the first phase to form is a lithium-rich amorphous phase [169]. At the end of the charge, the alloy recrystallizes into a metastable $Li_{15}Si_4$. After the first amorphization of silicon, the delithiation proceeds as a smooth single phase (Figure 1.19c). The small bump at the beginning corresponds to the transition from the crystalline metastable phase to the amorphous solid solution. The process is understood in terms of the large difference in crystalline structure between silicon and the intermediate phases, which leads to a high nucleation barrier and mechanical stress. For this reason, even if crystalline phases have lower Gibbs energy, amorphization is the preferred route at room temperature [170]. Unfortunately, the formation of the lithium-rich phase at the beginning of the charge process, results in the maximum stress at the interface. Moreover, limiting the total amount of lithium alloyed, as for indium, does not result in a decrease of stress. Starting with already amorphous silicon is beneficial, in order to mitigate electrode cracking. As a drawback, the low electronic conductivity of crystalline silicon (1×10^{-2} S cm), is further decreased in amorphous silicon (1×10^{-5} S cm). In thin-film configuration, properly tuning the thickness of the anode may prevent cracking and enhance cycling performance [171]. Stable cycling is demonstrated for 100 nm thick amorphous silicon. Even if silicon possesses a huge capacity density, such a tiny anode can only account for $70\,\mu\mathrm{A\,h\,cm^{-2}}$ areal capacity, which is quite a low value for real applications.
Deposition of silicon is a finely mastered topic, and the book of Wolf and Tauber [29] is the ideal starting point for anyone craving more details.

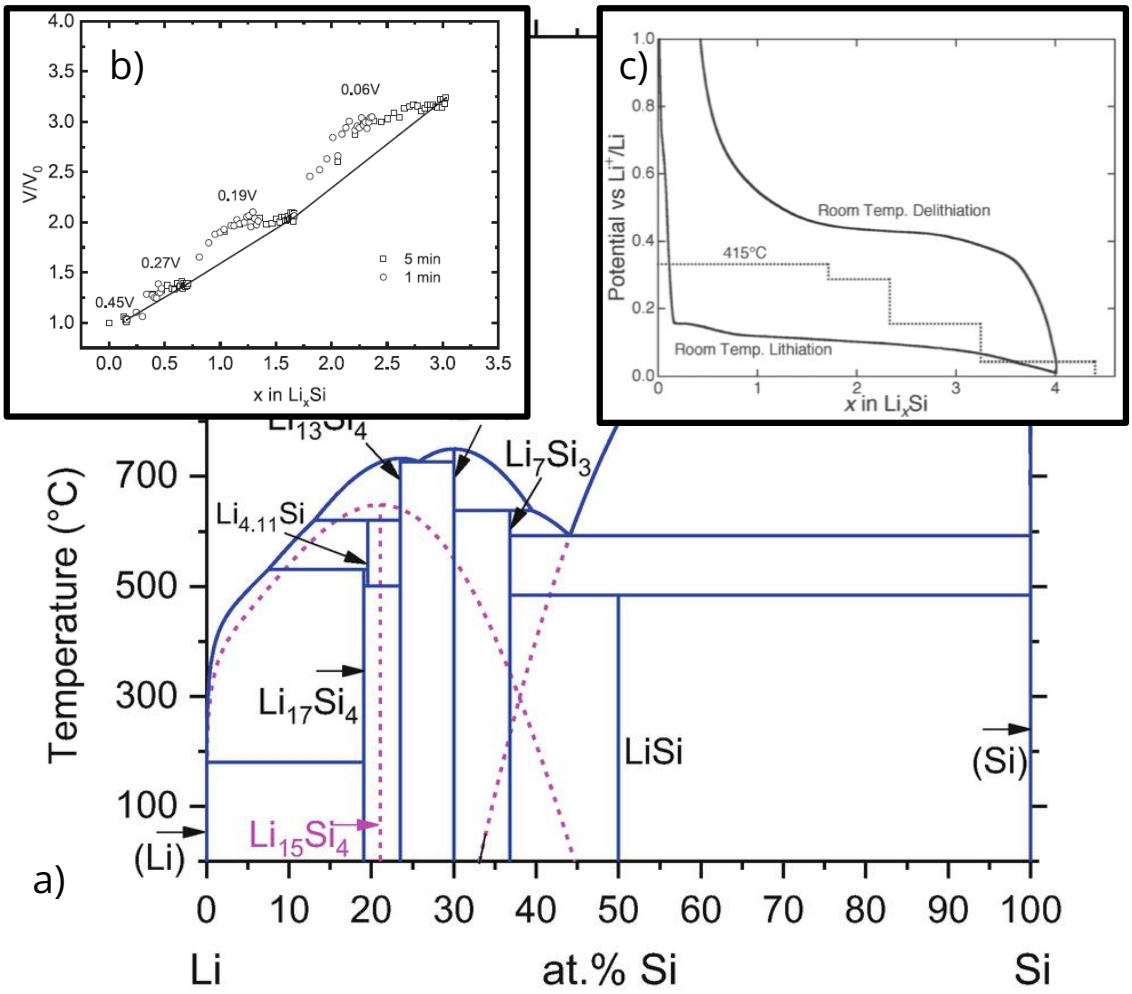

Figure 1.19: a) Si−Li system phase diagram (reproduced with permission from [153]); b) Volume variation as a function of the intercalation fraction (reproduced with permission from [168]); c) Voltage variation as a function of the intercalation fraction (reproduced with permission from [169])

TiO_2

The last electrode in this review will be TiO_2. As for silicon, both crystallized and amorphous phases exist and can intercalate lithium. This is, in fact, the only intercalation anode in this review:

$$x\,Li^+ + TiO_2 + xe^- \rightleftharpoons Li_xTiO_2$$

TiO_2 can crystallize with different group symmetry (polymorphs) and it is named accordingly: rutile, anatase, brookite, hollandite, TiO_2-β [174]. Each polymorph possesses a different disposition of the channel available for lithium diffusion but the only one that is actually exploitable is the anatase (tetragonal, with space group $I4_1/amd$). Anatase can intercalate up to $x = 0.5$ before its amorphization [172, 173]. In Figure 1.20a the voltage profile for crystalline and amorphous electrodes is shown. The crystalline one exhibits a phase transition plateau linked with the two thermodynamically stable phases TiO_2 and $Li_{0.5}TiO_2$. At higher states of intercalation, the crystalline phase converts to an amorphous phase, and the profiles are superimposed. The amorphous electrode shows an ideal solid solution voltage profile. In correspondence with the phase

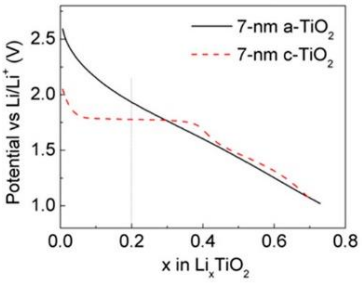

(a) LI_xTiO_2 Voltage variation as a function of the intercalation fraction (reproduced with permission from [172])

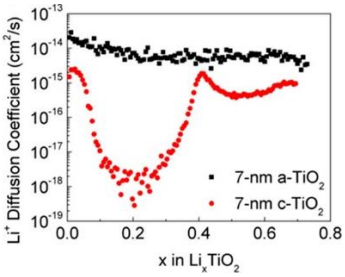

(b) Lithium diffusion variation as a function of the intercalation fraction (reproduced with permission from [172])

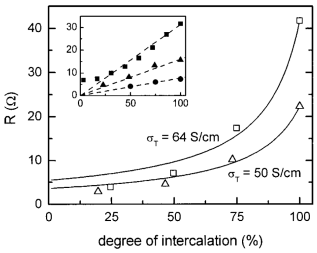

(c) Resistance variation as a function of the intercalation fraction. intercalation degree 100 is equivalent to $Li_{0.5}TiO_2$ (reproduced with permission from [173])

Figure 1.20: TiO_2 summary

transition, the chemical diffusion coefficient of the crystalline phase is strongly suppressed, as reported in Figure 1.20b. For both the crystalline phase and the amorphous phase, the ion diffusion is quite sluggish. Coupled with a very low electronic conductivity, this makes titanium oxide an extremely poor electrode from a dynamic point of view [175, 176]. The resistance varies by two orders of magnitude between the two stable phases, resulting in a continuous variation of the resistance as a function of the intercalation fraction (Figure 1.20c). This characteristic is exploited to realize variable resistance [177], but makes this material quite useless in the domain of thin-film anodes. A last remark is the big gap in reported results between powder and thin-film electrodes. In particular, thin-film seems to exhibit much higher electronic conductivity, on the order of $100\,\mathrm{S\,cm}$. [173, 178], up to 4 orders of magnitude higher. The authors attribute the difference to the grain boundary conductivity, which decreases in dense thin films. In any case, both ionic and electronic conductivity are far below that of other anodes. A final point is the very high crystallization temperature of anatase, which makes it incompatible with most part available solid electrolytes.

Conclusion on anode materials for TFBs

In the context of thin-film all-solid-state batteries, a lot of work is still required to fully evaluate the potential of each anode material. Few works report a full cell from which the performance can be clearly assessed. A possible bias, coming from the half-cell study, concerns the cycling performance of the materials. In particular, most of the studies focus on fully charging and discharging the anode in order to maximize the declared volumetric capacity density. If we compare the capacity density of anode and cathode, it will be clear that a huge gap divides the two classes of materials. Because the cell capacity will eventually be limited by the cathode capacity, an additional degree of freedom is available when choosing the anode. Either the anode can be made much thinner than the cathode to increase the volumetric capacity density, or it can be used in the most favorable alloying region. As a matter of example, it may be wise to use only the first $10\,\%$ of a thick tin anode and limit the volume expansion instead of making a tiny anode that will withstand a huge mechanical stress. Unluckily, the cycling performance of anodes at limited depths-of-discharge is a topic completely absent in the present literature.

3. Solid Electrolytes for TFBs

We already introduced a first classification of electrolytes from the point of view of the diffusion medium. In this section, we will take the time to analyze how the ions' conduction works in different cases, with a particular focus on the electrolyte employed to realize a thin-film solid-state cell. In Figure 1.21 a more detailed and thin-film-oriented classification of the electrolyte is proposed. The broad class is *homogeneous electrolyte*: materials composed of a single, homogeneous phase. A first macro-division aims to differentiate between solid electrolytes and solvent+salt electrolytes. In particular, the latter is composed of a solvent in which a conducting salt is dissolved. This enables a fine control on the quantity of carrier, or mobile ions, in the electrolyte, while solid electrolytes are usually much harder to tune and study because the carrier concentration is fixed by fabrication conditions. On the second level, the division proceeds according to differences in the mechanism of ion diffusion. In particular, the solid electrolytes are here split into two families: crystalline and glassy solid electrolytes. I also added the family of *gel electrolyte*, which, as already pointed out, is a mix of polymer and liquid solvent. Sometimes the same name is used to indicate a subfamily of the polymer electrolyte that divides into high-molecular-weight and low-molecular-weight polymer electrolytes, depending on the length of the polymer chain composing it. Because low-molecular-weight polymer electrolytes are much less stiff and usually more ion-conductive, they may be confused with gel polymer electrolytes, which are instead closer to a polymer+liquid composite electrode.

With the background on thin-film and fabrication processes acquired so far, it is easier to understand the interest in differentiating between homogeneous electrolytes and composite electrolytes. Composite electrolytes were defined as a mixture of two (or more) electrolytes from the same or different classes of homogeneous electrolytes. It has already been pointed out how, in the roll-to-roll process, in order to avoid the cracking of the electrolyte during handling, composite electrolyte tends to be bulky, hence unpopular. On the other hand, in thin-film processing, the actual fabrication of composite electrolytes is strongly limited. The high-throughput techniques used in ICs manufacturing do not allow depositing heterogeneous materials. Even if it is possible to realize composite electrodes with sol-gel and solvent casting, the control over film thickness and morphology is very low. For these reasons, composite electrodes are not very popular in thin films either and won't be considered in the following sections.

I will use the improper classification *thin-film solid electrolyte* to address all homogeneous electrolytes that can be deposited as thin films by any of the fabrication processes introduced before. That comprises crystalline, glassy and high-molecular-weight electrolytes.

However, the real star of thin-film batteries are solid electrolytes. The thin film production process enables direct deposition of electrolytes, solving the two main issues of this class: poor interface contact and fragility during handling. This allows us to exploit the superior ionic conductivity of solid electrolytes without additional issues with respect to liquid electrolytes. As for the latter class, the interface stability with respect to the electrodes will be the main concern, and it needs to be evaluated not only during the operation of the cell but for the whole deposition process as well.

Before starting with the material review, let's complete our physical understanding of an electrochemical cell.

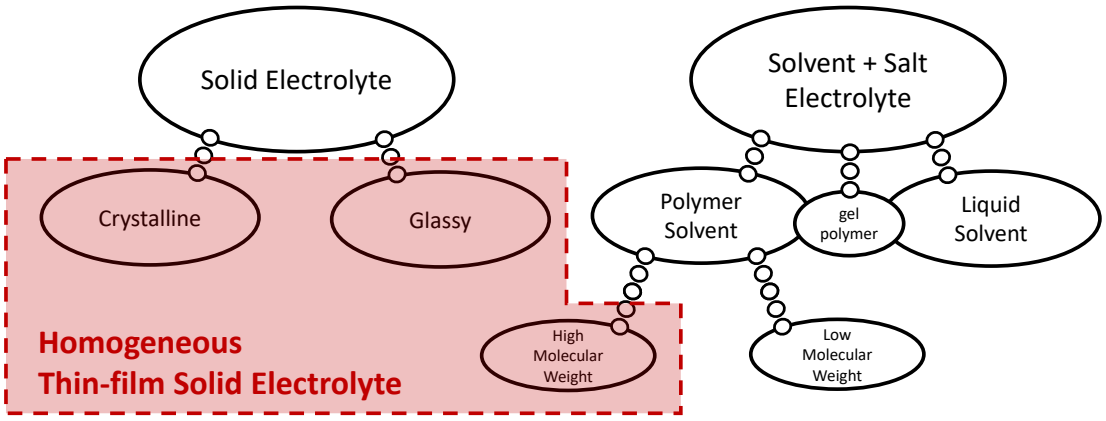

Figure 1.21: Classification of homogeneous/single-component electrolyte.

3.1 Physics of solid electrolyte

The physics of solid electrolytes is closely related to the concepts already introduced for electrodes. In fact, the electrode and electrolyte were already differentiated in terms of electronic conductivity. It is this single difference that determines the need for different physical treatments for the two. In solid electrolytes, one of the main hypotheses both in the derivation of the voltage curve and the diffusion mechanisms is the non-interaction between lithium ions inside the electrode. Local electroneutrality is the first step toward ion independence, and it is ensured by high electron conductivity. If an extra ion is added, it is possible to immediately screen its charge by means of a conduction electron. In the case of electrolytes, the electron conduction is very low or almost zero, and local electroneutrality holds no more. This leads to the formation of charge density variations and the building up of an electric field inside the material. Historically, in dilute liquid electrolytes, the ions are considered non-interacting, due to the screening of the polar solvent molecules [53]. This is, in general, not true in the case of a solid electrolyte, where long-range interaction between ions can appear.
However, the big difference with respect to electronic conductive materials is the possibility to displace the ions by means of an external electric field, which can considerably speed up the ions' movement compared to concentration-gradient-based diffusion. This is in fact the subject of the following subsection [19, 52].

Ion drift in ionic solid

From the electrode physics section, we recall the expression linking the flux of ions and the chemical potential:

$$J = -cD\frac{\partial \mu}{\partial x} \tag{1.15}$$

Where the chemical potential for a constant volume insertion reaction was defined as the derivative of the Gibbs free energy with respect to the intercalation fraction.

$$\mu = \frac{\partial G}{\partial n}_{T,V} \tag{1.16}$$

For charged species, the total energy of the system will be increased by the Coulomb interaction between each ion and the surrounding electric field: intuitively, it is much harder to stuff a box

with springs than with marbles. In order to account for the extra term, it is convenient to define the electrochemical potential as:

$$\tilde{\mu} = \mu + zF\phi \tag{1.17}$$

Where ϕ is the electric potential, z the charge of each ion, and F is the Faraday constant. We can rewrite the equation (1.15) to account for a gradient in the electric potential. In the one-dimensional case,

$$J = -cD\frac{\partial\tilde{\mu}}{\partial x} = -cD\left(\frac{\partial\mu}{\partial x} + zF\frac{\partial\phi}{\partial x}\right) \tag{1.18}$$

and more in general:

$$J = -cD\nabla\tilde{\mu} = -cD(\nabla\mu + zF\nabla\phi) \tag{1.19}$$

The surface current density can be defined from the particle flux by simply converting the moles to coulombs by means of the Faraday constant:

$$i = zFJ \tag{1.20}$$

From Ohm's law, we can then define the electrochemical mobility of ions in the absence of a chemical gradient as:

$$\sigma_{ion} = \frac{1}{\rho} = \left(\frac{i}{-\nabla\phi}\right)_{\nabla\mu=0} = c(zF)^2D \tag{1.21}$$

This quantity is usually addressed as **ion conductivity** in the literature. As for the chemical diffusion coefficient, σ_{ion} is proportional to the self diffusion coefficient: if the ions are in general more free to roam around, it will be easier to displace them by means of external means. As we will see in the review section, the electrolytes are often characterized by σ_{ion} instead of $\tilde{D}$. This is because, from σ_{ion}, it is straightforward to determine the internal resistance of the electrolyte, which is one of the main parameters when comparing different materials. I will continue to indicate with σ_{el} the electronic conductivity of the electrolyte in order to avoid confusion, but as already noticed, in the literature such consistency often lacks. Sometimes it is not obvious which of the two conductivities is considered when a general σ is reported.
An interesting parameter that links the two quantities is the *transfer number*. This parameter is inherited from the liquid electrolyte theory, where the two quantities to be compared are the anions and cations conductivities:

$$t_{cat} = \frac{\sigma_{cat}}{\sigma_{cat} + \sigma_{an} + \sigma_{el}} \approx \frac{\sigma_{cat}}{\sigma_{cat} + \sigma_{an}} \tag{1.22}$$

the same concept is sometimes used in solid-state electrolytes also when only the cations are mobile. In this case, from the definition of the total conductivity $\sigma = \sigma_{ion} + \sigma_{el}$ the transfer number of ions t_{ion} is:

$$t_{ion} = \frac{\sigma_{ion}}{\sigma} \tag{1.23}$$

In the classical anions-cations comparison, a transfer number closer to one (≈ 0.99) was considered a satisfactory result. However, when comparing electron and ion conductivity in an electrolyte, a ratio of several decades between the two may not be enough to be proud of the electronic resistance of our electrolyte.
Before delving into the different conduction mechanisms of each solid-state thin-film electrolyte, I would like to draw your attention to the mathematics behind the definition of ion conductivity. In particular, the hypothesis of zero chemical potential implies the absence of any concentration gradient. Zero does not exist in the real world, and the condition for the applicability of the formula (1.21) can be restated as:

$$\nabla\mu << zF\nabla\phi \tag{1.24}$$

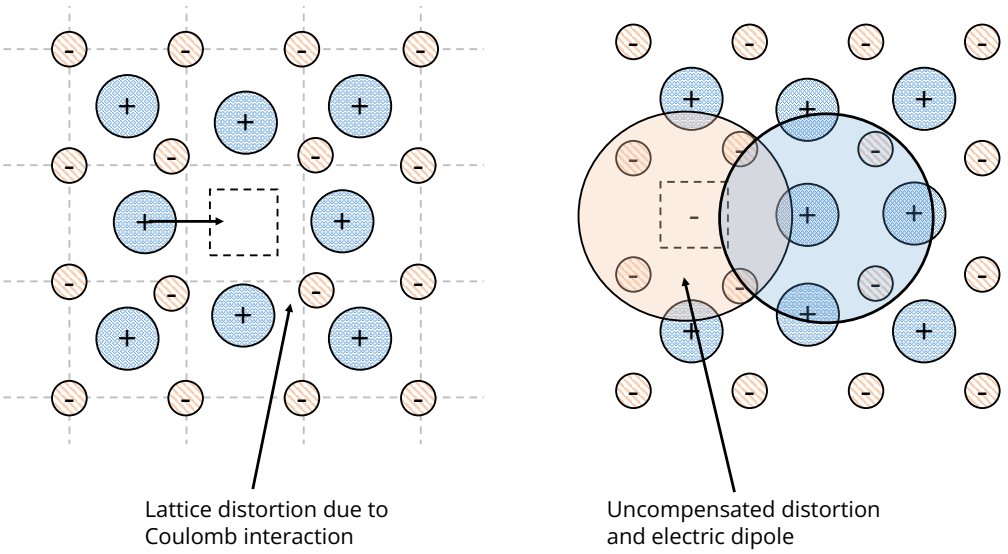

Figure 1.22: Defect diffusion in the ionic lattice. Before the jump, the crystalline rearrangement guarantees local electroneutrality. Just after the jump, a local electric dipole is formed between the vacancy and the displaced ion.

If the ion dynamic is dominated by the electric field, the ion conductivity can be readily extracted. In the modeling chapter, we will actually solve the equation for ion motion in the electrolyte, and we will take the time to get acquainted with the so-called *electrical double layer*. This is a placeholder for the less poetic "accumulation of ions inside the electrolyte at the electrode/electrolyte interface". This accumulation ($\nabla\mu \neq 0$) is usually concentrated in a few tens of nanometers at the electrode/electrolyte interface. If the total thickness of the electrolyte is much bigger than the size of the double layer, the hypothesis is satisfied almost everywhere, and the equation 1.21 can be used. This may not be the case for ALD-deposited electrolytes, where the total length of the electrolyte is comparable with the length of the interface accumulation. In this case, to test the hypothesis, it is possible to measure the conductivity at different polarization voltages. Assuming that the interface accumulation length varies with the imposed electric field, the apparent σ is expected to vary as well. For small enough polarization, the value should stabilize, and the equation 1.21 can be safely exploited again.

Crystalline solid electrolyte

The physical mechanism of ion conduction in a solid crystalline electrolyte is basically the same as that for an electrode [19]. In particular, the self-diffusion is enabled by the presence of crystal defects, which permit the ions' hopping between sites. We expect diffusion to increase with increasing temperature, as the number of defects increases according to the Boltzmann statistic (exponential increase). The main difference resides, as already pointed out, in the electroneutrality hypothesis. In particular, as soon as an ion jumps, it will leave a negative, uncompensated charge in its former site (Figure 1.22). At the same time, at its new position, its positive charge will be uncompensated as well, giving rise to an electric dipole. With time, the surrounding atoms will reorganize to compensate for the charge imbalance and restore electroneutrality. By defining the ion diffusion in a solid electrolyte, we defined the frequency of jump attempts per second. For ionic solids, another time constant has to be defined with respect to the relaxation

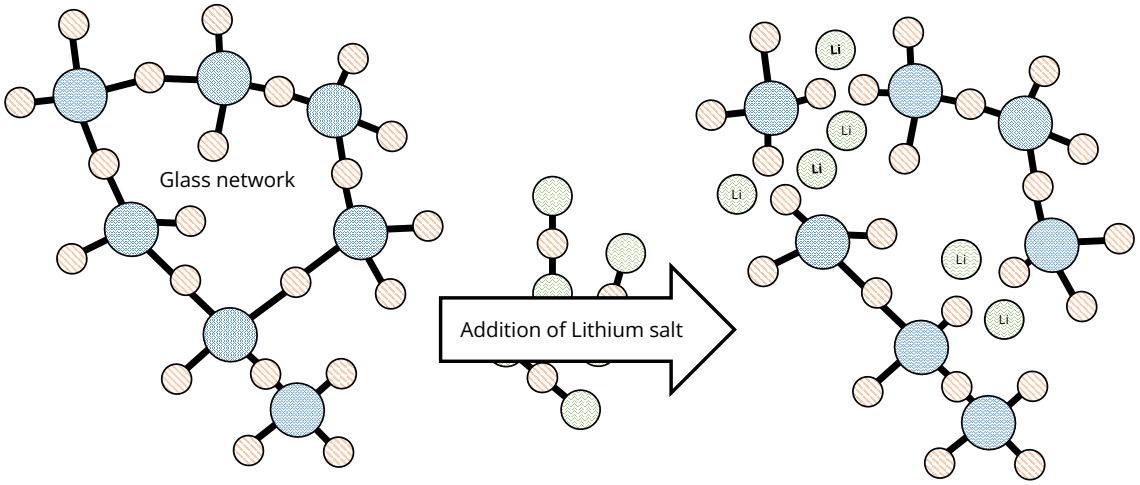

Figure 1.23: Glassy electrolyte formation by mixing of a glass (*network former*) and a ion salt (*network modifier*).

of the crystalline lattice after a jump. This can considerably change the physics of diffusion. Let's consider an ion succeeding in jumping from an already relaxed site (Figure 1.22). After the jump, a dipole is created, and the strong Coulomb attraction between the atom and the vacancy will increase the energy barrier for a successive jump (assuming another vacancy is available). The self-diffusion coefficient will then be lowered as long as the crystal lattice does not relax. After that, the self-diffusion coefficient will reverse back to its initial value. That means that one single jump is much easier to accomplish than multiple ones. One expects a dispersion in the self-diffusion, hence in the σ_{ion}, if the crystal is analyzed at different timescales. The system will appear more conductive when excited with a short pulse with respect to the long ones. This is not the case with electrodes, for which the ion conductivity is constant with respect to the excitation timescale.
Another effect of the appearance of electric dipoles is long-range ion motion. Dipoles may interact with each other, changing the effective energy barrier. In the case of lower energy, the creation of a dipole will enhance the mobility of the surrounding area and promote cooperative motion. This subject will not be further discussed in the present work; for additional details, refer to the bibliography [19, 52].

Glassy solid electrolyte

The second family of solid electrolyte are non-crystalline or glassy electrode [19]. These electrolyte are a bridge between polymer electrolyte and solid electrolyte, sharing feature with both classes. Their microscopic structure is quite similar to that of a polymer electrolyte. A glass network constitute the backbone of the electrolyte (like the polymers chain for polymer electrolyte), and a lithium salt (e.g., Li_2O) is added to the glass backbone in order to modify its structure. the two are called *network former* and *network modifier*. In figure 1.23 the formation of a glassy electrolyte from SiO_2 and Li_2O. The lithium salt breaks some of the bridging oxygen and the lithium is incorporated as ions in the structure. In this phase, the lithium ions are strongly bonded with the oxygen, and cannot move around the glass network. While the structure resemble a polymer electrolyte, the conduction mechanism are shared with the crystalline electrolyte. In fact, the diffusion process relies on the thermal formation of defect pairs (vacancy/interstitial-atom). In figure 1.24 a and b is shown the formation of a defect pair and the diffusion of the two. A

particular feature of glassy electrolyte is the difference in the capacity of the two defect types to diffuse. In crystal electrolyte the two defects have different energy barrier, but can both move in any directions. In the case of glassy electrolyte this is true only for interstitial defects. The diffusion of a vacancy needs a bounded lithium to jump into it. In crystalline solid the presence of an atom is ensure by the symmetry of the crystal lattice, while in glassy electrolyte the presence of lithium close to the vacancy is random, and fixed during the synthesis. That means that not all vacancy, once formed, will be able to move. Depending on the concentration of lithium in the glass, the diffusion mechanism can be limited to interstitial diffusion only, with negligible contribution of vacancy.
We already introduced the dispersion of conductivity with respect to the excitation time scale in crystalline electrolyte. In case of glassy electrolyte another element participate to the dispersion. If the excitation is fast, and only a single jump is executed, the conduction will be higher, due to environment relaxation, in the case o interstitial diffusion, but at the same time, much more vacancies will be able to participate, because no continuous diffusion path is needed, but a single bounded lithium atom nearby. For longer excitation time the vacancy will not participate to the overall conduction, which will be determined by the diffusion properties of interstitial atoms alone. Overall the conductivity of glassy electrolyte is expected to be lower than crystalline electrolyte, due to the poor diffusivity of vacancy.
Together with conductivity, another parameter of relevance in the domain of electrolytes is permittivity ϵ. The permittivity is the proportionality constant between the applied electric field $\boldsymbol{E}$ and the electric displacement field $\boldsymbol{D}$:

$$\boldsymbol{D} = \epsilon \boldsymbol{E} \tag{1.25}$$

The permittivity is usually expressed as the vacuum permittivity ($\epsilon_0 \approx 8.85 \times 10^{-12}\,\mathrm{F\,m^{-1}}$) times the relative permittivity (ϵ_r), which is a characteristic of each material and takes values in the range 1 to 100.

$$\epsilon = \epsilon_0 \epsilon_r \tag{1.26}$$

The relative permittivity is a measurement of the capacity of a material to screen the electric field with respect to vacuum ($\epsilon_r = 1$). Polar and mobile substances like water will show the highest relative permittivity (also called the dielectric constant). The capacity to screen the electric field is a particularly interesting feature in the case of electrolytes. The dissolution of a salt, or the creation of charged defects, requires the material to reorganize in order to screen the local charge imbalance. In the case of water, this is accomplished by rotation of the water molecules, while in glassy and crystalline electrolytes, it is accomplished by lattice distortion. It is therefore no surprise that solids in general will exhibit lower relative permittivity. Comparing relative permittivity between different electrolytes can help predict which one will show the highest mobile ion concentration, hence the highest ionic mobility. As for the ionic diffusion, different timescales will lead to different values of the dielectric constant. Because on a large timescale, long-range motion takes place in the electrolyte, it is not always straightforward to correctly apply the equation 1.25. This may lead to the extraction of an incorrect and absurd value of relative permittivity, which is too often the case in the literature.

High molecular weight polymer electrolyte

Probably the best way to introduce this class of electrolyte [19] is by pointing out the difference between a polymer and a glassy electrolyte: the scale of similarity. In glass, the substance similarity is at the scale of a few atoms: in SiO_2 silicon tetrahedrals are similar to each other, but at a larger scale, the disposition of groups of tetrahedrals is random. We can, in fact, define the

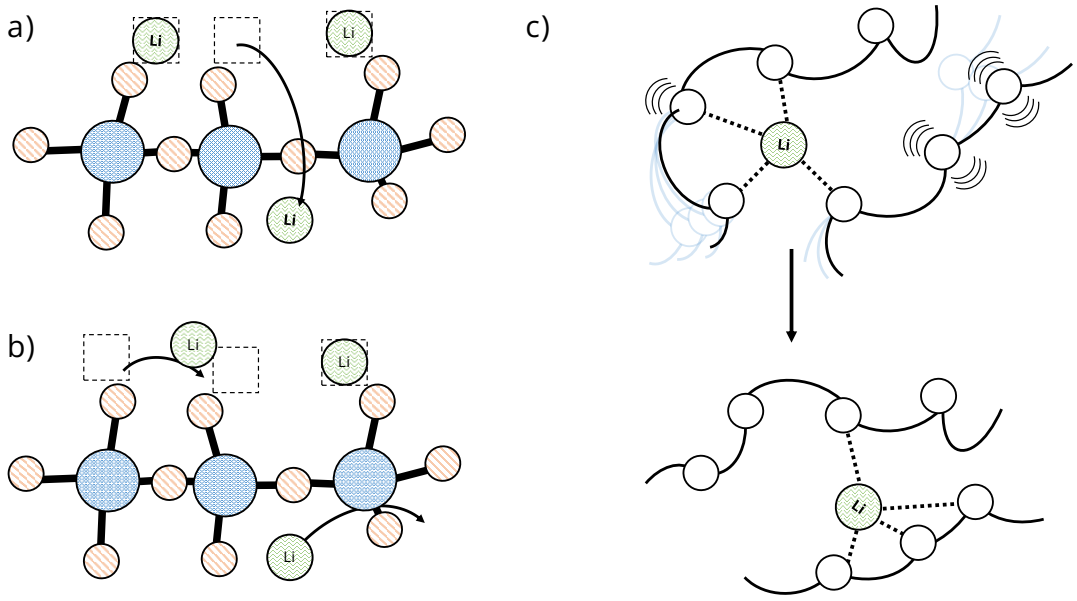

Figure 1.24: Diffusion mechanism in Glassy and polymer electrolyte. a) defect formation in glassy electrolyte; b) vacancy and interstitial defect diffusion; c) Thermal agitation of the polymer chain and ion exchange between two chains.

tetrahedral as the unit from which the glass network is built. In the case of polymers, the unit building block is composed of tens or thousands of atoms.
In order to obtain an ion-conducting electrolyte, a salt is usually dissolved into the polymer, much like in the case of a liquid electrolyte. A special case is represented by polyelectrolytes, in which the polymer is itself the cation. Glassy electrolytes are actually closer to polyelectrolytes because, in the former, the cations are embedded in the glass network and do not diffuse.
Diffusion in polymer electrolytes is largely different from that of solid electrolytes, which explains the gap in ion conduction between the two groups. Figure 1.24 shows the structure and the diffusion mechanism of polymer electrolytes. As for liquid electrolyte, once the salt is dissociated, the solvent molecule surrounds anions and cations in order to screen the electric field and reduce their interaction. In both cases, ions must ”displace” the solvent to diffuse. For polymer electrolytes, the size and mass of the polymeric chain make it almost impossible for the ions to displace it by thermal motion, and the reverse is true: it is the motion of the polymeric chain that displaces the ions. As reported in the figure, the torsion of the chain leads two chains to share and eventually exchange lithium ions. Because the chains are quite large, they won't move around at room temperature, but just rotate and deform. Even so, the self-diffusion of ions proceeds quite slowly. In fact, polymer electrolytes are much less conductive than crystalline and liquid electrolytes. The reduction of the chain size (molecular weight) and the addition of lithium salt can improve the conductivity to a level comparable to a glassy electrolyte at best [17, 18, 179].

3.2 Survey of thin-film solid electrolyte: selected papers

The second part of this section is dedicated to a brief review of the main materials that can be employed in realizing thin-film solid-state electrolytes [12, 180–183]. The review is mainly restricted to glassy and crystalline solid electrolytes, with PEO [11, 184–186] the only exception from polymer electrolytes. I decided to report it in the summary Table 1.3 as a matter of comparison to

give a more quantitative understanding of the gap in performance between the polymer and the other two families. Moreover, PEO is quite popular in the realization of polymer-solid composite electrolytes, and it is often encountered in the literature [13, 17, 187]. In the same table, I also decided to include the LiN electrolyte [188, 189] because this crystalline solid-electrolyte is the *non plus ultra* in terms of ion diffusion at room temperature. It is somehow the dream electrolyte, being highly electronically insulating and extremely simple and cheap to produce. Unluckily, the absence of any stabilizing transition metal makes it unstable, with a stability window of 400 mV only.
Before delving into a brief analysis of the main literature, I would like to comment on some general aspects of dealing with electrolyte bibliographical reviews. With respect to electrodes, it is much harder to achieve a real understanding of the status of the research for each electrolyte without spending a huge amount of time on each. In fact, the bibliographical results for even basic quantities like the dielectric constant or ionic conductivity diverge among different works. Two main reasons contribute to the dispersion of experimental results: inconsistency in the data analysis technique and variation in the actual electrolyte composition. The first is a diffuse problem in the field of electrolyte study. Plenty of papers do not report the complete mathematical procedure used to extract the physical parameters for the electrolyte [190–195] and often, when they do, the procedure is not correct. As an example, one of the commonest errors in the analysis of the dielectric properties of the electrolyte concerns the extraction of the dielectric constant variation with respect to the frequency. In particular, the dielectric constant is extracted with the parallel plate capacitor formula:

$$C = \epsilon_0 \epsilon_r \frac{A}{d} \tag{1.27}$$

Where A is the capacitor area and d the distance between the parallel plates. In most of the works, the distance d is kept constant for the whole frequency range. Notwithstanding, as I will explain more in detail in the third chapter, this distance actually varies from the size of the electrolyte to few nm when passing from the high to low frequency range. As a result, the dielectric constant value skyrockets to impossible values [184, 196–203].
The second reason for data dispersion is the stoichiometry variation among papers. I will focus on this point during the second chapter, where a more careful review of the bibliography of LiPON is provided. At that point, it will be clear what a ginormous amount of work is required to scratch the surface of the literature for a single electrolyte. For this reason, at this stage, I only propose a selection of papers focusing on the extraction of the ion conductivity and the dielectric constant. The collection of beautiful and poisonous flowers (an anthology indeed) on the next pages is meant more as a spur for an improvement of the quality of electrolyte studies than as a proper review.

LPS/LGPS electrolyte (glassy/semi-crystalline/crystalline)

Families of electrolytes with different compositions are usually grouped by means of an acronym comprising all the main atomic species. LPS refers to a family of glassy electrolytes composed of lithium (L), phosphate (P) and sulfur (S)[204]. The electrolyte is realized by mixing the network former P_2S_5 and the network modifier salt Li_2S. The most common formulations are 70:30 and 75:25 (mol %) [205, 206] but more exotic stoichiometry can be found as well [207]. The degree of crystallinity seems to strongly impact the ionic conductivity of LPS with up to three orders of magnitude variation in the reported value [206, 207]. But those are just details with respect to the marvelous value ($\epsilon_r = 53000$ at 100 Hz) of relative permittivity reported by Zhang et al. [202].

Electrolyte	**V_{win}** (V vs Li/Li^+)	σ_{el}^{-1} (Ω cm)	σ_{ion} (S cm^{-1})	$\epsilon'_{\omega=\infty}/\epsilon_0$
LPS	0 to 5	10^9	10^{-6} to 10^{-3}	-
LGPS	0 to 5	-	10^{-4} to 10^{-2}	-
LTP	0.5 to 3.5	10^2 to 10^9	10^{-7} to 10^{-5}	100
αLZP	0 to 5.5	10^9	10^{-6}	7
LAGP	1.5 to 5.5	10^8 to 10^{10}	10^{-4}	10
LATP	2.5 to 4.5	10^{10}	10^{-4}	30
LLZO	0 to 5	10^8	10^{-6} to 10^{-4}	60
LLTO	1.8 to 4.5	10^9	10^{-5}	200
LiPON	0 to 5.5	10^9 to 10^{15}	10^{-6}	20
LiSiON	0 to 6	10^8 to 10^{13}	10^{-5}	60
Li_3OCl	0 to 3	10^{11}	10^{-4}	15
LiN	0 to 0.4	10^{12}	10^{-3}	10
PEO	0 to 4	-	10^{-10} to 10^{-6}	5

Table 1.3: Properties of popular electrolyte materials at RT. From left to right: intrinsic (with respect to inert electrode) voltage stability window; average electron conductivity; average ion conductivity; high frequency dielectric constant. Sources are provided at each section.

No surprise, since the parallel plate capacitor formula is applied to the whole frequency spectrum without any modification.
Doping of LPS with germanium (LGPS) has proved a valid solution to improve its ionic conductivity [208]. LPS and LGPS have been deposited as thin films by evaporation [207] and PLD [209, 210].

LTP/LZP electrolyte (crystalline)

LTP ($LiTi_2(PO_4)_3$) is the prototype material of the broad family LMNP where M and N are transition metals. All LMNP electrolytes are based on PO_4 tetrahedra linked by transition metal atoms. They are crystalline solid electrolytes with different symmetry groups depending on the metal choice (NASICON-like, garnet, perovskite). LTP is somehow the simplest member of this family, with titanium as the only transition metal. At a closer look at its properties, one may question if this is an actual electrolyte. Possessing a high electron conductivity (for an electrolyte), it has been considered an anode material for some time [197]. Actually, it performs poorly in both roles due to its low ion diffusion coefficient and small stability window.
Its bibliography is haunted as well by the constant distance spectrum for dielectric constant extraction [197]. The same artifact can appear in the analysis of the variation of the conductivity with respect to the frequency [192]. The application of the *loss tangent* method for extracting the conductivity of an ionic conducting electrolyte is itself a complex task. As a quick recap, the concept of loss tangent is associated with heat dissipation in a dielectric capacitor—a capacitor in series with a resistor. The loss tangent is a mathematical device used to measure the thermal power dissipation due to electron conduction, starting from the complex impedance of the capacitor:

$$\tan\delta = \frac{\epsilon''(\omega)}{\epsilon'(\omega)} = \frac{\sigma}{\epsilon'(\omega)\omega} \tag{1.28}$$

Where the formula is valid for an ideal capacitor and an ideal resistor (ohmic conduction only). Its applicability to ion conductors is at least questionable. In particular, a delayed response to

an applied electric field (e.g., slow ion motion) will result in a large loss tangent, as in the case of conduction. Moreover, the capacitor is assumed to be ideal and is not meant to vary with frequency for equation 1.28 to be applicable.
LZP ($LiZr_2(PO_4)_3$) is the other single-metal electrolyte of the same family. It is again a poor ionic-conducting material but has a large stability window. Exploring the associated bibliography, impossible values for the dielectric constant can be found as well, this time without any indication about the extraction procedure [194]. The five-digit result seems to suggest a constant capacitance bias.
LTP and LZP are not very popular materials due to their poor properties. Thin film deposition has been reported for hydrothermal method [211] and RF sputtering [212].

LAGP/LATP electrolyte (crystalline)

The advanced versions of the two previous electrolytes, with the two transition metals aluminum/germanium (LAGP) and aluminum/titanium (LATP), are far more conductive and both have reasonable stability windows. They are a far more popular choice, with a large available bibliography and lots of quality studies [213, 214]. It is no surprise if it is among these works that a very good analysis of the evolution of the capacitance as a function of the frequency is reported by Ling et al. [215]. Here, the dielectric constant is extracted at high frequency and fixed as a constant to estimate the size of the low-frequency equivalent capacitor.
RF sputtering deposition of these materials has been largely reported, together with the effect of deposition parameters on the final film quality [216, 217]. PLD deposition has been reported as well [218].

LLZO/LLTO electrolyte (crystalline)

The other VIP couple of solid electrolyte is Li-La-Zr-O and Li-La-Ti-O. These are the oxide counterparts of the LTP family. The two are less performing than LAGP and LATP in terms of both electron insulation and ion conduction, but they are still a very popular option, widely employed in the literature. In this case of LLTO, the acronym is really just a place-holder for a plethora of different-stoichiometry compounds [190, 219, 220]. On the other hand, the LLZO usually refers exclusively to $Li_7La_3Zr_2O_{12}$.
In the literature both proper [221, 222] and biased [190, 195, 200] extraction of the dielectric constant are readily available. The literature dedicated to thin-film deposition is quite rich with reference for Rf sputtering [219, 220, 223, 224], ALD [225] and CVD [222] deposition.

LiPON and LiSiPON electrolyte (glassy)

LiPON is by far the mainstream choice for thin-film solid-state batteries. Not for its ion conduction, which is quite low, but thanks to the huge electron insulation and high stability windows. Moreover, this electrolyte has proven very stable with respect to both cathode materials and lithium metal during cycling [226]. A complete review is provided in the next chapter in the section dedicated to material deposition. A silicon-modified (LiSiPON) [227] and an iron-doped version ($Fe-LiPON$) [228] exist as well, with better ion diffusion properties. In particular, for iron-doping, the increase in ion diffusion results in a decrease in the band-gap and an increase in electric conduction. The overall price is a higher leakage current and a reduction of the stability windows below $5\,V$ [228].
RF sputtering is the preferred deposition technique for this electrolyte and its derivatives [201,

229, 230]. With its large bibliography LiPON is the perfect battleground for dielectric properties extraction [199, 231].

Li3OCl electrolyte (crystalline)

Li_3OCl of the anti-perovskite family [232–234] is an excellent ending to the present review. The family comprises all electrolytes with formulations Li_xOCl_{x-2} and Li_xOBr_{x-2} sharing the same crystal group. Proton-doped versions also exist (LiOHCl,LiOHBr). They are all very promising in terms of ion conductivity, and with a two-decade gap with respect to LiPON they lead the present review. Electron conduction is also very low, but they still miss good electrochemical stability. As for LiN this is the price to pay when no stabilizing transition metal is embedded in the formula. It is easy to imagine that fast ion conduction implies that lithium is not strongly bound to the crystal matrix, but as a consequence, it means that the atoms are not tightly bound as well and they can easily decompose [232, 234, 235]. Even if doubt still persists about the achievable performances of this family, they are extensively studied by the community[233]. Thin-film can be realized by means of RF magnetron sputtering [236] and PLD [237].

Conclusion on electrolyte materials for TFBs

Coming back to the summary Table 1.3, where the properties of the main members of each electrolyte family are listed, it is possible do draw some final remarks. As already highlighted, the ion conductivity and the stability windows tends to be complementary properties. both depends on the bonds nature and strength but in opposite ways. There are, anyway, candidates performing excellently in both parameters, like LGPS and LLZO. For each it is also possible to change the stoichiometry and optimize the material for the required application. Even if the latter electrolytes may be the preferred choice in term of dynamic performances, for electrolyte the behaviour under cycling must be considered as well. While electrodes may not resist cycling due to mechanical stress, electrolytes, instead, are impacted by the formation of lithium dendrites, leading to the short circuit of the cell. From this point of view, the most reliable choice is LiPON as it seems to be particularly efficient at preventing dendrite growth at high current density. The concluding section of the present chapter is dedicated to this particular aspect of solid electrolytes and its link with their physical properties.
In general, the field of solid electrolytes is the one with the largest number of open questions, in particular with respect to the stability of the electrolyte/electrode interface. In fact, the stability windows reported, usually refer to DC polarization with respect to inert electrodes. During full cell operation, the picture is completely different, both because the materials are not the same and the interface chemistry is modified accordingly, and because while a current is flowing, ion accumulation at the interface is not constant in time and depends on the redox reaction dynamics. Depending on the situation the nominal stability windows can be reduced or increased.

3.3 Dendrites formation in solid electrolyte

At the very beginning of this journey, we stated two main objectives to be reached with the new generation of batteries: cheap and large-scale on one side and reliable integrated energy storage on the other. In both cases, the use of lithium anode was an interesting option to increase the volumetric capacity density, but dendrite growth and poor stability with respect to liquid

electrolyte hindered its applicability in real cases. Polymer and solid electrolytes were developed in order to provide a more stable interface with respect to both chemical degradation and dendrite growth. In this final subsection, I would like to spend a little more time revising the dendrite growth dynamics and the physical parameters impacting it. As a general observation, dendrites start growing only at a high enough current density; the limit current density before short-circuiting is usually called *critical current density*. The higher the critical current density, the higher the electrolyte resistance to dendrite growth. Typical values for critical current are 0.1 to 10mA cm^{-2}.

Historically, solid electrolytes were considered a solution to dendrite growth due to their mechanical stiffness [238, 239]. Unluckily, as soon as they were implemented, not only was no beneficial impact observed, but dendrite growth was even easier than in liquid electrolytes [240, 241]. Only LiPON has demonstrated the capability to resist dendrite growth, and a certain consensus has developed in the past year about attributing it to its mechanical properties [239, 241] plus the good electrolyte/electrode interface obtained with PVD deposition. The main argument was that not only high mechanical stiffness is required but also a good interface to prevent microcracking, which can then promote dendrite penetration. During the years, results against this assumption accumulated [242], showing that also electrolytes with low stiffness could prevent dendrite growth. The consensus focused more on the ion diffusion coefficient. We already pointed out that dendrite growth in insertion electrodes takes place when the electrode reaction changes from ion-transfer to electron-transfer. This usually happens due to a low lithium concentration at the interface and an increase in electron tunneling. So the idea was that poor ionic conductivity was the reason for such lithium depletion at the interface, and increasing it would have been beneficial for dendrite growth. Once again, the experimental results were strongly against this theory: liquid electrolytes are in general more conductive from the point of view of ions than most parts of solid electrolytes, but LiPON and certain composite electrolytes from PEO [187, 242] are much better at preventing dendrite growth. Indeed, LiPON is one of the worst solid electrolytes in terms of ion conduction, and its stiffness is comparable with or even lower than that of other materials. Both the theories of mechanical stiffness and ionic conductivity can hardly explain its superior performance. It is only in 2019 that Han et al. proposed in a paper, which is already a must-read in the field [243], a coherent interpretation of the experimental data and a new perspective on dendrite growth. I will just briefly summarize the idea of this work and report the main intuition; for more quantitative details and experimental results, I recommend the original paper.

The idea sprouts from experimental results for LLZTO and LLZO [240, 243], which are more conductive, more stiff, and as dense as LIPON. Those electrolytes show extensive dendrite growth in the whole volume, in particular inside grain defects and cracks. An especially important experimental fact is the formation of disconnected particles of metallic lithium inside the electrolyte [244]. In fact, in the typical picture of this phenomenon (Figure 1.25 a), the dendrites nucleate at the anode/electrolyte interface and then extend into the electrolyte through cracks until the two electrodes are shorted [245]. This is in fact the main case of liquid electrolyte, but in solid electrolyte, the lithium seems to also precipitate directly inside the electrolyte. In this second case, the short-circuit is formed when enough particles precipitate and ensure a lithium metal path between anode and cathode (Figure 1.25 b) [246]. But how can lithium form in the bulk of a solid electrolyte? The answer is quite simple: electron-ion couple recombination. But for that to happen, unbounded electron states must exist in the middle of the electrolyte. Eventually, this hypothesis led Han et al. to compare different electrolytes not on the basis of mechanical or ionic properties but with respect to electron conductivity. This way the mystery is quickly

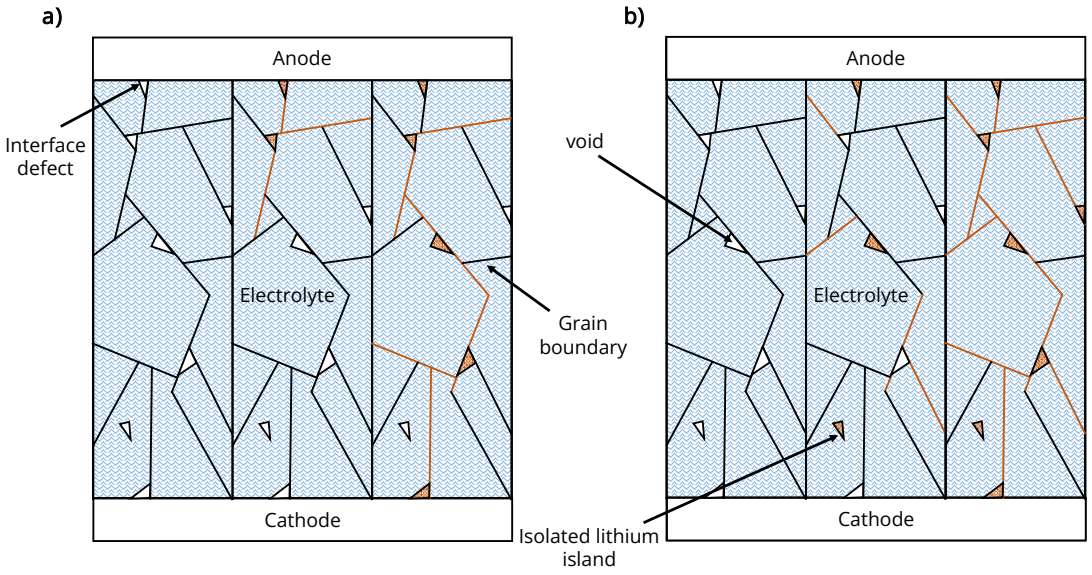

Figure 1.25: Formation of dendrites a) starting from interface defects to the bulk electrolyte, through cracks; b) volume nucleation at cracks and interface defects.

solved: LiPON has an electronic conductivity of $10 \times 10^{15}\,\Omega\,\text{cm}$ while LLZO only $10 \times 10^{8}\,\Omega\,\text{cm}$. Undoubtedly, mechanical stiffness, ion conductivity, and interface defects can promote and facilitate dendrite nucleation, but these properties cannot explain the general tendency reported by experimental results.

4. Anode-free Configuration for High Integration Level

This section concludes the general introductory chapter on thin-film solid-state batteries. It is dedicated to a particular configuration of batteries, which is the one adopted in the rest of the manuscript as a test vehicle. The anode-free configuration is a variant of the lithium metal anode. In the latter, the metal anode is deposited during the production process, while in the anode-free configuration, the anode is formed by the lithium stored in the cathode during the first charge. After the first charge, as shown in Figure 1.26, the two configurations are identical from a working point of view, with the only difference being the total quantity of lithium.

4.1 Advantages and drawbacks of anode-free configuration

Anode-free configuration is particularly interesting for improving the volumetric capacity density of a cell. In fact, the anode-free configuration is the minimum volume configuration because the anode contains only and exactly the amount of lithium needed for a full charge of the battery. Another quite important feature is the absence of lithium metal during production. The high reactivity and low evaporation temperature of lithium metal make it difficult to handle and lower the thermal budget. In the specific case of microbatteries for ICs integration, the soldering of the battery on the chip and the die-level stacking usually require a moderate temperature ($<200\,^{\circ}\text{C}$), and may result in melting and evaporation of the lithium anode. Moreover, the cell would be very sensitive to air, and unless very good sealing is applied, the lithium is expected

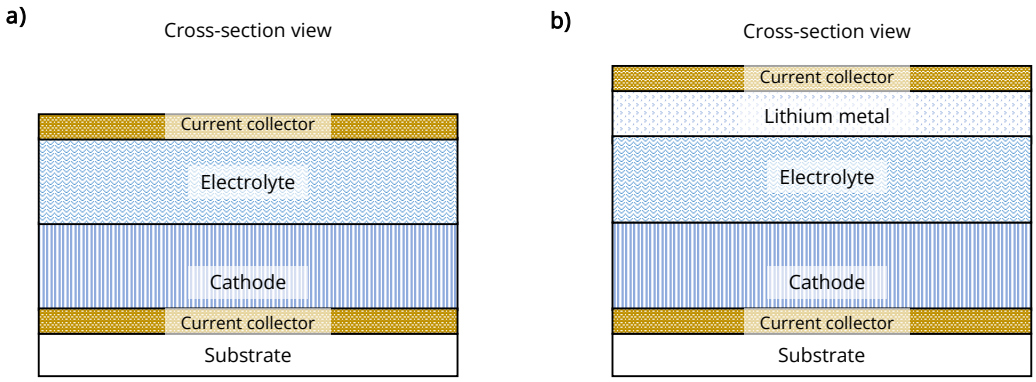

Figure 1.26: anode free configuration a) out-of-fab; b) after-first charge.

to oxidize during processing and storage of the intermediate device. These features make the anode-free configuration very appealing from the point of view of the manufacturing process, which is expected to be easier and cheaper than lithium metal anode [247].
The absence of extra lithium is at the same time the greatest advantage and the root of the main problems of this configuration. If the total lithium at disposal is exactly the quantity needed for charging the battery, each atom loss will result in a loss in the total capacity. This point is strongly impacting the performance of an anode-free configuration in the case of liquid electrolyte because lithium is highly reactive with commercial liquid electrolyte, and a great deal of it is consumed in side reactions. Solid electrolytes tend to be more stable with respect to lithium metal. Apart from higher intrinsic stability [248], the absence of diffusion of the electrolyte prevents fresh electrolyte from migrating to the anode surface and reacting with lithium. In the solid state, if the reaction is self-passivating (the by-product does not conduct electrons), after the formation of a thin passivation layer at the electrolyte/electrode interface, the side reaction stops. However, side reactions are not the only mechanism of lithium loss. In particular, during plating and stripping, some portion of lithium can end up being electrically disconnected and form the so-called ”dead-lithium”.
The loss of lithium results in a fast capacity decay in all anode-free configurations. Today, control over the plating-stripping process is believed to be one of the main tools used to control lithium morphology and prevent capacity loss. Various approaches can be employed, like the modification of the current collector, the application of pressure, or the addition of a stabilization layer between electrolyte and current collector [247–249]. All these approaches can mitigate the capacity loss up to a certain point. Instead, for the next section, I decided to focus on the control of lithium morphology by means of the charge/discharge protocol, which may prove a more comprehensive solution and provide a better understanding of the dynamic of lithium deposition.

4.2 Plating and stripping of metallic lithium

Anode-free thin-film batteries based on LiPON can properly cycle up to $1\,\mathrm{mA\,cm^{-2}}$ according to Neudecker et al. [250]. When the current is further increased, the capacity loss during cycling is increased as well. However, in their work, both charge and discharge current varied. The authors hypothesize the effect of charge current on the lithium morphology, but from their study it is not possible to draw a solid conclusion. Various works in the literature deal with the morphological variation of lithium during charge and discharge [251–255]. Inhomogeneous plating and

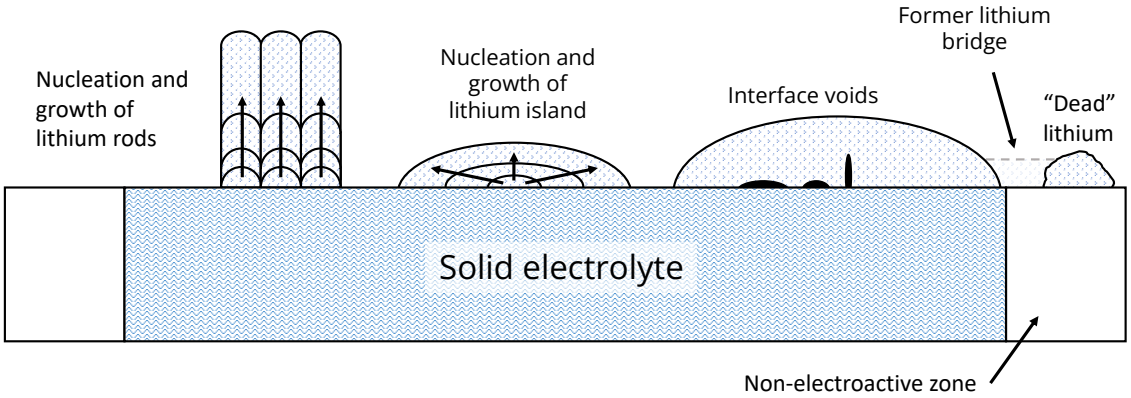

Figure 1.27: Lithium plating morphology and defects.

stripping can both lead to the formation of voids at the electrode/electrolyte interface, resulting in a smaller contact area. In this case, the lithium is not really lost by means of an irreversible reaction. The loss of capacity is instead linked with the charge/discharge protocol. For example, a discharge at constant current up to a certain minimum potential will be impacted by a decrease in the exchange interface. From the outside, the effect is an increase in the internal resistance, hence a crossing of the threshold earlier in the discharge. The capacity is still there but is not accessible at the required voltage and current.

Both charge and discharge can have an effect on the creation of topological defects. It is possible to differentiate between two main defects categories: void formation at the electrolyte/electrode interface and volume accumulation, which refers to the macroscopic formation of lithium deposits. The latter accounts for mechanical stress and rupture of the passivation layer. In this second case, the metal lithium can react with the external environment to form lithium oxide and hydroxide, resulting in an actual loss of available lithium. Even if no external contamination takes place, the absence of mechanical constrains can lead to the formation of ”dead” lithium. In particular, if the lithium gets plated outside the active area, the discharge may lead to the disconnection of such a zone, resulting in an additional loss of capacity (see Figure 1.27).

In any case, for an anode-free configuration, the first charge is of special interest, because of the formation of the lithium anode. The initial morphology of the anode influences the plating and stripping efficiency of the following cycles. In particular, the charge current density is reported to control the initial nucleation. In the case of low current density, lithium tends to form large, unconnected islands. Low current implies little lithium plated per unit time, which gives more time for lithium diffusion. Interface defects act as preferential nucleation sites. In the case of large charge current density, the initial nucleation is more uniform. Small, connected lithium spheres form in the first few seconds of nucleation. Because the surface is filled, further lithium plating must occur in the vertical direction, and the formation of nano-rods is observed [256–259]. The second mode should be preferred because it avoids the formation of voids at the interface, as in the case of large, unconnected islands [244].

List of Symbols

Symbol	Units	Description	Symbol	Units	Description
A	m^2	Surface	Q_A	$\mathrm{A\,h\,m}^{-2}$	Areal capacity density
C	F	Capacitance	Q_m	$\mathrm{A\,h\,kg}^{-1}$	Gravimetric capacity density
c	$\mathrm{mol\,m}^{-3}$	Volumetric particles density	Q_V	$\mathrm{A\,h\,m}^{-3}$	volumetric capacity density
$\boldsymbol{D}$	$\mathrm{C\,m}^{-2}$	Electric displacement field	ρ	$\mathrm{g\,cm}^{-3}$	Volumetric mass density
D	$\mathrm{m}^2\,\mathrm{s}^{-1}$	Self-diffusion coefficient	R	$\mathrm{J\,mol}^{-1}\,\mathrm{K}^{-1}$	Gas constant
D^*	$\mathrm{m}^2\,\mathrm{s}^{-1}$	Tracer diffusion coefficient	R_{ext}	Ω	Load resistance
$\tilde{D}$	$\mathrm{m}^2\,\mathrm{s}^{-1}$	Chemical diffusion coefficient	R_{int}	Ω	Internal resistance
d	m	length	R_{self}	Ω	Self-discharge resistance
ΔG_V	J	Vacancy energy formation	σ	$\Omega\,\mathrm{cm}$	Total conductivity
ΔG_b	J	Diffusion energy barrier	σ_{el}	$\Omega\,\mathrm{cm}$	Electron conductivity
ϵ	$\mathrm{F\,m}^{-1}$	Permittivity	σ_{ion}	$\Omega\,\mathrm{cm}$	Ion conductivity
ϵ'	$\mathrm{F\,m}^{-1}$	Real part of the permittivity	S	$\mathrm{J\,K}^{-1}$	Entropy
ϵ''	$\mathrm{F\,m}^{-1}$	Imaginary part of the permittivity	SOC	1	State-of-Charge
ϵ_0	$\mathrm{F\,m}^{-1}$	Vacuum permittivity	T	K	Temperature
ϵ_r	1	Relative permittivity	t_{ion}	1	Ion transfer number
$\boldsymbol{E}$	$\mathrm{V\,m}^{-1}$	Electric field	V	m^3	Volume
E	J	Internal energy	z	1	Charge number
E_g	J	Band-gap energy			
ϕ	V	Electric potential			
F	$\mathrm{C\,mol}^{-1}$	Faraday constant			
G	J	Gibbs free energy			
I	A	Electric current			
k	$\mathrm{J\,K}^{-1}$	Boltzmann constant			
J	$\mathrm{mol\,m}^{-2}\,\mathrm{s}^{-1}$	Diffusion flux			
j	$\mathrm{A\,m}^{-2}$	Electric current density			
m	g	Mass			
μ	$\mathrm{J\,mol}^{-1}$	Chemical potential			
$\tilde{\mu}$	$\mathrm{J\,mol}^{-1}$	Electrochemical potential			
ω	$\mathrm{rad\,s}^{-1}$	Angular frequency			
OCV	V	Open circuit voltage			
P	bar	Pressure			

Bibliography

All-solid-state batteries

[1] Hong Li. "Practical Evaluation of Li-Ion Batteries". en. In: *Joule* 3.4 (Apr. 2019), pp. 911–914. DOI: 10.1016/j.joule.2019.03.028.

[2] P. M. Biesheuvel, Yeqing Fu, and Martin Z. Bazant. "Diffuse charge and Faradaic reactions in porous electrodes". en. In: *Phys. Rev. E* 83.6 (June 2011), p. 061507. DOI: 10.1103/PhysRevE.83.061507.

[3] Deyang Qu. "Fundamental principals of battery design: Porous electrodes". en. In: Freiberg, Germany, 2014, pp. 14–25. DOI: 10.1063/1.4878477.

[4] Lok-kun Tsui et al. "Characterization of Electrochemical Surface Area and Porosity of Zirconia Sensors". en. In: *ECS Trans.* 77.11 (July 2017), pp. 1087–1094. DOI: 10.1149/07711.1087ecst.

[5] W.G. Pell and B.E. Conway. "Quantitative modeling of factors determining Ragone plots for batteries and electrochemical capacitors". en. In: *Journal of Power Sources* 63.2 (Dec. 1996), pp. 255–266. DOI: 10.1016/S0378-7753(96)02525-6.

[6] Thomas Christen and Martin W. Carlen. "Theory of Ragone plots". en. In: *Journal of Power Sources* 91.2 (Dec. 2000), pp. 210–216. DOI: 10.1016/S0378-7753(00)00474-2.

[7] Lukas Porz et al. "Mechanism of Lithium Metal Penetration through Inorganic Solid Electrolytes". en. In: *Adv. Energy Mater.* 7.20 (Oct. 2017), p. 1701003. DOI: 10.1002/aenm.201701003.

[8] Yifei Yuan et al. "Understanding materials challenges for rechargeable ion batteries with in situ transmission electron microscopy". en. In: *Nat Commun* 8.1 (Aug. 2017), p. 15806. DOI: 10.1038/ncomms15806.

[9] Daniel C. Hannah et al. "On the Balance of Intercalation and Conversion Reactions in Battery Cathodes". en. In: *Adv. Energy Mater.* 8.20 (July 2018), p. 1800379. DOI: 10.1002/aenm.201800379.

[10] Seung-Ho Yu et al. "Understanding Conversion-Type Electrodes for Lithium Rechargeable Batteries". en. In: *Acc. Chem. Res.* 51.2 (Feb. 2018), pp. 273–281. DOI: 10.1021/acs.accounts.7b00487.

[11] Lizhen Long et al. "Polymer electrolytes for lithium polymer batteries". en. In: *J. Mater. Chem. A* 4.26 (2016), pp. 10038–10069. DOI: 10.1039/C6TA02621D.

[12] Feng Zheng et al. "Review on solid electrolytes for all-solid-state lithium-ion batteries". en. In: *Journal of Power Sources* 389 (June 2018), pp. 198–213. DOI: 10.1016/j.jpowsour.2018.04.022.

[13] Mahmut Dirican et al. “Composite solid electrolytes for all-solid-state lithium batteries”. en. In: *Materials Science and Engineering: R: Reports* 136 (Apr. 2019), pp. 27–46. DOI: 10.1016/j.mser.2018.10.004.

[14] Penghui Yao et al. “Review on Polymer-Based Composite Electrolytes for Lithium Batteries”. en. In: *Front. Chem.* 7 (Aug. 2019), p. 522. DOI: 10.3389/fchem.2019.00522.

[15] Vo Pham Hoang Huy, Seongjoon So, and Jaehyun Hur. “Inorganic Fillers in Composite Gel Polymer Electrolytes for High-Performance Lithium and Non-Lithium Polymer Batteries”. en. In: *Nanomaterials* 11.3 (Mar. 2021), p. 614. DOI: 10.3390/nano11030614.

[16] James T. Frith, Matthew J. Lacey, and Ulderico Ulissi. “A non-academic perspective on the future of lithium-based batteries”. en. In: *Nat Commun* 14.1 (Jan. 2023), p. 420. DOI: 10.1038/s41467-023-35933-2.

[17] Z. Zhang et al. “Review on composite solid electrolytes for solid-state lithium-ion batteries”. en. In: *Materials Today Sustainability* 21 (Mar. 2023), p. 100316. DOI: 10.1016/j.mtsust.2023.100316.

[18] Xiaoxue Zhao et al. “A Review of Polymer-based Solid-State Electrolytes for Lithium-Metal Batteries: Structure, Kinetic, Interface Stability, and Application”. en. In: *Batteries & Supercaps* 6.4 (2023), e202200502. DOI: 10.1002/batt.202200502.

[19] Peter G. Bruce, ed. *Solid State Electrochemistry*. Chemistry of Solid State Materials. Cambridge: Cambridge University Press, 1994. ISBN: 978-0-521-59949-8. DOI: 10.1017/CBO9780511524790.

[20] Dong Zhou et al. “Polymer Electrolytes for Lithium-Based Batteries: Advances and Prospects”. en. In: *Chem* 5.9 (Sept. 2019), pp. 2326–2352. DOI: 10.1016/j.chempr.2019.05.009.

[21] K. Mizushima et al. “LixCoO2 (0<x<-1): A new cathode material for batteries of high energy density”. In: *Materials Research Bulletin* 15.6 (June 1980), pp. 783–789. DOI: 10.1016/0025-5408(80)90012-4.

[22] Roger Marchand. “Nitrogen-containing phosphate glasses”. en. In: *Journal of Non-Crystalline Solids* 56.1-3 (July 1983), pp. 173–178. DOI: 10.1016/0022-3093(83)90464-7.

[23] M. H. Lewis, ed. *Glasses and Glass-Ceramics*. en. Dordrecht: Springer Netherlands, 1989. ISBN: 978-0-412-27690-3 978-94-009-0817-8. DOI: 10.1007/978-94-009-0817-8.

[24] Fabian Duffner et al. “Large-scale automotive battery cell manufacturing: Analyzing strategic and operational effects on manufacturing costs”. en. In: *International Journal of Production Economics* 232 (Feb. 2021), p. 107982. DOI: 10.1016/j.ijpe.2020.107982.

[25] RenZong Hu et al. “Progress on Sn-based thin-film anode materials for lithium-ion batteries”. en. In: *Chin. Sci. Bull.* 57.32 (Nov. 2012), pp. 4119–4130. DOI: 10.1007/s11434-012-5303-z.

[26] Berik Uzakbaiuly et al. “Physical Vapor Deposition of Cathode Materials for All Solid-State Li Ion Batteries: A Review”. en. In: *Front. Energy Res.* 9 (May 2021), p. 625123. DOI: 10.3389/fenrg.2021.625123.

[27] Lain, Brandon, and Kendrick. “Design Strategies for High Power vs. High Energy Lithium Ion Cells”. en. In: *Batteries* 5.4 (Oct. 2019), p. 64. DOI: 10.3390/batteries5040064.

[28] Yang Lu et al. “Dry electrode technology, the rising star in solid-state battery industrialization”. en. In: *Matter* 5.3 (Mar. 2022), pp. 876–898. DOI: 10.1016/j.matt.2022.01.011.

[29] Stanley Wolf and Richard N. Tauber. *Silicon Processing for the VLSI Era: Process technology*. en. Lattice Press, 2000. ISBN: 978-0-9616721-6-4.

[30] Peter M. Martin. *Handbook of deposition technologies for films and coatings: science, applications and technology*. en. 3rd ed. Amsterdam: Elsevier, 2010. ISBN: 978-0-8155-2031-3.

[31] Robert Dorey. "Routes to thick films". en. In: *Ceramic Thick Films for MEMS and Microdevices*. Elsevier, 2012, pp. 35–61. ISBN: 978-1-4377-7817-5. DOI: 10.1016/B978-1-4377-7817-5.00002-X.

[32] XiaoPing Liang et al. "Research progress of all solid-state thin film lithium Battery". en. In: *IOP Conf. Ser.: Earth Environ. Sci.* 218 (Feb. 2019), p. 012138. DOI: 10.1088/1755-1315/218/1/012138.

[33] James A. Oke and Tien-Chien Jen. "Atomic layer deposition and other thin film deposition techniques: from principles to film properties". en. In: *Journal of Materials Research and Technology* 21 (Nov. 2022), pp. 2481–2514. DOI: 10.1016/j.jmrt.2022.10.064.

[34] Sina Karimzadeh et al. "Emerging Atomic Layer Deposition for the Development of High-Performance Lithium-Ion Batteries". en. In: *Electrochem. Energy Rev.* 6.1 (Dec. 2023), p. 24. DOI: 10.1007/s41918-023-00192-8.

[35] R. S. Sethi. "Electrocoating from molten salts". en. In: *J Appl Electrochem* 9.4 (July 1979), pp. 411–426. DOI: 10.1007/BF00617552.

[36] Chadd Kiggins, Mehmet Ates, and John Cook. "Lco electrodes and batteries fabricated therefrom". US20210242460A1. Aug. 2021.

[37] Seok Hee Lee et al. "A Comprehensive Review of Nanomaterials Developed Using Electrophoresis Process for High-Efficiency Energy Conversion and Storage Systems". en. In: *Energies* 11.11 (Nov. 2018), p. 3122. DOI: 10.3390/en11113122.

[38] Ruren Xu, Wenqin Pang, and Qisheng Huo. *Modern inorganic synthetic chemistry*. en. Amsterdam Boston Paris: Elsevier, 2011. ISBN: 978-0-444-53599-3.

[39] C. J. Brinker and G. W. Scherer. *Sol-gel science*. English. San Diego, CA (USA); Academic Press Inc., Jan. 1990.

[40] Kaoru Dokko et al. "Sol–gel fabrication of lithium-ion microarray battery". en. In: *Electrochemistry Communications* 9.5 (May 2007), pp. 857–862. DOI: 10.1016/j.elecom.2006.11.025.

[41] Ulrich Siemann. "Solvent cast technology – a versatile tool for thin film production". en. In: *Scattering Methods and the Properties of Polymer Materials*. Berlin, Heidelberg: Springer Berlin Heidelberg, 2005, pp. 1–14. ISBN: 978-3-540-25323-5 978-3-540-31510-0. DOI: 10.1007/b107336.

[42] Moon-Soo Park et al. "Performance evaluation of printed LiCoO2 cathodes with PVDF-HFP gel electrolyte for lithium ion microbatteries". en. In: *Electrochimica Acta* 53.17 (July 2008), pp. 5523–5527. DOI: 10.1016/j.electacta.2008.03.007.

[43] Archana Kaliyaraj Selva Kumar et al. "A mini-review: How reliable is the drop casting technique?" en. In: *Electrochemistry Communications* 121 (Dec. 2020), p. 106867. DOI: 10.1016/j.elecom.2020.106867.

[44] Yu Chen et al. "Efficient Dissolution of Lithium-Ion Batteries Cathode $LiCoO_2$ by Polyethylene Glycol-Based Deep Eutectic Solvents at Mild Temperature". en. In: *ACS Sustainable Chem. Eng.* 8.31 (Aug. 2020), pp. 11713–11720. DOI: 10.1021/acssuschemeng.0c03624.

[45] Albina Jetybayeva et al. "Recent advancements in solid electrolytes integrated into all-solid-state 2D and 3D lithium-ion microbatteries". en. In: *J. Mater. Chem. A* 9.27 (2021), pp. 15140–15178. DOI: 10.1039/D1TA02652F.

[46] Joscha Schnell et al. “All-solid-state lithium-ion and lithium metal batteries – paving the way to large-scale production”. en. In: *Journal of Power Sources* 382 (Apr. 2018), pp. 160–175. DOI: 10.1016/j.jpowsour.2018.02.062.

[47] Yangtao Liu et al. “Current and future lithium-ion battery manufacturing”. en. In: *iScience* 24.4 (Apr. 2021), p. 102332. DOI: 10.1016/j.isci.2021.102332.

[48] Moritz H. Futscher et al. “Monolithically-stacked thin-film solid-state batteries”. en. In: *Commun Chem* 6.1 (June 2023), p. 110. DOI: 10.1038/s42004-023-00901-w.

[49] Yang Li et al. “On-Chip Batteries for Dust-Sized Computers”. en. In: *Advanced Energy Materials* 12.13 (2022), p. 2103641. DOI: 10.1002/aenm.202103641.

Intercalation materials for thin-film cathodes

[19] Peter G. Bruce, ed. *Solid State Electrochemistry*. Chemistry of Solid State Materials. Cambridge: Cambridge University Press, 1994. ISBN: 978-0-521-59949-8. DOI: 10.1017/CBO9780511524790.

[25] RenZong Hu et al. “Progress on Sn-based thin-film anode materials for lithium-ion batteries”. en. In: *Chin. Sci. Bull.* 57.32 (Nov. 2012), pp. 4119–4130. DOI: 10.1007/s11434-012-5303-z.

[29] Stanley Wolf and Richard N. Tauber. *Silicon Processing for the VLSI Era: Process technology*. en. Lattice Press, 2000. ISBN: 978-0-9616721-6-4.

[36] Chadd Kiggins, Mehmet Ates, and John Cook. “Lco electrodes and batteries fabricated therefrom”. US20210242460A1. Aug. 2021.

[50] W Ross Mckinnon. “Physical Mechanisms of Intercalation Batteries”. en. PhD thesis. University of British Columbia, 1980.

[51] Ralph E. White, J. O’M. Bockris, and B. E. Conway, eds. *Modern Aspects of Electrochemistry*. en. Boston, MA: Springer US, 1983. ISBN: 978-1-4615-7463-7 978-1-4615-7461-3. DOI: 10.1007/978-1-4615-7461-3.

[52] Han-Ill Yoo. *Lectures on Kinetic Processes in Materials*. en. Cham: Springer International Publishing, 2020. ISBN: 978-3-030-25949-5 978-3-030-25950-1. DOI: 10.1007/978-3-030-25950-1.

[53] John O’M. Bockris and Amulya K. N. Reddy. *Modern Electrochemistry 1, Ionics*. 2nd ed. New York: Kluwer Academic Publishers, June 1998.

[54] John O’M. Bockris, Amulya K. N. Reddy, and Maria Gamboa-Aldeco. *Modern Electrochemistry 2A, Fundamentals of Electrodics*. 2nd ed. New York: Kluwer Academic Publishers, 2000.

[55] Wolfgang Schmickler. *Interfacial electrochemistry*. en. New York: Oxford University Press, 1996. ISBN: 978-0-19-508932-5.

[56] San-Cheng Lai. “Solid Lithium-Silicon Electrode”. en. In: *J. Electrochem. Soc.* 123.8 (Aug. 1976), p. 1196. DOI: 10.1149/1.2133033.

[57] Ram A. Sharma and Randall N. Seefurth. “Thermodynamic Properties of the Lithium-Silicon System”. en. In: *J. Electrochem. Soc.* 123.12 (Dec. 1976), pp. 1763–1768. DOI: 10.1149/1.2132692.

[58] A. G. Morachevskii and A. I. Demidov. “Lithium-silicon alloys: Phase diagram, electrochemical studies, thermodynamic properties, application in chemical power cells”. en. In: *Russ J Appl Chem* 88.4 (Apr. 2015), pp. 547–566. DOI: 10.1134/S1070427215040011.

[59] Myounggu Park et al. “A review of conduction phenomena in Li-ion batteries”. en. In: *Journal of Power Sources* 195.24 (Dec. 2010), pp. 7904–7929. DOI: 10.1016/j.jpowsour.2010.06.060.

[60] Jan N. Reimers and J. R. Dahn. “Electrochemical and In Situ X-Ray Diffraction Studies of Lithium Intercalation in Li x CoO2”. en. In: *J. Electrochem. Soc.* 139.8 (Aug. 1992), pp. 2091–2097. DOI: 10.1149/1.2221184.

[61] Michel Ménétrier et al. “The insulator-metal transition upon lithium deintercalation from LiCoO2: electronic properties and 7Li NMR study”. en. In: *J. Mater. Chem.* 9.5 (1999), pp. 1135–1140. DOI: 10.1039/a900016j.

[62] Xiang-Yun Qiu et al. “Electrochemical and electronic properties of LiCoO2 cathode investigated by galvanostatic cycling and EIS”. en. In: *Phys. Chem. Chem. Phys.* 14.8 (2012), p. 2617. DOI: 10.1039/c2cp23626e.

[63] F. Khatun et al. “Impact of Lithium Composition on Structural, Electronic and Optical Properties of Lithium Cobaltite Prepared by Solid-state Reaction”. en. In: *Journal of Scientific Research* 6.2 (Apr. 2014), pp. 217–231. DOI: 10.3329/jsr.v6i2.17900.

[64] Eibar Flores et al. “Operando Monitoring the Insulator–Metal Transition of $LiCoO_2$”. en. In: *ACS Appl. Mater. Interfaces* 13.19 (May 2021), pp. 22540–22548. DOI: 10.1021/acsami.1c04383.

[65] Doh-Kwon Lee and Han-Ill Yoo. “Electron-Ion Interference and Onsager Reciprocity in Mixed Ionic-Electronic Transport in TiO 2”. en. In: *Phys. Rev. Lett.* 97.25 (Dec. 2006), p. 255901. DOI: 10.1103/PhysRevLett.97.255901.

[66] L. Dahéron et al. “Electron Transfer Mechanisms upon Lithium Deintercalation from LiCoO2 to CoO2 Investigated by XPS”. In: *Chem. Mater.* 20.2 (Jan. 2008), pp. 583–590. DOI: 10.1021/cm702546s.

[67] Hui Xia, Li Lu, and G. Ceder. “Li diffusion in LiCoO2 thin films prepared by pulsed laser deposition”. en. In: *Journal of Power Sources* 159.2 (Sept. 2006), pp. 1422–1427. DOI: 10.1016/j.jpowsour.2005.12.012.

[68] Peter Panjan et al. “Review of Growth Defects in Thin Films Prepared by PVD Techniques”. en. In: *Coatings* 10.5 (May 2020), p. 447. DOI: 10.3390/coatings10050447.

[69] H Xia et al. “Electrochemical behavior and Li Diffusion study of LiCoO2 thin film electrodes prepared by PLD”. en. In: *Advanced Materials for Micro- and Nano-Systems (AMMNS)*. 2007, p. 6.

[70] Hélène Porthault et al. “Electrochemical Synthesis under Hydrothermal Conditions: A Promising One-Step Synthesis Route for $LiCoO_2$ Thin Films for Microbatteries Applications”. en. In: *Meet. Abstr.* MA2011-01.26 (Mar. 2011), pp. 1518–1518. DOI: 10.1149/MA2011-01/26/1518.

[71] M. E. Donders et al. “Atomic Layer Deposition of $LiCoO_2$ Thin-Film Electrodes for All-Solid-State Li-Ion Micro-Batteries”. en. In: *J. Electrochem. Soc.* 160.5 (2013), A3066–A3071. DOI: 10.1149/2.011305jes.

[72] Yin Zhang et al. “Re-evaluation of experimental measurements for the validation of electronic band structure calculations for $LiFePO_4$ and $FePO_4$”. en. In: *RSC Adv.* 9.2 (2019), pp. 1134–1146. DOI: 10.1039/C8RA09154D.

[73] Kun Tang et al. “Kinetic analysis on LiFePO4 thin films by CV, GITT, and EIS”. en. In: *Electrochimica Acta* 56.13 (May 2011), pp. 4869–4875. DOI: 10.1016/j.electacta.2011.02.119.

[74] Suat Pat et al. “LiFePO $_4$ thin film deposition onto Ag coated glass by RF magnetron sputtering”. en. In: *Mater. Res. Express* 5.11 (Sept. 2018), p. 116401. DOI: 10.1088/2053-1591/aadcc6.

[75] Jian Liu et al. “Rational Design of Atomic-Layer-Deposited LiFePO4 as a High-Performance Cathode for Lithium-Ion Batteries”. In: *Advanced Materials* 26.37 (2014), pp. 6472–6477. DOI: 10.1002/adma.201401805.

[76] O.Y. Chernyaeva et al. “The influence of process conditions on the phase composition of the LiFePO4 film obtained by the atomic layer method”. en. In: *Polyhedron* 157 (Jan. 2019), pp. 297–300. DOI: 10.1016/j.poly.2018.09.049.

[77] Xiaolong Liang, Rengui Xiao, and Xia Liao. “Preparation of lithium iron phosphate composites by electrodeposition with a tunnel structure on aluminium foil surface”. en. In: *Boletín de la Sociedad Española de Cerámica y Vidrio* 59.6 (Nov. 2020), pp. 251–258. DOI: 10.1016/j.bsecv.2019.12.003.

[78] Tsutomu Ohzuku, Masaki Kitagawa, and Taketsugu Hirai. “Electrochemistry of Manganese Dioxide in Lithium Nonaqueous Cell: III . X-Ray Diffractional Study on the Reduction of Spinel-Related Manganese Dioxide”. en. In: *J. Electrochem. Soc.* 137.3 (Mar. 1990), pp. 769–775. DOI: 10.1149/1.2086552.

[79] Tsutomu Ohzuku et al. “Electrochemistry of Manganese Dioxide in Lithium Nonaqueous Cells: IV . Jahn-Teller Deformation of in”. en. In: *J. Electrochem. Soc.* 138.9 (Sept. 1991), pp. 2556–2560. DOI: 10.1149/1.2086016.

[80] S.B. Tang, M.O. Lai, and L. Lu. “Study on Li+-ion diffusion in nano-crystalline LiMn2O4 thin film cathode grown by pulsed laser deposition using CV, EIS and PITT techniques”. en. In: *Materials Chemistry and Physics* 111.1 (Sept. 2008), pp. 149–153. DOI: 10.1016/j.matchemphys.2008.03.041.

[81] Michael M. Thackeray. “Manganese oxides for lithium batteries”. en. In: *Progress in Solid State Chemistry* 25.1-2 (Jan. 1997), pp. 1–71. DOI: 10.1016/S0079-6786(97)81003-5.

[82] J. Fischer et al. “Structural transformation of sputtered o-LiMnO2 thin-film cathodes induced by electrochemical cycling”. en. In: *Thin Solid Films* 549 (Dec. 2013), pp. 263–267. DOI: 10.1016/j.tsf.2013.08.095.

[83] K.-F. Chiu et al. “Modification of sputter deposited solid-state electrolyte thin films”. en. In: *Vacuum* 84.11 (June 2010), pp. 1296–1301. DOI: 10.1016/j.vacuum.2010.02.006.

[84] T H Hsueh et al. “Checkerboard deposition of lithium manganese oxide spinel (LiMn $_2$ O $_4$) by RF magnetron sputtering on a stainless steel in all-solid-state thin film battery”. en. In: *IOP Conf. Ser.: Mater. Sci. Eng.* 324 (Mar. 2018), p. 012004. DOI: 10.1088/1757-899X/324/1/012004.

[85] Xubin Chen et al. “Photonic methods for rapid crystallization of LiMn2O4 cathodes for solid-state thin-film batteries”. en. In: *Journal of Power Sources* 495 (May 2021), p. 229424. DOI: 10.1016/j.jpowsour.2020.229424.

[86] Zhen Quan et al. “Preparation of nanocrystalline LiMn2O4 thin film by electrodeposition method and its electrochemical performance for lithium battery”. en. In: *Journal of Power Sources* 244 (Dec. 2013), pp. 375–381. DOI: 10.1016/j.jpowsour.2012.12.087.

[87] Ping Liu et al. “Lithium-Manganese-Oxide Thin-Film Cathodes Prepared by Plasma-Enhanced Chemical Vapor Deposition”. en. In: *J. Electrochem. Soc.* 146.6 (June 1999), pp. 2001–2005. DOI: 10.1149/1.1391881.

[88] Ville Miikkulainen et al. “Atomic Layer Deposition of Spinel Lithium Manganese Oxide by Film-Body-Controlled Lithium Incorporation for Thin-Film Lithium-Ion Batteries”. en. In: *J. Phys. Chem. C* 118.2 (Jan. 2014), pp. 1258–1268. DOI: 10.1021/jp409399y.

[89] Alexander A. Delluva et al. “Cathode Interface Compatibility of Amorphous $LiMn_2O_4$ (LMO) and $Li_7La_3Zr_2O_{12}$ (LLZO) Characterized with Thin-Film Solid-State Electrochemical Cells”. en. In: *ACS Appl. Mater. Interfaces* 12.22 (June 2020), pp. 24992–24999. DOI: 10.1021/acsami.0c03519.

[90] Masaaki Isai and Mitsuhiro Nakamura. “Investigation of deposition condition of $LiMn_2O_4$ films prepared by RF magnetron sputtering”. en. In: *Trans. Mat. Res. Soc. Japan* 37.1 (2012), pp. 99–101. DOI: 10.14723/tmrsj.37.99.

[91] Julien, Mauger, and Hussain. “Sputtered LiCoO2 Cathode Materials for All-solid-state Thin-film Lithium Microbatteries”. en. In: *Materials* 12.17 (Aug. 2019), p. 2687. DOI: 10.3390/ma12172687.

[92] Shuji Yamada, Masashi Fujiwara, and Motoya Kanda. “Synthesis and properties of LiNiO2 as cathode material for secondary batteries”. en. In: *Journal of Power Sources* 54.2 (Apr. 1995), pp. 209–213. DOI: 10.1016/0378-7753(94)02068-E.

[93] Tian Rao et al. “Structural, electrochemical, and Li-ion diffusion properties of Mg&Mn dual doped LiNiO2 cathode materials for Li-ion batteries”. en. In: *Solid State Ionics* 376 (Mar. 2022), p. 115860. DOI: 10.1016/j.ssi.2022.115860.

[94] J. R. Dahn, U. von Sacken, and C. A. Michal. “Structure and electrochemistry of Li1±yNiO2 and a new Li2NiO2 phase with the Ni (OH)2 structure”. en. In: *Solid State Ionics* 44.1 (Dec. 1990), pp. 87–97. DOI: 10.1016/0167-2738(90)90049-W.

[95] M.G.S.R. Thomas et al. “Synthesis and structural characterization of the normal spinel Li[Ni2]O4”. en. In: *Materials Research Bulletin* 20.10 (Oct. 1985), pp. 1137–1146. DOI: 10.1016/0025-5408(85)90087-X.

[96] J. Morales, C. Pérez-Vicente, and J. L. Tirado. “Cation distribution and chemical deintercalation of Li1-xNi1+xO2”. en. In: *Materials Research Bulletin* 25.5 (May 1990), pp. 623–630. DOI: 10.1016/0025-5408(90)90028-Z.

[97] Matteo Bianchini et al. “There and Back Again—The Journey of $LiNiO_2$ as a Cathode Active Material”. en. In: *Angew. Chem. Int. Ed.* 58.31 (July 2019), pp. 10434–10458. DOI: 10.1002/anie.201812472.

[98] Xin Lai et al. “Synthesis of LiNiO2 thin film in LiOH solution by hydrothermal method”. en. In: *Journal of Alloys and Compounds* 487.1-2 (Nov. 2009), pp. L30–L32. DOI: 10.1016/j.jallcom.2009.08.060.

[99] Daocong Li et al. “Synthesis and characterization of LiNi0.9Co0.1O2 for lithium batteries by a novel method”. en. In: *Journal of Alloys and Compounds* 457.1-2 (June 2008), pp. L1–L5. DOI: 10.1016/j.jallcom.2007.02.146.

[100] V Bianchi. “Synthesis, structural characterization and magnetic properties of quasistoichiometric LiNiO2”. en. In: *Solid State Ionics* 140.1-2 (Mar. 2001), pp. 1–17. DOI: 10.1016/S0167-2738(01)00706-8.

[101] V Bianchi et al. “Electrochemical investigation of the Li insertion–extraction reaction as a function of lithium deficiency in Li1−xNi1+xO2”. en. In: *Electrochimica Acta* 46.7 (Jan. 2001), pp. 999–1011. DOI: 10.1016/S0013-4686(00)00681-2.

[102] M. Broussely et al. “Li/LixNiO2 and Li/LixCoO2 rechargeable systems: comparative study and performance of practical cells”. en. In: *Journal of Power Sources*. This volume contains the Proceedings of the 6th International Meeting on Lithium Batteries 43.1 (Mar. 1993), pp. 209–216. DOI: 10.1016/0378-7753(93)80116-7.

[103] M. Broussely et al. “LixNiO2, a promising cathode for rechargeable lithium batteries”. en. In: *Journal of Power Sources*. Proceedings of the Seventh International Meeting on Lithium Batteries 54.1 (Mar. 1995), pp. 109–114. DOI: 10.1016/0378-7753(94)02049-9.

[104] Han-Ki Kim, Tae-Yeon Seong, and Young-Soo Yoon. “Fabrication of a Thin Film Battery Using a Rapid-Thermal-Annealed LiNiO2 Cathode”. en. In: *Electrochem. Solid-State Lett.* 5.11 (Aug. 2002), A252. DOI: 10.1149/1.1510323.

[105] Maxim Maximov et al. “Atomic Layer Deposition of Lithium–Nickel–Silicon Oxide Cathode Material for Thin-Film Lithium-Ion Batteries”. en. In: *Energies* 13.9 (May 2020), p. 2345. DOI: 10.3390/en13092345.

[106] Masahiro Yoshimura, Kyoo-Seung Han, and Shunsuke Tsurimoto. “Direct fabrication of thin-film LiNiO2 electrodes in LiOH solution by electrochemical–hydrothermal method”. en. In: *Solid State Ionics* 106.1-2 (Feb. 1998), pp. 39–44. DOI: 10.1016/S0167-2738(97)00406-2.

[107] Jing-Jing Ding, Qian Sun, and Zheng-Wen Fu. “Layered Li (Ni1 / 4Mn1 / 2Co13) O2 as Cathode Material for All-Solid-State Thin-Film Rechargeable Lithium-Ion Batteries”. en. In: *Electrochem. Solid-State Lett.* 13.8 (May 2010), A105. DOI: 10.1149/1.3432254.

[108] Marc Strafela et al. “Dependence of the constitution, microstructure and electrochemical behaviour of magnetron sputtered Li–Ni–Mn–Co–O thin film cathodes for lithium-ion batteries on the working gas pressure and annealing conditions”. en. In: *International Journal of Materials Research* 108.11 (Nov. 2017), pp. 879–886. DOI: 10.3139/146.111552.

[109] Zhimin Qi et al. “LiNi0.5Mn0.3Co0.2O2/Au nanocomposite thin film cathode with enhanced electrochemical properties”. en. In: *Nano Energy* 46 (Apr. 2018), pp. 290–296. DOI: 10.1016/j.nanoen.2018.02.011.

[110] Yiman Zhang et al. “Understanding How Structure and Crystallinity Affect Performance in Solid-State Batteries Using a Glass Ceramic LiV_3O_8 Cathode”. en. In: *Chem. Mater.* 31.16 (Aug. 2019), pp. 6135–6144. DOI: 10.1021/acs.chemmater.9b01571.

[111] Qian Shi et al. “High-capacity LiV3O8 thin-film cathode with a mixed amorphous–nanocrystalline microstructure prepared by RF magnetron sputtering”. en. In: *Electrochemistry Communications* 11.11 (Nov. 2009), pp. 2169–2172. DOI: 10.1016/j.elecom.2009.09.022.

[112] Haimei Liu et al. “A large capacity of LiV3O8 cathode material for rechargeable lithium-based batteries”. en. In: *Electrochimica Acta* 56.3 (Jan. 2011), pp. 1392–1398. DOI: 10.1016/j.electacta.2010.10.049.

[113] R. Benedek, M. M. Thackeray, and L. H. Yang. “Atomic structure and electrochemical potential of Li 1 + x V 3 O 8”. en. In: *Phys. Rev. B* 60.9 (Sept. 1999), pp. 6335–6342. DOI: 10.1103/PhysRevB.60.6335.

[114] Jin Kawakita, Takashi Miura, and Tomiya Kishi. “Lithium insertion and extraction kinetics of Li1qxV3O8”. en. In: (1999).

[115] Tonghu Jiang and Michael L. Falk. “Calculations of the thermodynamic and kinetic properties of Li 1 + x V 3 O 8”. en. In: *Phys. Rev. B* 85.24 (June 2012), p. 245111. DOI: 10.1103/PhysRevB.85.245111.

[116] Yongsub Yoon et al. “Lattice orientation control of lithium cobalt oxide cathode film for all-solid-state thin film batteries”. en. In: *Journal of Power Sources* 226 (Mar. 2013), pp. 186–190. DOI: 10.1016/j.jpowsour.2012.10.094.

[117] Zhongxue Chen et al. “High Rate, Long Lifespan LiV3O8 Nanorods as a Cathode Material for Lithium-Ion Batteries”. en. In: *Small* 13.18 (2017), p. 1603148. DOI: 10.1002/smll.201603148.

[118] Qian Shi et al. “A diffusion kinetics study of Li-ion in LiV3O8 thin film electrode”. en. In: *Electrochimica Acta* 55.22 (Sept. 2010), pp. 6645–6650. DOI: 10.1016/j.electacta.2010.06.009.

[119] Shaikshavali Petnikota et al. “Amorphous Vanadium Oxide Thin Films as Stable Performing Cathodes of Lithium and Sodium-Ion Batteries”. en. In: *Nanoscale Res Lett* 13.1 (Dec. 2018), p. 363. DOI: 10.1186/s11671-018-2766-0.

[120] S. Oukassi, R. Salot, and J.P. Pereira-Ramos. “Elaboration and characterization of crystalline RF-deposited V2O5 positive electrode for thin film batteries”. en. In: *Applied Surface Science* 256.1 (Oct. 2009), pp. 149–155. DOI: 10.1016/j.apsusc.2009.07.115.

[121] Alexander Pearse et al. “Three-Dimensional Solid-State Lithium-Ion Batteries Fabricated by Conformal Vapor-Phase Chemistry”. en. In: *ACS Nano* 12.5 (May 2018), pp. 4286–4294. DOI: 10.1021/acsnano.7b08751.

[122] Xinyi Chen et al. “Cathodic ALD V2O5 thin films for high-rate electrochemical energy storage”. en. In: *RSC Adv.* 3.13 (2013), p. 4294. DOI: 10.1039/c3ra23031g.

[123] Victoria C. Ferrari et al. “Co-sputtering of lithium vanadium oxide thin films with variable lithium content to enable advanced solid-state batteries”. en. In: *J. Mater. Chem. A* 10.23 (2022), pp. 12518–12531. DOI: 10.1039/D2TA01021F.

[124] M. Muñoz-Castro et al. “Controlling the optical properties of sputtered-deposited Li *x* V2O5 films”. en. In: *Journal of Applied Physics* 120.13 (Oct. 2016), p. 135106. DOI: 10.1063/1.4964254.

[125] Ping Liu et al. “Fabrication of LiV2O5 thin-film electrodes for rechargeable lithium batteries”. en. In: *Solid State Ionics* 111.1-2 (Aug. 1998), pp. 145–151. DOI: 10.1016/S0167-2738(98)00184-2.

[126] Felix Mattelaer et al. “Atomic layer deposition of vanadium oxides for thin-film lithium-ion battery applications”. en. In: *RSC Adv.* 6.115 (2016), pp. 114658–114665. DOI: 10.1039/C6RA25742A.

[127] C Delmas, H Cognac-Auradou, and J M Cocciantelli. “The LixV205system: An overview of the structure modifications induced by the lithium intercalation”. en. In: (1994).

[128] Dah-Yeon Yoo et al. “Determination of Li+ Diffusion Coefficients in the LixV2O5 (x = 0 − 1) Nanocrystals of Composite Film Cathodes”. en. In: *ANAL. SCI.* 29.11 (Nov. 2013), pp. 1083–1088. DOI: 10.2116/analsci.29.1083.

[129] Ethan C. Self et al. “Structural and Electrochemical Characterization of Thin Film Li_2MoO_3 Electrodes”. en. In: *J. Electrochem. Soc.* 166.6 (2019), A1015–A1021. DOI: 10.1149/2.1161904jes.

[130] T Tsumura. “Lithium insertion/extraction reaction on crystalline MoO3”. en. In: *Solid State Ionics* 104.3-4 (Dec. 1997), pp. 183–189. DOI: 10.1016/S0167-2738(97)00418-9.

[131] Øystein S. Fjellvåg et al. “Crystallization, Phase Stability, and Electrochemical Performance of β-MoO $_3$ Thin Films”. en. In: *Crystal Growth & Design* 20.6 (June 2020), pp. 3861–3866. DOI: 10.1021/acs.cgd.0c00156.

[132] Jolanta Światowska-Mrowiecka et al. “Li-Ion Intercalation in Thermal Oxide Thin Films of MoO $_3$ as Studied by XPS, RBS, and NRA”. en. In: *J. Phys. Chem. C* 112.29 (July 2008), pp. 11050–11058. DOI: 10.1021/jp800147f.

[133] Wissem Methani et al. “Nanomechanical, Structural and Electrochemical Investigation of Amorphous and Crystalline MoO3 Thin-Film Cathodes in Rechargeable Li-Ion Batteries”. en. In: *Batteries* 8.8 (July 2022), p. 80. DOI: 10.3390/batteries8080080.

[134] A. M. Hashem et al. “Two-phase reaction mechanism during chemical lithium insertion into α-MoO3”. en. In: *Ionics* 13.1 (Mar. 2007), pp. 3–8. DOI: 10.1007/s11581-007-0065-3.

[135] W. C. West and J. F. Whitacre. “Long Cycle Life Elevated Temperature Thin-Film Batteries Incorporating MoO3 Cathodes”. en. In: *J. Electrochem. Soc.* 152.5 (Apr. 2005), A966. DOI: 10.1149/1.1887147.

[136] Kaiyuan Wei et al. “Tunable oxygen vacancies in MoO3 lattice with improved electrochemical performance for Li-ion battery thin film cathode”. en. In: *Ceramics International* 49.13 (July 2023), pp. 21729–21736. DOI: 10.1016/j.ceramint.2023.03.313.

[137] Todd M. McEvoy et al. “Electrochemical Preparation of Molybdenum Trioxide Thin Films: Effect of Sintering on Electrochromic and Electroinsertion Properties”. en. In: *Langmuir* 19.10 (May 2003), pp. 4316–4326. DOI: 10.1021/la027020u.

[138] Todd M. McEvoy and Keith J. Stevenson. “Elucidation of the electrodeposition mechanism of molybdenum oxide from iso- and peroxo-polymolybdate solutions”. en. In: *J. Mater. Res.* 19.2 (Feb. 2004), pp. 429–438. DOI: 10.1557/jmr.2004.19.2.429.

[139] Miika Mattinen et al. “Atomic layer deposition of crystalline molybdenum oxide thin films and phase control by post-deposition annealing”. en. In: *Materials Today Chemistry* 9 (Sept. 2018), pp. 17–27. DOI: 10.1016/j.mtchem.2018.04.005.

[140] Minghao Yu et al. “Interlayer gap widened α-phase molybdenum trioxide as high-rate anodes for dual-ion-intercalation energy storage devices”. en. In: *Nat Commun* 11.1 (Mar. 2020), p. 1348. DOI: 10.1038/s41467-020-15216-w.

[141] Qiuying Xia et al. “All-Solid-State Thin Film Lithium/Lithium-Ion Microbatteries for Powering the Internet of Things”. en. In: *Advanced Materials* 35.2 (2023), p. 2200538. DOI: 10.1002/adma.202200538.

[142] Mohammadreza Zamanzad Ghavidel et al. “Electrochemical Formation of Four Al-Li Phases (β-AlLi, Al $_2$ Li $_3$, AlLi $_{2-x}$, Al $_4$ Li $_9$) at Intermediate Temperatures”. en. In: *J. Electrochem. Soc.* 166.16 (2019), A4034–A4040. DOI: 10.1149/2.0061916jes.

[143] Y. Hamon et al. “Aluminum negative electrode in lithium ion batteries”. en. In: *Journal of Power Sources* 97-98 (July 2001), pp. 185–187. DOI: 10.1016/S0378-7753(01)00616-4.

[144] J. Schwenzel, V. Thangadurai, and W. Weppner. “Developments of high-voltage all-solid-state thin-film lithium ion batteries”. en. In: *Journal of Power Sources* 154.1 (Mar. 2006), pp. 232–238. DOI: 10.1016/j.jpowsour.2005.03.223.

[145] C.S. Nimisha et al. “Sputter deposited LiPON thin films from powder target as electrolyte for thin film battery applications”. en. In: *Thin Solid Films* 519.10 (Mar. 2011), pp. 3401–3406. DOI: 10.1016/j.tsf.2011.01.087.

[146] H. Okamoto. “Al-Li (Aluminum-Lithium)”. en. In: *J. Phase Equilib. Diffus.* 33.6 (Dec. 2012), pp. 500–501. DOI: 10.1007/s11669-012-0119-8.

[147] A. L. Santhosha et al. “The Indium−Lithium Electrode in Solid-State Lithium-Ion Batteries: Phase Formation, Redox Potentials, and Interface Stability”. en. In: *Batteries & Supercaps* 2.6 (2019), pp. 524–529. DOI: 10.1002/batt.201800149.

[148] Wen-Hsien Ho et al. “Electrochemical performance of In2O3 thin film electrode in lithium cell”. en. In: *Journal of Power Sources* 175.2 (Jan. 2008), pp. 897–902. DOI: 10.1016/j.jpowsour.2007.10.020.

[149] C. John Wen and Robert A. Huggins. “Thermodynamic and mass transport properties of “LiIn””. en. In: *Materials Research Bulletin* 15.9 (Sept. 1980), pp. 1225–1234. DOI: 10.1016/0025-5408(80)90024-0.

[150] J Songster and A.D Pelton. “The In-Li (Indium-Lithium) System”. en. In: *JPE* 12.1 (Feb. 1991), pp. 37–41. DOI: 10.1007/BF02663671.

[151] Yong Zhang et al. “Mesoporous In $_2$ O $_3$ nanofibers assembled by ultrafine nanoparticles as a high capacity anode for Li-ion batteries”. en. In: *RSC Adv.* 6.55 (2016), pp. 49782–49786. DOI: 10.1039/C6RA07804D.

[152] Yongning Zhou et al. “The electrochemistry of nanostructured In2O3 with lithium”. en. In: *Journal of Power Sources* 162.2 (Nov. 2006), pp. 1373–1378. DOI: 10.1016/j.jpowsour.2006.08.031.

[153] Dajian Li, Weibin Zhang, and Song-Mao Liang. “Operating Voltage of Li-Ion Batteries on the Basis of Phase Diagram and Thermodynamics”. en. In: *Nanostructured Materials for Next-Generation Energy Storage and Conversion: Advanced Battery and Supercapacitors*. Ed. by Qiang Zhen, Sajid Bashir, and Jingbo Louise Liu. Berlin, Heidelberg: Springer, 2019, pp. 445–464. ISBN: 978-3-662-58675-4. DOI: 10.1007/978-3-662-58675-4_13.

[154] Raja Sen and Priya Johari. “Understanding the Lithiation of the Sn Anode for High-Performance Li-Ion Batteries with Exploration of Novel Li–Sn Compounds at Ambient and Moderately High Pressure”. en. In: *ACS Appl. Mater. Interfaces* 9.46 (Nov. 2017), pp. 40197–40206. DOI: 10.1021/acsami.7b11173.

[155] I. A. Courtney et al. “*Ab initio* calculation of the lithium-tin voltage profile”. en. In: *Phys. Rev. B* 58.23 (Dec. 1998), pp. 15583–15588. DOI: 10.1103/PhysRevB.58.15583.

[156] Yingchun Cheng et al. “A global view of the phase transitions of SnO $_2$ in rechargeable batteries based on results of high throughput calculations”. en. In: *J. Mater. Chem. A* 3.38 (2015), pp. 19483–19489. DOI: 10.1039/C5TA03521J.

[157] David M. Stewart et al. “Tin Oxynitride Anodes by Atomic Layer Deposition for Solid-State Batteries”. en. In: *Chem. Mater.* 30.8 (Apr. 2018), pp. 2526–2534. DOI: 10.1021/acs.chemmater.7b04666.

[158] Loïc Baggetto et al. “Tin Nitride Thin Films as Negative Electrode Material for Lithium-Ion Solid-State Batteries”. en. In: *J. Electrochem. Soc.* 157.3 (2010), A340. DOI: 10.1149/1.3290778.

[159] Martin Winter and Jürgen O. Besenhard. “Electrochemical lithiation of tin and tin-based intermetallics and composites”. en. In: *Electrochimica Acta* 45.1-2 (Sept. 1999), pp. 31–50. DOI: 10.1016/S0013-4686(99)00191-7.

[160] Jiqiang Wang, I. D. Raistrick, and R. A. Huggins. “Behavior of Some Binary Lithium Alloys as Negative Electrodes in Organic Solvent-Based Electrolytes”. en. In: *J. Electrochem. Soc.* 133.3 (Mar. 1986), pp. 457–460. DOI: 10.1149/1.2108601.

[161] T. Brousse et al. “Thin-Film Crystalline SnO2-Lithium Electrodes”. en. In: *J. Electrochem. Soc.* 145.1 (Jan. 1998), pp. 1–4. DOI: 10.1149/1.1838201.

[162] Loïc Baggetto et al. “Reaction mechanism of tin nitride (de)lithiation reaction studied by means of 119Sn Mössbauer spectroscopy”. en. In: *Electrochimica Acta* 55.22 (Sept. 2010), pp. 6617–6631. DOI: 10.1016/j.electacta.2010.06.012.

[163] K.S. Park et al. “Characteristics of tin nitride thin-film negative electrode for thin-film microbattery”. en. In: *Journal of Power Sources* 103.1 (Dec. 2001), pp. 67–71. DOI: 10.1016/S0378-7753(01)00829-1.

[164] Hideyuki Morimoto, Shin-ichi Tobishima, and Hiromitsu Negishi. “Anode behavior of electroplated rough surface Sn thin films for lithium-ion batteries”. en. In: *Journal of Power Sources* 146.1-2 (Aug. 2005), pp. 469–472. DOI: 10.1016/j.jpowsour.2005.03.053.

[165] Mohd Zahid Ansari et al. “Low-Temperature Atomic Layer Deposition of Highly Conformal Tin Nitride Thin Films for Energy Storage Devices”. en. In: *ACS Appl. Mater. Interfaces* 11.46 (Nov. 2019), pp. 43608–43621. DOI: 10.1021/acsami.9b15790.

[166] J.-L Brousseau et al. “Electrical properties and topography of SnO2 thin films prepared by reactive sputtering”. en. In: *Applied Surface Science* 108.3 (Mar. 1997), pp. 351–358. DOI: 10.1016/S0169-4332(96)00679-4.

[167] M. Mohamedi et al. “Amorphous tin oxide films: preparation and characterization as an anode active material for lithium ion batteries”. en. In: *Electrochimica Acta* 46.8 (Jan. 2001), pp. 1161–1168. DOI: 10.1016/S0013-4686(00)00702-7.

[168] Harald Schmidt et al. “Volume expansion of amorphous silicon electrodes during potentiostatic lithiation of Li-ion batteries”. en. In: *Electrochemistry Communications* 115 (June 2020), p. 106738. DOI: 10.1016/j.elecom.2020.106738.

[169] Matthew T. McDowell et al. “25th Anniversary Article: Understanding the Lithiation of Silicon and Other Alloying Anodes for Lithium-Ion Batteries”. en. In: *Adv. Mater.* 25.36 (Sept. 2013), pp. 4966–4985. DOI: 10.1002/adma.201301795.

[170] Pimpa Limthongkul et al. “Electrochemically-driven solid-state amorphization in lithium-silicon alloys and implications for lithium storage”. en. In: *Acta Materialia* 51.4 (Feb. 2003), pp. 1103–1113. DOI: 10.1016/S1359-6454(02)00514-1.

[171] Qingliu Wu et al. “Investigations of Si Thin Films as Anode of Lithium-Ion Batteries”. en. In: *ACS Appl. Mater. Interfaces* 10.4 (Jan. 2018), pp. 3487–3494. DOI: 10.1021/acsami.7b13980.

[172] Jianchao Ye et al. “Amorphization as a Pathway to Fast Charging Kinetics in Atomic Layer Deposition-Derived Titania Films for Lithium Ion Batteries”. en. In: *Chem. Mater.* 30.24 (Dec. 2018), pp. 8871–8882. DOI: 10.1021/acs.chemmater.8b04002.

[173] Roel van de Krol, Albert Goossens, and Eric A. Meulenkamp. “Electrical and optical properties of TiO2 in accumulation and of lithium titanate Li0.5TiO2”. en. In: *Journal of Applied Physics* 90.5 (Sept. 2001), pp. 2235–2242. DOI: 10.1063/1.1388165.

[174] Suzhe Liang et al. “Anatase titanium dioxide as rechargeable ion battery electrode - A chronological review”. en. In: *Energy Storage Materials* 45 (Mar. 2022), pp. 201–264. DOI: 10.1016/j.ensm.2021.11.023.

[175] B Zachauchristiansen. “Lithium insertion in different TiO2 modifications”. en. In: *Solid State Ionics* 28-30 (Sept. 1988), pp. 1176–1182. DOI: 10.1016/0167-2738(88)90352-9.

[176] A. Weibel, R. Bouchet, and P. Knauth. “Electrical properties and defect chemistry of anatase (TiO2)”. en. In: *Solid State Ionics* 177.3-4 (Jan. 2006), pp. 229–236. DOI: 10.1016/j.ssi.2005.11.002.

[177] Ngoc-Anh Nguyen et al. “An Ultralow Power LixTiO2-Based Synaptic Transistor for Scalable Neuromorphic Computing”. en. In: *Advanced Electronic Materials* 8.12 (2022), p. 2200607. DOI: 10.1002/aelm.202200607.

[178] P. Mazzolini et al. “Tuning of Electrical and Optical Properties of Highly Conducting and Transparent Ta-Doped TiO $_2$ Polycrystalline Films”. en. In: *J. Phys. Chem. C* 119.13 (Apr. 2015), pp. 6988–6997. DOI: 10.1021/jp5126156.

Solid electrolytes

[11] Lizhen Long et al. “Polymer electrolytes for lithium polymer batteries”. en. In: *J. Mater. Chem. A* 4.26 (2016), pp. 10038–10069. DOI: 10.1039/C6TA02621D.

[12] Feng Zheng et al. “Review on solid electrolytes for all-solid-state lithium-ion batteries”. en. In: *Journal of Power Sources* 389 (June 2018), pp. 198–213. DOI: 10.1016/j.jpowsour.2018.04.022.

[13] Mahmut Dirican et al. “Composite solid electrolytes for all-solid-state lithium batteries”. en. In: *Materials Science and Engineering: R: Reports* 136 (Apr. 2019), pp. 27–46. DOI: 10.1016/j.mser.2018.10.004.

[17] Z. Zhang et al. “Review on composite solid electrolytes for solid-state lithium-ion batteries”. en. In: *Materials Today Sustainability* 21 (Mar. 2023), p. 100316. DOI: 10.1016/j.mtsust.2023.100316.

[18] Xiaoxue Zhao et al. “A Review of Polymer-based Solid-State Electrolytes for Lithium-Metal Batteries: Structure, Kinetic, Interface Stability, and Application”. en. In: *Batteries & Supercaps* 6.4 (2023), e202200502. DOI: 10.1002/batt.202200502.

[19] Peter G. Bruce, ed. *Solid State Electrochemistry*. Chemistry of Solid State Materials. Cambridge: Cambridge University Press, 1994. ISBN: 978-0-521-59949-8. DOI: 10.1017/CBO9780511524790.

[52] Han-Ill Yoo. *Lectures on Kinetic Processes in Materials*. en. Cham: Springer International Publishing, 2020. ISBN: 978-3-030-25949-5 978-3-030-25950-1. DOI: 10.1007/978-3-030-25950-1.

[53] John O’M. Bockris and Amulya K. N. Reddy. *Modern Electrochemistry 1, Ionics*. 2nd ed. New York: Kluwer Academic Publishers, June 1998.

[179] Zhigang Xue, Dan He, and Xiaolin Xie. “Poly(ethylene oxide)-based electrolytes for lithium-ion batteries”. en. In: *J. Mater. Chem. A* 3.38 (2015), pp. 19218–19253. DOI: 10.1039/C5TA03471J.

[180] John Christopher Bachman et al. “Inorganic Solid-State Electrolytes for Lithium Batteries: Mechanisms and Properties Governing Ion Conduction”. en. In: *Chem. Rev.* 116.1 (Jan. 2016), pp. 140–162. DOI: 10.1021/acs.chemrev.5b00563.

[181] Zhanlai Ding et al. “Review—Interfaces: Key Issue to Be Solved for All Solid-State Lithium Battery Technologies”. en. In: *J. Electrochem. Soc.* 167.7 (Mar. 2020), p. 070541. DOI: 10.1149/1945-7111/ab7f84.

[182] Atul Kumar Mishra et al. “Review—Inorganic Solid State Electrolytes: Insights on Current and Future Scope”. en. In: *J. Electrochem. Soc.* 168.8 (Aug. 2021), p. 080536. DOI: 10.1149/1945-7111/ac1dcc.

[183] Junlong Liu et al. “Review of the Developments and Difficulties in Inorganic Solid-State Electrolytes”. en. In: *Materials* 16.6 (Mar. 2023), p. 2510. DOI: 10.3390/ma16062510.

[184] S. Das and A. Ghosh. “Ionic conductivity and dielectric permittivity of polymer electrolyte plasticized with polyethylene glycol”. en. In: Uttar Pradesh, India, 2016, p. 110012. DOI: 10.1063/1.4948033.

[185] Mikael Unge et al. “Electronic conductivity of polymer electrolytes: electronic charge transport properties of LiTFSI-doped PEO”. en. In: *Phys. Chem. Chem. Phys.* 22.15 (2020), pp. 7680–7684. DOI: 10.1039/D0CP01130D.

[186] Xue Ye et al. “An ultra-thin polymer electrolyte for 4.5 V high voltage LiCoO2 quasi-solid-state battery”. en. In: *Chemical Engineering Journal* 455 (Jan. 2023), p. 140846. DOI: 10.1016/j.cej.2022.140846.

[187] Chunhua Wang et al. “Suppression of Lithium Dendrite Formation by Using LAGP-PEO (LiTFSI) Composite Solid Electrolyte and Lithium Metal Anode Modified by PEO (LiTFSI) in All-Solid-State Lithium Batteries”. en. In: *ACS Appl. Mater. Interfaces* 9.15 (Apr. 2017), pp. 13694–13702. DOI: 10.1021/acsami.7b00336.

[188] J. Wahl and U. Holland. “Local ionic motion in the superionic conductor Li3N”. en. In: *Solid State Communications* 27.3 (July 1978), pp. 237–241. DOI: 10.1016/0038-1098(78)90026-1.

[189] M Miyamura et al. “Electrochemical studies of lithium nitride solid electrolyte for electrochromic devices”. en. In: *Solid State Ionics* 3-4 (Aug. 1981), pp. 149–152. DOI: 10.1016/0167-2738(81)90073-4.

[190] Susana García-Martín, Ainhoa Morata-Orrantia, and Miguel Á. Alario-Franco. “Influence of the crystal microstructure on the dielectric response of the La0.67Li0.2Ti0.8Al0.2O3”. en. In: *Journal of Applied Physics* 100.5 (Sept. 2006), p. 054101. DOI: 10.1063/1.2221528.

[191] Peter Hockicko, Peter Bury, and Francisco Munoz. “Electrical and dielectric properties of LiPON glasses”. en. In: *2012 ELEKTRO*. Rajeck Teplice, Slovakia: IEEE, May 2012, pp. 488–492. ISBN: 978-1-4673-1179-3 978-1-4673-1180-9 978-1-4673-1178-6. DOI: 10.1109/ELEKTRO.2012.6225672.

[192] A. Venkateswara Rao et al. “Structural, spectroscopic and electrochemical study of V5+ substituted LiTi2(PO4)3 solid electrolyte for lithium-ion batteries”. en. In: *Bull Mater Sci* 37.4 (June 2014), pp. 883–888. DOI: 10.1007/s12034-014-0021-6.

[193] Peter Hockicko et al. “Structural and Electrical Properties of LiPO3 Glasses”. en. In: *AEEE* 13.2 (June 2015), pp. 198–205. DOI: 10.15598/aeee.v13i2.1250.

[194] C.R. Mariappan et al. “Ionic conduction and dielectric properties of yttrium doped LiZr2(PO4)3 obtained by a Pechini-type polymerizable complex route”. en. In: *Ceramics International* 44.13 (Sept. 2018), pp. 15509–15516. DOI: 10.1016/j.ceramint.2018.05.211.

[195] Rui Gu et al. “Dielectric properties and I-V characteristics of Li0.5La0.5TiO3 solid electrolyte for ceramic supercapacitors”. en. In: *Ceramics International* 45.7 (May 2019), pp. 8243–8247. DOI: 10.1016/j.ceramint.2019.01.128.

[196] D. L. Sidebottom, P. F. Green, and R. K. Brow. “Anomalous-diffusion model of ionic transport in oxide glasses”. en. In: *Phys. Rev. B* 51.5 (Feb. 1995), pp. 2770–2776. DOI: 10.1103/PhysRevB.51.2770.

[197] R. Ramaraghavulu and S. Buddhudu. “Analysis of structural, thermal and dielectric properties of LiTi2(PO4)3 ceramic powders”. en. In: *Ceramics International* 37.8 (Dec. 2011), pp. 3651–3656. DOI: 10.1016/j.ceramint.2011.06.025.

[198] A. Karmakar and A. Ghosh. “Dielectric permittivity and electric modulus of polyethylene oxide (PEO)–LiClO4 composite electrolytes”. en. In: *Current Applied Physics* 12.2 (Mar. 2012), pp. 539–543. DOI: 10.1016/j.cap.2011.08.017.

[199] Lucie Le Van-Jodin et al. “Dielectric properties, conductivity and Li+ ion motion in LiPON thin films”. en. In: *Solid State Ionics* 253 (Dec. 2013), pp. 151–156. DOI: 10.1016/j.ssi.2013.09.031.

[200] K. Vijaya Babu and V. Veeraiah. “Dielectric and impedance analysis of Li0.5La0.5Ti1-xZrxO3(x = 0.05 and 0.1) ceramics as improved electrolyte material for lithium-ion batteries”. en. In: *Materials Science-Poland* 34.3 (Sept. 2016), pp. 605–616. DOI: 10.1515/msp-2016-0092.

[201] Yurong Su et al. “Electrochemical properties and optical transmission of high Li^+ conducting LiSiPON electrolyte films: Electrochemical properties of high Li^+ conducting LiSiPON electrolyte films”. en. In: *Phys. Status Solidi B* 254.2 (Feb. 2017), p. 1600088. DOI: 10.1002/pssb.201600088.

[202] Nan Zhang et al. “Novel Research Approach Combined with Dielectric Spectrum Testing for Dual-Doped $Li_7P_3S_{11}$ Glass-Ceramic Electrolytes”. en. In: *ACS Appl. Mater. Interfaces* 11.31 (Aug. 2019), pp. 27897–27905. DOI: 10.1021/acsami.9b08218.

[203] Brahma Prakash Dubey et al. “Morphological, dielectric and transport properties of garnet-type Li6.25+yAl0.25La3Zr2-yMnyO12 (y = 0, 0.05, 0.1, and 0.2)”. en. In: *Solid State Ionics* 351 (Aug. 2020), p. 115339. DOI: 10.1016/j.ssi.2020.115339.

[204] Windhu Griyasti Suci et al. “Review of various sulfide electrolyte types for solid-state lithium-ion batteries”. en. In: *Open Engineering* 12.1 (June 2022), pp. 409–423. DOI: 10.1515/eng-2022-0043.

[205] K Minami et al. “Lithium ion conductivity of the Li2S–P2S5 glass-based electrolytes prepared by the melt quenching method”. en. In: *Solid State Ionics* 178.11-12 (May 2007), pp. 837–841. DOI: 10.1016/j.ssi.2007.03.001.

[206] Hirofumi Tsukasaki et al. “Crystallization behavior of the Li2S–P2S5 glass electrolyte in the LiNi1/3Mn1/3Co1/3O2 positive electrode layer”. en. In: *Sci Rep* 8.1 (Apr. 2018), p. 6214. DOI: 10.1038/s41598-018-24524-7.

[207] Sung Pil Woo et al. “A new approach: Li2S-P2S5 thin-films prepared by thermal evaporation as solid electrolytes”. en. In: *Journal of the Korean Physical Society* 69.4 (Aug. 2016), pp. 617–622. DOI: 10.3938/jkps.69.617.

[208] Noriaki Kamaya et al. “A lithium superionic conductor”. en. In: *Nature Mater* 10.9 (Sept. 2011), pp. 682–686. DOI: 10.1038/nmat3066.

[209] Narumi Ohta et al. “Solid electrolyte, thio-LISICON, thin film prepared by pulsed laser deposition”. en. In: *Journal of Power Sources* 146.1-2 (Aug. 2005), pp. 707–710. DOI: 10.1016/j.jpowsour.2005.03.062.

[210] Mitsuyasu Ogawa et al. “High-capacity thin film lithium batteries with sulfide solid electrolytes”. en. In: *Journal of Power Sources* 205 (May 2012), pp. 487–490. DOI: 10.1016/j.jpowsour.2012.01.086.

[211] Yanjie Liang et al. “Direct fabrication of thin-film LiTi2(PO4)3 electrodes using the hydrothermal method”. en. In: *Solid State Ionics* 296 (Nov. 2016), pp. 7–12. DOI: 10.1016/j.ssi.2016.08.006.

[212] Hee-Soo Kim et al. “Characterization of Sputter-Deposited $LiZr_2(PO_4)_3$ Thin Film Solid Electrolyte”. en. In: *J. Electrochem. Soc.* 162.10 (2015), A2080–A2084. DOI: 10.1149/2.0501510jes.

[213] Andrea Paolella et al. “Understanding the Reactivity of a Thin Li1.5Al0.5Ge1.5(PO4)3 Solid-State Electrolyte toward Metallic Lithium Anode”. en. In: *Advanced Energy Materials* 10.32 (2020), p. 2001497. DOI: 10.1002/aenm.202001497.

[214] Yasmine Benabed et al. “Assessing the Electrochemical Stability Window of NASICON-Type Solid Electrolytes”. en. In: *Front. Energy Res.* 9 (May 2021), p. 682008. DOI: 10.3389/fenrg.2021.682008.

[215] Shi-Gang Ling et al. “Enhanced ionic conductivity in LAGP/LATP composite electrolyte”. en. In: *Chinese Phys. B* 27.3 (Mar. 2018), p. 038201. DOI: 10.1088/1674-1056/27/3/038201.

[216] T. Mousavi et al. “Fabrication of Li1+xAlxGe2-x(PO4)3 thin films by sputtering for solid electrolytes”. en. In: *Solid State Ionics* 354 (Oct. 2020), p. 115397. DOI: 10.1016/j.ssi.2020.115397.

[217] Zhijian Sun et al. “Preparation and ion conduction of Li1.5Al0.5Ge1.5(PO4)3 solid electrolyte films using radio frequency sputtering”. en. In: *Solid State Ionics* 346 (Mar. 2020), p. 115224. DOI: 10.1016/j.ssi.2020.115224.

[218] Valerie Siller et al. “High performance LATP thin film electrolytes for all-solid-state microbattery applications”. en. In: *J. Mater. Chem. A* 9.33 (2021), pp. 17760–17769. DOI: 10.1039/D1TA02991F.

[219] RenJie Chen et al. “Preparation and performance of novel LLTO thin film electrolytes for thin film lithium batteries”. en. In: *Chin. Sci. Bull.* 57.32 (Nov. 2012), pp. 4199–4204. DOI: 10.1007/s11434-012-5292-y.

[220] Feihu Tan et al. “Stabilization of Li0.33La0.55TiO3 Solid Electrolyte Interphase Layer and Enhancement of Cycling Performance of LiNi0.5Co0.3Mn0.2O2 Battery Cathode with Buffer Layer”. en. In: *Nanomaterials* 11.4 (Apr. 2021), p. 989. DOI: 10.3390/nano11040989.

[221] Daniel Rettenwander et al. “Synthesis, Crystal Chemistry, and Electrochemical Properties of $Li_{7-2x}La_3Zr_{2-x}Mo_xO_{12}$ (x = 0.1–0.4): Stabilization of the Cubic Garnet Polymorph via Substitution of Zr^{4+} by Mo^{6+}”. en. In: *Inorg. Chem.* 54.21 (Nov. 2015), pp. 10440–10449. DOI: 10.1021/acs.inorgchem.5b01895.

[222] Christoph Loho et al. “Garnet-Type $Li_7La_3Zr_2O_{12}$ Solid Electrolyte Thin Films Grown by CO_2 -Laser Assisted CVD for All-Solid-State Batteries”. en. In: *J. Electrochem. Soc.* 164.1 (2017), A6131–A6139. DOI: 10.1149/2.0201701jes.

[223] Yuli Xiong et al. “Effects of annealing temperature on structure and opt-electric properties of ion-conducting LLTO thin films prepared by RF magnetron sputtering”. en. In: *Journal of Alloys and Compounds* 509.5 (Feb. 2011), pp. 1910–1914. DOI: 10.1016/j.jallcom.2010.10.086.

[224] Jordi Sastre et al. “Lithium Garnet $Li_7La_3Zr_2O_{12}$ Electrolyte for All-Solid-State Batteries: Closing the Gap between Bulk and Thin Film Li-Ion Conductivities”. en. In: *Adv Materials Inter* 7.17 (Sept. 2020), p. 2000425. DOI: 10.1002/admi.202000425.

[225] Eric Kazyak et al. “Atomic Layer Deposition of the Solid Electrolyte Garnet $Li_7La_3Zr_2O_{12}$”. en. In: *Chem. Mater.* 29.8 (Apr. 2017), pp. 3785–3792. DOI: 10.1021/acs.chemmater.7b00944.

[226] N.J. Dudney. “Solid-state thin-film rechargeable batteries”. en. In: *Materials Science and Engineering: B* 116.3 (Feb. 2005), pp. 245–249. DOI: 10.1016/j.mseb.2004.05.045.

[227] Theodosios Famprikis et al. “Composition Dependence of Ionic Conductivity in LiSiPO(N) Thin-Film Electrolytes for Solid-State Batteries”. en. In: *ACS Appl. Energy Mater.* 2.7 (July 2019), pp. 4782–4791. DOI: 10.1021/acsaem.9b00415.

[228] Shuyu Zhou et al. “Fast Li+ migration in LiPON electrolytes doped by multi-valent Fe ions”. In: *Journal of Energy Chemistry* 75 (Dec. 2022), pp. 349–359. DOI: 10.1016/j.jechem.2022.08.044.

[229] Dan Na et al. “A Solid-State Thin-Film Electrolyte, Lithium Silicon Oxynitride, Deposited by using RF Sputtering for Thin-Film Batteries”. en. In: *J. Korean Phys. Soc.* 76.9 (May 2020), pp. 855–859. DOI: 10.3938/jkps.76.855.

[230] Qiuying Xia et al. “Amorphous LiSiON Thin Film Electrolyte for All-solid-state Thin Film Lithium Battery”. en. In: *Journal of Inorganic Materials* 37.2 (2022), p. 230. DOI: 10.15541/jim20210132.

[231] Peter Hockicko, Peter Bury, and Francisco Munoz. “Analysis of Dielectric Properties of Lithium Phosphate Glasses”. en. In: *Komunikácie* 15.2A (July 2013), pp. 33–39. DOI: 10.26552/com.C.2013.2A.33-39.

[232] Alexandra Emly, Emmanouil Kioupakis, and Anton Van der Ven. “Phase Stability and Transport Mechanisms in Antiperovskite Li_3OCl and Li_3OBr Superionic Conductors”. en. In: *Chem. Mater.* 25.23 (Dec. 2013), pp. 4663–4670. DOI: 10.1021/cm4016222.

[233] Jingfeng Zheng, Brian Perry, and Yiying Wu. “Antiperovskite Superionic Conductors: A Critical Review”. en. In: *ACS Mater. Au* 1.2 (Nov. 2021), pp. 92–106. DOI: 10.1021/acsmaterialsau.1c00026.

[234] Wei Xia et al. “Antiperovskite Electrolytes for Solid-State Batteries”. en. In: *Chem. Rev.* 122.3 (Feb. 2022), pp. 3763–3819. DOI: 10.1021/acs.chemrev.1c00594.

[235] William D. Richards et al. “Interface Stability in Solid-State Batteries”. en. In: *Chem. Mater.* 28.1 (Jan. 2016), pp. 266–273. DOI: 10.1021/acs.chemmater.5b04082.

[236] Stephen J. Turrell et al. “Fabrication of thin solid electrolytes containing a small volume of an Li_3OCl-type antiperovskite phase by RF magnetron sputtering”. en. In: *Mater. Adv.* 3.24 (2022), pp. 8995–9008. DOI: 10.1039/D2MA00971D.

[237] Xujie Lü et al. “Antiperovskite Li3OCl Superionic Conductor Films for Solid-State Li-Ion Batteries”. In: *Advanced Science* 3.3 (2016), p. 1500359. DOI: 10.1002/advs.201500359.

[238] Charles Monroe and John Newman. “The Impact of Elastic Deformation on Deposition Kinetics at Lithium/Polymer Interfaces”. en. In: *J. Electrochem. Soc.* 152.2 (2005), A396. DOI: 10.1149/1.1850854.

[239] Michael A. Citrin et al. “From ion to atom to dendrite: Formation and nanomechanical behavior of electrodeposited lithium”. en. In: *MRS Bull.* 45.11 (Nov. 2020), pp. 891–904. DOI: 10.1557/mrs.2020.148.

[240] Yaoyu Ren et al. “Direct observation of lithium dendrites inside garnet-type lithium-ion solid electrolyte”. en. In: *Electrochemistry Communications* 57 (Aug. 2015), pp. 27–30. DOI: 10.1016/j.elecom.2015.05.001.

[241] Chunhua Wang et al. “Dendrite-free all-solid-state lithium batteries with lithium phosphorous oxynitride-modified lithium metal anode and composite solid electrolytes”. en. In: *Nano Res.* 12.1 (Jan. 2019), pp. 217–223. DOI: 10.1007/s12274-018-2205-7.

[242] Rachna Khurana et al. “Suppression of Lithium Dendrite Growth Using Cross-Linked Polyethylene/Poly(ethylene oxide) Electrolytes: A New Approach for Practical Lithium-Metal Polymer Batteries”. en. In: *J. Am. Chem. Soc.* 136.20 (May 2014), pp. 7395–7402. DOI: 10.1021/ja502133j.

[243] Fudong Han et al. “High electronic conductivity as the origin of lithium dendrite formation within solid electrolytes”. en. In: *Nat Energy* 4.3 (Mar. 2019), pp. 187–196. DOI: 10.1038/s41560-018-0312-z.

[244] Till Fuchs et al. “Current-Dependent Lithium Metal Growth Modes in “Anode-Free” Solid-State Batteries at the Cu|LLZO Interface”. en. In: *Advanced Energy Materials* 13.1 (Jan. 2023), p. 2203174. DOI: 10.1002/aenm.202203174.

[245] Ziyang Ning et al. “Visualizing plating-induced cracking in lithium-anode solid-electrolyte cells”. en. In: *Nat. Mater.* 20.8 (Aug. 2021), pp. 1121–1129. DOI: 10.1038/s41563-021-00967-8.

[246] Thorben Krauskopf et al. “Lithium-Metal Growth Kinetics on LLZO Garnet-Type Solid Electrolytes”. en. In: *Joule* 3.8 (Aug. 2019), pp. 2030–2049. DOI: 10.1016/j.joule.2019.06.013.

Anode-free configuration for high integration level

[244] Till Fuchs et al. “Current-Dependent Lithium Metal Growth Modes in “Anode-Free” Solid-State Batteries at the Cu|LLZO Interface”. en. In: *Advanced Energy Materials* 13.1 (Jan. 2023), p. 2203174. DOI: 10.1002/aenm.202203174.

[247] Zhengkun Xie et al. “Anode-free rechargeable lithium metal batteries: Progress and prospects”. en. In: *Energy Storage Materials* 32 (Nov. 2020), pp. 386–401. DOI: 10.1016/j.ensm.2020.07.004.

[248] Christian Heubner et al. “From Lithium-Metal toward Anode-Free Solid-State Batteries: Current Developments, Issues, and Challenges”. en. In: *Advanced Functional Materials* 31.51 (2021), p. 2106608. DOI: 10.1002/adfm.202106608.

[249] Sanjay Nanda, Abhay Gupta, and Arumugam Manthiram. “Anode-Free Full Cells: A Pathway to High-Energy Density Lithium-Metal Batteries”. en. In: *Advanced Energy Materials* 11.2 (2021), p. 2000804. DOI: 10.1002/aenm.202000804.

[250] B. J. Neudecker, N. J. Dudney, and J. B. Bates. ““Lithium-Free” Thin-Film Battery with In Situ Plated Li Anode”. en. In: *J. Electrochem. Soc.* 147.2 (2000), p. 517. DOI: 10.1149/1.1393226.

[251] Michael J. Wang et al. “Enabling “lithium-free” manufacturing of pure lithium metal solid-state batteries through in situ plating”. en. In: *Nat Commun* 11.1 (Dec. 2020), p. 5201. DOI: 10.1038/s41467-020-19004-4.

[252] Hongyi Pan et al. “Fast Li Plating Behavior Probed by X-ray Computed Tomography”. en. In: *Nano Lett.* 21.12 (June 2021), pp. 5254–5261. DOI: 10.1021/acs.nanolett.1c01389.

[253] Eric Kazyak et al. “Understanding the electro-chemo-mechanics of Li plating in anode-free solid-state batteries with operando 3D microscopy”. en. In: *Matter* 5.11 (Nov. 2022), pp. 3912–3934. DOI: 10.1016/j.matt.2022.07.020.

[254] Lucile Magnier et al. “Quantification of the Local Topological Variations of Stripped and Plated Lithium Metal by X-ray Tomography”. en. In: *ACS Appl. Mater. Interfaces* 12.37 (Sept. 2020), pp. 41390–41397. DOI: 10.1021/acsami.0c10860.

[255] John A. Lewis et al. “Linking void and interphase evolution to electrochemistry in solid-state batteries using operando X-ray tomography”. en. In: *Nat. Mater.* 20.4 (Apr. 2021), pp. 503–510. DOI: 10.1038/s41563-020-00903-2.

[256] Fumihiro Sagane et al. “Effects of current densities on the lithium plating morphology at a lithium phosphorus oxynitride glass electrolyte/copper thin film interface”. en. In: *Journal of Power Sources* 233 (July 2013), pp. 34–42. DOI: 10.1016/j.jpowsour.2013.01.051.

[257] Munekazu Motoyama et al. “In Situ Scanning Electron Microscope Observations of Li Plating/Stripping Reactions with Pt Current Collectors on LiPON Electrolyte”. en. In: *J. Electrochem. Soc.* 165.7 (2018), A1338–A1347. DOI: 10.1149/2.0411807jes.

[258] Hikaru Sano et al. “Effect of Current Density on Morphology of Lithium Electrodeposited in Ionic Liquid-Based Electrolytes”. en. In: *J. Electrochem. Soc.* 161.9 (2014), A1236–A1240. DOI: 10.1149/2.0331409jes.

[259] Yong-Gun Lee et al. “High-energy long-cycling all-solid-state lithium metal batteries enabled by silver–carbon composite anodes”. en. In: *Nat Energy* 5.4 (Mar. 2020), pp. 299–308. DOI: 10.1038/s41560-020-0575-z.

"[..] homo faber fortunae suae [...]"

Appius Claudius Caecus

"[..] Every man is the artifex of his destiny [...]"

trad. from **Appius Claudius Caecus**

CHAPTER II

Thin-film Batteries Fabrication Process

ABSTRACT

The subject of this chapter is the fabrication process of a thin-film all-solid-state micro-batteries. The device here described is used as a test vehicle in all experimental chapters. This chapter also provides a first characterization of the device as a solid foundation for the following physical modeling.

In the first section, the device is presented, and the fabrication process is reviewed and analyzed. The effect of process parameters on the final film quality is discussed.

The second section is dedicated to the physical and chemical characterization of the final device. The main purpose is to verify the quality and spatial homogeneity of the different films. Particular attention is devoted to the cathode characterization in order to assess the spatial homogeneity of the crystal phase and crystalline orientation.

Table of Contents

1. Materials and Deposition

Surviving the bibliographical jungle may leave us a bit tired, but it has also provided us with a compass to guide our steps through the next chapters. No surprise, the choice of material and design chosen to address the miniaturization of a cell: $LiCoO_2$ (LCO) cathode for high capacity and power density, LiPON to ensure good resistance to dendrite growth, and the anode-free configuration to minimize the total volume and improve back-end compatibility with ICs processing. The very same stack with which the anode-free configuration was first demonstrated. It may seem improbable to be able to improve a twenty-years-old device, but with a bit of simulation and prospect, everything is possible.
For intellectual property reasons, I will not be able to provide the reader with the amount of detail he deserves about the optimization of the production process. Some details are available in [1] concerning the tools and the flow.
However, a large literature is present on the RF sputtering of $LiCoO_2$ and LiPON and I will here review the effects of the main parameters on the quality and properties of the films, in order to propose at least a clearer view on the challenges one may encounter during the fabrication of thin-film batteries.
Before delving into the analysis of the deposition process, I will just recall the cross-section structure of a thin-film battery. In figure 2.1, the schematic of the cell used in the rest of this work is shown. The substrate is a silicon wafer with a thermal oxide to provide electrical insulation between different cells on the wafer. The cathode current collector is platinum, and $LiCoO_2$ is deposited on top of it. Follows the electrolyte and the titanium current collector, which is the seed layer for the lithium anode plating. In order to operate the cell in the air, several microns of parylene are added to the structure. Electrical contact is recovered by means of titanium vias through the polymer.

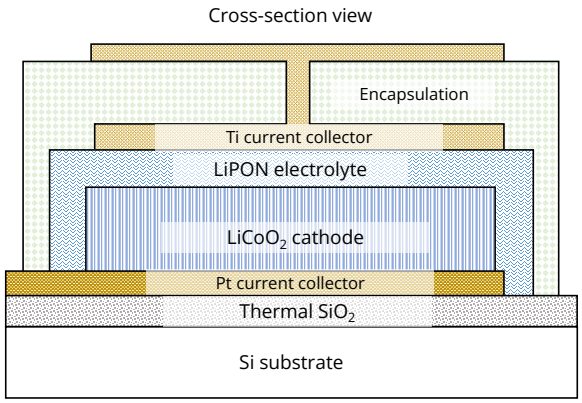

Figure 2.1: Anode free thin-film battery schematic, as realized for the present work.

1.1 PVD sputtering setups and parameters

Both the cathode and the electrolyte are deposited by means of RF magneton sputtering. The sputtering process has been briefly introduced in the first chapter, but I will use the present section to add more details on the physics behind the deposition. It is in fact essential to understand the working principle of sputtering in order to critically evaluate the effect of process parameters on the film deposition. Sputtering was enhanced over time, from the first setup,

called DC sputtering, to RF and Rf magneton sputtering. It is, in fact, simpler to introduce each of the three and point out the difference and the reason for each modification.

DC sputtering

In Figure 2.2a the setup for the DC sputtering is reported. The deposition takes place under vacuum, inside the deposition chamber. Two electrodes are placed inside the chamber, and a high electric field is applied. Typical polarization voltages are on the order of several kilovolts. The sputtering process relies on a type of plasma called *glow discharge*. This phenomenon takes place when an inert gas, like argon, is placed in an electric field. As soon as a first gas atom is ionized, for example, by cosmic radiation, the electric field will split the positive charged ion and the negative electron. The electric field accelerates the charged particles towards the respective electrode (anode for electrons, cathode for ions). During the motion, the electron may hit a neutral gas atom, and if the energy of the electron is high enough, the atom will be ionized as well, creating a new ion-electron pairs. Because electrons are the only capable of generating new charged particles, the chain reaction is doomed to end as soon as the first electron reaches the anode and is neutralized. It is here that the ions come to the rescue. If the ions have enough energy, when they reach the cathode surface, they will hit the surface and eject particles from the cathode material. Atoms, ions, and electrons can be emitted. If an electron is emitted, it will be accelerated in the opposite direction, and a new chain reaction will start. If the applied voltage is high enough, the self-sustained reaction, called glow discharge, results in a constant flux of ions and electrons, hence a current flowing through the reaction chamber.
While the ions generated by collision on the target accelerate back to the target and may trigger more emission of particles, the neutral atoms will simply continue in the direction they have been ejected. Those atoms may be deviated or ionized, but if they reach the anode surface, they are deposited onto it. The deposition of the new film on the anode is then accomplished.
An important aspect of the glow discharge is the distribution of charges across the deposition chamber. The ions and electrons tend to accumulate near their respective absorption interfaces. That can be intuitively understood considering that all the ions generated by collision at the cathode interface, cannot escape far away from the surface, because the electric field tends to pull them back to the surface. That means that the volume close to the cathode will have a higher density of ions with respect to the rest of the deposition chamber. The same applies for electrons on the anode side. This spatial charge results in two *double layers*, at the two electrode interfaces. The double layers are highly charged, and hence the electric field will be particularly high in those regions. In fact, most of the voltage drop takes place near the two interfaces, and the system can be represented by two capacitors in series.
The main issue with DC sputtering is the necessity to keep the cathode and anode neutral when electrons and ions impinge on them. If a charge layer builds up, this will prevent further collisions and kill the glow discharge. DC sputtering is hence limited to the deposition of conductive films that ensure a conductive path for the whole duration of the deposition.

RF sputtering

In order to deposit insulating materials, an RF excitation is applied instead of a DC one to the two electrodes. This way, the charge accumulated on the electrodes is balanced automatically with each cycle. If the voltage is enough to trigger a glow discharge, positive charges accumulate on the electrode during one half-cycle and are neutralized by the positive electron during the second half-cycle. In order for the glow discharge to be constantly active, the two half-cycles

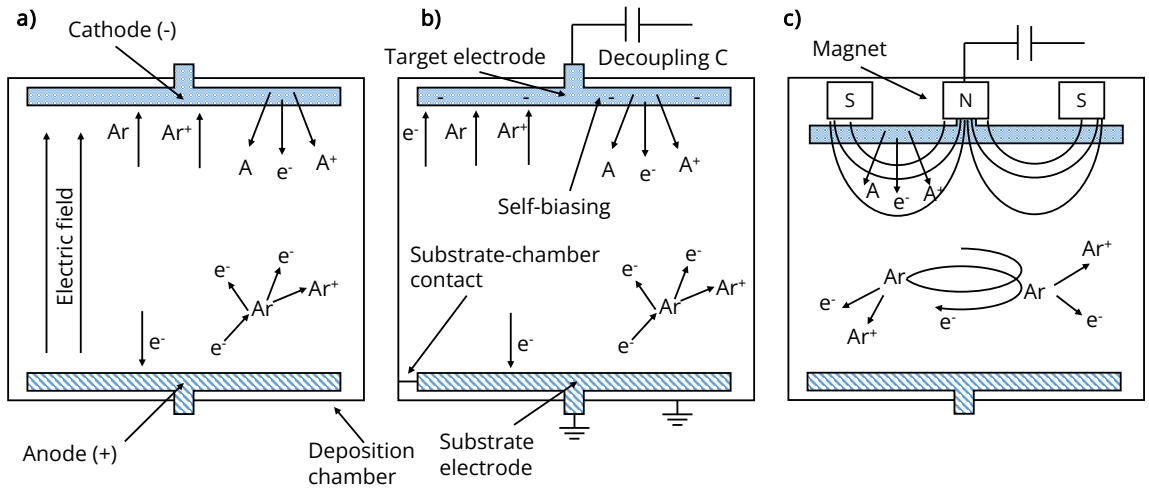

Figure 2.2: Sputtering configurations: a) DC sputtering; b) RF sputtering; c) RF magneton sputtering.

must be faster than the time it takes for the glow discharge to be suppressed due to charge accumulation. Experimentally, the plasma is stable for around $1\,\mu s$ hence, an excitation on the order of $1\,MHz$ is required to ensure stable plasma in the reaction chamber. So far, so good, but this way, both electrodes are bombarded by ions and no net deposition is accomplished. In order to create the required asymmetry, it is possible to exploit the two double layers. As long as the two electrodes have the same size, the voltage drop will be symmetrically distributed between them. The general relationship for two capacitors in series with capacitances C_1 and C_2 is $\frac{V_1}{V_2} = \frac{C_2}{C_1}$. But how do you increase the size of one of the two capacitors without changing the set-up? The clever idea is shown in Figure 2.2b: the deposition electrode is shorted to the deposition chamber, resulting in a large capacitance imbalance (the electrode and deposition chamber are a single, large-area electrode). This way, most of the RF voltage is concentrated at the target electrode.
So far, we considered the target to be insulating, which is indeed beneficial. If the target is conductive or partially conductive, a fraction of the charge accumulated during the first half-cycle is removed, and during the second half-cycle, fewer particles with opposite charge are required to achieve net balance. Any further charge will charge the electrode and prevent further impact on the electrode. This is in fact negative because we want to maximize the number of impinging ions, hence the number of ejected atoms. In order to solve this issue, a blocking capacitor is added in series to the target electrode to prevent any charge leakage.

RF magneton sputtering

Both DC and RF sputtering rely on the linear motion of electrons between the anode and cathode to ionize the gas atoms. Most of the secondary electrons emitted do not actually cause further ionization before being reabsorbed. The quite low degree of ionization determines a poor deposition rate. In order to strongly increase the effective path of electrons, thereby increasing the ionization probability, RF magneton sputtering was introduced. As reported in Figure 2.2c the configuration is the same as RF sputtering, with the addition of two magnets behind the target electrode. The cross-section shows two south poles, but actually this is usually a toroidal shape, running around the outer rim of the target, and the north pole is usually a single bar, placed in

the middle of the electrode. The magnetic field lines are reported in the figure. The effect of the magnetic field is to transmit a circular motion to the electrons. The spiral path largely increases the total ionization, boosting the deposition rate up to a hundred times.
In the present work and, in general, for most of the literature, RF magneton sputtering is the preferred configuration for both its flexibility in material choice and the high deposition rate.

Process parameters

The RF magneton sputtering deposition process can be tuned by means of several parameters, which affect deposition rate, film morphology, and stoichiometry. Of utter importance is the control of the plasma features. We already pointed out that the degree of ionization, which can be measured by the current flowing through the deposition chamber, should be as high as possible to ensure a high deposition rate. The simplest way to increase the ionization probability is to increase the energy of the electrons. This is done by increasing the electric field, that is, the amplitude of the RF excitation. In the literature, this parameter is often reported in the form of a power: the product between the imposed polarization and the current density. This is mostly due to the machine configuration, which permits directly setting and controlling the power instead of the bare voltage. Unluckily, voltage and current are not linearly related, and power alone is not enough to completely describe the deposition conditions [2, 3]. This makes it harder to estimate the combined effect of the deposition parameters when only the power is reported.
The number of ions impinging on the substrate can also be increased by increasing the partial pressure of the gas in the chamber. Even if the degree of ionization is constant, if more atoms are available to scatter electrons, the current density will increase. Notwithstanding, the effect of the gas pressure on the deposition rate may not be straightforward. The gas ions and the neutral target atoms will experience a higher number of collisions as well. This results in a lower bombarding energy on the target and a lower number of neutral atoms to be deposited. Moreover, the very same neutral atoms could hit the target with lower energy, resulting in poor adhesion, or be diverted to the chamber wall. A small increase in the gas pressure may be beneficial, but the positive effect will vanish for large pressure values.
Another parameter to control in order to increase the deposition rate without actually increasing the ionization probability is the target-to-substrate distance. Intuitively, the closer the two electrodes are, the higher the number of neutral atoms that will deposit on the substrate. Because the minimum ejection angle from the target to avoid the substrate increases. Too close a distance may result in the opposite effect because it also reduces the effective path of electrons, hence the ionization probability.
More complex parameters can be introduced, with different effects depending on the specific material to be deposited. Introducing other gas species, like oxygen and nitrogen, allows the deposition of material with different stoichiometry with respect to the target by means of impurity incorporation.
The temperature control of both target and substrate can impact the deposition rate and the final morphology and crystallinity of the film. In particular, partial crystallization is possible when the substrate electrode is heated. The same effect is experienced by changing the deposition substrate, which may promote the growth of certain crystalline orientations. The active bias of the substrate and the mechanical properties of the target (density, composition, age) may as well impact the deposition rate.
As it will be clear in the next section, the literature concerning process parameter effects is largely incomplete. Few studies focus on the effect of deposition parameters for LCO and LiPON, and

most of them do not report the complete set of parameters, leading to large, unexplained variations in deposition rate and film morphology. This is partially understandable due to the large effort needed to refine a deposition flow, which is usually patented or hidden as an industrial secret instead of being shared with the scientific community. *Excusatio non petita, accusatio manifesta*, I will be included in this obscurantist lot. The following critical review of the LCO and LiPON bibliographies is my penance for having betrayed science.

1.2 PVD $LiCoO_2$

When depositing lithiated materials, the first important point to be aware of is the deposition substrate. In the anode section, we pointed out how many pure materials (metals and silicon) can easily intercalate lithium ions. If cathode material is deposited on such a substrate, there is the risk, in particular during heating treatment, of losing active lithium from the electrode by migration into the substrate. Moreover, the electrode material itself may react with the metal and form an oxide or other passivating layers, which may electrically isolate the electrode and the current collector, like in the case of titanium and iron [4]. Platinum is a mainstream substrate for LCO deposition, and it is also the one used in the present work. As already anticipated, RF magneton sputtering is the preferred deposition method in the literature. In general, the sputtering target is composed of pressed, crystallized LCO powder, sometimes mixed with cobalt carbonate. The deposited film, according to the deposition condition, can be amorphous or partially crystallized. Usually, a high temperature step after deposition is performed in air at around $700\,^{\circ}$C to obtain a crystalline phase favorable to lithium diffusion (diffusion channels perpendicular to the deposition substrate). The final properties are controlled by both the deposition condition and the subsequent annealing. The important properties to monitor and control are the deposition rate, the density of the film, and the orientation of the crystal planes. This last point is essential for a material with 2D diffusion channels like LCO. If the diffusion planes are not correctly aligned in the direction of the electric field, the rating performance of the device is severely impacted [4–6]. Various techniques are reported in the literature to obtain the right crystal orientation, depending on the deposition substrate. The most successful approaches are annealing during deposition [5], oxygen introduction in the deposition chamber [7], and post-deposition annealing [8]. The effect of the latter is strongly influenced by the thickness of the LCO layer and the nature of the substrate [9]. The change in orientation during high-temperature crystallization is due to the difference in thermal expansion coefficient between the substrate and the LCO. In the case of a mismatch, the LCO will reorganize in order to minimize the strain energy. The competition between surface and volume strain energy determines the final texture. For thin layers ($<1\,$µm) surface strain energy tends to dominate, and the obtained crystal orientation is unfavorable: diffusion planes oriented parallel to the substrate. For thicker layers, the volume strain energy dominates, and the right orientation can be obtained [10, 11]. In Figure 2.3, a schematic view of the reorientation process is proposed. CoO_2 planes perpendicularly oriented with respect to the substrate can easily accommodate the mechanical stress with respect to parallel planes due to the difference in covalent and ionic bond stiffness.
Concerning the deposition rate, the literature is quite difficult to interpret for two main reasons: the first is the absence, for most of the publications, of the complete set of deposition parameters. The second is a diffuse disagreement on the quantitative effect of each parameter. For example, the influence of the oxygen/argon fraction is studied by many authors, but for quite similar sets of parameters, the reported deposition rate largely differs. In table 2.1 the main literature results are reported. As an example, Liao et al. [12] measured a growth rate of $14\,\mathrm{nm\,min^{-1}}$ at comparable deposition conditions with respect to Zhu et al. [13], but in the latter

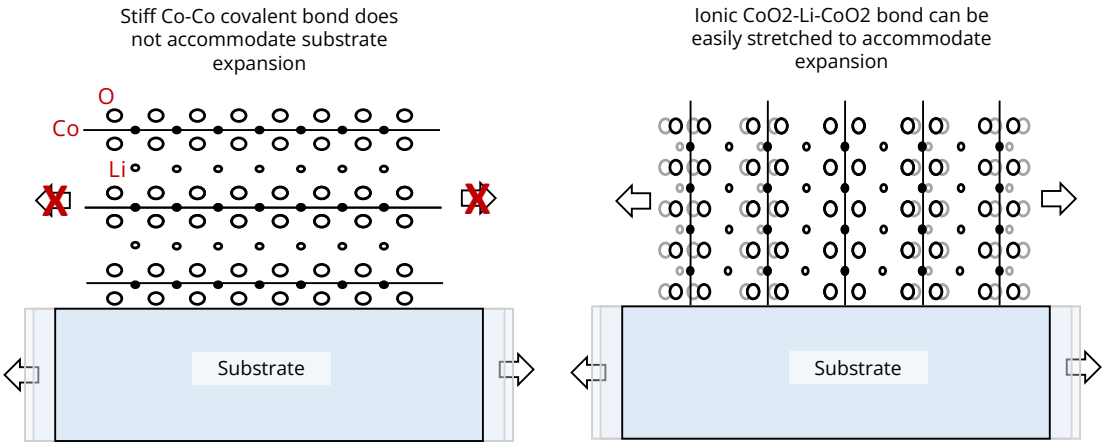

Figure 2.3: LCO crystal planes reorientation during high temperature crystallization.

the deposition rate is 4 times lower. While the total deposited thickness should not impact the effect a priori, it seems that this parameter, too often forgotten, may play an important role. Another parameter rarely considered is the condition and properties of the sputtering target, which in most of the literature are barely described, even if some studies highlighted the effect of target conditioning on the final film morphology [14, 15]. The final target density and production process (cold/hot pressing, annealing) impact the mechanical resistance of the target to ion bombardment. A stiff target will require higher impact energy for atom ejection, and the deposition rate will be reduced. With so many parameters, it is not enough to consider a few publications to assess the actual effect on deposition. Following, I propose a critical review of the effect of RF magneton sputtering parameters on the observed deposition rate. First by considering the results of single studies, and then by comparing the aggregate data from the whole available literature. Focusing on the deposition rate is relevant from at least two main points of view. First, the deposition rate is itself an input parameter when higher-order features are studied. As a matter of fact, the crystalline orientation and the stoichiometry (in particular for LiPON) of the deposited film are influenced by the deposition rate. Being able to control and model is a fundamental step to avoid spurious correlations. For example, we may have the impression that the pressure has a certain effect on the final stoichiometry, but in fact it is acting on the deposition rate, which is the real variable controlling the stoichiometry. Second, the study of the deposition rate is fundamental when very thick cathodes have to be deposited. Without optimization, the deposition may take several days. This is not only a problem of machine availability but also reflects on the final cost of the device.

Effect of working pressure

The effect of working pressure on the deposition of LCO is separately evaluated by four main studies [12, 16–18]. Two over four does not report the deposition rate [16, 17]. The study of Liao et al. of 2006 is indeed the only large database on the topic, but the total thickness of the film is not reported. The process parameters strongly differ from those in the study by Ziebert et al. of 2010. In particular, the former has a $25\,\%$ of oxygen inclusion in the plasma atmosphere and a controlled heating of the substrate to $250\,^{\circ}$C. Moreover, the pressure range is quite different: Ziebert reports the deposition rate only for very high pressure (10 and 25 Pa) while Liao does not

Ref.	Power (W)	Power/surface (W cm^{-2})	Pressure (Pa)	Ar (%)	Thickness (nm)	Dep. rate (nm min^{-1})
Ziebert-2010	200	4.53	10	100	2800	20
Michel-2020	NA	2.2	0.1	100	1195	19.92
Rao-2013	200.55	4.4	0.5	90	450	15
Xie-2008	100	5.1	2	100	850	14.17
Liao-2006	125	6.12	2.66	75	NA	13.9
Liao-2006	100	4.9	2.66	75	NA	13.9
Xie-2007	100	5.1	2	100	1460	12.17
Jeon-2005	150	1.84	0.66	90	NA	8.3
Turrell-2021	200.55	4.4	0.5	100	1200	8
Yoon-2013	150	7.35	0.65	90	350	5.83
Yoon-2011	196.25	2.5	1.7	100	NA	5.6
Fragnaud-1996	350	1.74	8	100	NA	4
Zhu-2010	100	4.9	2.7	75	466	2.59
Yibo-2019	100.01	2.6	1	38	2460	2.05
Kim-2004	80	3.92	0.66	75	50	1.67
Bohne-2010	300	0.96	1	75	400	1.67
Bohne-2010	300	0.96	1	75	1600	1.67
Wang-1996	50	2.45	2.6	75	NA	1.2
Jan-2019	180	3.95	0.67	33	1650	1.14
Lee-1999	50	2.45	0.66	75	400	0.83

Table 2.1: deposition parameter and deposition rate collected from the literature.

exceed 7 Pa. Both report a negative effect of the increase in working pressure on the deposition rate. That is indeed in line with the physical picture. The suggested formula to link the deposition probability p_d and the working pressure exploits the relationship between working pressure P and mean free path λ: $P\lambda = C$ where C is a constant that depends on the gas composition.

$$p_d = Ae^{-\frac{d}{\lambda}} = Ae^{-\frac{dP}{C}} \tag{2.1}$$

Where d is the target-to-substrate distance and A is a constant that depends on other deposition parameters.

Effect of RF power

Four main works report the effect of increasing the RF power on the deposition rate [12, 19–21]. All four agree on the beneficial effect of power on the deposition rate, but as for the working pressure, each data set is collected at different deposition conditions concerning the other parameters. The ratio of argon and oxygen in the plasma atmosphere varies from a minimum of $33\,\%$ argon in Jan et al. of 2019 up to $100\,\%$. The absolute value and the effect of the power increase are strongly mediated by the difference in plasma composition and target-to-substrate distance. The first-order effect of power Pw on deposition rate can be expressed as:

$$p_d = APw \tag{2.2}$$

Where A is a constant dependent on other deposition parameters.

Effect of atmosphere composition

In the early stages of the development of LCO sputtering, the introduction of oxygen has been identified as a route to obtain certain crystalline orientations without post-deposition annealing. Unfortunately, this technique has the drawback of lowering the deposition rate. Notwithstanding, the use of a mixed atmosphere is still a popular solution, which makes it more difficult to decorrelate the effects of other deposition parameters. The best studies on the subject are the already cited Liao et al. of 2006 [12] and the two works of Trask [7] and Michel [22]. All authors agree on the negative effect of the increase in oxygen partial pressure on the deposition rate. While the two more recent studies show a decaying exponential relationship with a large drop in deposition rate as soon as oxygen is introduced, followed by a linear zone, the older work of Liao seems to suggest a linear or slightly parabolic dependence. The main reason for this difference may be found in the other parameters, in particular the working pressure, which in Liao is five times higher than the other two. The RF power is also higher in the older paper, by about two times. In order to account for this variation, an exponential equation can be used with an exponential constant that is a function of the other process parameters:

$$p_d = A + B[Ar] + Ce^{-D(1-[Ar])} \tag{2.3}$$

Where D in particular is a function of other process parameters.

Effect of substrate temperature

The effect of the substrate temperature on the deposition rate is often disregarded. In many studies, the substrate temperature is neither controlled nor monitored and usually fluctuates between room temperature and a few hundred degrees Celsius. In the case of floating substrates, the deposition temperature is indirectly controlled by the RF power: the higher the power, the higher the steady-state temperature of the substrate [20]. For direct control of substrate temperature, Michel [22], Zhu [13] report an increase in the deposition rate with temperature, while Yoon 2011 [23] and Yoon 2013 [5] report a decrease in the deposition rate with increasing substrate temperature. The discrepancy in the absolute values is easily explained by the different working pressure and oxygen molar fraction of each dataset.
Because the effect seems to be pretty low and because most of the available measurement relies on floating substrate, the substrate temperature will not be included in the aggregate analysis at the end of this section. Moreover, the reported temperature is usually the temperature of the substrate, but the actual temperature that influences the deposition rate is the temperature at the surface of the deposited film, which may be higher than the measurement one depending on the thermal conductivity of the film.

Effect of target distance

The last parameter to be controlled is the target-to-substrate distance. We already pointed out the effect of the distance in the working pressure section. No studies on this particular parameter are available in the literature, but simulation on the LCO deposition [24] confirms the exponential decay of the deposition rate as a function of the target distance. No additional equation is required but 2.1.

Aggregate effect of process parameters

Summing up all the effects listed so far, it is possible to write a unique equation describing the deposition rate of LCO:

$$p_d = (A + B[Ar] + C_1 e^{-D(1-[Ar])}) P w e^{-\frac{dP}{C_2}} \tag{2.4}$$

The value of each parameter can be optimized by means of Bayesian inference [25] using the dataset presented in the literature. I tried four different models with respect to the D coefficient :

$$\text{lco.1:} \qquad D = D_0 \tag{2.5}$$

$$\text{lco.2:} \qquad D = D_0 + D_1 P \tag{2.6}$$

$$\text{lco.3:} \qquad D = D_0 + D_2 P w \tag{2.7}$$

$$\text{lco.4:} \qquad D = D_0 + D_1 P + D_2 P w \tag{2.8}$$

The results are reported in Figure 2.4 for all four models. PSIS (Pareto-smoothed importance sampling) and WAIC (Watanabe-Akaike information criterion) statistical tests [25] suggest lco.2 and lco.4 to be the best models in terms of prediction power. The values for each parameter are quite close for the two models, and I reported the detailed values for model lco.4 in Table 2.2. All parameters started with a Gaussian prior with $\mu = 0$ and $\sigma = 2$ and the total number of unique points from the literature was 42.

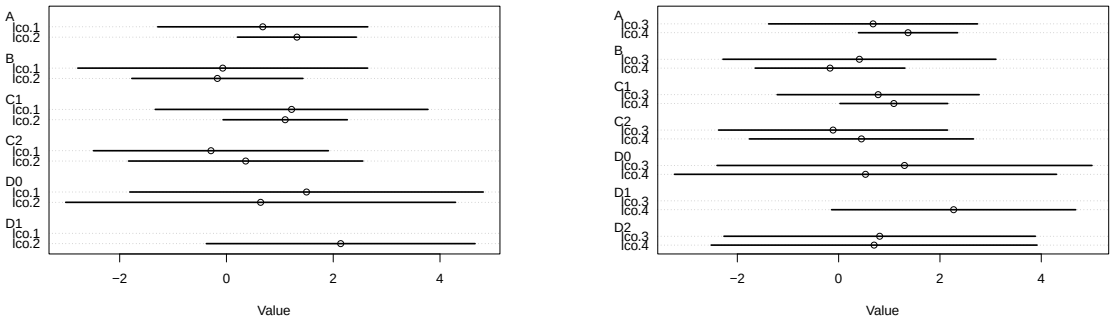

Figure 2.4: Estimated parameter effect for four different models of the LCO growth rate for RF magneton sputtering deposition.

Param.	**Mean**	**Std**	$5.5\,\%$	$94.5\,\%$
A	1.33	0.52	0.05	2.14
B	-0.12	0.78	-1.29	1.13
C_1	1.07	0.56	0.26	1.92
$0.01/C_2$	0.44	1.14	-1.40	2.25
D_0	0.54	1.87	-2.44	3.58
D_1	2.26	1.26	0.32	4.38
D_2	0.71	1.65	-1.78	3.52

Table 2.2: Effect of process parameter on deposition rate as estimate from model lco.4.

The results are far from satisfactory, with a lot of uncertainty about the effect of the parameters. Apart from the mean value effect (negative or positive), which seems to agree with our

hypothesis, the exact value of each parameter cannot be estimated. We already anticipated how some effects, like the temperature of the substrate and target properties, are not accurately described in the literature. The missing information introduces lots of variability in the deposition rate that cannot be described by the available parameters alone. As a matter of example, the parameter C_2 which can be easily fitted for a single database [12], cannot be determined when all datasets are combined.

1.3 PVD LiPON

LiPON is an enhanced version of a well-known glassy electrolyte, Li_3PO_4. The basic structure of the latter is exactly the one described in the previous chapter: the network former is the phosphorous oxide P_2O_5 with lithium oxide as network modifier [26]. Li_3PO_4 can crystallize in different structures, but they are in general less ionic conductive than the amorphous counterpart [27]. We pointed out how the conductivity of a glassy electrolyte is determined by the formation of lithium vacancies and interstitial defects. The nitrogen is introduced as a doping agent to increase the number of vacant lithium ions and improve the conductivity of glassy Li_3PO_4. The final stoichiometry is influenced by the deposition conditions, and the generic formula LiPON accounts for tens of slightly different compounds. Nitrogen doping is easily accomplished by means of PVD. The use of nitrogen as a sputtering gas guarantees the inclusion of a certain number of impurities in the film. Deposition parameters like gas pressure and power are hence expected to have a strong impact on the performance of the electrolyte, in particular on the ionic conductivity. The general effect seems to be an increase in conductivity at higher nitrogen content [26, 28–33]. The only work that suggests a decrease in the ionic conductivity with respect to the nitrogen content is Suzuki et al. of 2011 [34]. As for LCO, even if there is a strong agreement on the tendency, the fluctuation of the absolute value of conductivity is so large as to mask any general tendency with respect to the process parameters. Some effort has been invested in the interpretation of the variation of the ionic conductivity on the basis of the electrolyte composition and, in particular, on the local chemical environment of oxygen and nitrogen atoms. Fleutot et al. [32] suggested a double substitution mechanism. For low doping levels, nitrogen mainly substitutes the bridging oxygen atoms, which are linked with two phosphates. In this configuration, nitrogen forms three single bonds with phosphate atoms. If enough nitrogen is introduced, the bridging oxygen is completely replaced by nitrogen. Additional nitrogen must be incorporated as double-bonding nitrogen (P−N=P). In Figure 2.5 the three different chemical environments are reported. As a matter of fact, the agglomerate data from all relevant litera-

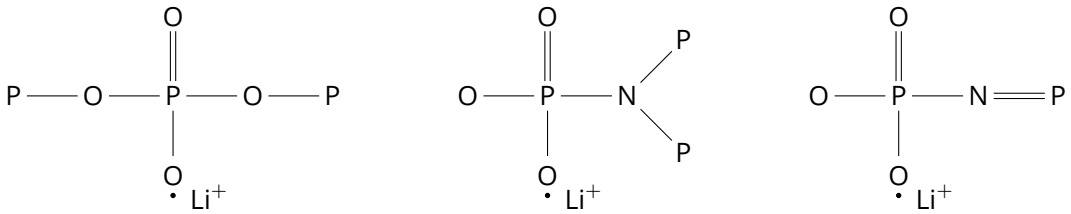

Figure 2.5: from left to right: un-doped LI_3PO_4 local environment; LiPON local environment with bridging nitrogen; LiPON local environment with double bonding nitrogen.

ture sources reported in Figure 2.6a strongly disagrees with this interpretation. In particular, the data from Mani et al. reports a LiPON with a low doping level and all nitrogen in double bonding position. A more interesting correlation is obtained if the ratio between double and triple bonding nitrogen is plotted against the deposition rate (Figure 2.6b). The double bonding sites are substituted by nitrogen preferentially at low deposition rates, while at higher deposition rates,

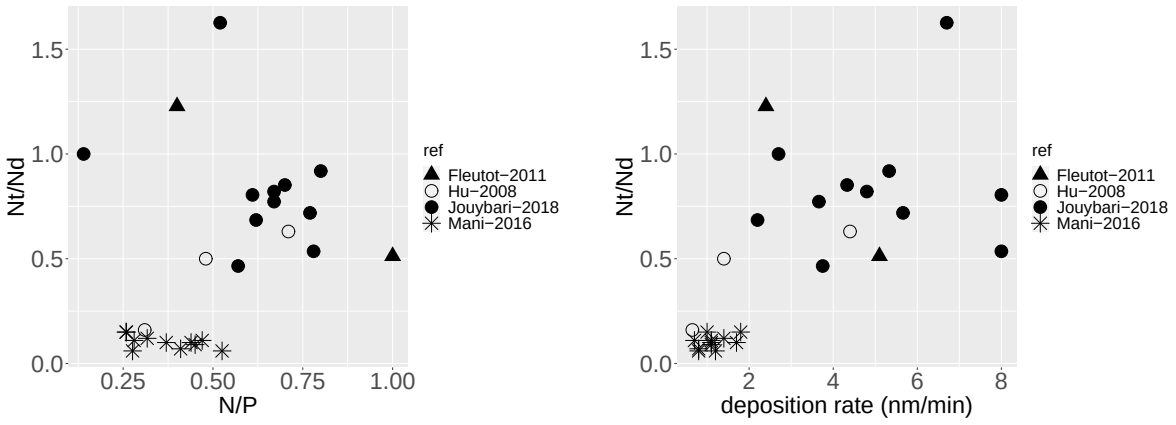

(a) (b)

Figure 2.6: variation of the ratio between triple (N_t) and double (N_d) bonding nitrogen as a function of the total nitrogen incorporation and the deposition rate.

the occupancy of the triple bonding is increased.

Much easier to analyze is the deposition rate. In the next sections, I will propose, as for LCO a statistical model to control the deposition rate of LiPON by tuning the deposition parameters. The problem is simpler in this case because the sputtering atmosphere is always pure nitrogen, and the experimental variability is drastically reduced.

Effect of working pressure

As for LCO, we expect the gas pressure to reduce the deposition rate. No matter the plasma gas species, increasing the gas density will reduce the mean free path of electrons, ions, and neutral species, reducing the ion bombardment on the target and the energy of the neutral species depositing on the substrate. The database provided by Hamon [29] confirm the general hypothesis, but three other databases report various other tendencies: a negative parabola for Jouybari [26] and Vieira [35]; a positive parabola in Mani [33]. In order to partially explain such variability, we first recall the equation 2.1 introduced for the LCO:

$$p_d = Ae^{-\frac{d}{\lambda}} = Ae^{-\frac{dP}{C}} \tag{2.9}$$

The four reported references have quite different values of target-to-substrate distance, and the effect of pressure may result suppressed: if the distance is high, the exponential is already in the very low derivative tail, and a further increase in the value of the exponential argument by means of increasing pressure has a very low effect. The effect reported may also be attributed to the target age, which seems to have a strong effect on the deposition rate, as reported by Jouybari [26]. Depending on the order of the experiments, this may result in a positive or negative correlation, and it may mask the effect of pressure.

Effect of RF power

The effect of sputtering power is an increase in electron and ion energy, resulting in a higher ionization degree in the plasma. The beneficial effect on the deposition rate is confirmed by different works [24, 26, 28–30]. In this case, not only the tendency but also the absolute effect of RF power density is confirmed by the whole bibliographical corpus.

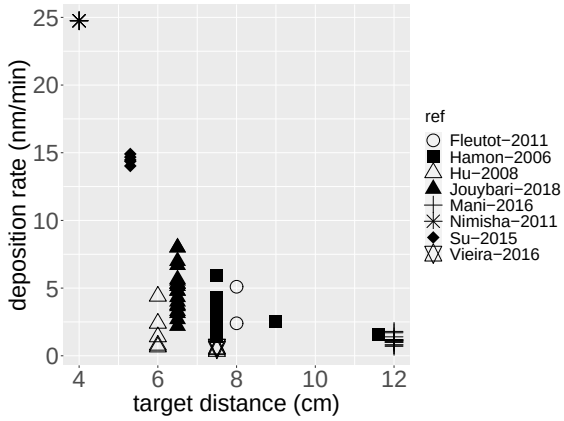

(a) Effect of target distance on the deposition rate. Data from main publications.

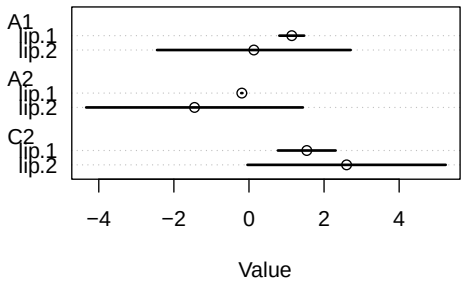

(b) Estimated parameter effect for two different models of LiPON growth rate for RF magneton sputtering deposition.

Figure 2.7

As for LCO the relationship is mainly linear; only Hu [30], which tested really low power levels, shows an initial sublinear relationship for values lower than $100\,\mathrm{W}$. Notwithstanding, assessing the effect of power may be tricky. If the power is normalized over the target surface, the power density in Hu [30] is comparable to or higher than the remaining literature due to its small target size. In order to decide if power density or absolute power is the more apt variable to predict the deposition rate, we will exploit the statistical analysis of the last section in the context of the aggregate effect of deposition parameters.

Effect of substrate temperature

As already pointed out for LCO, the substrate is often at a floating temperature, which depends on the imposed RF power. Few studies measure or impose a constant temperature on the substrate. Mani [33] is the only work with a temperature sweep. A slight decrease in deposition rate is reported, but as for LCO the effect seems negligible, and it will be disregarded in the aggregate analysis.

Effect of target distance

The target-to-sustrate distance is another poorly studied parameter, with only one systematic work from Hamon [29] dealing with it. Luckily, this parameter is available for most of the publications, and the exponential decay reported by Hamon and already included in equation 2.1 is strongly supported by the aggregate data from all publications, as shown in figure 2.7a

Aggregate effect of process parameters

In order to estimate the aggregate effect of the main deposition parameters (power Pw, distance d, pressure P), the following model is used:

$$p_d = A_1(Pw + A_2 Pw^2)e^{-C_2 dP} \tag{2.10}$$

Two models are tested, one with power expressed in $\mathrm{W\,cm^{-2}}$ (lip.1) and another with power density expressed in W (lip.2) as predictor. In Figure 2.7b the estimated value and standard

deviation for each parameter effect is reported. The power density is indeed a much better predictor, as shown by the more precise estimation of the first model. With the same amount of data (44 data point from the literature), the estimation for LiPON is superior to that for LCO. This is mainly due to the constant plasma atmosphere, which reduces process variability and enables a more precise result. The exact values for the model lip.1 are reported in table 2.3. Both models have a Gaussian prior with $\mu = 0$ and $\sigma = 2$ on all parameters.

Param.	**Mean**	**Std**	$5.5\,\%$	$94.5\,\%$
A_1	1.14	0.17	0.88	1.42
A_2	-0.19	0.01	-0.20	-0.18
C_2	1.54	0.39	0.99	2.22

Table 2.3: Effect of process parameters on deposition rate as estimate from model lip.1.

2. Physical Characterization

The cell realized according to the schematic in figure 2.1 has been analyzed with different tools in order to assess the quality and structure of each layer. LCO was realized with thickness from $5\,\mu m$ to $30\,\mu m$ while LiPON between $4\,\mu m$ and $6\,\mu m$. In this section, I will present the results of scanning electron microscopy, Raman and X-ray diffraction in order to analyze the layers' chemistry and morphology. In the last section, operando confocal microscopy measurements are reported. This measurement permits us to follow the lithium plating and stripping during the charge discharge process and study the plating morphology. The aim of these characterizations is mainly to determine the homogeneity of materials and of lithium plating. If homogeneity is ensured, the analysis of the cell can be simplified and the equation order in the simulation section reduced by means of symmetry. In particular, the whole third chapter relies on the hypothesis of homogeneity in terms of material properties before and during the charge-discharge process in order to implement the 1D diffusion equation.
In the following sections, I will briefly introduce each characterization technique and provide a minimum bibliography before presenting the result for the LCO/LiPON cell. While a targeted bibliography will be provided for each technique, a more comprehensive and comparative text on the main techniques for material characterization may sometimes be useful to choose the right tool for each question to be answered. The book of Leng [36] is, of course, far from exhaustive in its treatment of each technique, but it has the great advantage of proposing a comparative view, which is often missing. From X-ray diffraction to thermal analysis, all the main techniques are addressed, and the bibliography at the end of each chapter is a valuable way to delve into the details of a technique of our choice.

2.1 SEM imaging

The first and probably mainstream technique to assess the topology and thickness of thin films is scanning electron microscopy (SEM). This technique can be exploited for an incredibly large portfolio of analyses, ranging from thickness measurement to crystal phase assessment. For any doubt on the topic, I suggest the broad textbook of Goldstein as a first approach resource [37]. It is incredibly complete from the point of view of topics, but at the cost of a quite superficial approach to many subjects. It is more a handbook than a textbook, but the bibliography at the end of each chapter will lead the curious reader in the right direction.

Principle of electron microscopy

Electron microscopy is probably the most widespread characterization technique in the field of micro and nanotechnologies. The main reason is not the ease of use but the apparently intuitive and direct reading of the images. Looking like white and black photos, the majority of users exploit this technique as a fancy imaging system for precise thickness measurement, film morphology, and interface quality visualization. Those are indeed some of the straightforward outputs an electron microscope can provide when used in secondary electron scanning mode, but there is much more.

As a quick recap, electron microscopy consists of bombarding the sample with a focused electron beam with a defined energy in a vacuum environment. Two main phenomena take place between the impinging electron and the sample atoms: elastic scattering of electrons by the atom nuclei and inelastic scattering between beam electrons and inner and outer shell electrons. Two main imaging mechanisms exist: the first is based on the probing of the quantity of electrons scattered back (BSE) by elastic scattering (back-scattered electrons have the same energy as beam electrons); the second is based on measuring the energy of the emitted outer-shell electron during inelastic scattering. Those secondary electrons (SE) have a lower energy than the beam electrons.

Back-scattering is mainly impacted by the atomic weight of the specimen (directly proportional) and the energy of the beam (inversely proportional). It can be used to create a contrast between layers of different atomic compositions. The main limitation is poor sensitivity to light elements. On the other hand, secondary electron emission depends on the binding energy of the outer-shell electron, and is not limited by the atomic weight. While we tend to perceive scanning electron microscopy as a "surface image", as in photography, we should remember that the actual signal is produced by several hundreds of nanometers. As an example, the penetration depth of a 20 keV electron in pure copper is around 1200 nm. This huge penetration concerns mainly inelastic scattering, that is to say, secondary electrons. Elastic scattering can be probed only if no inelastic scattering has already decreased the electron energy (in order to classify an electron as back-scattered, it has to have the same energy as the impinging electron), which results, for BSE, in a much lower probing depth: less than 1 nm at the same conditions. The lighter the specimen and the more energetic the electron beam, the deeper the electrons can reach. Secondary electrons, when enough energy is lost, are absorbed by the target material. Coupled with the emission of secondary electrons, inelastic scattering results in a charge imbalance inside the specimen. If the sample is not conductive enough or is not coated with conductive material, the electrons pile up during observation, resulting in various artifacts (specimen charging). The sample may even be damaged and modified by the impinging beam.

While secondary and back-scattering electrons are standard results found in most recent publications, inelastic scattering produced another signal in the range of X-rays. Due to relaxation of excited states of inner-shell electrons, characteristic X-rays are produced altogether with a continuous spectrum from the beam electrons by bremsstrahlung. Probing X-ray radiation is accomplished by energy dispersive spectroscopy (EDS). Because in the present work electron microscopy was not exploited to its full power, I will not treat EDS nor mingle with the detailed effects of morphology, crystallinity, and other parameters on the SE and BSE signals. As a last remark, I would like to highlight how a great deal of additional information can be obtained only by comparing the output from different signals (SE, BSE, and EDS), which cannot be extracted by single channel analysis. Different dependencies with respect to topology, atomic weight, and beam energy can be exploited to clarify and correct various artifacts. The curious reader can refer to [37] for additional information.

Electron microscopy of cell cross-section

Figure 2.8 shows the cross-section of a thin-film all-solid-state cell, as described in the schematic of Figure 2.1. No passivation layer was deposited, and the topmost layer is the titanium anode current collector. The cell was imaged as out-of-fab, so no metallic lithium is present between the electrolyte and the current collector. From the bottom, we first observe the thermal oxide and the thin platinum cathode current collector, on top of which $10\,\mu m$ of $LiCoO_2$ are deposited. LCO layer is composed of long columnar grains. The columns seem to be continuous single-crystal structures. The lateral size of the column is a few hundred nanometers. At the interface between the platinum and the LCO the grains are smaller and denser. This is the nucleation layer of LCO which then acts as a seed layer for the growth of larger crystals. The seed layer is less than $1\,\mu m$ and the overall layer can be considered homogeneous along its thickness. The density of the cathode is close to $99\,\%$ with few voids visible between the columns.
On top of the cathode, a uniform layer of LiPON is deposited. The interface between the cathode and the electrolyte does not present voids or defects and is expected to result in low interface resistance. In fact, it is this interface that is of paramount importance in all-solid-state cells. As we pointed out in the first chapter, a good contact between electrode and solid electrolyte cannot be realized in the standard roll-to-roll process, and that is the main motivation for switching to sputtering deposition. LiPON layer itself is of very good quality in terms of homogeneity, with no voids or defects visible at this scale. On top of it, the titanium current collector is deposited. This final layer has a two-zone contrast. The brighter layer in contact with the electrolyte may be partially oxidized titanium. The homogeneity hypothesis seems to be valid over the whole active stack.

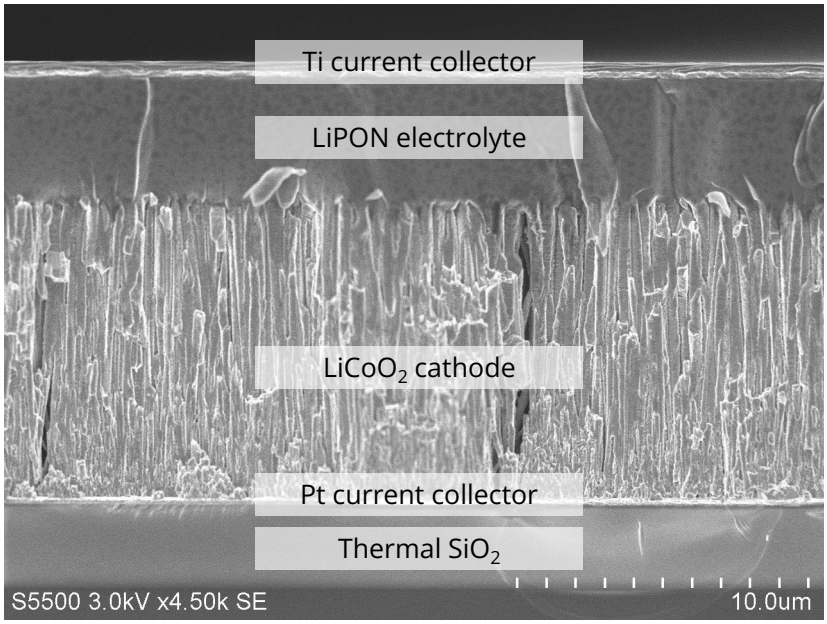

Figure 2.8: SEM crossection of LCO/LiPON cell as out-of-fab.

2.2 X-ray diffraction

SEM can be exploited to probe the topographic homogeneity of the stack, but it is quite hard to obtain detailed information on the crystal orientation of the film. We already pointed out that in 2D diffusion materials, the orientation of the diffusion planes with respect to the substrate

is of paramount importance to obtaining good performance at high current density. The film here analyzed has been annealed to $700\,^{\circ}$C to fully crystallize the LCO. As reported in the review of the first section of the present chapter, the annealing of LCO films thicker than $1\,\mu$m usually results in a favorable orientation. X-ray diffraction is the best tool to analyze the relative orientation of a film. Notwithstanding, with respect to standard powder diffraction, thin-film analysis needs some extra care in the data treatment according to the measurement setup. I will briefly revise the principle of X-ray diffraction, and in particular, X-ray diffraction for thin film, before presenting the results for the stack here considered. As a general bibliography on the subject, I suggest the text of Suryanarayana [38], featuring a practical and clear approach, and the book of Coppens [39] for a more physically focused approach. As a monograph on thin film, the textbook by Birkholz [40] is an excellent starting point, with a rich bibliography at the end of each chapter.

Principle of X-ray diffraction

We already introduced the possibility of probing a material by X-ray in the electron microscopy section. In that case, the X-ray radiation was emitted by the excitation and relaxation of inner-shell electrons during electron inelastic scattering. X-rays emitted in such a way are incoherent, that is to say, the phase of the radiation is an independent random variable of each single emission. X-ray diffraction, as well as Raman scattering, which is treated in the next section, exploits phenomena linked to coherent monochromatic radiation. In order to ensure phase coherence in the output signal, a coherent input excitation is necessary. X-ray diffraction is based on the elastic scattering of a coherent, monochromatic X-ray beam by the inner-shell electron of the sample. The output radiation will not only depend on the characteristics of the single scatter center, but thanks to interference phenomena, the regular arrangement of atoms, that is to say the crystalline lattice, will add a spatial dependency to the output intensity. In fact, in the case of X-ray diffraction, a signal will be registered or not as a function of the position of the detector. From a mathematical point of view, the output signal distribution in space is the Fourier transform of the electron density inside the sample. For a crystalline material, the output signal is discrete because the transformed density is periodic. Of course, a real periodic lattice should be infinite and defect-free. Luckily, the periodicity has to be evaluated on the scale of X-rays ($10\,$nm to $10\,$pm), hence, hundreds of nanometer-sized crystals are already closed enough to ”infinity” for the approximation to be valid.

This technique is extremely sensitive to any variation in the disposition of atoms in the crystal lattice, which is both a strength and a weakness. While it is quite straightforward to qualitatively assess the disposition of atoms (geometry and symmetry), it is a much harder task to interpret the result from a quantitative point of view. This is particularly true in the case of thin films. The only way to obtain good results in terms of crystal lattice parameters is to have a high-quality reference with known crystal parameters. While lattice and phase determination are of the utmost importance in general, thin-film analysis is usually more concerned with the spatial orientation of the crystal than with its exact lattice parameters. As a matter of fact, a slight variation in the lattice of LCO is not expected to strongly impact the rating performance of the cell, while the wrong orientation of the diffusion channel may result in a terrific decrease in the diffusion coefficient. For this reason, the most investigated parameter is the fraction of each crystal orientation. Apart from single-oriented crystals, for which the analysis is quite direct, in the presence of multiple orientations, the analysis is far from easy. The standard procedure to estimate the fraction of each orientation, is to compare the diffraction intensities between different orientations. Notwithstanding, a relative reference is necessary because the intensity ratios

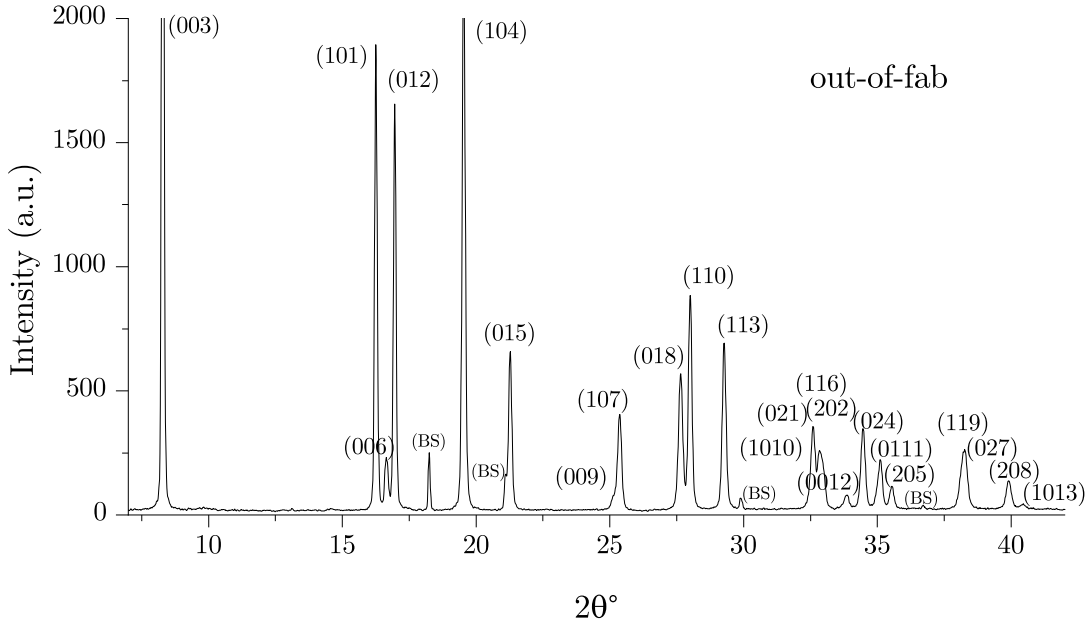

Figure 2.9: Xray diffraction spectra of LCO before charging.

are not a function of presence alone. Usually, powder diffractograms are used as a reference for random-oriented crystals. That is to say, if a specimen has the same intensity ratios between different orientations as the powder reference, the specimen is randomly oriented. A deviation from powder reference can be attributed to preferential orientation, or texturing, under certain conditions. A very important condition is the size distribution with respect to the crystal orientation. In fact, the diffracted intensity is a function of the crystal volume. If a certain orientation corresponds to a different distribution of crystal size with respect to another orientation, the signal deviates from the powder reference without reflecting a real difference in crystal orientation.

In the case of thin-films the probing setup can differs with respect to standard powder measurement (the so-called $\theta/2\theta$). The configuration often used is grazing incidence, or GIXRD. This technique exploits a very small incidence angle (on the order of a few degrees) to maximize the thickness of material crossed by the X-ray beam. In the standard $\theta/2\theta$ configuration the incidence angle is changed for each point (it is in fact equal to θ), hence the thickness crossed by the X-ray is a function of the measured angle. As a result, the attenuation in the $\theta/2\theta$ configuration is a function of the measured angle, while in the GIXRD the attenuation is almost constant at any measured angle. As a result, GIXRD tends to show higher intensity with respect to the $\theta/2\theta$ configuration at lower measured angles. Once again, this is a negligible correction if the film is strongly textured, but can lead to biased results if multiple orientations are present. As a matter of fact, software programs like VESTA when generating diffraction patterns, usually report the theoretical intensity for an infinitely thick sample, with constant attenuation at any diffraction angle. As a result, the simulate ratios between peaks are in general closer to the one measured in GIXRD, where the attenuation is more or less constant, than to the $\theta/2\theta$ configuration.

In the following section, the results for synchrotron X-ray diffraction are reported. Thanks to the tiny beam width of the synchrotron X-ray source, it is possible to perform a 2D mapping of the cross-section of the cell in order not only to probe the overall crystal orientation but also to cor-

relate the distribution with the cathode z position. As for the SEM analysis, our main objective is to demonstrate the spatial homogeneity of the film texture to validate the hypothesis exploited in the modeling section.

Xray mapping of LCO cathode cross-section

In figure 2.9 the X-ray spectrum of the cathode section of a thin-film solid-state cell is shown. All peaks have been indexed and finely match the theoretical position for hexagonal $LiCoO_2$. Additional peaks, indexed as *BS*, are generated by the lead beam stopper. The raw data, before the crystalline orientation fraction analysis, has been corrected to account for attenuation artifacts and restricted (synchrotron detectors are much larger and more complex) to be comparable with the GIXRD reference. In fact, the setup of the synchrotron setup is equivalent to a GIXRD one with a zero incidence angle. A detailed description of the X-ray data analysis procedure is reported in the fourth chapter of the present work. Once the pre-treatment procedure is completed, the data can be analyzed in terms of the intensity ratio between the various peaks. In Table 2.4 the theoretical and measured intensity ratio for the first 7 main peaks (intensity higher than $10\,\%$ of the main peak) is reported.

Peak index	**Peak position (2θ)**	**Theoretical intensity**	**Measured intensity**
(003)	$8.53°$	100	100
(104)	$19.94°$	65.97	2.77
(101)	$16.56°$	44.51	3.3
(015)	$21.72°$	15.93	< 1
(012)	$17.29°$	14.80	23.42
(018)	$28.23°$	12.40	< 1
(110)	$28.45°$	11.86	< 1

Table 2.4: relative intensity of the first 7 peaks with respect to the (003) peak intensity. Theoretical peaks are calculated by VESTA. Measured peaks are from the film substrate.

Thanks to the high resolution of the synchrotron beam, the X-ray profile can be acquired at different positions along the cross-section. A difference is observed between the LCO close to the electrolyte and the bulk LCO. In Table 2.5 the theoretical and measured X-ray intensities at three different positions (top, center, and bottom) are reported. The diffraction plane (003) correspond to diffusion channel oriented parallel to the LiPON and a very poor lithium diffusion. (101) and (012) planes are instead quite favourable, with diffusion channels perpendicularly aligned. From the experimental data it is possible to conclude that the film is strongly (012) oriented in the bottom and middle parts, while the top part presents residues of the (003) orientation. As previously reported, the film is expected to have a (003) texture before high-temperature annealing. The thermal expansion mismatch between the substrate and the LCO led to a new crystal arrangement and the formation of a more favourable environment for lithium diffusion. The crystal orientation change is promoted by the stress at the collector-cathode interface. It is then possible that the constraint is reduced further from the substrate, leading to a partial reorganization on the top surface of the cathode.

X-ray analysis is a particularly powerful technique when operando measurement is required. The penetration of X-rays into the passivation layer permits the operation of the encapsulated battery in air conditioning and, at the same time, the acquisition of the diffraction pattern of cell materials. We already discussed the phase transition of LCO during the charge process. The transition between the two hexagonal phases is characterized by a change in the *c* vector. The

Peak index	Theoretical I	Measured I top	Measured I middle	Measured I bottom
(003)	100	100	100	17.38
(104)	65.97	2.77	6.59	13.75
(101)	44.51	3.3	5.91	6.74
(015)	15.93	< 1	2.67	4.92
(012)	14.80	23.42	46.99	100
(018)	12.40	< 1	< 1	< 1
(110)	11.86	< 1	< 1	< 1

Table 2.5: relative intensity of the first 7 peaks with respect to the (003) peak intensity at different vertical position in the cathode thin-film. Theoretical peaks are calculated by VESTA.

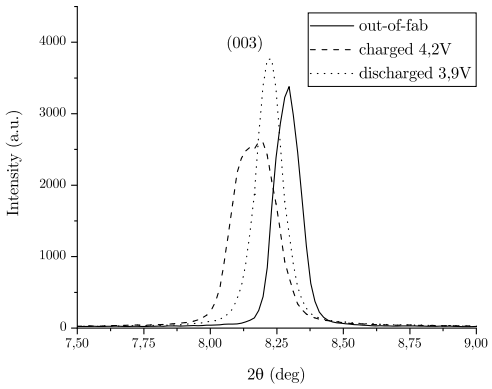

Figure 2.10: Evolution of the (003) diffraction peak during cycling.

lattice vector change during phase transition is large, making it particularly easy to observe in any X-ray configuration. With the high resolution obtained by synchrotron radiation, it is also possible to probe with high precision the *c*-axis expansion for the whole charge process and to map it in space. The *c*-axis expansion results in a lowering in the diffraction angle of a few fractions of a degree. In Figure 2.10 the evolution between out-of-fab, charged, and discharged states is proposed. The total variation is less than half a degree. The discharge state differs from the initial state because the phase transition cannot be reversed at the current rating used for this particular measurement. An in-depth analysis of the X-ray profile as a function of position is delayed to the fourth chapter, after the introduction of the modeling tools necessary to interpret such data.

2.3 Raman spectroscopy

Raman spectroscopy is also based on photon scattering from a coherent, monochromatic source. Compared to X-rays, one big difference is the energy of the incident beam. Instead of exciting the core orbital, Raman scattering uses far less energy in order to excite the vibrational motion of atoms along the chemical bonds. The technique is mainly used to probe the chemical environment, hence the bonds between atoms. Different crystal structures usually result in different bonding atoms or different bond lengths, and can be distinguished by means of Raman spectra. Thanks to its simple set-up and probing conditions, Raman has gained lots of popularity as a standard characterization technique in the field of batteries, and in particular for LCO

cathode [41–44]. It is in fact possible to determine not only the crystal phase of LCO, but also the intercalation state. In fact, the change in crystal lattice parameter, which is clearly visible in X-ray diffraction, results in a shift of the Raman peaks too. After a short review of the principles of Raman spectroscopy, the results for a 2D mapping of LCO are proposed. For details on this technique, I suggest the excellent introductory text of Ferraro [45], which is particularly rich in terms of visual examples but at the same time rigorous in its theoretical treatment. An ample bibliography at the end of each chapter helps the reader dig into any additional aspect of the subject.

Principle of Raman spectroscopy

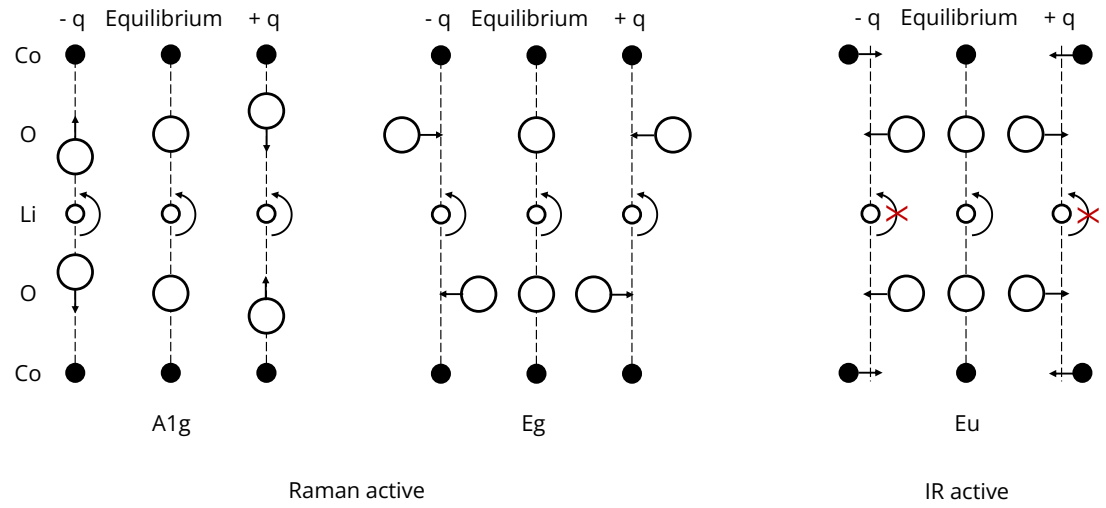

Figure 2.11: The Raman active and and example of infra-red active oscillation modes of $LiCoO_2$. Lithium acts as center of symmetry.

The vibration of chemical bonds is a relatively low-energy phenomenon compared to X-ray diffraction. The typical photon wavelength for bond stretching and oscillation is on the order of a fraction of a millimeter down to the micrometer. It is indeed lower than visible light in the infrared band. In fact, Raman spectroscopy is often associated with another technique called infrared (IR) spectroscopy. The two are somehow complementary descriptions of the same phenomenon. IR spectroscopy studies the radiation absorption by molecular vibration as a function of frequency. When the excitation frequency matches the resonance frequency of a certain bond, a peak in the spectrum is registered. In order for a bond to exhibit a variation in radiation absorption as a function of the excitation frequency, the dipole moment associated with the bond should vary during vibration. On the other hand, Raman spectroscopy uses a constant-frequency source, and all bonds are excited at the same time. The first-order variation of the polarizability during oscillation results in the re-emission of radiation at a different frequency with respect to the input one. While IR spectra are registered at the excitation frequency for different excitation wavelengths, Raman spectra are found by keeping the excitation frequency constant and measuring the response at a wavelength different from the excitation one. Notably, for vibrations possessing a center of symmetry, the IR and Raman activities are mutually exclusive. This is usually the case in crystalline materials, where the lattice symmetry results in a vibrational symmetry. In particular, if during the vibration the symmetry is preserved, the

vibration mode is Raman active, while if the symmetry is broken, it will be IR active. As an example, the two Raman modes and an IR mode of LCO are reported in figure 2.11. While the rotation symmetry is preserved at any instant of the vibration in the Raman active mode, in the IR mode the central symmetry of the equilibrium state is lost. Recalling that in order to vary the absorption as a function of the frequency, the dipole moment has to vary during oscillation. It is straightforward to understand why centrosymmetry vibration does not show such properties: the total dipole moment is equal to zero. As long as the center of symmetry is preserved, the dipole moment is guaranteed to stay constant at zero, no matter the atomic configuration.

2D micro-Raman mapping of LCO cathode cross-section

In Figure 2.12a the Raman spectra for two different zones of the LCO cathode are reported. The E_g and A_{1g} peaks are well resolved and close to the theoretical values of $485\,\mathrm{cm}^{-1}$ and $595\,\mathrm{cm}^{-1}$ respectively. Raman spectrum is known to drift to lower wavelengths as soon as the lithium is extracted. The phase transition between the two hexagonal phases (lithium rich and lithium poor), described in the LCO review, can also be appreciated in the Raman signature as a splitting of the two peaks.
In Figure 2.12b and 2.12c the peak position is mapped with respect to the position of a LCO cross-section. Green spots correspond to a slightly delithiated zone. This small heterogeneity of the film has been related to surface topology. In fact, the exciting laser has a certain penetration depth, and the collected signal is an average of several micrometers. We can assume that the very surface of the sample, which is probed at ambient atmosphere, is probably oxidized. In the case of a hole in the film, created during the sample preparation, the signal will be more impacted by the surface stoichiometry, resulting in a slight shifting of the Raman peaks. It is in fact the extreme sensitivity of this technique that permits the visualization of such a small deviation, but overall, the film can be considered homogeneous from the point of view of the local chemical environment.

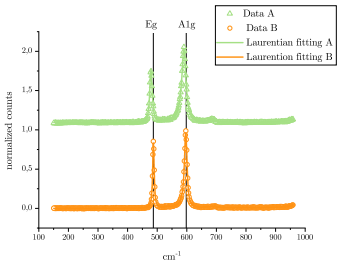

(a) Raman spectrum of LCO. Out-of-fab sample.

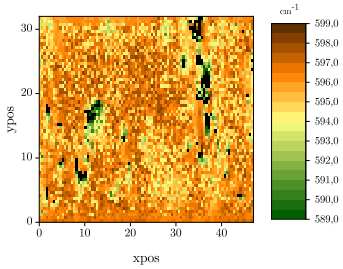

(b) 2D mapping of E_g Raman peak for LCO cross-section. Out-of-fab sample.

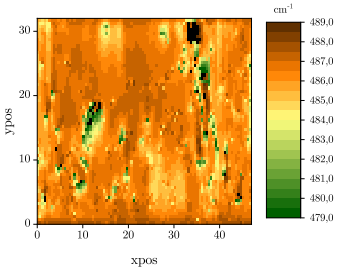

(c) 2D mapping of A_{1g} Raman peak for LCO cross-section. Out-of-fab sample.

Figure 2.12

2.4 Confocal microscopy

Last but not least, I will dedicate this last section to optical (or light) microscopy and in particular to confocal optical microscopy. Optical microscopy is often perceived as an old technique that has less to offer the microtechnology domain with respect to electron microscopy. Even if it is true that the resolution of optical microscopy is limited by light diffraction to around $200\,\mathrm{nm}$,

the large amount of configurations available permits to acquire the same image from different *perspective* and to gain a deep understanding of the sample with a much simpler set-up with respect to other techniques. A particularly interesting upgrade of light microscopy is *confocal* microscopy. This technique permits the acquisition of 3D images at the maximum resolution permitted by light diffraction in a standard reflection mode. In the case of anode-free microbatteries, confocal microscopy can be exploited to image the lithium plating at the anode side and assess the spatial uniformity of the process. This is of particular interest in the framework of dimensional reduction for cell modeling. As long as the battery is homogeneous and behaves isotropically, the physical modeling can be simplified from 3D to 1D, with a large gain in terms of computation time. After assessing the intrinsic homogeneity of the LCO, the dynamic homogeneity of the anode is the last tile to complete the picture. Before presenting the results, a fast recap of the working principles and the artifacts to be aware of for confocal microscopy is presented in the next section. For a general treatment of the optical microscopy techniques family, I would suggest Leng [36] and the relative bibliography.

Principle of Confocal microscopy

With respect to standard light microscopy, confocal microscopy is realized by means of two main modifications to the measurement set-up. First, the light source is a laser with a wavelength in the visible range (460 to 630nm). The need for a laser light source is not the coherence itself, but the very small focus size. While the lateral resolution of the image is limited by light diffraction to around 200 nm depending on the laser wavelength, the vertical resolution depends on the focus depth and, with a good laser source, can be reduced to a few nanometers [46]. The second fundamental element needed to realize 3D imaging is a pinhole aperture just in front of the detector. In Figure 2.13a a typical confocal microscopy configuration is reported. The aim of the pinhole is to filter all incoming rays except those from the focal plane of the objective lens. This way, the signal entering the detector is only the one reflected from the focal plane, and changing the z position of the sample makes it possible to image different planes. The pinhole and the optics also limit the vertical resolution when they permit the out-of-focus ray to impinge on the detector. 2D mapping can be obtained by either dislocating the sample or the laser by means of a mirror, like in SEM.
In Figure 2.13b an example image for a 5 µm thick LCO cell. The confocal image can simultaneously image a large aspect ratio feature, like the flank of the cell, and a nanometer-size feature on the surface of the cell. In particular, it is possible to appreciate the general shape of the cell (in red) and process defects on the top of the cell surface (in green). The gray triangle is the probing tip used to polarize the anode of the cell.
Steps and high aspect ratio features can, in some cases, lead to artifacts due to unwanted reflection [47]. While the maximum resolution is usually specified by the instrument producer, it is possible, by means of careful calibration, to push the instrument beyond its limit by data post-processing [48]. In the case of the microbattery we expect the system to fail in collecting the data at the step edge between the battery and the substrate, but since our main interest is the areal distribution of lithium during charge on the anode surface, no error should be induced by artifacts in the peripheral region.

Operando confocal mapping of lithium plating expansion

An anode-free configuration is characterized by lithium plating at the interface between the electrolyte and the anode current collector. Measuring the total volume variation permits access to

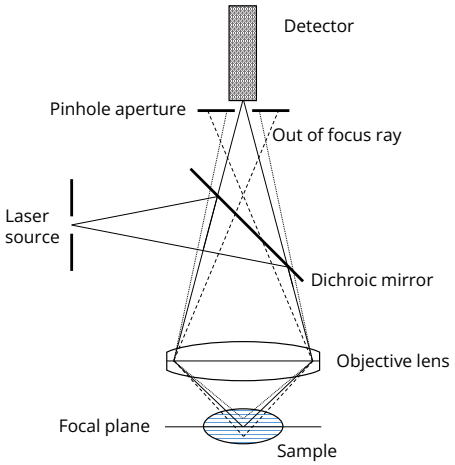

(a) Schematic representation of the confocal microscopy setup.

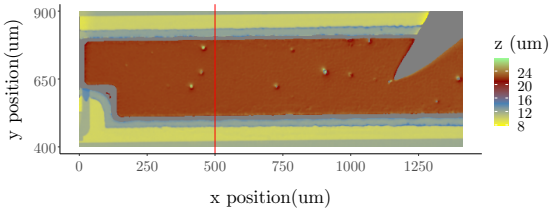

(b) Confocal image of a microbattery. The red line is the section plane for 1D imaging.

Figure 2.13

the volume of plated lithium. At the same time, the monitoring of the charge and discharge currents by a potentiostat permits a precise determination of the moles of lithium displaced in time. Comparing the two quantities makes it possible to determine the density of plated lithium and the presence of voids or a mossy deposition of lithium. Any deviation from the theoretical density can, in fact, be attributed to suboptimal plating. The second feature to be monitored is the spatial distribution of plated lithium on the anode surface and its evolution in time.

In order to both evaluate the volume expansion and the lithium distribution, the first frame is used as a reference for the height of the cell. Any variation is then interpreted as lithium growth. In Figure 2.14a the evolution of the profile along the cut line of Figure 2.13b is reported for the first step, a fully charged and discharged cell. The initial profile, in red, is quite flat. On the cell border, the artifact related to the edge aspect ratio is visible as a bump in the measured thickness. In the fully charged profile in blue, the thickness increase is clearly appreciable in conjunction with the topology of the deposited lithium. To be aware of the difference in the scale of the two axes. The x-axis is almost 500 times larger than the y-axis, hence the deposition heterogeneity is largely magnified. The lithium peaks are much closer to smooth hills than sharp peaks, and apart from a slight accumulation on the right edge, the profile is quite homogeneous. Even more important is the profile after discharge. The lithium is in fact recovered homogeneously on the whole surface, and no dead lithium spots are visible. Once again, the right edge presents a slight bump, but most of it has been absorbed during the discharge.

The average vertical displacement is calculated for the whole cell at different time steps and compared to the electrical data for the displaced charge. In Figure 2.14b the two profiles are superimposed on different scales in order to highlight the identical behavior of the two quantities. The good agreement between the two quantities implies that the density of plated lithium is constant at any instant of the cycling process. As further verification, the displace charge quantity can be calculated from the theoretical lithium density ($0.53\,\mathrm{g\,cm^{-3}}$) and compared to the measured ones. In Table 2.6 the obtained values at three different time steps are reported. The result is a perfect match between the measured and calculated capacity, showing an op-

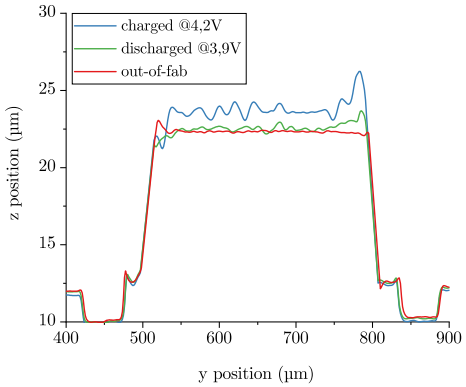

(a) Section of confocal image at different state of charge along the section plane.

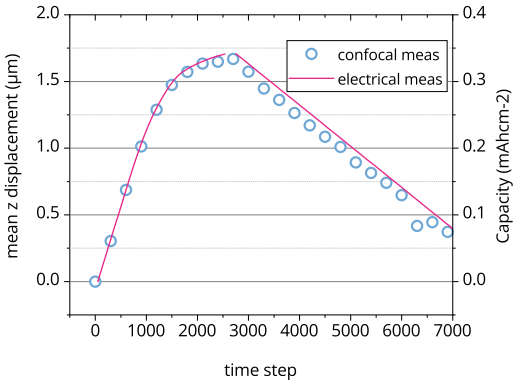

(b) mean z position and estimated capacity. In red the capacity from electrochemical measurement.

Figure 2.14

timal lithium plating close to lithium's theoretical density. The same analysis were performed for different thickness of LCO cathode, and consistency with the $5\,\mu m$ results were found up to $30\,\mu m$.

time step	**mean dz** (µm)	**Estimated Q** (mA h cm^{-2})	**Measured Q** (mA h cm^{-2})
5	1.29	0.26	0.27
10	1.67	0.34	0.34
25	0.27	0.06	0.09

Table 2.6: mean thickness

Bibliography

Materials and deposition

[1] S. Oukassi et al. “Millimeter scale thin film batteries for integrated high energy density storage”. en. In: *2019 IEEE International Electron Devices Meeting (IEDM)*. San Francisco, CA, USA: IEEE, Dec. 2019, pp. 26.1.1–26.1.4. ISBN: 978-1-72814-032-2. DOI: 10.1109/IEDM19573.2019.8993483.

[2] Brian Chapman. *Glow Discharge Processes: Sputtering and Plasma Etching*. Wiley, 1980. ISBN: 978-0-471-07828-9.

[3] A.A. Onoprienko, V.V. Artamonov, and I.B. Yanchuk. “Effect of magnetron discharge power on the resistivity and microstructure of carbon films”. en. In: *Surface and Coatings Technology* 200.14-15 (Apr. 2006), pp. 4174–4178. DOI: 10.1016/j.surfcoat.2004.12.003.

[4] Jung Pil Noh et al. “The Effects of Substrate and Annealing on Structural and Electrochemical Properties in $LiCoO_2$ Thin Films Prepared by DC Magnetron Sputtering”. en. In: *j nanosci nanotechnol* 12.7 (July 2012), pp. 5937–5941. DOI: 10.1166/jnn.2012.6399.

[5] Yongsub Yoon et al. “Lattice orientation control of lithium cobalt oxide cathode film for all-solid-state thin film batteries”. en. In: *Journal of Power Sources* 226 (Mar. 2013), pp. 186–190. DOI: 10.1016/j.jpowsour.2012.10.094.

[6] J. Xie et al. “Li-ion transport in all-solid-state lithium batteries with LiCoO2 using NASICON-type glass ceramic electrolytes”. en. In: *Journal of Power Sources* 189.1 (Apr. 2009), pp. 365–370. DOI: 10.1016/j.jpowsour.2008.08.015.

[7] Jason Trask et al. “Optimization of 10-µm, sputtered, LiCoO 2 cathodes to enable higher energy density solid state batteries”. en. In: *Journal of Power Sources* 350 (May 2017), pp. 56–64. DOI: 10.1016/j.jpowsour.2017.03.017.

[8] P. J. Bouwman et al. “Structural Analysis of Submicrometer LiCoO2 Films”. en. In: *J. Electrochem. Soc.* 148.4 (Apr. 2001), A311. DOI: 10.1149/1.1353570.

[9] Julien, Mauger, and Hussain. “Sputtered LiCoO2 Cathode Materials for All-solid-state Thin-film Lithium Microbatteries”. en. In: *Materials* 12.17 (Aug. 2019), p. 2687. DOI: 10.3390/ma12172687.

[10] J B Bates et al. “Preferred Orientation of Polycrystalline Li Co O2 Films”. en. In: *Journal of The Electrochemical Society* (2000).

[11] Laura Bohne, Tjalf Pirk, and Wolfram Jaegermann. “Investigations on the influence of the substrate on the crystal structure of sputtered LiCoO2”. en. In: *J Solid State Electrochem* 17.8 (Aug. 2013), pp. 2095–2099. DOI: 10.1007/s10008-011-1377-9.

[12] Cheng-Lung Liao, Yueh-Hsun Lee, and Kuan-Zong Fung. "The film growth and electrochemical properties of rf-sputtered LiCoO2 thin films". en. In: *Journal of Alloys and Compounds* 436.1-2 (June 2007), pp. 303–308. DOI: 10.1016/j.jallcom.2006.07.033.

[13] Xianjun Zhu et al. "LiCoO2 cathode thin film fabricated by RF sputtering for lithium ion microbatteries". en. In: *Surface and Coatings Technology* 204.11 (Feb. 2010), pp. 1710–1714. DOI: 10.1016/j.surfcoat.2009.10.057.

[14] J.F. Whitacre, W.C. West, and B.V. Ratnakumar. "The influence of target history and deposition geometry on RF magnetron sputtered LiCoO2 thin films". en. In: *Journal of Power Sources* 103.1 (Dec. 2001), pp. 134–139. DOI: 10.1016/S0378-7753(01)00849-7.

[15] C.S. Nimisha et al. "Studies on the target conditioning for deposition of LiCoO2 films". en. In: *Vacuum* 83.6 (Feb. 2009), pp. 1001–1006. DOI: 10.1016/j.vacuum.2008.12.002.

[16] Chenglin Wang et al. "LiCoO2 thin film cathode sputtered onto 500 °C substrate". en. In: *Electrochimica Acta* 354 (Sept. 2020), p. 136668. DOI: 10.1016/j.electacta.2020.136668.

[17] Sophie Tintignac et al. "High performance sputtered LiCoO2 thin films obtained at a moderate annealing treatment combined to a bias effect". en. In: *Electrochimica Acta* 60 (Jan. 2012), pp. 121–129. DOI: 10.1016/j.electacta.2011.11.033.

[18] C. Ziebert et al. "Constitution, microstructure, and battery performance of magnetron sputtered Li–Co–O thin film cathodes for lithium-ion batteries as a function of the working gas pressure". en. In: *Surface and Coatings Technology* 205.5 (Nov. 2010), pp. 1589–1594. DOI: 10.1016/j.surfcoat.2010.07.110.

[19] Der-Jun Jan et al. "Evaluation of lithium cobalt oxide films deposited by radio frequency magnetron sputtering as thin-film battery cathodes". en. In: *Jpn. J. Appl. Phys.* 58.8 (Aug. 2019), p. 085501. DOI: 10.7567/1347-4065/ab2c45.

[20] Shin-Wook Jeon et al. "As-deposited LiCoO2 thin film cathodes prepared by rf magnetron sputtering". en. In: *Electrochimica Acta* 51.2 (Oct. 2005), pp. 268–273. DOI: 10.1016/j.electacta.2005.04.035.

[21] B. Wang et al. "Characterization of Thin-Film Rechargeable Lithium Batteries with Lithium Cobalt Oxide Cathodes". en. In: *J. Electrochem. Soc.* 143.10 (Oct. 1996), pp. 3203–3213. DOI: 10.1149/1.1837188.

[22] Fabian Michel et al. "Structural and Electrochemical Characterization of Radio Frequency Magnetron-Sputtered $LiCoO_2$ Thin Films". en. In: *Phys. Status Solidi A* 217.20 (Oct. 2020), p. 2000382. DOI: 10.1002/pssa.202000382.

[23] Y. S. Yoon et al. "Influence of Two-Step Heat Treatment on Sputtered Lithium Cobalt Oxide Thin Films". en. In: *J. Electrochem. Soc.* 158.12 (2011), A1313. DOI: 10.1149/2.036112jes.

[24] C.S. Nimisha et al. "Sputter deposited LiPON thin films from powder target as electrolyte for thin film battery applications". en. In: *Thin Solid Films* 519.10 (Mar. 2011), pp. 3401–3406. DOI: 10.1016/j.tsf.2011.01.087.

[25] Richard McElreath. *Statistical rethinking: a Bayesian course with examples in R and Stan*. en. Second edition. Chapman & Hall/CRC texts in statistical science series. Boca Raton, FL: CRC Press, 2020. ISBN: 978-0-367-13991-9.

[26] Yaser Hamedi Jouybari et al. "The influence of sputter conditions on the properties of LiPON and its interfaces". en. In: *Journal of Power Sources* 394 (Aug. 2018), pp. 160–169. DOI: 10.1016/j.jpowsour.2018.05.023.

[27] Naoaki Kuwata et al. “Thin Film Batteries with Li3PO4 Solid Electrolyte Fabricated by Pulsed Laser Deposition”. en. In: *ECS Trans.* 16.26 (Mar. 2009), pp. 53–60. DOI: 10.1149/1.3111821.

[28] C. H. Choi et al. “Radio-Frequency Magnetron Sputtering Power Effect on the Ionic Conductivities of Lipon Films”. en. In: *Electrochem. Solid-State Lett.* 5.1 (2002), A14. DOI: 10.1149/1.1420926.

[29] Y. Hamon et al. “Influence of sputtering conditions on ionic conductivity of LiPON thin films”. en. In: *Solid State Ionics* 177.3-4 (Jan. 2006), pp. 257–261. DOI: 10.1016/j.ssi.2005.10.021.

[30] Zongqian Hu, Dezhan Li, and Kai Xie. “Influence of radio frequency power on structure and ionic conductivity of LiPON thin films”. en. In: *Bull Mater Sci* 31.4 (Aug. 2008), pp. 681–686. DOI: 10.1007/s12034-008-0108-z.

[31] Zongqian Hu et al. “Influence of sputtering pressure on the structure and ionic conductivity of thin film amorphous electrolyte”. en. In: *J Mater Sci* 46.23 (Dec. 2011), pp. 7588–7593. DOI: 10.1007/s10853-011-5734-y.

[32] B. Fleutot et al. “Investigation of the local structure of LiPON thin films to better understand the role of nitrogen on their performance”. en. In: *Solid State Ionics* 186.1 (Mar. 2011), pp. 29–36. DOI: 10.1016/j.ssi.2011.01.006.

[33] Prabhu Doss Mani et al. “Ionic conductivity of bias sputtered lithium phosphorus oxynitride thin films”. en. In: *Solid State Ionics* 287 (Apr. 2016), pp. 48–59. DOI: 10.1016/j.ssi.2016.01.046.

[34] Naoki Suzuki et al. “A lithium phosphorous oxynitride (LiPON) film sputtered from unsintered Li3PO4 powder target”. en. In: *Solid State Ionics* 191.1 (June 2011), pp. 49–54. DOI: 10.1016/j.ssi.2011.04.001.

[35] E M F Vieira et al. “Electrical insulation properties of RF-sputtered LiPON layers towards electrochemical stability of lithium batteries”. en. In: *J. Phys. D: Appl. Phys.* 49.48 (Dec. 2016), p. 485301. DOI: 10.1088/0022-3727/49/48/485301.

Physical characterization

[36] Yang Leng. *Materials Characterization*. en. John Wiley & Sons, Ltd, 2013. ISBN: 978-3-527-67077-2.

[37] Joseph I. Goldstein et al. *Scanning Electron Microscopy and X-Ray Microanalysis*. en. New York, NY: Springer New York, 2018. ISBN: 978-1-4939-6674-5 978-1-4939-6676-9. DOI: 10.1007/978-1-4939-6676-9.

[38] C. Suryanarayana and M. Grant Norton. *X-Ray Diffraction*. en. Boston, MA: Springer US, 1998. ISBN: 978-1-4899-0150-7 978-1-4899-0148-4. DOI: 10.1007/978-1-4899-0148-4.

[39] Philip Coppens and Philip Coppens. *X-Ray Charge Densities and Chemical Bonding*. International Union of Crystallography Texts on Crystallography. Oxford, New York: Oxford University Press, June 1997. ISBN: 978-0-19-509823-5.

[40] Mario Birkholz. *Thin Film Analysis by X-Ray Scattering*. en. John Wiley & Sons, Ltd, 2005. ISBN: 978-3-527-60759-4.

[41] Minoru Inaba et al. “Raman study of layered rock-salt LiCoO2 and its electrochemical lithium deintercalation”. en. In: *Journal of Raman Spectroscopy* 28.8 (1997), pp. 613–617. DOI: 10.1002/(SICI)1097-4555(199708)28:8<613::AID-JRS138>3.0.CO;2-T.

[42] Rita Baddour-Hadjean and Jean-Pierre Pereira-Ramos. “Raman Microspectrometry Applied to the Study of Electrode Materials for Lithium Batteries”. en. In: *Chem. Rev.* 110.3 (Mar. 2010), pp. 1278–1319. DOI: 10.1021/cr800344k.

[43] H L Liu et al. “Electronic structure and lattice dynamics of Li $_x$ CoO $_2$ single crystals”. en. In: *New J. Phys.* 17.10 (Sept. 2015), p. 103004. DOI: 10.1088/1367-2630/17/10/103004.

[44] Yasutaka Matsuda et al. “In situ Raman spectroscopy of Li CoO2 cathode in Li/Li3PO4/LiCoO2 all-solid-state thin-film lithium battery”. en. In: *Solid State Ionics* 335 (July 2019), pp. 7–14. DOI: 10.1016/j.ssi.2019.02.010.

[45] John R. Ferraro, Kazuo Nakamoto, and Chris W. Brown. *Introductory Raman spectroscopy*. en. 2nd ed. Amsterdam ; Boston: Academic Press, 2003. ISBN: 978-0-12-254105-6.

[46] Chang-Soo Kim and Hongki Yoo. “Three-dimensional confocal reflectance microscopy for surface metrology”. en. In: *Meas. Sci. Technol.* 32.10 (Oct. 2021), p. 102002. DOI: 10.1088/1361-6501/ac04df.

[47] Mike Conroy and Joe Armstrong. “A comparison of surface metrology techniques”. en. In: *J. Phys.: Conf. Ser.* 13.1 (Jan. 2005), p. 458. DOI: 10.1088/1742-6596/13/1/106.

[48] Tobias Pahl et al. “Rigorous 3D modeling of confocal microscopy on 2D surface topographies”. en. In: *Meas. Sci. Technol.* 32.9 (Sept. 2021), p. 094010. DOI: 10.1088/1361-6501/abfd69.

"[..] esprimere gli inesprimibili concetti, farci sentir le cose insensibili e veder le invisibili [...]"

from *Il cannocchiale aristotelico, Trattato sulla metafora*, **Emanuele Tesauro**

"[..] to express the inexpressible concepts, to make us perceive the imperceptible matters, and to make the invisible, visible [...]"

trad. from *The Aristotelian Telescope, Treatise on metaphor*, **Emanuele Tesauro**

CHAPTER III

Solid-state Thin-film Batteries Modelling

ABSTRACT

This chapter addresses the modeling of thin-film solid-state batteries, first from a theoretical point of view with a description of equations and underlying physics, and then from an experimental point of view by defining, fitting and simulating a model for thin-film cells. The main reason behind the development of such a model is the possibility to investigate and access the internal behavior of the cell and its variation with respect to the physical properties of materials. Eventually, once the model is validated against experimental measurement, it is possible, based on modeling results, to develop and optimize new solutions and architectures. The comparison between the electrical/physical measurements and the model is delayed to the last chapter.

In the first section, drift-diffusion modeling is proposed, and the main equations are presented, together with a brief literature review.

The second section is devoted to the formulation of the Butler-Volmer equation for solid-state interface and the comparison with the classical redox equation.

The third section reports the experimental results concerning the extraction of $LiCoO_2$ *chemical diffusion coefficient and physical parameters of* LiPON*.*

The last section of this chapter introduces the model results concerning lithium distribution in various layers. Moreover, the predicted dynamic performance of the stack for various simulation conditions is analyzed.

Contents

1. Drift-diffusion model

We are eventually ready to plunge into the core of this work. In the present and next chapter, I will present the complete modeling framework for an all-solid-state thin-film cell, analyze the numerical solution, and compare the results with the experimental evidence collected by electrical and operando physical characterization.
The quantity to be studied is the concentration of lithium ions inside the electrodes and the electrolyte and its evolution during the charge-discharge process. To accomplish such results, the final model, presented in Section 3, is composed of three main ingredients. First, the description of atomic diffusion in the electrodes; second, the description of ion drift in the solid electrolyte; and third, the description of the redox reaction at the electrode/electrolyte interfaces. The main idea behind the following sections is to derive the physical equation from bare thermodynamic reasoning in order to understand the hypothesis behind the most common formulations found in the literature. In many cases, the standard equations are obtained from too strict or different hypotheses with respect to the all-solid-state framework of the present work. By deriving the equations from scratch, it will be easier to adapt the formulation to the particular case under examination.
Ion diffusion has already been introduced in the first chapter from a microscopical point of view, together with the concept of diffusion coefficient. I will start the present section with a more detailed analysis of the diffusion equation and its standard solutions. Following, equations for a metallic cathode and a perfectly insulating electrolyte are proposed. As a closure to the section, the most popular models reported in the literature for all-solid-state batteries are reviewed.

1.1 General formulation of diffusion equation and analytical solution

The microscopy picture of ion diffusion in solid has already been analysed in the first chapter. The dependency of charge carrier and of jump probability with respect to temperature has been stated and linked to the Boltzmann distribution. It is now the case to zoom a bit out and consider the problem from an higher prospective ignoring the actual underling diffusion mechanism, in order to focus on the form of diffusion equation and its general solution. The quantity of our interest is not the single ion any more, but the ion concentration in space and its variation in time. We already expressed the problem in those terms when defining the chemical diffusion coefficient, but now we will take the time to recast all formalities to obtain the general diffusion law and better understand under which condition it is derived. For further details on diffusion equation please consult either Modern electrochemistry of Bockris [1, 2] or the lecture of professor Yoo [3]. For thermodynamic and phase transition I referred mainly to The textbooks of Hillert [4], Rodrigues [5], and Landau-Liftshitz [6].

First order diffusion: Fick's First and Second Law

Diffusion's laws were first discovered as empirical laws, and in particular, the master mold of those equations is the heat conduction equation (also called Fourier's law). This equation describes the diffusion of thermal energy as a function of time and has the form of a partial derivative equation:

$$\frac{\partial u}{\partial t} = -\vec{\nabla} \cdot \vec{J} \tag{3.1}$$

Where u is the energy density and J the heat flux. This equation is nothing but the mathematical expression of **mass conservation** in differential form, when no source or sink are present. That

is to say, it is valid as long as no "matter" can be created or annihilated inside the considered domain. In human syntax, it should read something like "if the quantity of u varies, it means that something crossed the domain's boundary".
Now, the fascinating ingredient of this equation is the flux J, that is to say, the driving force that is in charge of bringing balance to the world. As long as this force exists, the system is not in equilibrium:

$$\frac{\partial u}{\partial t} \neq 0 \tag{3.2}$$

In the case of ion diffusion, the driving force was first identified by A.E. Fick as the concentration gradient and expressed as an empirical law called Fick's first law:

$$\vec{J} = -D\vec{\nabla}c \tag{3.3}$$

Substituting this equation in the continuity equation leads to Fick's second law:

$$\frac{\partial c}{\partial t} = \vec{\nabla} \cdot \left(D\vec{\nabla}c\right) \tag{3.4}$$

Fick's laws are both empirical and similar to other linear laws, like Ohm's or Fourier's laws. It implies that they are not rigorously valid physically, but are more to be considered an approximation of the real underling physical world. They are, in particular, first-order linear approximations of the Taylor series expansion around the zero force point. What does that exactly mean? Well, let's consider a general phenomenon where a certain driving force F_d leads to a flux J of a certain quantity. Around the equilibrium point ($F_d = 0$) it will always be possible to expand the flux as a Taylor series of the form:

$$J = J_0 + F_d \left(\frac{\partial J}{\partial F_d}\right)_{F_d=0} + F_d^2 \frac{1}{2!} \left(\frac{\partial^2 J}{\partial F_d^2}\right)_{F_d=0} + ... \tag{3.5}$$

Where $J_0 = 0$ at equilibrium if no other force is present. Now, if the driving force is small enough for the first-order term to dominate, the expansion can be truncated to the first order in the form:

$$J \approx F_d \left(\frac{\partial J}{\partial F_d}\right)_{F_d=0} = -D\nabla c \tag{3.6}$$

Where ∇c is the driving force and the diffusion coefficient is the first-order coefficient of the Taylor expansion. Following this reasoning, Fick's law is expected to break at a high enough concentration gradient. Luckily, at least for the liquid case, the concentration gradient required results in a local concentration higher than the solubility limit of the salt at room temperature, and the equation can be carelessly employed.
So far, all equations have been expressed for the general case of multidimensional diffusion. As repeatedly highlighted in the second chapter, the whole point of physical characterization was to assess the homogeneity of the device and reduce the modeling to one single dimension, perpendicular to the deposition substrate. In this simplified framework, Fick's second law can be restated as:

$$\frac{\partial c}{\partial t} = \frac{\partial}{\partial x}\left(D\frac{\partial c}{\partial x}\right) = D\frac{\partial^2 c}{\partial x^2} \tag{3.7}$$

Where the rightmost equality holds for a constant diffusion coefficient. We can now take the time to study this partial derivative equation in order to catch the salient feature of its solution and gain some intuitive understanding of its doing.

Steady-state solution of Fick's laws

A steady-state solution is obtained by imposing the equilibrium condition:

$$\frac{\partial c}{\partial t} = 0 \tag{3.8}$$

It follows from equation 3.7 that the general solution is of the form:

$$c(x) = A + Bx \tag{3.9}$$

Intuitively, the only way to have zero curvature is either the constant function or a straight line everywhere in the domain. The constants A and B are determined by means of boundary conditions. Boundary conditions are necessary because the continuity equation can only describe what happens *inside* the domain, and additional information about the *external* world must be provided in the form of boundary conditions. Boundary conditions are of two main types: Dirichlet boundary conditions and Neumann boundary conditions. The former specifies a constant value of the solution at the boundary ($x = x_{bd}$), e.g. $c(x_{bd}) = 0$. The latter provides information about the first derivative of the solution at the domain edge, e.g. $\left(\frac{\partial c}{\partial x}\right)_{x=x_{bd}} = 0$. When both Dirichlet and Neumann boundary conditions are given, they are called Cauchy boundary conditions. Dirichlet boundary conditions are usually linked to an infinite source. For example, diffusion from a big reservoir to a small reservoir can be approximately described as diffusion from an infinite reservoir to a finite reservoir by restricting the equation domain to the small reservoir and imposing a Dirichlet boundary condition at the interface between the two. That type of approximation is particularly useful to reduce the computational burden in 2D or 3D problems, where the big reservoir would usually account for the major part of the simulated domain without actually contributing much to the final solution. In fact, only a small variation in the concentration of the big reservoir is expected.
On the other hand, Neumann boundary conditions are used when the flux of diffusing species is controlled at some inlet or at some blocking interface. As an example, the end of a container impeding the diffusion of the ions will be described in terms of the Neumann boundary condition as a blocking interface: $\left(\frac{\partial c}{\partial x}\right)_{x=x_{bd}} = 0$, that is to say, nothing can transit across the interface.
Quite often, when describing a diffusion problem, we end up with lots of boundary conditions. Actually, the number of boundary conditions *necessary* to completely specify the problem is just equal to the number of parameters in the solution. For example, a steady-state 1D problem needs two boundary conditions to determine the A and B parameters. In the next section, a strategy to reduce the number of boundary conditions will be proposed. This is quite useful to collapse redundant conditions and ensure the right number of constraints are provided for the problem to be solvable.

Transient-state solution of Fick's laws

Solving a partial differential equation (PDE) can be done following several paths. I will here briefly propose the kernel approach, which is, from my point of view, the one granting more insight into the behavior of the equation.
As already pointed out, Fick's second law is nothing but the heat conduction equation under disguise. That means that plenty of work and analysis, performed for the heat diffusion, can be directly inherited to understand ion diffusion.
The kernel approach consists in finding a sort of elementary solution of the PDE in an infinite domain, e.g., the real number line, for a Dirac delta initial distribution. That is to say, the initial

condition for the concentration ($c(x,t)$) reads:

$$c(x,0) = C_0\delta(x) \tag{3.10}$$

At the beginning of time, the concentration is zero everywhere but at a single point, where it takes the value C_0. The well-known heat kernel for such an initial condition is the Gaussian distribution:

$$c(x,t) = \frac{C_0}{\sqrt{4\pi Dt}} e^{-\frac{x^2}{4Dt}} \tag{3.11}$$

Interesting enough, the solution of the diffusion equation is the maximum entropy distribution. That is to say, the solution represents the loss of knowledge we experience over time about the position of each ion. At the beginning of time, we knew exactly the position of each ion. The diffusion, which we already identify as a random walk process, led to a loss of certainty about the position. The Gaussian distribution is the maximum entropy, that is to say, the most probable guess, for estimating the position of the distribution of the ions after a certain time. The effect of the diffusion coefficient is to determine the rate of knowledge loss. We already linked the diffusion coefficient with the root-mean-square displacement, and we can now more rigorously derive the relationship by using the kernel solution:

$$< x^2 >= \int_{-\infty}^{+\infty} dx\, x^2 \frac{c(x,t)}{C_0} = \int_{-\infty}^{+\infty} dx\, \frac{x^2}{\sqrt{4\pi Dt}} e^{-\frac{x^2}{4Dt}} = 2Dt \tag{3.12}$$

Where the distribution is normalized to 1 by the initial distribution constant C_0. The solution of the integral is a well-known mathematical problem, and it is obtained by integration by parts.
The same formula is often used in literature and in textbooks to estimate the diffusion length L after a certain time τ as:

$$L^2 = 2D\tau \tag{3.13}$$

The kernel solution was indeed obtained by imposing quite strict initial hypotheses, and in particular, the most important is not the distribution itself but the extension of the domain. The domain is assumed to be infinity, that is to say, no matter the time, the distribution will always have more space to diffuse. In real life, after a certain time, the diffusing species will encounter a barrier, for example, the edge of the container, or the electrode, which impede further diffusion. At that point, the kernel solution won't be enough to describe the evolution of ions' concentration. In fact, the kernel solution is also called the "short-time solution" because, in real cases, it is valid only for a time short enough for the domain to be considered infinity. The equation 3.13 is used as a measurement of the validity of the short-time approximation. As long as L^2 is much shorter than the distance (d_{edge}) to the edge of the domain, the kernel equation can be used. For a more rigorous definition of "much shorter," it is always possible to estimate the error by calculating the quantity of ions that have already reached the (e.g., right) blocking interface and fixing the ratio of the total quantity of ions equal to the tolerated error e.g., $0.5\,\%$:

$$\frac{\int_{d_{edge}}^{+\infty} dx\, c(x,t)}{\int_0^{+\infty} dx\, c(x,t)} \leq 0.005 \tag{3.14}$$

The integral at the numerator does not have any analytical solution for the kernel solution and is usually called *complementary error function* ($erfc$). The numerator is nothing but the integral of the right half of the ion distribution, and it is always equal to $\frac{C_0}{2}$. The twin of the $erfc$ is the *error function*, which generally reads:

$$erf(x) = \frac{2}{\sqrt{\pi}} \int_0^x dy\, e^{-y^2} \tag{3.15}$$

While the $erfc$ is a measurement of the ions that have already "touched" the boundary, the erf measures the quantity of ions that are still inside the domain.
After this short *excursus* we can come back to the solution, and in particular the general solution of the diffusion equation for any initial distribution and a finite domain. The extension of the kernel to an initial distribution of choice is quite straightforward. In fact, no matter what shape a curve takes, it will always be possible to decompose it into an infinite series of Dirac deltas. As long as the ions do not interact, each Dirac delta will diffuse on its own, and the final solution can be computed by convolution of the kernel solution and the initial distribution $c_{init}(x)$ as:

$$c(x,t) = \int_{-\infty}^{+\infty} dz \, \frac{c_{init}(z)}{\sqrt{4\pi Dt}} e^{-\frac{(x-z)^2}{4Dt}} \tag{3.16}$$

Where the value of the initial distribution has the same role as C_0 in the kernel solution.
So far, the solution is still valid only for an infinite domain or a short time. In order to get the general solution, we need to use the separation of variables on the initial equation by assuming the solution to be in the form $c(x,t) = f(x)g(t)$ and recasting the equation as:

$$\frac{\partial f(x)g(t)}{\partial t} = D\frac{\partial^2 f(x)g(t)}{\partial x^2} \tag{3.17}$$

$$f(x)\frac{dg(t)}{dt} = Dg(t)\frac{d^2 f(x)}{dx^2} \tag{3.18}$$

$$\frac{1}{Dg(t)}\frac{dg(t)}{dt} = \frac{1}{f(x)}\frac{d^2 f(x)}{dx^2} = -k^2 \tag{3.19}$$

$$\tag{3.20}$$

Where the last constant $-k^2$ is expressed to make sure it is negative and to avoid divergent solutions (positive time derivative). The time solution is easily solved by the familiar Gaussian distribution:

$$g(t) = g_0 e^{-k^2 Dt} \tag{3.21}$$

While the space-dependent solution is nothing but the well-known wave equation, and its general solution can be expressed, in a finite domain, as an infinite Fourier series:

$$f(x) = \sum_n (a_n sin(k_n x) + b_n cos(k_n x)) \tag{3.22}$$

The complete solution is, then:

$$c(x,t) = f(x)g(t) = \sum_n (a_n sin(k_n x) + b_n cos(k_n x)) e^{-k_n^2 Dt} \tag{3.23}$$

Where the constant g_0 is absorbed in the Fourier coefficients a_n and b_n. The coefficients are then determined by means of boundary conditions.
Before focusing on the application of the diffusion equation to real physical systems, I will end this section by introducing a strategy to reduce the boundary conditions to independent conditions only. This can be done by introducing a new variable $\eta = \frac{x}{\sqrt{(t)}}$. This variable substitution is called the Boltzmann transform and reduces Fick's second law into the following ordinary differential equation:

$$-\frac{1}{2}\eta\frac{dc}{d\eta} = \frac{d}{d\eta}\left(D\frac{dc}{d\eta}\right) \tag{3.24}$$

Let's consider a set of boundary conditions for a diffusion problem where two semi-infinite domains at concentrations c' and 0 are brought into contact at $x = 0$:

$$c(x > 0, 0) = c' \tag{3.25}$$
$$c(x < 0, 0) = 0 \tag{3.26}$$
$$c(x \to +\infty, t) = c' \tag{3.27}$$
$$c(x \to -\infty, t) = 0 \tag{3.28}$$

And in terms of η they reduce to:

$$c(\eta \to +\infty) = c'$$
$$c(\eta \to -\infty) = 0$$

That is exactly the right number of independent constraints to solve the 1D equation.

1.2 Diffusion in metallic solids

I will now apply Fick's diffusion law to more specific cases, which are important in the modeling of electrochemical cells. In the introduction, we already identified different classes of materials according to the chemical reaction at the interface (alloying and intercalating electrodes) and according to their electrical conductivity (electrodes and electrolytes). The present section focuses on diffusion in electrode materials for both alloying and intercalating reactions. The two materials actually differ not only at the interface level but also in the diffusion process, which is slightly different in the two cases. The common point is the electronic conductivity of the diffusion matrix, that is to say, not only the ion-ion interaction can be discarded, but also imposing an external electric field does not result in any effect on the ions. This can be easily understood in terms of the skin effect: the electric field in a conductor is concentrated outside and on the first few nanometers of the surface of the conductor. If the electric field cannot penetrate inside the electrode, it cannot interact with the ions' motion. It should be noted that the ion-ion interaction hypothesis is somehow core to the treatment of the diffusion problem. In the present section, we will also analyze the consequences of non-negligible interaction on the formulation of the diffusion problem.

Component diffusivity in the case of binary alloy

Let's start by analyzing the problem in the case of an alloying electrode. An important point to remember when dealing with this kind of electrode is to consider not only the atoms being added as mobile species, but also the base alloying metal. If it is true that lithium diffuses inside, for example, aluminum, the opposite is also true. This process is called *interdiffusion* and is a bit trickier to treat with respect to simple diffusion. In the end, we would like to express the problem in terms of lithium diffusion alone, but in order to do so, we have to somehow include the simultaneous diffusion of the alloying metal in the equation. The reason to do so is that, by considering lithium diffusion alone, we are somehow assuming the other metal to act as a diffusion matrix. But from the final perspective, the diffusion matrix should be at rest while the lithium diffuses around. Because both are moving, it's like the lithium is diffusing in a mobile matrix. From the lithium reference frame, of course, the diffusion does respect Fick's law, and

we can write the one-dimensional Fick's first law for each of the two diffusion species as:

$$J_1 = -\tilde{D}_1 \frac{\partial c_1}{\partial x} \tag{3.29}$$

$$J_2 = -\tilde{D}_2 \frac{\partial c_2}{\partial x} \tag{3.30}$$

Where c_1 and c_2 are the molar concentrations of the two metals But in the new frame of reference, where the metal matrix is fixed and only the lithium diffuses, we have to include the **drift** of the matrix inside the diffusion equation of lithium, which is restated as:

$$J_1 = -\tilde{D}_1 \frac{\partial c_1}{\partial x} + c_1 v \tag{3.31}$$

Where v is the local speed of the metal matrix. Or alternatively, from the alloying metal reference frame:

$$J_2 = -\tilde{D}_2 \frac{\partial c_2}{\partial x} + c_2 v \tag{3.32}$$

In order to link the metal matrix velocity with the actual diffusion of the alloying metal, we need a very important hypothesis, which we already state, to hold: no volume change with composition. Only under this assumption is it possible to write a relationship between the two molar concentrations at any composition:

$$c_1 + c_2 = c_0 = \frac{1}{V_m} \tag{3.33}$$

Where V_m is the molar volume of the alloy. We can now apply Fick's second law to c_0:

$$\frac{\partial (c_1 + c_2)}{\partial t} = -\frac{\partial}{\partial x} (J_1 + J_2) = 0 \tag{3.34}$$

Which means $J_1 + J_2 = A$ is constant. Because at the diffusion boundaries (either at infinity or at the blocking interface), the flux must go to zero, hence $A = 0$. The condition $J_1 = -J_2$ is nothing but the condition for the diffusion in the two diffusion matrix reference frames to be equivalent, which is indeed the aim of changing the reference frame. At this point, we can then equate the diffusion in the two new reference frames to find the matrix drift velocity:

$$-\tilde{D}_1 \frac{\partial c_1}{\partial x} + c_1 v = \tilde{D}_2 \frac{\partial c_2}{\partial x} + c_2 v \tag{3.35}$$

$$v = \frac{1}{c_1 + c_2} \left(\tilde{D}_1 \frac{\partial c_1}{\partial x} + \tilde{D}_2 \frac{\partial c_2}{\partial x} \right) \tag{3.36}$$

By defining the mole fraction $N_i = \frac{c_i}{c_1 + c_2}$, and using the constant volume hypothesis ($\sum_i N_i = 1$) the velocity can be expressed as:

$$v = \frac{1}{c_1 + c_2} \left(\tilde{D}_1 \frac{\partial c_1}{\partial x} + \tilde{D}_2 \frac{\partial (c_0 - c_1)}{\partial x} \right) \tag{3.37}$$

c_0 derivative is zero, and back to equation 3.31 we can express the diffusion from the point of view of the matrix reference frame as:

$$J_1 = -\tilde{D}_1 \frac{\partial c_1}{\partial x} + N_1 \left(\tilde{D}_1 \frac{\partial c_1}{\partial x} - \tilde{D}_2 \frac{\partial c_1}{\partial x} \right) = -(N_2 \tilde{D}_1 + N_1 \tilde{D}_2) \frac{\partial c_1}{\partial x} \tag{3.38}$$

So in the new frame of reference, the apparent diffusion coefficient of lithium alone, called *interdiffusion coefficient* is:

$$\tilde{D} = N_2 \tilde{D}_1 + N_1 \tilde{D}_2 \tag{3.39}$$

That means that in an alloying electrode, the actual diffusion coefficient differs from the self-diffusivity $\tilde{D}_1$ of lithium.

Even if this theoretical analysis is a good starting point, it can be rarely applied to real cases. Large volume variations typical of alloying electrodes invalidate both Fick's law and the derivation of the apparent diffusion coefficient. The inclusion of such effects is described in the coming sections.

The effect of chemical potential

Experimentally, in both alloying and intercalating electrodes, the diffusion coefficient is often a function of the intercalation fraction. That means that locally (around an equilibrium point), the diffusion still proceeds along the concentration gradient, but the speed of the diffusion is a function of the particular equilibrium point. Unfortunately, that is the best-case scenario. In not-so-rare cases, Fick's law is found to be actually false: diffusion takes place in the presence of a zero concentration gradient or against the diffusion gradient. Why that happens and which Fick's law hypothesis is violated in these cases is the topic of the present section.
The culprit is the non-interaction particle hypothesis, of course. In particular, the hypothesis wasn't restricted to interactions between ions but also between ions and the diffusion matrix. While the first part of the hypothesis can be considered quite valid in the case of metallic matrix due to the electronic screening, the interaction of the diffusing species with the matrix can hardly be disregarded. When the diffusion coefficient was first defined in terms of jump probability, the energy barrier of the matrix was one of the main ingredients. Of course the matrix acts on the ions, but because for each force, an equal and opposite force is acting, the same is true for the ions, which exert a force on the matrix. What we may expect is that the diffusion coefficient will vary as a function of the stoichiometry because, by varying the number of particles, we also change the matrix. That is indeed the first case where Fick's law is still locally valid, but the diffusion coefficient varies with the stoichiometry. Sometimes the interaction between the ions and the matrix is so strong that the nearby ions "sense" each other by means of the mediated interaction with the diffusion matrix. In such cases, Fick's law is observed to be invalid at the local scale. It should be noted that in the liquid case, the interaction between the ions and the matrix, which is the liquid solvent, is far weaker and Fick's law is usually valid.
A more robust formulation of diffusion in solid is needed to account for these cases. We expect it to be reduced to Fick's law under appropriate conditions. In order to do so, we need to restart from the beginning, ignoring the microscopic mechanism of diffusion and focusing on a statistical treatment only, that is to say, we ask His Majesty the thermodynamics to comes to the rescue. As a quick reminder, thermodynamic is based on the following simple mathematical argument. Let's consider a system macroscopically characterized by a certain parameter, E. Microscopically, the system is characterized by a collection of variables, X_n. For each microstate, that is to say, set of values of the variables X_n, the parameter E will take a value E_n. We can group all the microstates with the same value of parameter E, because we will not be able to and/or are not interested in distinguishing them apart. Let's N_n be the number of microstates with the same macroscopic state, E_n. For each macroscopic state, we define the entropy of the state as:

$$S(E_n) = \ln N_n \tag{3.40}$$

The logarithm is just for convenience, in order for the entropy to be additive: when two systems with entropy S_1 and S_2 are united, the entropy of the new system is the sum of the entropy of two smaller systems: $S = S_1 + S_2$. As a matter of fact, for two systems to have the exact value E_n, it means that there is a subset of X_n parameters that can be exchanged between particles without modifying the parameter E. Combinatorics teaches us that we expect the number of

microstates to be proportional to the factorial of the number of particles times the number of exchangeable parameters. In general, we can call n, the number of degrees of freedom, the product of the number of particles and of parameters. Then, a macro-state with n degrees of freedom should be realized by means of any the $n!$ equivalent microstates.
Everyone knows that a system at equilibrium tends to maximize entropy. Statistically, what happens is that the system with the higher entropy is indeed the most probable, and by observing the system, we will almost always find it in the macro-state E_n with maximum entropy. But what "almost always" actually means. It is indeed quite straightforward to be convinced of the principle by a simple calculation. As the number of degrees of freedom is proportional to the number of particles, in an actual system it is usually on the order of the Avogadro number. That means that the ratio of the number of microstates between two macro-states with only one degree of freedom of difference will be $\frac{n!}{(n-1)!} = n$. That is to say, the macro-state with one additional degree of freedom is $N_A \sim 10^{23}$ time more probable!
Convinced or not by this over-simplified reasoning, systems *do* maximize entropy when passing from a non equilibrium state to an equilibrium state. In general, entropy variation is not such an easy quantity to measure and Gibbs free energy ($G = U - TS + pV$) or Helmholtz free energy ($F = U - TS$) are preferred. In the end, entropy maximization is equivalent to free energy minimization.
What was the purpose of this thermodynamic amusement, you may ask. The point was to lay a solid foundation for the following. Let's go back to the diffusion problem. In particular, let's consider two sub-systems, A and B, with N_A and N_B ion concentration and G_A and G_B Gibbs free energy. We want to know if the particles will migrate from system A to system B. Statistically speaking, we expect to observe a migration of particles from system A to system B if the total Gibbs free energy $G = G_A + G_B$ decreases during the transition. When an infinitesimal quantity of particles dN is displaced from A to B, the Gibbs free energy will vary accordingly:

$$dG_A = -\left(\frac{\partial G_A}{\partial N}\right)_{p,T} dN = -\mu_A dN \tag{3.41}$$

$$dG_B = \left(\frac{\partial G_B}{\partial N}\right)_{p,T} dN = \mu_B dN \tag{3.42}$$

$$dG = dG_B + dG_A = (\mu_B - \mu_A) dN \tag{3.43}$$

Where μ_i is the *chemical potential* of each sub-system. Assuming $\mu_A > \mu_A$ at t-zero, the migration from A to B will continue until $\mu_B = \mu_A$. This is indeed the condition for the minimization of the total Gibbs free energy:

$$\frac{dG}{dN} = (\mu_B - \mu_A) dN = 0 \tag{3.44}$$

It must be noted how the condition for global minimum does not imply local minima for the two subsystems ($\mu_i \neq 0$) but instead a weaker constraint of constant chemical potential.
We are then ready to reformulate the diffusion equation in a much general form, by exploiting the chemical potential gradient instead of the concentration gradient as a driving force of diffusion:

$$J = -cD\frac{\nabla \mu}{RT} \tag{3.45}$$

Where the gas constant is used to convert the chemical potential ($\mathrm{J\,mol^{-1}}$) to pure number and get the flux expressed in $\mathrm{mol\,m^{-2}\,s^{-1}}$. The term $M = \frac{D}{RT}$ is called mechanical mobility and has the unit of $\mathrm{m^2\,mol\,s^{-1}\,J^{-1}}$.
As for Fick's law, this formula is a first order Taylor expansion of the ion flux around an equilibrium point. The diffusion coefficient may still vary as a function of concentration, but the law

itself is always locally valid. We can also see how the new formulation can be reduced to Fick's first law:

$$J = -c\frac{D}{RT}\frac{\partial \mu}{\partial x} = -\frac{D}{RT}\frac{\partial \mu}{\partial \ln c}\frac{\partial c}{\partial x} = -D\frac{\theta(c)}{RT}\frac{\partial c}{\partial x} = -\tilde{D}\frac{\partial c}{\partial x} \tag{3.46}$$

Where $\theta(c)$ is the enhancement factor introduced in the first chapter (eq. 1.13). Diffusion against concentration gradient appears when $\theta(c) < 0$, while diffusion in the absence of concentration gradient is caused by discontinuity in the derivative of μ. If mu is not differentiable with respect to concentration, the substitution in equation 3.46 cannot be performed. Discontinuity in the chemical potential is associated with phase transition, which is the topic of the next subsection.

Handling phase transition

Phase transformation is a hot topic in the field of battery modeling. The main reason is the general invalidity of most of the dynamic formulations of the diffusion problem inside the phase transition region. That is to say, when two phases with different thermodynamic properties are present at the same time inside the modeling domain. In the previous section, we saw that Fick's equation itself is no longer valid at the phase boundary region: even if at equilibrium the chemical potential is constant across the two phases, its first derivative usually shows a first-order discontinuity with respect to concentration. The general problem is composed of two different sub-problems: nucleation of new phases and expansion of new phases.

During phase nucleation in the domain, a sudden split in concentration is experienced. That is to say, an ion-rich and an ion-poor phase form by separation. It is actually possible to mimic this separation with a sudden drop in the diffusion coefficient. In the first chapter, the phase transition plateau was in fact linked to a large drop in the diffusion coefficient. This approach does actually work for the dynamic simulation of phase transitions, but it won't model properly neither the relaxation of the phase boundary nor the formation of the two phases from the quenching of a melt. In fact, the phase transition is only induced by the dynamic but does not actually involve any modeling of the interface energy between different phases. Expressed differently, the interface between the two phases will be unstable, and given enough time, the model based on the diffusion coefficient alone will relax into a single phase with homogeneous concentration. In the actual phase transition, the two phases are at thermodynamic equilibrium, and intermediate stoichiometry phases are not stable.

In order to actually model the interface energy contribution, a higher-order expansion of the chemical potential is a possible solution. This approach is mainstream in the literature and is usually referred to as *Cahn-Hilliard Model* [7]. When we defined the chemical potential, the implicit hypothesis, which is actually valid for any standard thermodynamic analysis, was equilibrium. This implies maximum entropy, or minimum Gibbs free energy, and authorizes a first-order expansion of any quantity of interest. Actually, the condition is usually even stricter, and we should talk of *stable equilibrium*. This further condition implies that small variations of the thermodynamic quantity are suppressed, and the system does not move from the equilibrium position. In the case of phase transition, the system is actually very sensitive to small variations, for example, fluctuations in concentration. If the phase transition threshold is crossed, the system will drift far away from the initial equilibrium point, which is indeed an *unstable equilibrium*. Under those conditions, it is then necessary to consider higher-order terms in the Taylor expansion of the local Gibbs free energy. In particular, the higher-order terms with respect to the spatial position.

In the previous treatment, we considered the transport of a dN between two domains and wrote the total Gibbs free energy as a function of the local concentration alone. We were disregarding

any interaction at the boundary between the two domains, assuming that we were able to move the atoms back and forth for free. In order to account for the extra interface force during phase transition, the total Gibbs free energy G should be rewritten as:

$$G = \int_V dV\, g = \int_V dV\, g_0(c) + k_1 \nabla c + k_2 \nabla^2 c + k_3 (\nabla c)^2 + ... \tag{3.47}$$

Where g is the new local Gibbs free energy and $g_0(c)$ is the usually local Gibbs free energy. By considering the term up to the second order and applying the Gauss theorem, the equation is reduced to:

$$G = \int_V dV\, g_0(c) + k(\nabla c)^2 = G_0(c) + \int_V dV\, k(\nabla c)^2 \tag{3.48}$$

k represents the interaction energy at phase boundaries and determines whether phases are miscible ($k \leq 0$) or not ($k > 0$). At this point, it is enough to retrace the same reasoning of the previous section to obtain the driving force of diffusion. The first term, $G_0(c)$, is nothing but the former Gibbs free energy and will account for the standard Fickian diffusion term. The second term introduces the typical cubed term of the Cahn-Hilliard formulation, and the new 1D diffusion equation reads:

$$J = -cM \frac{\partial \mu}{\partial x} - 2ckM \frac{\partial^3 c}{\partial x^3} \tag{3.49}$$

The same result is obtained by direct introduction of the generalized chemical potential w in equation 3.46.

$$w = \mu(c) + 2k \frac{\partial^2 c}{\partial x^2} \tag{3.50}$$

I avoided on purpose the whole mathematical treatment of the Cahn-Hilliard problem because I will not use it in my formulation. Notwithstanding, the model is often encountered in the literature, and an introduction to the subject is due to carry on a proper critical review of the bibliography.

1.3 Diffusion in dielectric solids

It is now time to adapt the diffusion equation to the last component of the electrochemical cell: the electrolyte. The main difference with respect to the electrode is the electronic conductivity of the electrolyte, which at this stage we will consider to be near zero. As a consequence, an external electric field will be able to permeate the interior of the material and interact directly with the ions. It must be noted how the ions are still considered neutral with respect to each other; that is to say, we are not questioning the non-interaction hypothesis between ions. In fact, in the first chapter, ion neutralization by crystal structure relaxation was introduced in order to justify this hypothesis. In the case of an external field, the ions are still considered independent, and the diffusion is based on a random walk. As a matter of fact, the effect of the electric field consists of adding a bias to the direction of the random walk by decreasing the energy barrier in the direction of the electric field and increasing the one in the opposite direction. In Figure 3.1 a pictorial representation of the effect of a constant electric field on the potential landscape seen by an atom is reported. The atom will move in the direction of the field due to a higher jump probability in one direction, but the intrinsic jump probability, that is to say, the mechanical mobility, or the rate at which an atom will try to jump, is still linked to the Boltzmann distribution. We then expect the flux of ions, linked to the electric field, to still be proportional to the very same self-diffusivity introduced for the random walk.

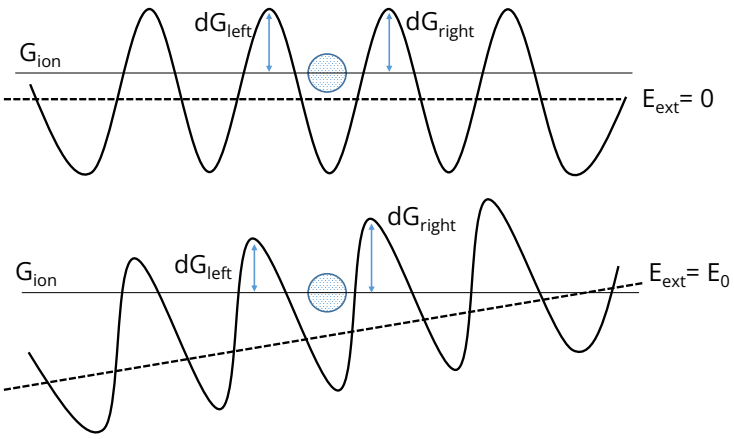

Figure 3.1: Effect of an external electric field on the potential profile. G_{ion} is the Gibbs free energy (function of temperature and composition) of ions, while dG_{left} and dG_{right} are the energy barriers each ion needs to overcome to jump to adjacent sites.

Charge particles in an electric field

Instead of trying to verbosely express the physics, it may be a much better strategy to just come back to the definition of Gibbs free energy and chemical potential and try to modify it in the case of an external electric field. The simplest way to introduce this additional effect is to recall the formal definition of the chemical potential and get some more sense out of it. The chemical potential is the variation of the Gibbs free energy when the local concentration of particles is modified at constant pressure and volume. It can be seen as the energy required to bring an extra particle from infinity into the subsystem.

$$\mu = \left(\frac{\partial G}{\partial N}\right)_{p,T} dN \tag{3.51}$$

In the presence of an external electric field, when bringing an ion (positively charged) from infinity, where the electric potential is set at zero, to inside the subsystem, an extra energy term is expected to appear. If we define the electric potential ϕ inside the subsystem and ze_0 the charge of the ions as a multiple of the electron charge, the work done to bring the charge from infinity is $ze_0\phi$. The total Gibbs free energy is then the energy to add the neutral particles plus the energy to add the charge, and the *electrochemical potential* can be introduced as:

$$\tilde{\mu} = \left(\frac{\partial G}{\partial N}\right)_{p,T} dN = \mu + zF\phi \tag{3.52}$$

Where F is the Faraday constant used to convert the equation in terms of J mol^{-1}. Because it is actually the Gibbs free energy and not the chemical potential itself that determines the ions' migration, it is possible to directly substitute the electrochemical potential inside the diffusion equation as the new driving force in the presence of an external electric field, obtaining the so-called *drift-diffusion* equation:

$$J = -c\frac{D}{kT}\frac{\partial \tilde{\mu}}{\partial x} = -c\frac{D}{kT}\frac{\partial}{\partial x}\left(\mu + zF\phi\right) = -\tilde{D}\frac{\partial c}{\partial x} - czF\frac{D}{kT}\frac{\partial \phi}{\partial x} \tag{3.53}$$

The diffusion equation is now characterized by two terms, the first accounting for diffusion by chemical gradient and the second linked exclusively to the external electric field. In particular,

it is common to redefine the coefficient for the second term under the form of an electric conductivity as:

$$\sigma_{ion} \equiv \left(\frac{zFJ}{E}\right)_{\frac{\partial \mu}{\partial x}=0} = c(zF)^2 \frac{D}{RT} \tag{3.54}$$

Where the electric field is defined as $E = -\frac{\partial \phi}{\partial x}$. The unit of measure of σ_{ion} is $\mathrm{S\,m^{-1}}$, as already reported in the electrolyte review of the first chapter. We can see that D and σ_{ion} even if related, actually differ. In particular, D is an intrinsic property linked to the potential landscape inside the crystal, and it should not vary with the concentration (unless other effects take place). Instead, the very definition of σ_{ion} incorporates the ion concentration. That means that two samples of the same electrolyte with the same diffusion coefficient, may show different electric conductivities if the concentration of mobile lithium is different. Moreover, because the definition implies a zero chemical gradient, the enhancement factor does not have any effect on the value of σ_{ion}. The derivation of the electric conductivity is often related to the Einstein relation between mechanical mobility and self-diffusivity. In general, the Einstein relation is true as long as the energy follows the Boltzmann statistics, that is to say, the non-interacting particle hypothesis holds true. Exploiting this link permits one to directly write the drift diffusion equation without actually defining the electrochemical potential (see [8]), but is nothing more than a shortcut with respect to the complete treatment of the problem.

Ion-ion interaction and dielectric properties

As a final act in the theoretical treatment of bulk physics, it is necessary to sketch a minimum framework to take into account the ion-ion interaction. So far, this effect has been disregarded by invoking crystal relaxation as a mechanism to mask the electric charge of an ion. Notwithstanding, the material is not conductive, and for large accumulations, it will not be able to compensate for the charge imbalance. As a result, locally, there will be a net charge accumulation or depletion. In order to avoid calculating the single ion-ion interaction, the best option is to exploit a mean field approach. In fact, from the point of view of each ion, the electric field generated by a volume with a large charge accumulation has the same effect as an external electric field. We may exploit Poisson's equation to link the local charge density ρ with the lithium concentration and the induced electric field E_ind:

$$\nabla \cdot \vec{E_{ind}} = \frac{\rho}{\epsilon_r \epsilon_0} \tag{3.55}$$

Where ϵ_0 is the vacuum permittivity and ϵ_r is the dielectric constant of the material. As already pointed out, the dielectric constant includes the effect of screening on the local electric charge due to crystal relaxation. In general the dielectric constant is a function of the excitation frequency, as already discussed, but it should also vary as a function of the local charge $\epsilon_r = f(\rho)$. In fact, we expect a complete screening at very low concentrations and a loss of effectiveness as the charge density is increased. I will disregard any dependency at this stage.
Concerning the local charge density, it is of course related to the difference between the local ions' concentration $c(x)$ and the equilibrium concentration c_{eq}:

$$\rho(x) = F(c(x) - c_{eq}) \tag{3.56}$$

The effective electric field to be used in the drift-diffusion equation is the sum of the external field and the internally induced field, leading to:

$$J = -\tilde{D}\frac{\partial c}{\partial x} - czF\frac{D}{kT}(E_{ext} + E_{ind}) \tag{3.57}$$

It has to be noted how the definition of the electric conductivity implies zero chemical gradient, hence zero concentration gradient and zero induced field, so the new formulation does not impact its value.
It should be noted that in the 1D formulation as stated above, the ions do interact with each other as long as they do not share the same x-position. The electric interaction is calculated from a volume element dV acting on another volume element dV, which in the 1D formulation reduces to dx. But the interaction inside the dV element itself is not considered: we can hypothetically pile an infinite number of ions into an infinitesimal volume element. In order to avoid such non-physical behavior, one last modification is necessary to the diffusion equation. So far, we treated the chemical potential as a given quantity, but we already defined it as a function of the intercalation fraction for a material with N available sites. Recalling equation 1.4, it is possible to redefine the electrochemical potential as:

$$\tilde{\mu} = \mu + zF\phi = E_0 + kTN_a \ln\left(\frac{x_c}{1-x_c}\right) + zF\phi \tag{3.58}$$

Where $x_c = \frac{c}{c_{max}}$ is the intercalation fraction. Even if this expression is valid for non-interacting ions, it will prevent the infinite accumulation of ions thanks to the explosion of the entropy term for $x_c = 0$ and $x_c = 1$ ($\ln \to \pm\infty$). The only additional hypothesis is that the sites that can accommodate the ions are finite. That is equivalent to imposing zero interaction energy up to a certain threshold ($c = c_{max}$) and infinite interaction energy for higher concentrations.
Section three will deal with the estimation of the different material parameters for the cell to be modeled. In particular, the dielectric constant is needed to include the mean field interaction between ions and limit charge accumulation. Unluckily, the formulation is quite simple, and the dielectric constant hides lots of hypotheses and different effects. For this reason, it should be regarded as an "effective" parameter used to deal with multiple complex effects.

Variation of self-diffusion coefficient with intercalation fraction

So far, we have described how the chemical diffusion coefficient and the diffusion equation are influenced by stoichiometry and their effects on the motion of ions. More precisely, the motion of ions under small perturbations of equilibrium. The variation in the diffusion equation comes from the variation of the first derivative of the chemical potential with respect to the equilibrium point. But what about the self-diffusion coefficient? It was derived under equilibrium conditions, that is to say, constant chemical potential. That means that all the effects so far described do not impact the self-diffusion itself. Notwithstanding, it must be noted that in the first chapter, when it was derived, the treatment concerned a single ion: we described the self-diffusion, or the random walk, by means of a jump attempt frequency and a successful jump rate. The number of jumps per second was defined as the product of the attempt times the success rate. The attempt frequency is linked to thermal motion and is not expected, at first order (no ion-ion or ion-matrix interactions), to vary with the intercalation fraction. Instead, the probability of success must depend on the availability of free sites nearby. Even if they do not interact, it is impossible for two ions to occupy the same site. It must be noted that we are talking about free sites for diffusion. If the diffusion is based on thermally generated interstitial defects, it is impossible to reach saturation of the diffusion sites; it would mean that all the crystal atoms are in the interstitial position, which is absurd. On the contrary, in the case of diffusion by vacancy, as for most intercalation cathodes, the saturation of the diffusion sites is the initial state when the crystal is completely filled with ions. More correctly, in the case of an electrode, as soon as the lithium is de-intercalated, the vacancy density is dominated by the stoichiometry, and the

thermally generated defects are negligible. In order to account for this effect, an extra term linked to the intercalation fraction (x_c) should be added to the definition of the self-diffusion coefficient. In particular, for an intercalating electrode, it is expected to vary as [9]:

$$D = (1 - x_c)D_0 \tag{3.59}$$

Once again, this relationship has nothing to do with the chemical potential or the diffusion process treated so far. It is the intrinsic variation of the self-diffusion, at equilibrium. It may be confusing that free sites are counted twice, once in the chemical potential (eq. 3.58)and once in the self-diffusion. Actually, the two refer to very different effects. In particular, the former is used to describe the difficulty of finding a free site when an ion is introduced from the outer world: when an ion is brought from infinity to inside the crystal, if the crystal is already filled, it takes a lot of time (and work) to find an available site. In the former, the number of ions is fixed, and the phenomenon under description is their thermal agitation. Stated differently, one refers to the motion of ions between two subsystems at different chemical potentials, and the other to the motion of ions inside a subsystem at equilibrium.

1.4 Review of drift-diffusion model for solid-state batteries

Before switching to interfaces, I will briefly review the literature on bulk modeling. The focus is not on the results or the strategy to get to the solution, but the choice of equation itself. Most of the papers model all domains at the same time, and modeling choices in different domains often influence each other. Notwithstanding, I preferred to review each domain separately for a more clear comparison.

anode

Alloying and plating anodes are very difficult to implement in the standard framework so far developed due to the large volume expansion and its effect on the diffusion problem. In fact, the whole thermodynamic treatment is nullified when the constant volume hypothesis is violated. A second problem related to volume expansion is the large mechanical stress, which depends on the actual 3D topology of the cell and cannot be reduced to a 1D formulation. As a consequence, most models just disregard lithium diffusion in the anode bulk [10–12]. The modeling domain often starts at the electrolyte/anode interface, and the lithium concentration at this interface is considered constant at any time step. In the case of the lithium metal anode, as long as the aim of the model is the static or dynamic performance of the cell and the cycling performance is not addressed, the assumption is quite reasonable. As a matter of fact, diffusion in alloys is much faster than diffusion in intercalation materials; hence, the anode is rarely the limiting factor for dynamic performances. On the other hand, it is often one of the main responsible for capacity decay during cycling.
Some works are available in the 2D domain and try to follow the lithium plating evolution for the lithium metal anode [13–15], but they mainly refer to the liquid configuration, where no external mechanical constraint is imposed on the lithium growth.
Concerning the effect of volume expansion in alloying and intercalating anodes and the resulting stress on the lithium diffusion, the literature is quite vast (here a small selection to dig into the topic [16–20]), but concerns mainly single particles analysis to be exploited in the framework of composite electrode according to the porous electrode theory [21]. In general, the adopted solution is the inclusion of an extra term in the definition of the chemical potential of the electrode,

which accounts for the stress energy:

$$\mu = E_0 + kTn_a \ln\left(\frac{x_c}{1-x_c}\right) + E_{stress} \tag{3.60}$$

A review of the main equation for the stress energy can be found in the textbook of Bishop et al. [22]. A very popular formulation under the assumption of small elastic deformation is:

$$E_{stress} = -\Omega\sigma_h \tag{3.61}$$

Where Ω is the partial molar volume and σ_h the hydrostatic stress.
Recent works are also dedicated to all-solid-state batteries [23–27], but the here proposed models do not differ from the ones used for single particles. As a general concern, these models do not consider the variation of thermodynamic properties with respect to the intercalation fraction. In fact, the very same hydrostatic stress is expected to vary during intercalation, and equation 3.61 is a linearization around an equilibrium point. Even if the small stress hypothesis greatly simplifies the expression of the total Gibbs energy, it is, in the end, quite useless for the majority of anodes, which exhibit large volume variation. Measurement of the evolution of the Gibbs free energy at different intercalation states and its direct implementation in the definition of the chemical potential are still the best options for a reliable model implementation. I will return to this subject during the definition of my own model in the third section of the present chapter.

cathode

Residing on the bright side of the moon, cathodes are quite straightforward to model in the constant volume thermodynamic framework. The main discrepancy found among different works is the handling of the chemical potential and the variation of the diffusion coefficient as a function of the intercalation fraction. Concerning the $LiCoO_2$ itself, the model is sometimes defined with a constant diffusion coefficient [10]. In the result section, I will extensively comment on the effect of this choice on the simulation results. More often, the variation of the diffusion coefficient is experimentally determined and used as a stand-alone parameter in Fick's equation [11, 28, 29]. This approach exploits the decomposition of the diffusion equation as reported in equation 3.46. Another possible variation of the diffusion equation is the explicit insertion of the ion-ion interaction term inside the definition of the chemical potential instead [12, 30]. In this case, the equation is cast in terms of μ and the interaction is expanded as a first-order function of the lithium concentration as follows:

$$\mu = E_0 + kTN_a \ln\left(\frac{x_c}{1-x_c}\right) + RT\chi(1-2x_c) \tag{3.62}$$

Where χ is the first-order interaction energy term. The extra energy here defined is centered, as the entropy, at $x_c = 0.5$, in order to preserve the chemical potential symmetry. Higher-order expansion is also possible but is not quite a popular choice due to the need for careful determination of multiple parameters [31].
An alternative formulation exploits the Cahn-Hilliard theory presented previously to account for phase transitions and phase separation. During the years, it has been extensively applied to both $LiFePO_4$ and $LiCoO_2$ cathodes modelling [30, 32–36]. The model provides a hard transition dynamic with stable phase boundaries. The price is the extra k parameter which cannot be directly measured and is usually fitted to obtain the desired charge/discharge profile. I will add extra commentary on my choice not to use this formulation at the end of this chapter and in the following one.

electrolyte

Concerning the electrolyte domain, equation 3.58 is broadly employed with some minor modifications by the whole literature. A common variant is obtained under the approximation of "diluted solution", by considering $x_c \sim 0$ [33, 37]. This formalism comes from the liquid electrolyte domain. In this context, "diluted solution" corresponds to a non-interacting condition that is in fact satisfied at a low ion concentration. Notwithstanding, the applicability of such simplification in the case of equation 3.58 is harder to justify for two main reasons. First, the equation was already derived under the zero ion-ion interaction hypothesis. Second, in liquid electrolyte, the screening capability of the solvent is much stronger than that of the solid electrolyte crystal; hence, even at very low concentrations, there is no guarantee for a complete screening in the second case. As a matter of fact, it is not straightforward to estimate the value of c_{max} for the solid electrolyte, as I will show in detail in the section dedicated to parameter identification.
Another common assumption is electroneutrality in the bulk electrolyte. The charge accumulation is artificially forced at the boundary between electrolyte and electrode [12, 28, 29]. Even if this is the actual behavior of the electrolyte, it is obtained automatically in the steady-state solution without any additional conditions. On the other hand, when analyzing the system at high frequency, this constraint will modify the actual behavior of the electrolyte. In fact, it takes some time for the electrolyte to reach internal electroneutrality through crystal structure relaxation. In steady state, this delay may be disregarded, but it is the foundation of the frequency response of the system.
In the opposite direction, there are works that propose a very complex formulation of the electrolyte electrochemical potential [37] and compare the obtained shape of lithium accumulation inside the electrolyte to justify such a choice. This approach has two pitfalls. First, the *actual* lithium profile is quite hard to probe; hence, the model cannot be validated directly. Second, complex equations usually require lots of additional parameters, which are fitted by means of the very same data that are then used to validate the model. For example, you may need to exploit the bode response to fit the chemical potential. As a consequence, the model with more parameters will accomplish a better fit and will be considered more accurate, but in the end, that is just called **overfitting**. In my opinion, if we don't want to go deep enough in statistical analysis to be able to test the accuracy by means of sensitivity analysis, the best option is to follow the *Ockham's razor* and adopt the simplest possible model. As a prize, the great advantages of fast solutions and fitting couples with ease of analysis. Hiding our ignorance under tons of unknown parameters is hardly the right answer and will not broaden our understanding of the subject.

2. Butler-Volmer Equation for All-solid-state Batteries

Once the treatment of bulk physics is complete, the last ingredient to add to the model is the reaction dynamic at the boundary between the electrodes and the electrolyte. Electron and ion transfer reactions were anticipated in the first section as the two reaction mechanisms in plating, alloying, and intercalating electrodes. Both are electrochemical reactions, meaning that electrons are exchanged. There is a major difference between classical chemical reactions and electrochemical reactions. In the former, two substances colliding with enough energy react to form new products, and the chemical bonds change in type and nature. The reaction dynamic of such a process is controlled by the thermal energy of atoms (vibrational, rotational, etc.), which permits breaking the old bond and forming new ones. As a result, temperature is the key parameter to control the reaction speed. On the other end, the latter is based on the transition of

electrons between different quantum states. Even more interesting, the two actors in the reaction (the oxidizing and the reducing species) never come into contact with each other. The reaction is mediated by the electrode, which is in charge of shuttling electrons back and forth from one species to the other. Once the atoms are close enough to the electrode for the electrons to tunnel to or from the electrode surface, the thermal motion of the atoms can be completely disregarded. In fact, electron tunneling is much faster than any thermal motion associated with molecules, which are immobile from the electron perspective. As a consequence, the problem is reduced to the study of electrons alone. Temperature is still a parameter of interest because the energy distribution of electrons does depend on it, but, as we will briefly discover, there is a much more interesting way of increasing electron energy.
For a general bibliography, I will suggest the textbooks of Girault [38] and Bockris [2] for the classical formulation and Schmickler [39] for the intercalating electrode case.

2.1 Classical formulation

In dealing with this last aspect of the electrochemical cell, all the main hypotheses of diffusion are still valid. In particular, the system is assumed to be at equilibrium, and only first-order variations of the different thermodynamic quantities will be considered. I will start by deriving the equation for the reaction rate at the interface between electrode and electrolyte in the classical liquid framework, and then discuss the necessary modifications to adapt it to the solid-solid intercalation cell.

Equilibrium at electrode electrolyte interface

The system of reference is composed of a metal electrode and an electrolyte that contains two species that can be converted one into the other by means of a redox reaction: $A^+ + e^- \longrightarrow B$. The initial concentrations of the two are a_0 and b_0 and the metal potential is at zero with respect to the reference at infinity (as for the calculation of the electrochemical potential). An important point that I will stress again in the next chapter is that at this stage, the whole electrochemistry takes place inside the solution. The electrode is just a mean to exchange electrons from one species to another. When the solution and the electrode are brought into contact (see Figure 3.2), the electron in solution and the electron on the metal are not in equilibrium, that is to say, $\tilde{\mu}_m \neq \tilde{\mu}_s$. In terms of Gibbs energy, it is then favorable (maximization of entropy) for electrons to move from one sub-system to another. For the sake of the analysis, let's assume that electrons start jumping from the solution to the electrode. As a result, the concentration of A^+ will increase and that of B will decrease for the same quantity. Because the system is so isolated, the electrons will pile up and generate an electric field. After a short time, a new equilibrium is reached (see Figure 3.2). Deep inside the solution, the concentration of the two species is the same as in the initial states, while near the interface, a gradient is present. Because the two species are charged, the electroneutrality of the solution does not hold near the interface, and a net charge accumulation of the same magnitude and opposite sign as the quantity of electrons on the metal is created. Far from the interface, the two distribution, on the metal and in the electrolyte, neutralize each other and the electric field is zero. Once equilibrium is reached, zero net current flows across the interface of electrode and electrolyte. This equilibrium is obtained by a balance of two currents: one of electrons that from the metal jump into A^+ species sites (cathodic current density j_c) and one that accounts for electrons escaping the B site to reach the metal surface (anodic current density j_a). Once again, the two species do not directly interact with each other, and the two electron populations are independent. The equilibrium condition can be written in

terms of the two currents density as follows:

$$j_c + j_a = j_{tot} = 0 \tag{3.63}$$

Around the equilibrium point, the current density can be expanded as a function of the interface concentration and at the first order:

$$j_a = c_a(x=0)k_aF \tag{3.64}$$

$$j_c = -c_c(x=0)k_cF \tag{3.65}$$

Where the first-order coefficients k_c and k_a are called **electrochemical rate constants**. Substituting the first-order expansion in equation 3.63 we obtain a relation between the rate constants:

$$\frac{k_c}{k_a} = \frac{c_a(x=0)}{c_c(x=0)} \tag{3.66}$$

The same equilibrium can also be described from the thermodynamic point of view as $\tilde{\mu}_m = \tilde{\mu}_s$.

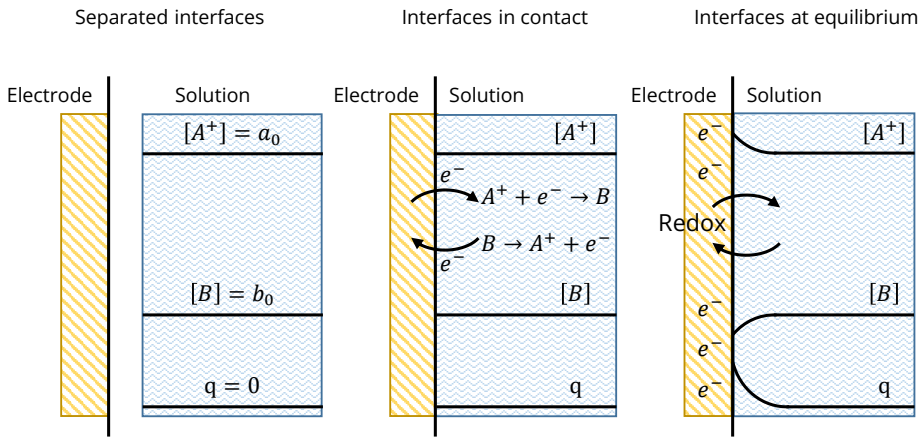

Figure 3.2: Evolution of the concentration of oxidise species $[A^+]$, reduce species $[B]$ and net charge density (q) inside the electrolyte solution at the moment of first contact with the electrode.

Current under equilibrium perturbation

What we are interested in is the variation of the electrochemical rate with respect to the chemical potential. Assuming that the potential is displaced with respect to equilibrium, we expect a flux to appear in order to counterbalance the external variation. To do so, let's consider a reaction taking place at a certain energy ϵ: because electrons can transit (without loss of energy) only among states with the same energy, only the electrons with the right energy will take part in the reaction. The reaction dynamic will hence, at first order, be a linear function of the available electronic states. The mean number of electrons with a certain energy in a system at electrochemical potential $\tilde{\mu}_0$ is expressed by the Fermi-Dirac distribution:

$$< n >= \frac{1}{e^{(\epsilon-\tilde{\mu}_0)/kT}+1} \approx e^{(\tilde{\mu}_0-\epsilon)/kT} = e^{-\epsilon/kT}e^{\tilde{\mu}_0/kT} \tag{3.67}$$

The equilibrium electrochemical rate will be proportional to the number of available electrons at the right energy level times a constant, which expresses the probability for an electron to actually jump from one state to the other. In fact, the first term, which is proportional to the energy at which the reaction takes place, is the Arrhenius equation: the higher the energy, the

fewer the available states.
When the electrochemical potential is varied around the equilibrium point, we assume all quantities are fixed and the increase in the number of jumps per second is uniquely proportional to the increase in available electronic states ($k_c \propto \frac{\partial <n>}{\partial \tilde{\mu}}$). In particular, if $k_{c0} = k_c(\tilde{\mu}_{c0})$ is the cathodic rate constant at equilibrium, the new rate constant under a perturbation of the electrochemical potential can be expressed as:

$$k_c(\tilde{\mu}_c) = Ae^{-\epsilon/R_gT}e^{\tilde{\mu}_c/R_gT} = Ae^{-\epsilon/R_gT}e^{(\tilde{\mu}_c-\tilde{\mu}_{c0}+\tilde{\mu}_{c0})/R_gT} = k_{c0}e^{(\tilde{\mu}_c-\tilde{\mu}_{c0})/R_gT} \tag{3.68}$$

The Boltzmann constant k is substituted by the gas constant $R_g = N_a k$, where N_a is the Avogadro's number, in order to express chemical potential in J mol^{-1}, as in the thermodynamic formulation of ion diffusion. The same reasoning applies to the anodic rate constant, and the final expression of the current density under a perturbation of the electrochemical potential is:

$$j = c_a(0)k_{a0}Fe^{(\tilde{\mu}_a-\tilde{\mu}_{a0})/R_gT} - c_c(0)k_{c0}Fe^{(\tilde{\mu}_c-\tilde{\mu}_{c0})/R_gT} \tag{3.69}$$

Perturbation by means of an external electric field

So far, we have managed to describe the effect of a variation in the electrochemical potential on the anodic and cathodic currents around the equilibrium point. In practice, the electrochemical potential can be varied by applying an external electric field. According to the definition of the electrochemical potential, the variation around the equilibrium point $\phi_{ext} = 0$ is:

$$\tilde{\mu} - \tilde{\mu}_0 = \eta F \tag{3.70}$$

η is called over-potential and is the actual extra potential that displaces the reaction. When the cell potential is measured at equilibrium, the OCV (defined in the first chapter) can be expressed as:

$$OCV = -\frac{1}{F}\tilde{\mu}_0 = -\frac{1}{F}\mu_0 - \phi_0 \tag{3.71}$$

Where μ_0 is the chemical potential at equilibrium and ϕ_0 is the equilibrium electric field linked to the built-in charge accumulation. An important point to be noted, is that the potential to be inserted in the definition of the chemical potential, has the opposite sign with respect to the measured voltage drop between the anode and the cathode. This is relevant when coupling this equation with the diffusion equation for electrolyte. In fact, if the potential is calculated with respect to the anode-cathode system of reference, before being inserted in equation 3.52 the sign must be reversed. More correctly, here we are referring to the half-cell OCV, while the total OCV presented in the first chapter was considered with respect to the anode-cathode potential difference (the electrolyte contribution appears in both, and the final value does not depend on it).
When an external potential V_ext is applied, the equilibrium is forced to move to a new position:

$$V_{ext} = -\frac{1}{F}\tilde{\mu} = -\frac{1}{F}\mu_0 - F\phi_{ext} \tag{3.72}$$

Where the applied potential is assumed to be small and the chemical potential to stay constant. The variation is completely absorbed by the built-in field at the interface, and the over-potential is:

$$\eta = V_{ext} - OCV = \phi_0 - \phi_{ext} \tag{3.73}$$

Before integrating the overpotential in equation 3.69 two considerations are necessary. The first concerns the effect on the two electron populations. As a matter of fact, the effect of the electric

field should revert from the electrode to the electrolyte. When the electrode's electrochemical potential increases, from the perspective of the electrolyte, it is equivalent to a decrease in potential. The second consideration concerns the link between the external potential and the actual potential perceived by the electrons. In fact, the ohmic drop will be divided between the two. In general, we may expect the potential to be equally split between the metal electrons and the electrolyte electrons, which is often the case in practice. More generally, an extra parameter $0 < \alpha < 1$ can be introduced to model an eventual unbalance and to split unevenly the total η. Summing up, the variation of the electrochemical potential with respect to the external field is:

$$\tilde{\mu}_a - \tilde{\mu}_{a0} = \alpha(\phi_0 - \phi_{ext})F = \alpha\eta F$$
$$\tilde{\mu}_c - \tilde{\mu}_{c0} = (1-\alpha)(\phi_{ext} - \phi_0)F = -(1-\alpha)\eta F$$

The expression for the current flowing across the electrode interface under an external potential is:

$$j = c_a(0)k_{a0}Fe^{\alpha\eta F/R_gT} - c_c(0)k_{c0}Fe^{-(1-\alpha)\eta F/R_gT} \tag{3.74}$$

This equation is referred to as the **Butler-Volmer** equation. It must be noted that the equilibrium condition implies that all quantities remain constant. Equation 3.74 is valid as long as the extra current does not result in any extra accumulation of electrons or ions at the interface: the current must be immediately compensated both in the electrolyte and in the electrode. This is one of the main points to be addressed when transposing the equation to the solid domain, and in particular for the intercalation electrode, due to the variation of the lithium concentration during charge and discharge.

2.2 Butler-Volmer for intercalation and alloying electrodes

The equation derived in the first section is valid, at equilibrium, only for a liquid electrolyte and an inert metal electrode. In the present section, the equation will be modified in order to account for the intercalation mechanism and the variation of the electrochemical potential of the electrode during lithium insertion. By chance, the two sets of equations are quite similar, and even if the liquid formulation is used for intercalating electrodes, only a minor difference will result in the general behavior. Notwithstanding, the effect of critical phenomena associated with phase transition cannot be properly modeled without the solid-state formulation.

Equilibrium for ion-transfer reaction

The difference between electron-transfer and ion-transfer reactions was briefly introduced in the first chapter. The actual movement of ions in order to accomplish plating, alloying or intercalation makes the actual picture of an electrochemical cell radically different from the standard derivation of the Butler-Volmer equation. As a matter of fact, as far as the ion motion is concerned, the electron, being much faster, can be completely disregarded. It is instead the dynamics of ions that is the limiting step of the reaction, and the equation must be restated from the beginning, starting from the energy distribution of the latter.
The transfer can take place as soon as the ions are close enough to the surface. Then, for the transfer to be possible, the ions require enough energy to break free from the electrode crystal or the electrolyte coordination cell (both in liquid and solid electrolytes). Then, an available site on the electrode or in the electrolyte (only in the solid case) is needed for the ions to cross the interface. The picture is far more complex than in the previous case, and three ingredients are

necessary for a successful transit: an ion near the surface, enough energy to break the old chemical bonding, and a free site at the arrival. On the last point, in the case of liquid electrolytes, the situation differs from the solid ones. We already pointed out how the number of "available" (non-interacting) sites in liquid electrolyte is basically infinity (above the solubility limit of the salt), while the ion-ion interaction in solids cannot be easily disregarded. That means that while in the former case the number of available sites in the electrolyte is of no importance, it should be considered in the latter.
Starting from the equilibrium condition of equation 3.63, it is possible to rewrite the anodic and cathodic current density dependency with respect to both the reactant at the interface and the availability of site at the electrode and electrolyte interface:

$$j_a = c_2 \left(1 - \frac{c_1}{c_{1max}}\right) k_a F \tag{3.75}$$

$$j_c = -c_1 \left(1 - \frac{c_2}{c_{2max}}\right) k_c F \tag{3.76}$$

Being c_1 the lithium concentration at the electrode interface and c_2 at the electrolyte interface and c_{1max} and c_{2max} the available site concentration at the cathode and the electrolyte. The equation can be adapted for liquid electrolyte by imposing $\frac{c_2}{c_{2max}} \sim 0$ or for plating of lithium on lithium by $c_1 = 1$ and $\frac{c_1}{c_{1max}} \sim 0$. The direct inclusion of the arrival site dependency will prevent the reaction from continuing even if no sites are available at the interface. This is the counterpart of the infinite accumulation problem during diffusion, solved by means of the entropy term in equation 3.58. In both cases, the non-interaction hypothesis for ions is still valid.

Equilibrium perturbation

The derivation of the perturbation current obtained previously is no longer valid for the ion-transfer reaction. The new problem concerns the study of the ions' energy distribution, which is needed to overcome the energy barrier at the electrode/electrolyte interface. Even if the correct statistic to be used is now the Bose-Einstein, under the approximation of $\frac{\epsilon - \tilde{\mu}}{kT} \gg 1$ the density of state at energy ϵ is the same as for electrons:

$$< n >= \frac{1}{e^{(\epsilon - \tilde{\mu}_0)/kT} - 1} \approx e^{(\tilde{\mu}_0 - \epsilon)/kT} = e^{-\epsilon/kT} e^{\tilde{\mu}_0/kT} \tag{3.77}$$

Which is nothing but the Boltzmann distribution. Now, in the case of ion transfer, we are supposed to consider the whole spectrum of energy and not only the exact amount needed to overcome the energy barrier. Actually, assuming a classical picture, the reaction-concerned states ($< N >_r$) are only the ones with an energy *higher* than the energy barrier E_b, hence:

$$< N >_r = \int_{E_b}^{\infty} d\epsilon \, \frac{1}{e^{(\epsilon - \tilde{\mu}_0)/kT} - 1} \approx e^{\tilde{\mu}_0/kT} \int_{E_b}^{\infty} d\epsilon \, e^{-\epsilon/kT} = C e^{\tilde{\mu}_0/kT} e^{-E_b/kT} \tag{3.78}$$

Where C is the integration constant and the approximation condition is $(E_b - \mu) >> kT$. Sometimes the same argument is used in the case of electrons, but electron tunneling should be included as well: electrons with lower energy also have a chance to cross the barrier. I preferred to keep the electron discussion as simple as possible because, in the end, I will not use it in my model. My main point is, in fact, to highlight that the similarity between the two processes comes from the same approximation, which reduces the electron and ion statistics to an identical formulation. Anyway, the two are not bound to be identical.
It is now enough to differentiate the number of reaction states to obtain the variation under

equilibrium perturbation ($k_c \propto \frac{\partial <N>_r}{\partial \tilde{\mu}}$) and following the same steps from equation 3.68 the expression for the current density is obtained:

$$j = j_a - j_c = c_2 \left(1 - \frac{c_1}{c_{1max}}\right) k_{a0} F e^{\alpha \eta F / R_g T} - c_1 \left(1 - \frac{c_2}{c_{2max}}\right) k_{c0} F e^{-(1-\alpha)\eta F / R_g T} \tag{3.79}$$

The Boltzmann constant is substituted with the gas constant as before. The inclusion of the electric field is obtained without any modification with respect to the classical formulation. Notwithstanding, equation 3.79 is still not enough for a real intercalation electrode, as the evolution of the built-in potential ϕ_0 as a function of the intercalation state is missing.

Electrode potential variation with intercalation fraction

Butler-Volmer equation was derived around an equilibrium point, assuming all interface concentrations are constant even after the application of the external electric field. As a matter of fact, the equilibrium position is accounted for by the steady-state reaction rates k_{a0} and k_{c0}. If the equilibrium position varies (e.g. large variation of the interface concentration), the two constants should vary accordingly. Even if this is not the case (experimentally), the built-in potential will change, and the effective over-potential η may change in time. While the effect of the reaction rate should be evaluated case by case in order to decide if it has to be included or not, the variation of the built-in potential has an exponential effect on the current and cannot be disregarded. By recalling the definition of the over-potential, in the case of a variable built-in field, we have:

$$\eta(c) = -\frac{1}{F}(\tilde{\mu} - \tilde{\mu}_0(c)) = \phi_0(c) - \phi_{ext} = V_{ext} - OCV(c) \tag{3.80}$$

Experimentally, if the external potential is kept constant at V_{ext} the over-potential is expected to vary with the same shape as $OCV(c)$. For example, If a plateau is present in the electrochemical potential, a current plateau will be measured during the intercalation of ions as well. In the liquid framework, the variation of the potential with respect to the local quantity of ions is sometimes accounted for by means of the Nernst equation, which is nothing but the expression of the chemical potential of a dilute, non-interacting system used to develop the classical formulation :

$$OCV = OCV_0 + \frac{RT}{nF} \ln\left(\frac{c_c(\infty)}{c_a(\infty)}\right) \tag{3.81}$$

Where OCV_0 is the electrochemical potential at standard conditions [38]. Of course, this expression makes no sense for an intercalating electrode, but in the review section we will have the possibility to see how it is sometimes adapted for the solid-state formulation. Including equation 3.80 the general expression for an intercalation electrode and a solid-electrolyte interface current density becomes:

$$j = c_2 \left(1 - \frac{c_1}{c_{1max}}\right) k_{a0} F e^{\alpha(V_{ext} - OCV(c))F / R_g T} - c_1 \left(1 - \frac{c_2}{c_{2max}}\right) k_{c0} F e^{-(1-\alpha)(V_{ext} - OCV(c))F / R_g T} \tag{3.82}$$

When describing a full cell, each electrode current needs to be described by the equation 3.82. The total current in the cell will be imposed by a full balance between the two interfaces and the dynamics of lithium inside the electrolyte. In particular, at equilibrium, the current density crossing the first electrode (j_1), the flux of ions in the electrolyte (J_{ely}), and the current density crossing the second electrode (j_2) will balance:

$$j_1 = J_{ely} F = j_2 \tag{3.83}$$

This is the same current that will flow on the external circuit, charging or discharging the cell. The complex balance is determined by the ions' diffusion (in the electrode and electrolyte) and interface reaction rate. In particular, the total imposed V_{ext} will be divided between the three currents. In figure 3.3, a schematic of the voltage drop across the three domains is shown. The electrochemical potential of the two electrodes ($\tilde{\mu}_1$ and $\tilde{\mu}_2$) and inside the electrolyte ($\tilde{\mu}_e$) is traced as well. The electric field increase at the two interfaces has to be explicitly calculated to determine the three currents [40]. In particular, the two effective overpotentials to be used in the Butler-Volmer equation are:

$$\eta_1 = \phi_{01} - \phi_{ext1}$$
$$\eta_2 = \phi_{02} - \phi_{ext2}$$

While the electric field driving ion diffusion in the bulk electrolyte is:

$$E = -\nabla\phi_{ext3} \tag{3.84}$$

The main effect on equation 3.82 is the decrease of the actual over-potential. The ohmic drop in each zone is determined according to the equilibrium condition 3.83 and the ion concentration at the two interfaces. Depending on the limiting factor, the actually measured dependency of the full cell current density with respect to the applied external potential may follow the Butler-Volmer equation ($j \propto exp(V)$) or the drift-diffusion equation ($j \propto V$). In the latter case, the overall reaction is limited by the drift in the electrolyte, and the majority of the voltage is absorbed by it: $\phi_{ext3} \gg \eta_1, \eta_2$. In the opposite scenario, the reaction at one of the interfaces is the bottleneck, and the external voltage is concentrated on the electrode $\eta_1, \eta_2 \gg \phi_{ext3}$. Those are, of course, extreme cases when the two dynamics largely differ.
Before eventually assembling the complete model, I will make a small digression to review the literature about interface reactions for thin-film solid-state batteries.

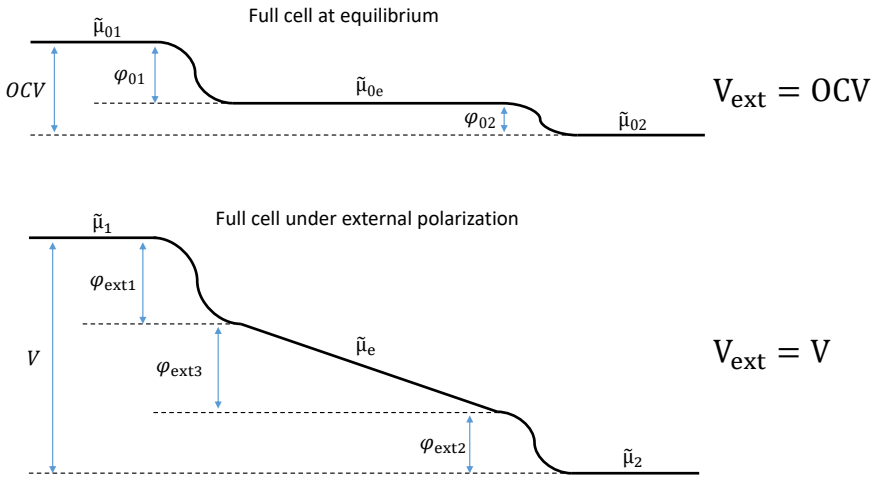

Figure 3.3: Distribution of the external polarisation across the two interfaces and the bulk electrolyte in a full cell.

2.3 Review of electrode-electrolyte interface equation

Three main points are of interest when reviewing the interface modeling for intercalating electrodes and solid electrolytes. The first is how the availability of arrival sites is treated; the second

is how the over-potential is calculated; and the third is how the variation of the electrode potential with intercalation fraction is included. These three points represent the discrepancies in the solid-solid formulation with respect to the classical formulation. Examining some publications on the topic, it will be clear how the three exhibit different levels of general agreement. In particular, only the second one has a broadly accepted formulation, while the first is usually disregarded and the third is too often superficially treated. In the following, I will review the main variations with respect to the formulation proposed so far.

Inclusion of available site on the electrode

The availability of arrival sites is a common aspect of both solid and liquid formulations, as long as an intercalation electrode is present. Additionally, the solid electrolyte reaction equation may require the same term to be included to account for the available sites in the electrolyte. The inclusion of a limit on the available site in the electrolyte diffusion equation by means of the electrochemical potential, as proposed by Landstorfer et al. [40] is an intermediate solution often encountered. The electrolyte current density will be:

$$j_e = -\frac{M}{F}\left(\frac{RT}{1-c_2} - 2\alpha c_2\right)\nabla c_2 - M c_2 \nabla\phi \tag{3.85}$$

Where alpha accounts for the solubility limit of ions in the electrolyte. Even if the final effect is to limit excessive accumulation at the interface, the whole burden is on the electrolyte's chemical potential. As a result, a higher accumulation, and hence a higher electric field, is expected to develop at the interface to limit the reaction with respect to the complete formulation. If the vacancy concentration also appears in the Butler-Volmer equation, the accumulation is limited by both the diffusion and the interface dynamics, resulting in a less extreme interface concentration.
This is anyway a best-case scenario, where at least the solubility limit problem is taken into consideration. Quite often the arrival concentration is not even discussed, and the classical formulation is used without modification [10–12, 17, 28, 29]. A major problem in those formulations is the use of the "average concentration" of lithium inside the electrode in the reaction rate constant expression. As I will comment more in depth when addressing the use of the Nernst equation, the average concentration is valid exclusively in the case of the classical formulation and should never be used for intercalating electrodes. It may be used for the electrolyte potential in a dilute condition; hence, it does not pose a particular problem in a liquid configuration. Of course, when dealing with solid electrolytes, it is better not to assume a dilute condition but instead use the full electrochemical potential, as in 3.85, and let the solver decide.
As a final remark, the simplification of the electrochemical potential was an interesting *modus operandi* of the last century in order to reduce the complexity of equations and be able either to solve them analytically or to reduce the calculation time. Nowadays, the solution of a complete electrochemical potential does not require much more time than the solution of simplified forms, thanks to the increased performance of computers. It is no longer necessary to impose too strict hypotheses, and the mentality should drift in favor of more complete descriptions instead of analytically solvable ones.

Calculation of the interface potential

Concerning the actual over-potential η to be used in the equation, most of the literature agrees on the formula [17, 40–44]

$$\eta = \phi_s - \phi_e - U(c) \tag{3.86}$$

Where $U(c) = OCV(c)$ is the equilibrium potential at electrode intercalation fraction c, while ϕ_s and ϕ_e are the extra electric fields in the electrode and in the electrolyte that develop under cell polarization. The parameter α is then added to unevenly divide the total drop on the anodic and cathodic currents. At the electrode/electrolyte interface, the model accounts for both the totality of the electrons on the metal (as a delta distribution) and a part of the ions' accumulation in the electrolyte. The potential would then be discontinuous. In reality, there exists a thin, empty layer that spatially separates the electrons on the metal from the ions in solution. It is usually called **electrical double layer** and is characterized by a linear drop in the electric potential. Once the double layer is crossed, the electric potential varies according to the ions' distribution in the electrolyte. The size of the empty zone is linked to the α parameter, and it is actually a function of the equilibrium point. In fact, the double layer structure physically resembles the diode capacity [8] which is known to vary with respect to the charge density at the interface. Intuitively, if a larger electron density accumulates on the electrode, the first row of ions in the electrolyte will be attracted closer to the interface. Accumulation mainly depends on the system's characteristics and on the current passing through it. If the current is low enough, the double layer thickness and the α parameter can be considered constants.

Use of Nernst equation for intercalation electrodes

The Nernst equation (3.81), introduced at the end of the previous section, was used in the classic formulation to link the electrochemical potential measured under certain standard conditions (temperature, pressure, electrolyte concentration, etc.) to the experimentally measured potential under different equilibrium conditions. It was also used to account for the accumulation of ions at the electrode interface. The Nernst equation links the bulk concentration, which is assumed to be equal to the equilibrium concentration, to the standard potential. That is to say, if the system is relaxed, the equilibrium concentration of the different reducing and oxidizing species will equal the concentration far from the interfaces. For intercalation electrodes, the equation is usually modified by taking the average value of the whole domain instead. This is a more correct formulation when the domain is not infinite with respect to the accumulation zone. Actually, this is less incorrect but still absurd. In fact, the potential of the electrode does not vary the same way as that of a dilute electrolyte. Once again, the Nernst equation can be used for the solid electrolyte under the right hypothesis, but will never be valid for the electrode. In fact, the potential of electrodes can exhibit both fast variations and large plateaus, and taking the average concentration to estimate the equilibrium potential without explicit use of the $OCV(c)$ does not make any sense. Most of the authors [10, 17, 19, 45] probably just use the already developed Butler-Volmer equation (see [38]), where the Nernst equation has already been embedded without considering the particular case under which the formula was developed:

$$j = j_0 \left(\frac{c_R(0)}{c_R(\infty)} e^{\alpha \eta F / R_g T} - \frac{c_O(0)}{c_O(\infty)} e^{-(1-\alpha)\eta F / R_g T} \right) \tag{3.87}$$

Or even worse, the simplified equation where the surface concentration is assumed to be equal to the concentration in the bulk (low current approximation):

$$j = j_0' \left(e^{\alpha \eta F / R_g T} - e^{-(1-\alpha)\eta F / R_g T} \right) \tag{3.88}$$

Where j_0 is called exchange current density, because at zero over-potential it is equal to the anodic and cathodic current being "exchanged" across the interface.

3. PDE model and parameters extraction

3.1 Model Implementation

Before starting with the model specification, in Figure 3.4 the geometry and domain division of the device under study is reported. The x-axis zero is set at the current collector/electrode interface. The first domain encountered is the $LiCoO_2$ cathode, which is considered a perfect electron conductor. Both the current and potential applied at the current collector are directly transposed at the next interface, while the domain is modeled to account for the ion diffusion. Ion flux is purely diffusive in this zone because the electric potential is constant by virtue of metallic conduction. The intercalation fraction x_1 for $Li_{x1}CoO_2$ is linked to the lithium concentration c_1 by the maximum lithium concentration in the cathode $x_1 = \frac{c_1}{c_{1max}}$. Follows the electrolyte domain, where both drift and diffusion are modeled. In this domain, the electric potential must be calculated at each x point by means of Poisson's equation. The two interfaces between the electrolyte and the two electrodes account for both the electron accumulation on the metal interface and the redox current by means of the modified Butler-Volmer equation. The cell is completed by the anode. Even if the cell to be modeled is anode-free, after a few seconds of charge, the lithium metal anode is formed, and the configuration reduces to a lithium-metal battery. In the present model, I will consider a metallic lithium anode and not an anode-free stack. In fact after the first nucleation the two configurations are identical. Metal plating is not limited by lithium diffusion in the anode but mainly by mechanical constraints on the lithium expansion. The mechanical effects are of second order in assessing the static and dynamic performance and are disregarded. If cycling is addressed, this simplification is no longer valid. The bulk lithium anode is hence not modeled; only the interface reaction has to be accounted for. The anode-current collector interface is fixed as a zero-volt reference for the electric potential calculation. The electric field drop on the anode-electrolyte double layer must be accounted for by calculating the charge accumulation at the lithium electrode interface.

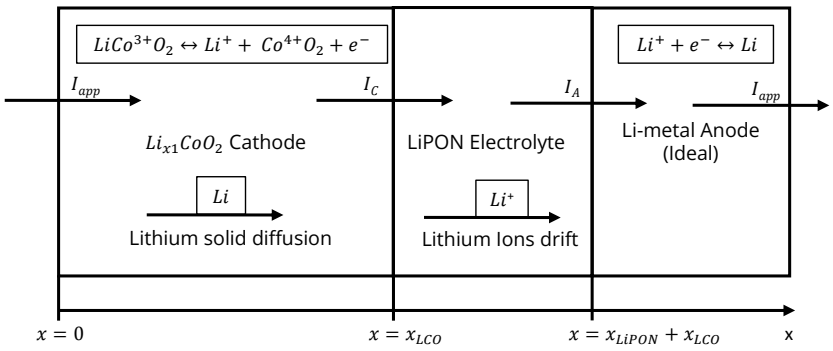

Figure 3.4: Definition of the geometry and domains for 1D simulation of thin-film solid-state battery.

Equation set

In the cathode domain ($0 < x < x_{LCO}$), the variable of interest is the lithium concentration c_2 measured in mol m^{-3} The diffusion of ions is modeled by the pure diffusion equation:

$$J_1 = -c_1(1 - x_1)\frac{D_1}{RT}\frac{\partial \mu_1}{\partial x} \tag{3.89}$$

Where $D_1(1 - x_1)$ is the self-diffusion coefficient and μ_1 the chemical potential of lithium. At the current collector interface, the blocking electrode Neumann boundary condition has to be imposed to prevent further ion diffusion:

$$J_1|_{x=0} = 0 \tag{3.90}$$

On the other side, the situation is a bit more complex. Here two fluxes meet: J_1 from the cathode and J_2 from the electrolyte. The flux of ions allowed to cross the interface J_{12} is fixed by another Neumann boundary condition, equal to the reaction current determined by the Butler-Volmer equation;

$$j_{12} = J_1|_{x=x_{LCO}}F = -J_2|_{x=x_{LCO}}F \tag{3.91}$$

$$j_{12} = c_1\left(1 - \frac{c_2}{c_{2max}}\right)k_{c01}Fe^{-(1-\alpha_1)\eta_1 F/R_g T} - c_2\left(1 - \frac{c_1}{c_{1max}}\right)k_{a01}Fe^{\alpha_1\eta_1 F/R_g T} \tag{3.92}$$

Where the convention is a positive sign for the current entering the cathode during charge (oxidation of the cathode) to be coherent with the experimental data. Before jumping into the next domain, a last boundary condition must be imposed on the electric field. The electric potential drop between the electrode and the electrolyte is fixed by the surface density of electrons (σ_{12}) according to the Neumann boundary condition:

$$\left.\frac{\partial \phi}{\partial x}\right|_{x=x_{LCO}} = -\frac{\sigma_{12}}{\epsilon_0\epsilon_r} \tag{3.93}$$

The surface charge density on the electrode can be calculated from the externally imposed current density j_{ext} as:

$$\sigma_{12}(t) = \int_0^t dt\,(j_{ext} - j_{12}) \tag{3.94}$$

The latter equation just states that the current entering the cell from the outside is either transformed at the electrode/electrolyte interface into ions or accumulated in the form of a point charge on the electrode surface. The accumulation is positive when the external current is higher than the reaction current, and vice versa. The accumulation is then converted into an overpotential by means of the following equation:

$$\eta_1 = -\frac{\sigma_{12}A_{elec}}{C_{dl12}} \tag{3.95}$$

Where A_{elec} is the electrode interface and C_{dl12} the capacitance associated with the double layer at the cathode interface according to the formula:

$$C_{dl12} = \epsilon_0\epsilon_r\frac{A_{elec}}{d_{dl12}} \tag{3.96}$$

Where d_{dl12} is the double layer thickness at the cathode interface and ϵ_r the high-frequency relative permittivity of LiPON. If the external current is higher than the reaction current j_{12} a positive accumulation piles up on the electrode and a negative overpotential is established. According to equation 3.92 cathodic current increases and equilibrium is reached when $j_{ext} = j_{12}$ and the

charge accumulation stops.
Switching to the electrolyte domain, the new quantity of interest is the ion concentration c_2. Diffusion is controlled by the equation:

$$J_2 = c_2(1-x_2)\frac{D}{kT}\frac{\partial \tilde{\mu_2}}{\partial x} = c_2(1-x_2)\frac{D}{kT}\frac{\partial}{\partial x}\left(\mu_2 - zF\phi\right) \tag{3.97}$$

The sign of the electric potential ϕ is inverted as anticipated in the previous section because the cathode-anode reference is adopted for the solution of the electric potential (see boundary condition for ϕ below). The chemical potential of lithium in LiPON can be expressed in terms of relative concentration $x_2 = \frac{c_2}{c_{2max}}$:

$$\mu_2 = E_{02} + kTN_a \ln\left(\frac{x_2}{1-x_2}\right) \tag{3.98}$$

The last boundary condition at the electrolyte/anode interface equates the electrolyte flux to the reaction current density j_{23}:

$$J_2|_{x=x_{LCO}}F = j_{23} = c_2 k_{a02} F e^{\alpha_2\eta_2 F/R_gT} - \left(1-\frac{c_2}{c_{2max}}\right)k_{c02}Fe^{-(1-\alpha_2)\eta_2F/R_gT} \tag{3.99}$$

Where the current is positive when the ions are reduced from the electrolyte and plated onto the anode. The ions' concentration at the electrode does not impact the dynamic of the reaction, as already pointed out.
The electric field must be computed as well in the electrolyte domain. In particular, the Poisson equation is used, starting from the charge accumulation with respect to the equilibrium concentration c_{2eq}:

$$-\frac{\partial^2\phi}{\partial x^2} = \frac{\rho_2}{\epsilon_0\epsilon_r} = \frac{F(c_2 - c_{2eq})}{\epsilon_0\epsilon_r} \tag{3.100}$$

At the right boundary, the electric potential is subject to a double Cauchy boundary condition:

$$\begin{aligned}\phi|_{x=x_{LCO}+x_{LiPON}} &= 0\\ \left.\frac{\partial\phi}{\partial x}\right|_{x=x_{LCO}+x_{LiPON}} &= -\frac{\sigma_{23}}{\epsilon_0\epsilon_r}\end{aligned}$$

Where the charge accumulated on the anode is obtained in the same way as for the cathode:

$$\sigma_{23}(t) = \int_0^t dt\,(j_{23} - j_{ext}) \tag{3.101}$$

and the overpotential is calculated as:

$$\eta_2 = -\frac{\sigma_{23}A_{elec}}{C_{dl23}} = -\frac{\sigma_{23}d_{dl23}}{\epsilon_0\epsilon_r} \tag{3.102}$$

In this case, the accumulation is positive if the reaction current (positive) is higher than the external current (positive). Coherently, the overpotential and the reaction current decrease until equilibrium is reached. This way, the electric path is closed, and the cell description is completed. As a closing remark, it should be noted how this formulation is implemented in terms of an imposed external current. That means that constant current simulation is the natural charge-discharge method. In order to be able to impose a constant voltage operation, an extra equation is included. In particular, the voltage control can be simulated by means of a voltage-controlled current source: the external controller increases the input current until the voltage setpoint is reached. The simplest integral form for such a control current is:

$$I_{ext} = \int_0^t dt\,\frac{\phi_{ext} - \phi|_{x=x_{LCO}}}{R_s} \tag{3.103}$$

Where R_s is a constant (measured in Ω s) used to tune the frequency response of the controller in order to obtain a stable simulation. The higher the R_s the stronger the controller's response to the external input. This parameter is of particular interest when high-frequency simulations are performed, and the frequency response of the controller may mask that of the system if it is too slow. In the case of charge-discharge simulation, a value around $1 \times 10^3\,\Omega$ s is enough to ensure a response in the order of a few seconds.

Weak form and COMSOL implementation

To reproduce the partial differential equation model so far defined in COMSOL Multiphysics and solve it, it has to be converted to an alternative form that is directly compatible with the particular algorithm sued: the finite element methods [46]. The new formulation, called *weak form*, is used mainly to reduce the derivation order of the equation by means of a mathematical device called *the test function*: $test(x)$. I will not delve into the details of the weak formulation but just quickly report the correct form of each of the equations from the preceding section. This new formulation is not as intuitive to analyze as the integral one, and I preferred to report the equation set in both forms.
The two diffusion equations in weak form read:

$$0 = \int_{\Omega} \partial S \left(test(c_i) \frac{\partial c_i}{\partial t} - test \left(\frac{\partial c_i}{\partial x} \right) c_i (1 - x_i) \frac{D_i}{kT} \frac{\partial \tilde{\mu}_i}{\partial x} \right) \tag{3.104}$$

Where $i = 1, 2$ for cathode and anode domains, respectively. Poisson's equation is reduced by one derivation order by the same means and is implemented according to:

$$0 = \int_{\Omega} \partial S \left(test \left(\frac{\partial \phi}{\partial x} \right) \frac{\partial \phi}{\partial x} - test(\phi) \frac{\rho_2}{\epsilon_0 \epsilon_r} \right) \tag{3.105}$$

The equations are then inserted into COMSOL by means of the **Weak Form PDE** interface. The boundary condition can be directly specified without any modification with respect to the standard form of the previous section.
The derivative of the electrochemical potential ($\frac{\partial \tilde{\mu}_i}{\partial x}$) of the cathode and electrolyte must be defined as variables associated with the appropriate domain in the **Definition** section of the COMSOL model interface. These quantities are automatically updated for each computational step and are coupled among different physics (ion diffusion, electric field) in order to ensure the self-consistency of the solution. Also, the charge density inside the electrolyte must be manually computed from the same COMSOL panel. If the variables are specified multiple times for each domain, the solver would treat them as different quantities at each time step, and the solution may not converge.

Mesh and solver parameters

The last step for a complete configuration of the solver is the specification of the mesh and other solver parameters. The finite element algorithm computes the solution only for a finite number of specified points in the domain. The mesh refers to the ensemble of such points and takes the shape of a grid over the domain. At each intersection point of the grid, the solution is computed, and an extrapolation is used to connect the points and obtain the full solution. The interpolating function $test(x)$ has already been introduced. For all simulations, the Lagrange quadratic function was used as the test function. Figure 3.5 reports the mesh as defined for the 1D cell simulation, I reported the equivalent mesh in 2D for clarity, but the actual mesh

resembles the x-axis division on the bottom of the image. The LCO is divided into an equally spaced segment of 200 nm, up to the interface with the electrolyte. At the interface, the last 200 nm step of the mesh is refined with 30 additional points, with distance reducing down to few pm according to the geometric progression:

$$a_n = r a_{n-1} \tag{3.106}$$

Where $r = 100$ is called the growth factor. The electrolyte domain is meshed similarly, with the bulk in constant step and the interfaces following the same geometric progression. The aim of interface mesh refinement is to keep as light as possible the simulation. In fact, the bulk is not expected to show very fast variation, and a coarse mesh is enough for the main feature to be properly simulated. On the other hand, the formation of the electrical double layer and lithium accumulation in general are expected to be local phenomena, with distribution on the scale of a few nm. Increasing the mesh quality only in the strategic zone is the optimum way to obtain a high-quality and fast simulation. Once the mesh is set, the solver can be configured. There

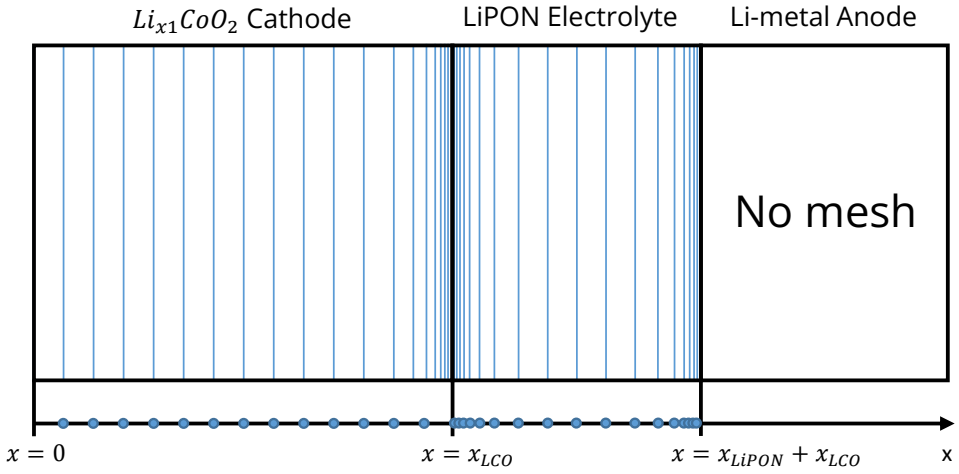

Figure 3.5: Mesh definition for each domain of the 1D simulation.

are three main options at this point concerning the initial equilibrium of the system. In fact, the system, as defined, is not yet at equilibrium; the built-in charge has not formed yet at the electrode/electrolyte interface. The first option is just to ignore the problem and impose a rest time of a few seconds before the cell polarization is applied, for the simulation to reach a steady state. The second option is to first perform a **Stationary** simulation without any polarization applied, and then use the result as the initial value for the lithium and electric field distribution in the **Time Dependent** simulation. A third option, which I adopted, is to perform a time-dependent simulation without polarization and use it as a stationary solution. This is in fact equivalent to the second method, but in this case it is possible to access the temporal evolution during equilibrium formation, which may be useful for debugging. In COMSOL, even if the simulation does not converge, it is still possible to access the results before the last converging point for a transient simulation and try to figure out what went wrong. On the other side, stationary simulations either converge or do not, and no intermediate results are available.
For all simulations presented in this section, I used, as a non-linear solver, the *Constant Newton* method with a minimum of 100 iterations. Relative tolerance was set to 1×10^{-3} and the tolerance factor to 1. In the case of high-frequency simulation, the relative tolerance has been varied

between 1×10^{-4} and 1×10^{-9} until convergence is reached. All parameter splits are realized with the **Parametric Sweep** interface.

3.2 Extraction of Drift-Diffusion parameter for the solid Electrolyte

With the model up and running, the last step before starting a simulation is determining the input physical parameters. Starting with the solid electrolyte, three main parameters are required to define its bulk properties: the density of mobile lithium c_{2eq}, the ion self-diffusion coefficient D_2, and the high-frequency dielectric constant ϵ_r. A priori, the model also requires the maximum lithium concentration in LiPON c_{2max}, to prevent excessive accumulation. Actually, in bulk electrolyte, the ion motion is completely dominated by the drift in the electric field, and the concentration is close to equilibrium. Only at the interfaces does the lithium accumulation vary significantly, and the maximum lithium concentration has an actual impact on the results. This latter parameter is further discussed in the subsection dedicated to interface reaction.
In order to experimentally study the electrolyte properties alone, a reduced electrochemical stack is realized without the LCO cathode, as reported in Figure 3.6a. The stack is composed of an electrolyte in between two metal current collectors, and will be addressed as *MIM* (metal-insulator-metal) device. In order to study the LiPON properties, the small signal transfer function of the system is extracted by means of **Electrochemical Impedance Spectroscopy** (EIS) [38, 47, 48]. This is but an alternative name for frequency response analysis (i.e., Fourier/Laplace transform and Bode plot), as commonly used in linear electric circuits, applied to electrochemical systems. The technique is based on the properties of linear time-invariant (LTI) systems. In particular, the time-domain response of an LTI system is completely described by its transfer function in the frequency domain. The transfer function refers to the current response of the system to an input sinusoidal voltage signal ($V_in = V_0 sin(\omega t)$) (or vice versa). In particular, for an LTI system, the output current takes the form:

$$I_{out} = A_\omega V_0 sin(\omega t + \phi_\omega) \tag{3.107}$$

Where A_ω is the amplitude (in Ω) and ϕ_ω the phase shift, associated with the particular input frequency ω. The response at different frequencies can be represented in two separate graphs, one describing the evolution of the phase shift and the other that of the amplitude with respect to the input frequency (Bode plot). Alternatively, with a loss of information with respect to the frequency, the amplitude and the phase shift are united into a complex number ($Z(\omega) = A_\omega sin(\phi_\omega) + iA_\omega cos(\phi_\omega)$) and represented as a vector in the complex plane (Nyquist plot). In Figure 3.6b and 3.6c, the Bode and Nyquist plot for a $4\,\mu$m LiPON MIM structure at room temperature are reported. On the x-axis the angular frequency is converted into temporal frequency $\omega = 2\pi f$ for a more natural reading. As anticipated, in the Nyquist plot there is a loss of information concerning the frequency associated with each point, and the often adopted solution is to note it on each salient feature of the spectrum. Starting from the EIS data, there are multiple options to extract the electrolyte physical parameters. One possibility is the linearization of the differential equation and the definition of an equivalent linear circuit. The equivalent circuit parameters (resistance, capacitance, etc.) are then fitted with respect to the experimental data, and the physical parameters are extracted afterward. The main drawback of this approach is the linearization procedure, which tends to oversimplify the system. As a result, multiple equivalent circuits can be proposed to represent the same data without much chance of distinguishing between them. A second approach consists of the direct fitting of the physical PDE model. In this case, no additional hypotheses are needed, and the fitting parameters are actual physical quantities. In the following, I will propose the linearization approach,

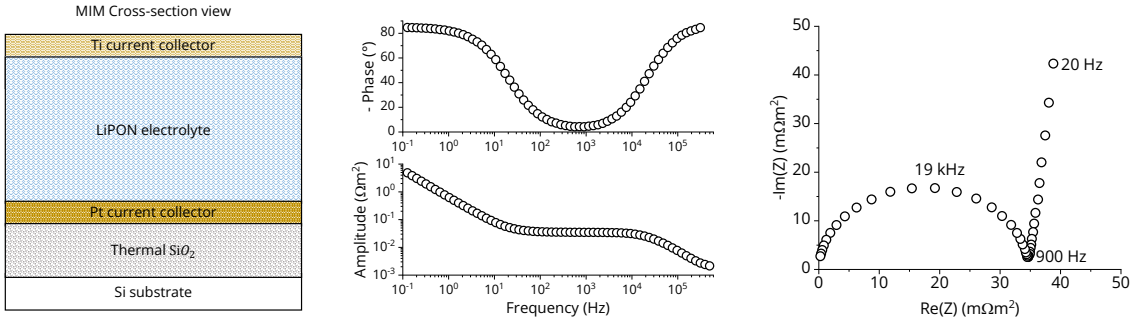

(a) Schematic cross section of a LiPON MIM capactior

(b) Bode plot of the MIM transfer function.

(c) Nyquist plot of the MIM transfer function.

Figure 3.6

which is far less time-consuming than PDE optimization. The present work does not report the theory of PDE linearization, which consists of cumbersome Laplace transforms and does not provide many insights on the topic. The textbook of Girault [38] is an excellent reference for a complete derivation, while the analysis from Archer and Armstrong [49] dedicated to solid-state electrolytes is enough for a quick recap of the main equivalent circuits. It must be noted that the linearization results depend on the equation set; if any modification with respect to the canonical derivation is implemented, it is wise to redo the calculation to make sure the standard equivalent circuits element applies to the particular case.

EIS equivalent model and fitting

The first step to fitting an EIS spectrum is to define an equivalent circuit that is expected to mimic the system's behavior. For example, a semicircle in the Nyquist plane is the response of a parallel RC circuit. Visually, we expect to find this same element in the electrolyte model. The second point is to identify what each element in the circuit represents from a physical point of view and try to link its value with some physical parameters of the system. In the case of a MIM, no reaction is expected at the two interfaces at low voltage. We expect the system to behave, at order zero, as a parallel plate capacitor with a surface equal to the electrodes area A_{elec} and distance equal to the thickness d_{ely} of the electrolyte:

$$C_{geom} = \epsilon_0 \epsilon_r \frac{A_{elec}}{d_{ely}} = \frac{1}{\omega A_\omega} \tag{3.108}$$

C_{geom} is called the geometric capacitance of the electrolyte. ϵ_r is the pure dielectric constant in high frequency: for very fast pulses, the lithium ions are not capable of displacing, and no accumulation is expected at the interfaces; hence, the polarization of the material is limited to the electronic polarization, as in a standard dielectric ($C_{high_f} = C_{geom}$). As the frequency of the input signal is decreased, the ions will be able first to make, on average, only one jump and then to diffuse. We already introduced the concept of the double time constant, associated with solid electrolyte. A first time constant is associated with the jump rate, and a second time constant is associated with the relaxation time of the crystal. If the input signal is faster than the jump rate, on average, the lithium ions will not move during the measurement. If the input is in between the jump rate and the relaxation time, the ions, on average, will make a single successful jump. Eventually, as the frequency decreases below the relaxation time, the ions will diffuse, and long-range motion takes place. It must be noted that it is only in the latter case that the ions actually

"feel" the blocking nature of the electrolyte/electrode interface; for a frequency high enough, the ions will behave like no barrier for diffusion exists. It follows that the electrolyte is expected to resemble a resistor for intermediate frequencies and convert back to a capacitor once the ions start to accumulate at the interfaces. This is exactly what we observe on the Bode plot: $90°$ phase shift and $-45°$ linear drop on the amplitude (capacitor-like) at the border and constant amplitude and $0°$ phase shift (Resistor-like) in the middle. In the final stage, the electric field drop is concentrated at the electrical double layer, and the bulk is at constant potential. That means that the distance to be used in the definition of the equivalent capacitor at low frequency is the size of the double layer and not the thickness of the electrolyte:

$$C_{dl} = \epsilon_0 \epsilon_r \frac{A_{elec}}{d_{dl}} \tag{3.109}$$

The total capacitance at low frequencies is composed of two double-layer capacitors in series:

$$C_{low_f} = \left(\frac{1}{C_{dl1}} + \frac{1}{C_{dl2}} \right)^{-1} = \frac{C_{dl}}{2} \tag{3.110}$$

Where the last equality holds for a symmetric device. The high-frequency capacitance is usually used to determine the dielectric constant of the electrolyte, and the low-frequency one determines the size of the electrical double layer. This is possible if the dielectric constant is assumed to be the same in bulk and at the interface. Of course, it is enough for the interface to be slightly off-stoichiometry with respect to the bulk for the hypothesis not to be true. Moreover, the size of the double layer may vary with the input frequency, which often results in a variation of the double layer capacitance with respect to the frequency.
Concerning the physical meaning of the middle frequency resistor, it is linked with the ion motion under an applied electric field, hence with the self-diffusion coefficient of the electrolyte. In particular, if we assume the ion's motion accounts for the whole measured current and the motion is dominated by drift:

$$j_{out} = F j_{ion} = c_{2eq} F^2 \frac{D_2}{RT} E_{in} \tag{3.111}$$

Where E_{in} is the electric field in the electrolyte generated by the input signal. If the accumulation at the interface is zero and the field is constant inside the electrolyte, it is possible to use the parallel plate capacitor formula linking the field and the potential:

$$j_{out} = c_{2eq} F^2 \frac{D_2}{RT} \frac{V_{in}}{d_{ely}} \tag{3.112}$$

from which the amplitude A_ω:

$$A_\omega = \frac{V_{in}}{j_{out} A_{elec}} = \frac{RT d_{ely}}{A_{elec} F^2 c_{2eq} D_2} = R_{mid_f} = R_{ely} \tag{3.113}$$

In this case, only the product of the two parameters c_{2eq} and D_2 can be determined from the measurement. In fact, the parameter that is often reported in the literature is the conductivity σ_{ion} as defined in equation 3.54. While it is a viable option to fit the three elements (C_{geom}, C_{dl}, R_{ely}) separately, they are often considered altogether in the full equivalent circuit. The base circuital elements can be arranged in various topologies, like the two proposed in Figure 3.7a and 3.7b. It is my personal and unpopular preference to favor the leftmost, in particular in the case of a full cell. I find it more clear in terms of where the ions and electrons reside. If we consider the capacitor to act as a domain boundary (ions and electrons cannot jump from one side to the other), in the first circuit, ions can access the central resistor, and only electrons accumulate on the geometric capacitor. The double-layer capacitor acts, as in the physical picture, as a border

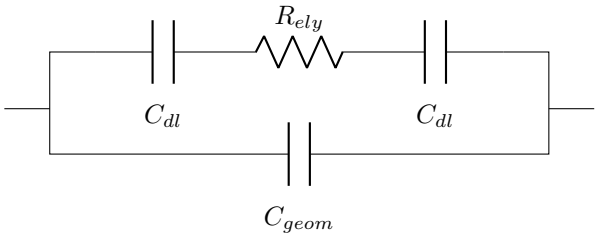

(a) Circuit 1: Unorthodox equivalent circuit for a solid-electrolyte capacitor.

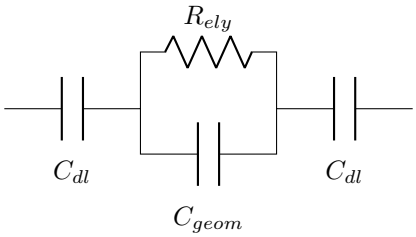

(b) Circuit 2: Orthodox equivalent circuit for a solid-electrolyte capacitor.

Figure 3.7

with ions on one side and electrons on the other. That is not the case with the second topology. The double-layer capacitance is often substituted by a more flexible circuital element called a constant-phase element (CPE). This element is characterized by a fractional derivative in the time domain and an exponential factor $0.5 < n < 1$ in the frequency domain:

$$CPE = \frac{1}{jQ\omega^n} \tag{3.114}$$

This kind of element was introduced to model the effect of surface roughness in liquid and solid electrolytes [49–51], which results in a less than $90°$ phase shift signature. As long as the value of n is not too far from one ($n > 0.85$) it is commonly accepted to consider it an effect of the surface roughness. It must anyway be noted that the shift reported for the β-alumina in [50] refers to micrometer-size roughness. At the same time, the size of the capacitor is the double layer thickness, and picometer size roughness may be enough to modify the capacitor slope.
The two circuits can be easily fitted to experimental results by the least-squares method. In Table 3.1 the extracted values for the various parameters are reported according to the fitting of the two circuits and the manual extraction of each element alone. Two circuits give exactly

Method	C_{geom} (F m^{-2})	ϵ_r	C_{dl} (F m^{-2})	n_{dl}	d_{dl} (nm)	R_{ely} (Ω m^2)	σ_{ion} (S cm^{-1})
Circuit 1	2.3×10^{-4}	104	0.3	0.93	1.5	34.5×10^{-3}	1.16×10^{-6}
Circuit 2	2.3×10^{-4}	104	0.3	0.93	1.5	34.4×10^{-3}	1.16×10^{-6}
Manual	1.84×10^{-4}	83	0.26	1	1.4	34.7×10^{-3}	1.15×10^{-6}

Table 3.1: LiPON physical parameters as extracted with different methods (electrolyte thickness of 4 µm at $24\,°$C).

the same response and are hence not distinguishable. The manual fitting slightly differs because the double-layer capacitor was assumed to be ideal.

c_{2eq} *and* c_{2max} *concentration in* LiPON

In order to complete the description of the solid electrolyte, it is necessary to specify the equilibrium concentration c_{2eq} and the maximum lithium concentration c_{2max}. The first quantity refers to the average number of mobile lithium ions available for diffusion. Inside σ_{ion} extracted in the previous subsection, the information about lithium concentration and self-diffusion is mixed. The zero-order approach is to estimate the free lithium by means of other techniques or use the value reported in the literature. In the end, σ_{ion} is the sole important parameter for bulk

modeling, and both approaches will lead to the same result. It is only at the interface, where the contraction gradient develops, that a difference is expected. Concerning the maximum lithium concentration, without further developing the theory of solid-state electrolytes, the only possibility is to treat it as a model parameter to be optimized for the best fit. In particular, as long as the accumulation at the interface is low, the dilute approximation holds and c_{2max} has no effect on the simulation output. The dilute condition can be verified a posteriori by evaluating the simulated interface accumulation.
I decided to use the literature as a starting point for the mobile lithium concentration c_{2eq}. Once again, no consensus is found, and the values oscillate from $80\,\%$ of the total lithium or 2×10^4 mol m^{-3} [52] down to 4×10^{-2} mol m^{-3} [53], passing by intermediate values of 150 mol m^{-3} [47]. I decided to use a conservative value of 100 mol m^{-3} which results in a self-diffusion coefficient around 10^{-15} m^2 s^{-1} according to the previously extracted ion conductivity. The starting value for the maximum lithium concentration is then set to $c_{2max} = 2c_{2eq}$ to keep the system symmetric as a first approximation. For different values, the lithium preferentially accumulates on the positive or negative electrode, and the two double-layer capacitors differ.

3.3 GITT extraction of lithium diffusion inside cathode

The LCO domain needs to be fed with the different physical parameters as well. The physical characterization of chapter one ensures an almost ideal density of LCO everywhere, and the theoretical maximum lithium concentration can be safely used: $c_{1max} = 5.6 \times 10^4$ mol m^{-3}. To extract the self-diffusion coefficient, the enhancement factor and the variation of the electrochemical potential with respect to the intercalation fraction, the Galvanostatic Intermittent Titration Technique (GITT) [54, 55] was used. In the following, a quick recap of this technique and the results for the device under test are reported.

Theory of GITT

The link between the chemical diffusion coefficient $\tilde{D}$ and the chemical potential μ was expressed in equation 3.46. As a recap, the two are related by means of the chemical enhancement factor θ:

$$\tilde{D}(c) = \theta(c)\frac{D(1-x_c)}{kT} \tag{3.115}$$

$$\theta(c) = \frac{\partial\mu}{\partial \ln c} \tag{3.116}$$

With the self diffusion coefficient variation with intercalation fraction x_c included. Moreover, the equilibrium electrochemical potential $\tilde{\mu}$ is linked to the open circuit potential ($OCV(c)$) by the equation:

$$OCV(c) = -\frac{\tilde{\mu}}{F} \tag{3.117}$$

Where all quantities refer to thermodynamic equilibrium. From this set of equations, there are two possibilities: either to measure the variation of the diffusion coefficient with respect to the concentration and extract the chemical potential, or to measure the OCV variation with respect to the concentration and extract the chemical enhancement factor. The GITT technique permits doing both at the same time, with the possibility of an a posteriori consistency check between the two quantities.
The most important ingredient of the GITT is the short-time solution of the diffusion equation

presented in the first section. In particular, for a constant flux boundary condition, the lithium concentration at the electrode/electrolyte interface reads [1, 54]:

$$c(x=0,t) = c_0 \pm \frac{1}{\sqrt{\tilde{D}}}\left[\frac{2\sqrt{t}}{\sqrt{\pi}} exp\left(-\frac{x^2}{4\tilde{D}t}\right) - x\tilde{D}^{1/2} erfc\left(\frac{x^2}{4Dt}\right)^{1/2}\right] = c_0 \pm \frac{2\sqrt{t}}{\sqrt{\pi\tilde{D}}} \tag{3.118}$$

Where the sign depends on the sign of the imposed flux.
Now, this solution is actually applicable only if $\tilde{D}$ is constant. Restricting the measure to short-time ($t \ll \frac{L^2}{\tilde{D}}$) is not enough to satisfy this hypothesis, and an additional small-signal restriction is necessary. In particular, if the imposed flux and the measurement time are small enough, the chemical diffusion coefficient can be considered constant, and it is possible to write $\tilde{D}$ as:

$$\sqrt{\tilde{D}}(c=c_0) = \frac{2\sqrt{t}}{\sqrt{\pi}(c_0 \pm c(x=0,t))} \tag{3.119}$$

or in differential form for an infinitesimal displacement:

$$\sqrt{\tilde{D}}(c=c_0) = \frac{2}{\sqrt{\pi}}\left(\frac{dc(t)}{d\sqrt{t}}\right)^{-1} \tag{3.120}$$

The main issue with this equation is that we don't have a direct method to measure the lithium concentration at the exchange interface. What is measured is the voltage response of the cell V_{cell} which, at first approximation, can be expressed as:

$$V_{cell}(t) = OCV(t) + R_{int}I_0 \tag{3.121}$$

Where I_0 is the input current and R_{int} the equivalent internal resistance of the cell. The internal resistance can be measured by means of EIS and extracted with an equivalent circuit. The results are then corrected for the ohmic loss, and the OCV is obtained:

$$OCV(t) = V_{cell}(t) - R_{int}I_0 \tag{3.122}$$

If the characteristic variation of the OCV with respect to the intercalation fraction is known, it is possible to invert the equation and estimate the interface concentration as:

$$c(x=0,t) = OCV^{-1}(V_{cell}(t) - R_{int}I_0) \tag{3.123}$$

In the 80s, when the method was developed, the equation was further simplified in order to enable a direct extraction procedure [54, 55]. In particular, by assuming a locally linear behavior of the potential with respect to the interface concentration (which is usually true under the small-signal, short-time hypothesis), the equation 3.120 can be simplified to:

$$\sqrt{\tilde{D}}(c=c_0) \propto \frac{OCV(c_0) \pm OCV(c_1)}{V_{cell}(t=0^+) \pm V_{cell}(t)(t=t_1^-)} \tag{3.124}$$

Where t_1 is the measurement time and c_1 the average lithium concentration at the end of the measurement. The $t = 0^+$ is used to specify that the voltage should be measured after the transient of the applied current in order to account for the ohmic drop. The same for $t = t_1^-$ means the last point is measured before the current is turned off. This way, the term $R_{int}I_0$ is the same in both the initial and the final measured voltage and simplifies.
In order to obtain $OCV(c_0)$ and $OCV(c_1)$ the measurement is structured as follows:

1. The OCV of the battery at equilibrium is measured ($OCV(c_0)$).
2. A short and small pulse of current is applied to the cell, and the $V_{cell}(t)$ is measured

3. The cell is disconnected, and a relaxation time is imposed to reach a new equilibrium.
4. The OCV of the cell at equilibrium is measured ($OCV(c_1)$).
5. Back to step 2.

The main drawback of using equation 3.124 is managing to guarantee the short-time condition. While a pulse is small compared to the total capacity of the cell, which is the same for any concentration value, the time constraint depends on the size of the cell *and* on the chemical diffusion coefficient, which is an unknown quantity. Because $\tilde{D}$ may change by several orders of magnitude, it is difficult to design an experiment that is at the same time efficient and that respects the hypothesis. The most conservative approach is to have an estimation of the minimum expected diffusion coefficient and set the measurement time accordingly, but in some cases this may be smaller than a second, and the data quality will be severely impacted for the point with a higher diffusion coefficient.
Modern times, modern solutions, we should not be afraid to use more complex equations, as long as the computer can solve them at our place. In particular, it is possible to start from a more general solution of the concentration at the interface than equation 3.118. In particular, following the work of McKinnon [9] the general interpolation formula is:

$$c(x=0,t) = c_0 \pm \sqrt{\frac{t\tau}{\tau_0^2}} coth \sqrt{\frac{\tau}{t}} \tag{3.125}$$

Where $t_0 = \frac{Q_0}{I_0}$ is the time to fully deplete or fill the electrode with capacity Q_0, and $\tau = \frac{L^2}{D}$ is the usual diffusion time constant. This equation can be used regardless of the measurement time (as long as the diffusion coefficient is constant). It is to be noted that for $t << \tau$ the short-term solution is recovered. The concentration $c(x=0,t)$ is obtained by inversion of the OCV according to equation 3.123.

Experimental measurement

In order to perform the GITT measurement, a $5\,\mu$m thick LCO was used in order to reduce the relaxation time required for equilibrium to be reached. The measurement was performed at room temperature inside an argon-filled glovebox. The protocol used is the following:

1. The OCV of the battery at equilibrium is measured ($OCV(c_0)$).
2. A $100\,$nA pulse of current is applied for $600\,$s to the cell and the $V_{cell}(t)$ is measured
3. The cell is relaxed for $3\,$h to reach a new equilibrium.
4. The OCV of the cell at equilibrium is measured ($OCV(c_1)$).
5. Back to Step 2.

It should be noted that the application of the current is not particularly short. That is an advantage of using the general-time solution instead of the short-time one. In particular, during each pulse $0.5\,\%$ of the total lithium is displaced. The protocol was applied for both positive and negative pulses.
The obtained raw data consists of the measurement of the OCV (Figure 3.8a) and a series of voltage pulse responses (Figure 3.8b). A small hysteresis is visible between the charge and discharge OCV at high intercalation fractions ($0.1 < x < 0.3$). Moreover, even at $100\,$nA, it is not

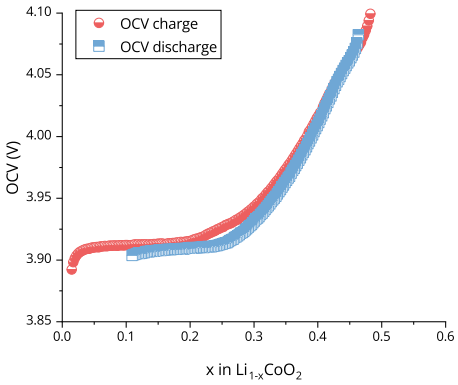

(a) Measured OCV from GITT technique for charging and discharging cell.

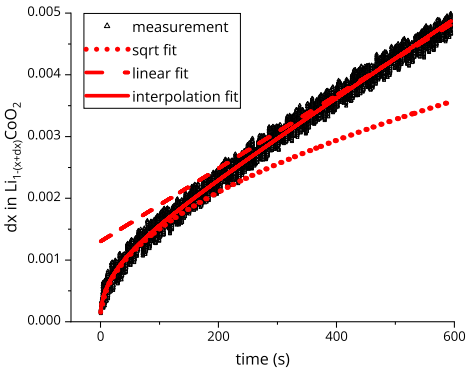

(b) Example of voltage response to current pulse and associated fitting curves.

Figure 3.8

possible to fully intercalate the lithium due to the tiny diffusion coefficient below $x = 0.1$. Concerning the pulse response of Figure 3.8b, the short-time, long-time and interpolation formulas are reported. Up to $100\,\mathrm{s}$ the response follows the short-time solution and is correctly fitted by the square root of time. Then the curve switches to long-time linear behavior. The interpolation formula is capable of following the whole curve.

Extracted diffusion coefficient

Starting from the variation of the interface concentration, it is possible to extract the chemical diffusion coefficient. Three different procedures have been tested on the same dataset: the first is based on the fitting of the short-time solution (3.119) on the first part of the data; the second uses the linearized short-time solution (eq. 3.124) on the first part of the data; and the third consists of fitting the interpolation equation (eq. 3.125) on the entire measure. The results for the three procedures on the discharge dataset are reported in Figure 3.9a. For low concentrations of lithium ($x > 0.3$) the three procedures are in agreement. In this region, the diffusion coefficient is quite high, and all hypotheses are satisfied. At higher lithium concentrations, the linearized equation extraction fails due to the strong interface accumulation: the associated large OCV variation nullifies the linear relationship between charge concentration and OCV. Both the general square root method, when restricted to the first part of the data, and the interpolation equation successfully deal with the low diffusion coefficient zone. In fact, the sole source of problems is incomplete relaxation and a wrong estimation of the OCV, but as long as the OCV is correct, the two methods can be applied.
In Figure 3.9b the extracted values for both charge and discharge are reported. The same hysteresis as in the OCV is visible in the extracted diffusion coefficient. In particular, due to phase transition, in the zone $0.75 < x < 0.95$ it is difficult to ensure a complete and proper relaxation. Anyway, from the point of view of the simulation, these differences are but small details. The most important feature is the large variation from 8×10^{-14} to $1 \times 10^{-16} \mathrm{m^2\,s^{-1}}$ of the diffusion coefficient. In the next section, I will take the time to review the simulation results for different diffusion coefficients and further discuss this point.

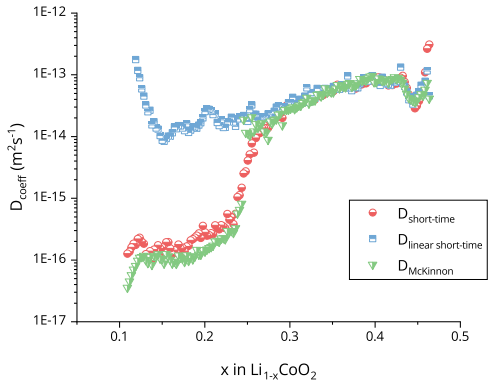

(a) Chemical diffusion coefficient extracted with different methods for discharging cell.

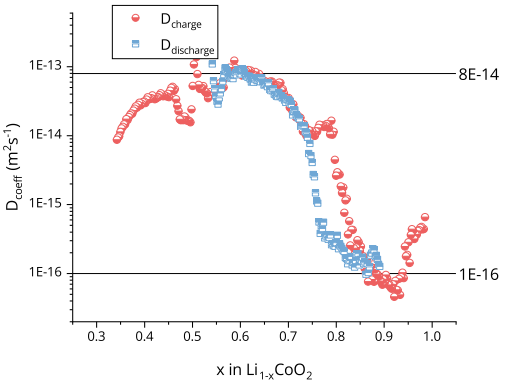

(b) Chemical diffusion coefficient extracted for charging and discharging cell.

Figure 3.9

3.4 Interface reaction parameters

Before commenting the simulation results , the physical description of the interface reaction according to equations 3.92 and 3.99 needs to be tuned for the stack under analysis. In particular, the four rate constants k_{c01}, k_{a01}, k_{c02}, and k_{a02} have to be specified. In order to extract these four parameters, it is possible to use the Tafel curves [38]. In order to apply such a method, two conditions must be met: a three-electrode configuration, to separate the anode and cathode contributions, and a reaction-limited current. None of the two is satisfied by the device under test. The first point can be overcome by simply splitting the total contribution equally between the anode and cathode. The fact that the second is not satisfied implies that only a very small fraction of the ohmic drop happens at the interface, and the major part of the voltage drop is inside the bulk electrolyte (see figure 3.3). Moreover, the current will be entirely fixed by the LiPON conductivity, and the cell will show a linear dependency of the current with respect to the applied potential and vice versa. In order to model such a system, it is possible to set the interface reaction to a high enough value for it to be negligible. As an example, a value around $10^2\,\mathrm{A\,m\,mol^{-1}}$ satisfies such hypothesis. The ratio between each interface couple ($\frac{k_{a01}}{k_{c01}}$) determines the equilibrium accumulation of lithium. Because the built-in potential is already taken into account by the chemical potential, it is possible to set to zero the equilibrium accumulation by imposing $i_c = i_a$ at equilibrium concentration and zero over-potential.

4. Simulation Results for Thick Cathodes

In this last section, I will report the simulation results for a $30\,\mu\mathrm{m}$ thick $LiCoO_2$ cathode and $4\,\mu\mathrm{m}$ thick LiPON cell. In the first part, the lithium distribution inside the cathode during charge and discharge, and the effect of diffusion coefficient variation are discussed. Then the focus is shifted to the electrolyte. First, the lithium profile is discussed for the full cell, and then the effect of the various physical parameters on the electrical double layer of a MIM device is addressed. The choice of studying the EDL on a MIM structure comes from the already mentioned limitation of the full stack. In particular, the dynamics is dominated by the bulk electrolyte, and the interface accumulation is very small. Instead, for a MIM, the whole imposed potential drop appears at the interfaces, and a large accumulation is expected. This way, the effects of the different

parameters are amplified and easy to discuss. The conclusions do apply for the full stack as well.

4.1 Lithium ions profile inside cathode electrode

In order to study the evolution of lithium ions inside the cathode, the model is charged and discharged under the following conditions:

- Starting from full intercalation ($c_1(x, t = 0) = c_{1max}$) a constant potential of 4.3 V is imposed, and a three-hour charge is simulated.

- Starting from half intercalation ($c_1(x, t = 0) = 0.5c_{1max}$) a constant current of 0.2 mA cm^{-2} or 2 mA cm^{-2} is imposed, and discharge is simulated down to 3 V.

Simulation results are saved at each 10 s time step. The running time of the simulation is a few seconds. In order to study the effect of the diffusion coefficient, all simulations are run for both a constant diffusion coefficient ($D =10^{-14}$ m^2 s^{-1}) and the variable diffusion coefficient ($D = D(c)$) extracted in the previous section.

Effect of diffusion coefficient during charge

In Figure 3.10, the evolution of the lithium profile inside the cathode is reported for different time steps. On the left side of each plot, at $x = 0$ there is the current-collector/cathode interface, while at $x = 30$ the cathode/electrolyte interface. In the left panel (Figure 3.10a), the profile was simulated with a constant diffusion coefficient. Since the beginning of the charge, the lithium profile is bending at the electrolyte interface due to the flux of lithium toward the anode. The depletion is more or less constant during the whole simulation. Near the end, when the overpotential starts decreasing, the current drops and the lithium gradient relaxes. On the right panel (Figure 3.10b) the same simulation is run with a variable diffusion coefficient. In this case, the diffusion coefficient is very low for high intercalation states and then stabilizes for $x_1 < 0.75$ at around 1×10^{-13} m^2 s^{-1}. The behavior is reflected in the lithium profile inside the cathode. At the beginning of the charge, the surface is immediately depleted down to $x_1 = 0.75$ and two phases are present. The lithium-rich near the current collector, and the lithium-poor near the electrolyte interface. The phase boundary (vertical line profile) moves deep into the cathode until the LCO is fully transformed into $Li_{0.75}CoO_2$. From this point on, the charge proceeds smoothly, with a very low lithium gradient along the cathode thickness. In the two simulations, the average diffusion coefficient is the same, but the lithium profile is greatly impacted by its local variations. An important point to remark is that in both cases, it is possible to fully charge the cathode, and the low diffusion coefficient does not impact the cell dynamics. This result is strongly related to the ”direction” of the phase transition. During charge, the cathode is transformed from a poor ion-conducting to a high ion-conducting material. As a result, each time an ion is extracted, it gets easier to extract more lithium, and no limitation is induced. This is not the case for the discharge.

Effect of diffusion coefficient during discharge

In Figure 3.11, the discharge profile is simulated for both constant and variable diffusion coefficients and for two different current regimes. Starting from the constant diffusion, in Figure

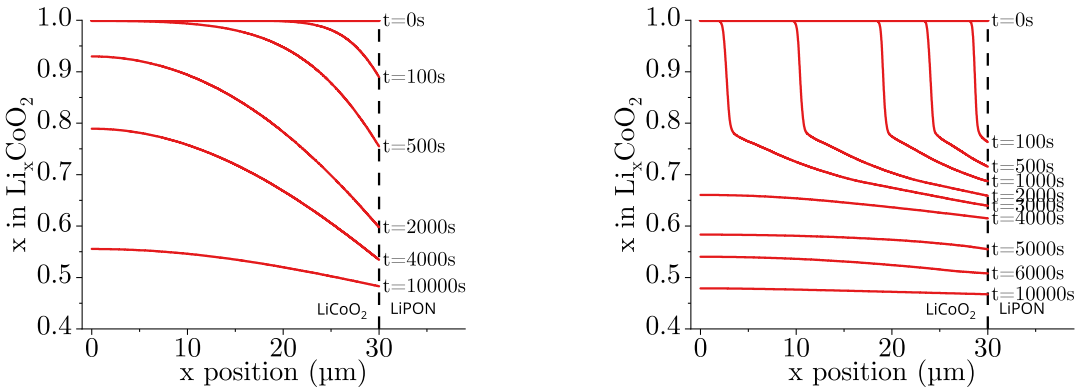

(a) Constant diffusion coefficient.

(b) Variable diffusion coefficient.

Figure 3.10: Simulated lithium concentration profile during constant voltage charge at $4.2\,\mathrm{V}$ for different diffusion coefficient.

3.11a and 3.11b, the two profiles are shown. In particular, for the low discharge current, the accumulation is small and constant through all the discharge, and about $90\,\%$ of the charge capacity is inserted back into the cathode. When the current increases, the profile gets steeper, and the interface reaches lithium saturation much faster than the bulk. The recovered capacity is less than $30\,\%$.

When the variable diffusion coefficient is implemented, the situation is radically changed, as reported in Figure 3.11c and 3.11d. In the case of a low current, the profile is quite flat until the phase transition is reached. The drop in diffusion coefficient induces a positive feed: the more the lithium is accumulated, the slower it diffuses and the faster it accumulates. This effect results in a local and sudden accumulation at the first micrometers of the electrode/electrolyte interface. Compared to the constant diffusion, in this case the recovered capacity is around $60\,\%$. When the current is increased, the situation is quite similar: the first part of the discharge is achieved with a low lithium gradient, and suddenly it stops as the accumulation at the interface reaches the phase transition threshold. Compared to the constant diffusion coefficient, the capacity loss between low and high current rates is lower in the second case. Because the second model has a higher diffusion coefficient in the first zone, it is capable of delivering this part of capacity more efficiently at high current.

Compared to the charge, during the discharge the cathode transits from a high ion-conductive state to a low ion-conductive state; as a consequence, it is not possible to cross the phase boundary, and the lithium is blocked at the interface. It is important to note the asymmetric behavior in the two cases. Usually, when a cell is dynamically characterized, the speed of charge and discharge are rarely distinguished. In fact, for a constant diffusion coefficient, the same limitation is present, no matter the direction of the current. Instead, what the simulation is suggesting is that it should be possible to impose a much higher current during the charge than during the discharge. The LCO would then be a fast-charging and slow-discharging material. This is indeed quite fortunate, due to the fast charge we usually aim for, while the discharge current is constant and imposed by the application.

As a final remark, I will recall the Cahn-Hilliard model for phase transition. In this case, the boundary between the two phases is stabilized by an additional term in the chemical potential. With a variable diffusion coefficient, it is possible to mimic the phase transition, but as soon as the cell is relaxed, the two-phase domain vanishes. In particular, the accumulation at the in-

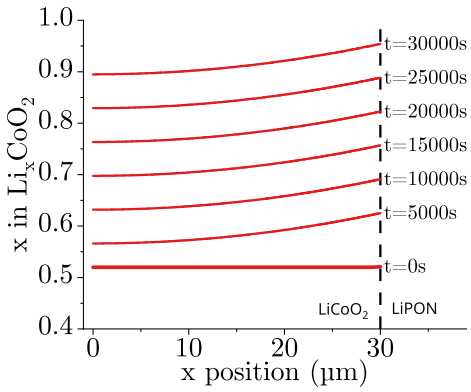

(a) Constant D, slow discharge at $0.25\,\mathrm{mA\,cm^{-2}}$

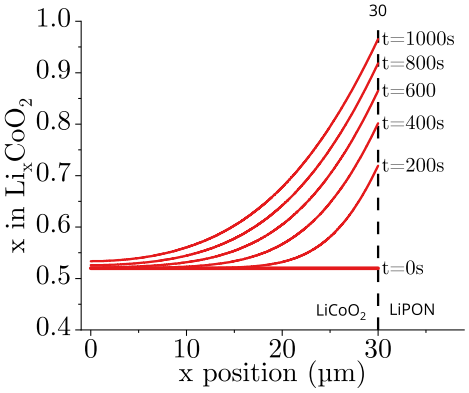

(b) Constant D, fast discharge at $2.5\,\mathrm{mA\,cm^{-2}}$

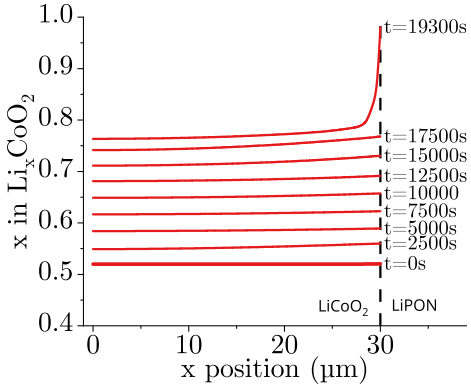

(c) Variable D, slow discharge at $0.25\,\mathrm{mA\,cm^{-2}}$

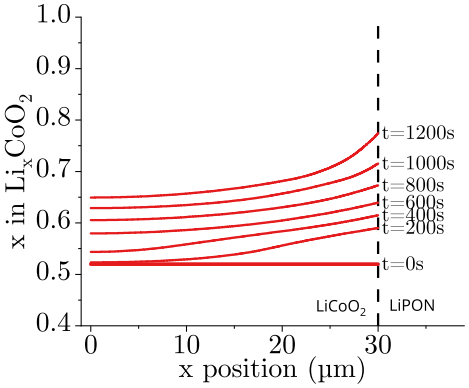

(d) Variable D, fast discharge at $2.5\,\mathrm{mA\,cm^{-2}}$

Figure 3.11: Simulated lithium concentration profile during discharge for different diffusion coefficient and variable discharge conditions.

terface in Figure 3.11c will disappear, while using the Cahn-Hilliard model, it is predicted to be stable due to interface energy. At this stage, both models would predict the same dynamic behavior. My choice of a variable diffusion coefficient is motivated mainly by other experimental considerations, as reported in the next chapter.

4.2 Lithium profile in solid electrolyte and electrical double layer

The second domain to be analyzed is the electrolyte and how the electric field is distributed during cell operation. Because the system was designed to be limited by the lithium drift in the electrolyte, we already expect very little accumulation at the interfaces and the whole potential drop to be absorbed by the bulk LiPON. I also decided to simulate a profile for a reaction-limited system in order to prove the flexibility of the model. Then, I focused mainly on the analysis of an MIM structure, which is the extreme case where, in fact, the reaction is zero. In this case, the whole potential drop is absorbed by the electrical double layer, making it easier to study its variation under a physical parameter sweep.

Profile evolution during constant potential charge

In an electrochemical cell, when an external potential is applied, a current starts flowing through the cell. The current value is fixed by the balance between the reaction at the interface and the drift in the bulk electrolyte. In Figure 3.12a the simulated voltage profile inside the electrolyte is shown. The linear drop in the bulk accounts for the major part of the applied potential, and only a small accumulation is visible at the interfaces. As the polarization increases, the slope of the voltage increases as well. The rise in the slope is linear with the applied potential. Considering the current balance, it is possible to calculate the current flowing in the cell by taking the ion flux at any point in the electrolyte. In particular, the current at the middle point can be expressed by the drift equation alone, assuming a zero concentration gradient:

$$j_{drift} \propto -M \frac{\partial \phi}{\partial x} \tag{3.126}$$

As the potential derivative increases linearly with the applied potential, the current is expected to do the same, and the system V-I characteristics are linear, as in a resistor.
In Figure 3.12b, the simulation is performed with a much higher self-diffusion of LiPON. With the same applied potential, the voltage profile inside the electrolyte has changed. Most of the total potential is concentrated at the interfaces, and only a small fraction is accounted for in the bulk electrolyte. If the current dependency on the applied external potential is calculated again, it shows a typical exponential behavior, of reaction-controlled kinetics.

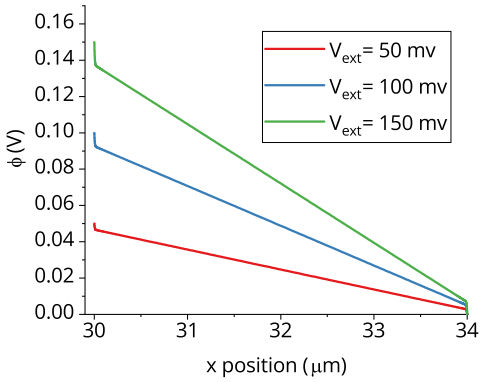

(a) Voltage drop for drift-controlled current at different applied over-potential.

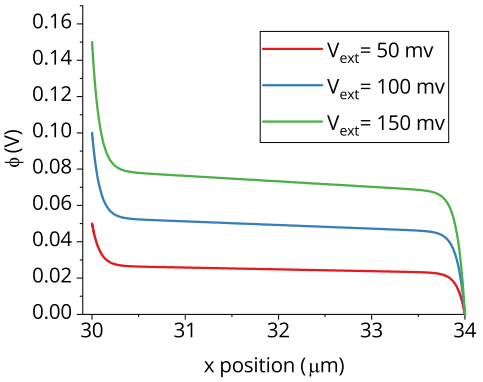

(b) Voltage drop for reaction-controlled current at different applied over-potential.

Figure 3.12

Effect of self-diffusion coefficient on the EDL in a MIM system

At this point, it is possible to study the effect of the LiPON physical parameters on the shape of the electrical double layer. Of course, in the case of a drift-controlled system, the effect is reduced, and it is more interesting to build an ad hoc model of a MIM structure where no reaction takes place.
The first parameter to be tested is the self-diffusion coefficient. In Figure 3.13a, the variation of the lithium concentration at the electrode/electrolyte interface is reported. Quite disappointingly, no difference in the profile seems to be caused by the variation of the self-diffusion coef-

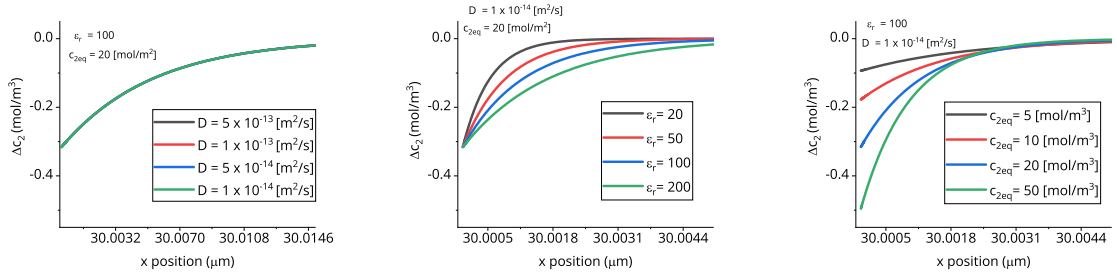

(a) Electrical double layer for different values of the electrolyte self-diffusion under 100 mV DC polarization.

(b) Electrical double layer for different values of the electrolyte dielectric permittivity under 100 mV DC polarization.

(c) Electrical double layer for different values of the electrolyte carrier equilibrium concentration under 100 mV DC polarization.

Figure 3.13

ficient. For the moment, let's just continue the analysis, and we will come back to this point in the conclusion.

Effect of dielectric permittivity on the EDL in a MIM system

A second possibility is to vary the dielectric constant ϵ_r of LiPON for the same system. The main effect is the broadening of the distribution (Figure 3.13b) and it can be interpreted as follows: the dielectric constant is a measure of the screening of the electric field by means of the crystal matrix. At high dielectric constants, the effect of the electric field is reduced, and a more flat, diffusion-driven distribution results. Moreover, the dielectric constant has no effect on the peak value of the distribution at the interface. The results can be interpreted as an effect of the screening of the electric potential. In particular, near the electrode-electrolyte interface, the electric field generated by the interface charge is at its maximum, and its value does not change much for different dielectric constants. The deeper in the electrolyte, the more the field is masked by the electrolyte, and the larger the impact of the dielectric constant.

Effect of carrier concentration on the EDL in a MIM system

The last parameter I will consider is the equilibrium concentration of lithium in the electrolyte c_{2eq}. In Figure 3.13c the sweep on this last parameter is reported. The general effect is an increase in the maximum value of the profile for higher value of the carrier concentration. In the previous section, we stated that the carrier concentration and the self-diffusion coefficient are not distinguishable from an electrical point of view. Which is true, at least for the high- and medium-frequency ranges. Starting from this consideration, one may expect the two to have the same effect on the lithium profile, which seems not to be the case. To be convinced of the results, we may explicitly write the drift-diffusion current at equilibrium including the definition of the electrochemical potential to get:

$$j_{tot} = D_2 \frac{\partial c_2}{\partial x} - \frac{D_2}{kT} c_2 F \frac{\partial \phi}{\partial x} = 0 \tag{3.127}$$

Curiously enough, in the final expression, there is no dependency on the equilibrium concentration in the diffusion current, while the drift current is increased proportionally to the carrier concentration. As a result, for an increase in the mobile lithium concentration, an increase in

the profile slope is expected as well:

$$\frac{\partial c_2}{\partial x} = \frac{c_2 F}{kT}\frac{\partial \phi}{\partial x} \tag{3.128}$$

Moreover, the self-diffusion coefficient is the same in both drift and diffusion currents. In accordance with the simulation, there is no preferential effect of the diffusion coefficient on the shape of the double layer. This is actually a very important result because it means that, in the physical model, it should be possible to distinguish the effect of the dielectric constant and of the carrier concentration at low frequency, and a direct fitting of the EIS spectra may result in a more precise description of the system with respect to the equivalent circuit.

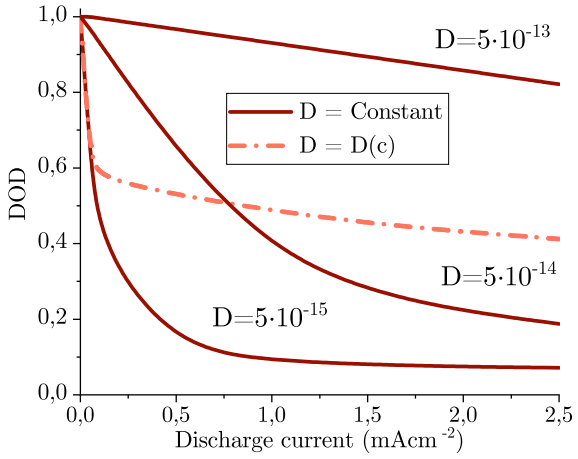

Figure 3.14: Simulated maximum depth of discharge for a constant current discharge until $3\,\mathrm{V}$ as a function of the discharge current density for $30\,\mu\mathrm{m}$ thick LCO cell.

4.3 Rate performance

Starting from the simulation of the lithium concentration evolution during discharge, it is possible to extract the predicted rating performance of the device. In particular, it is possible, with a parameter sweep on the discharge current, to trace the variation of the delivered capacity, expressed as depth-of-discharge (DOD = $\frac{Q_{discharge}}{Q_{charge}}$), as a function of the current in a Ragone-like plot. In Figure 3.14 the results for the LCO constant and variable diffusion coefficient are shown. Three constant diffusion values have been simulated. The three values have been selected with respect to the experimental values of Figure 3.9b to be higher, equal, and lower of the measured diffusion coefficient in the zone $0.35 \leq x \leq 0.75$. While the three constant simulations show a more or less constant loss of capacity as the current density is increased, the variable diffusion is characterized by two different regions. The first, at very low current density, corresponds to a fast loss of capacity. In the second, the capacity stabilizes, and a relatively flat region appears. Compared to the constant diffusion, the first zone has the same slope as the $D = 5 \cdot 10^{-15}$ constant diffusion curve. At higher currents, the slope is the one of $D = 5 \cdot 10^{-13}$, but the curve is translated downward. As a matter of fact, the simulation with a constant diffusion coefficient equal to the average value of the variable one is the least similar to the variable diffusion one. In order to better understand the piecewise behavior of the variable diffusion, it is enough to recall the lithium profile of Figure 3.11c. The plateau is correlated to the region at a low intercalation state, which is characterized by fast ion diffusion and is less sensitive to the current increase.

On the other hand, the lithium-rich phase possesses a very low diffusion coefficient and, even at a low current rate, cannot be replenished. The first loss in Figure 3.14 represents such a domain, which, as soon as the current is increased from zero, is no longer exploitable. Even if, for a single discharge current, it is possible to define a constant diffusion coefficient model with the same capacity loss as the variable diffusion one, it is not possible to capture the whole dynamic behavior of the battery.
As a last remark, I want to point out that the initial state was the same for each simulation. In experimental characterization, often both charge and discharge currents vary. As a consequence, the initial point of discharge differs. In particular, if any limitation is affecting the charge capacity, the discharge will be impacted as well, even if no limitation applies. In the case of LCO, the charge is not limited, and only minor artifacts would be introduced. Anyway, since electrodes are often asymmetric systems, it would be a better practice to separately analyze the charge and discharge dynamic behavior.

List of Symbols

Symbol	Units	Description
α	1	Symmetry factor
A	m^2	Surface
C	F	Capacitance
c	$\mathrm{mol\,m}^{-3}$	Volumetric particles density
$\boldsymbol{D}$	$\mathrm{C\,m}^{-2}$	Electric displacement field
D	$\mathrm{m}^2\,\mathrm{s}^{-1}$	Self-diffusion coefficient
D^*	$\mathrm{m}^2\,\mathrm{s}^{-1}$	Tracer diffusion coefficient
$\tilde{D}$	$\mathrm{m}^2\,\mathrm{s}^{-1}$	Chemical diffusion coefficient
d	m	length
ΔG_V	J	Vacancy energy formation
ΔG_b	J	Diffusion energy barrier
ϵ	$\mathrm{F\,m}^{-1}$	Permittivity
ϵ'	$\mathrm{F\,m}^{-1}$	Real part of the permittivity
ϵ''	$\mathrm{F\,m}^{-1}$	Imaginary part of the permittivity
ϵ_0	$\mathrm{F\,m}^{-1}$	Vacuum permittivity
ϵ_r	1	Relative permittivity
η	V	Over-potential
$\boldsymbol{E}$	$\mathrm{V\,m}^{-1}$	Electric field
E	J	Internal energy
E_g	J	Band-gap energy
ϕ	V	Electric potential
F	$\mathrm{C\,mol}^{-1}$	Faraday constant
G	J	Gibbs free energy
I	A	Electric current
k	$\mathrm{J\,K}^{-1}$	Boltzmann constant
k_a	$\mathrm{m\,s}^{-1}$	Anodic reaction rate constant
k_c	$\mathrm{m\,s}^{-1}$	Cathodic reaction rate constant
J	$\mathrm{mol\,m}^{-2}\,\mathrm{s}^{-1}$	Diffusion flux
j	$\mathrm{A\,m}^{-2}$	Electric current density
m	g	Mass
μ	$\mathrm{J\,mol}^{-1}$	Chemical potential
$\tilde{\mu}$	$\mathrm{J\,mol}^{-1}$	Electrochemical potential

Symbol	Units	Description
ω	$\mathrm{rad\,s^{-1}}$	Angular frequency
OCV	V	Open circuit voltage
P	bar	Pressure
Q_A	$\mathrm{A\,h\,m^{-2}}$	Areal capacity density
Q_m	$\mathrm{A\,h\,kg^{-1}}$	Gravimetric capacity density
Q_V	$\mathrm{A\,h\,m^{-3}}$	volumetric capacity density
ρ	$\mathrm{C\,m^{-3}}$	Volumetric charge density
R	$\mathrm{J\,mol^{-1}\,K^{-1}}$	Gas constant
R_{ext}	Ω	Load resistance
R_{int}	Ω	Internal resistance
R_{self}	Ω	Self-discharge resistance
σ	$\mathrm{C\,m^{-2}}$	Surface charge density
σ_{el}	$\Omega\,\mathrm{cm}$	Electron conductivity
σ_{ion}	$\Omega\,\mathrm{cm}$	Ion conductivity
S	$\mathrm{J\,K^{-1}}$	Entropy
SOC	1	State-of-Charge
T	K	Temperature
t_{ion}	1	Ion transfer number
V	$\mathrm{m^3}$	Volume
z	1	Charge number

Bibliography

Drift-diffusion model

[1] John O'M. Bockris and Amulya K. N. Reddy. *Modern Electrochemistry 1, Ionics*. 2nd ed. New York: Kluwer Academic Publishers, June 1998.

[2] John O'M. Bockris, Amulya K. N. Reddy and Maria Gamboa-Aldeco. *Modern Electrochemistry 2A, Fundamentals of Electrodics*. 2nd ed. New York: Kluwer Academic Publishers, 2000.

[3] Han-Ill Yoo. *Lectures on Kinetic Processes in Materials*. en. Cham: Springer International Publishing, 2020. ISBN: 978-3-030-25949-5 978-3-030-25950-1. DOI: 10.1007/978-3-030-25950-1.

[4] Mats Hillert. *Phase Equilibria, Phase Diagrams and Phase Transformations: Their Thermodynamic Basis*. 2nd ed. Cambridge: Cambridge University Press, 2007. ISBN: 978-0-521-85351-4. DOI: 10.1017/CBO9780511812781.

[5] José Francisco Rodrigues, ed. *Mathematical Models for Phase Change Problems*. en. Basel: Birkhäuser Basel, 1989. ISBN: 978-3-0348-9926-0 978-3-0348-9148-6. DOI: 10.1007/978-3-0348-9148-6.

[6] L. D. Landau and E. M. Lifshitz. *Statistical Physics*. Third Edition. Oxford: Butterworth-Heinemann, 1980. ISBN: 978-0-08-057046-4.

[7] John W. Cahn and John E. Hilliard. "Free Energy of a Nonuniform System. I. Interfacial Free Energy". In: *The Journal of Chemical Physics* 28.2 (Aug. 2004), pp. 258–267. DOI: 10.1063/1.1744102.

[8] Robert Pierret. *Semiconductor Device Fundamentals*. Second Edition. Addison Wesley, 1996. ISBN: 978-0-201-54393-3.

[9] W Ross Mckinnon. "Physical Mechanisms of Intercalation Batteries". en. PhD thesis. University of British Columbia, 1980.

[10] D. Danilov, R. A. H. Niessen and P. H. L. Notten. "Modeling All-Solid-State Li-Ion Batteries". en. In: *J. Electrochem. Soc.* 158.3 (2011), A215. DOI: 10.1149/1.3521414.

[11] L.H.J. Raijmakers et al. "An advanced all-solid-state Li-ion battery model". en. In: *Electrochimica Acta* 330 (Jan. 2020), p. 135147. DOI: 10.1016/j.electacta.2019.135147.

[12] L. Cabras, V. Oancea and A. Salvadori. "A novel two-mechanism full battery model for solid state Li-ion batteries: review and comparisons". en. In: *arXiv:2104.05424 [cond-mat]* (May 2021).

[13] J. Deconinck. "Mathematical modelling of electrode growth". en. In: *J Appl Electrochem* 24.3 (Mar. 1994). DOI: 10.1007/BF00242886.

[14] Z.H. Qiu and H. Power. “Prediction of electrode shape change involving convection, diffusion and migration by the boundary element method”. en. In: *Journal of Applied Electrochemistry* 30.5 (May 2000), pp. 575–584. DOI: 10.1023/A:1003931202125.

[15] Andrew J Pascall, Kyle T Sullivan and Joshua D Kuntz. “Morphology of Electrophoretically Deposited Films on Electrode Strips”. en. In: *J. Phys. Chem. B* (2013), p. 6.

[16] Xiangchun Zhang, Wei Shyy and Ann Marie Sastry. “Numerical Simulation of Intercalation-Induced Stress in Li-Ion Battery Electrode Particles”. en. In: *J. Electrochem. Soc.* 154.10 (2007), A910. DOI: 10.1149/1.2759840.

[17] Esther Bohn et al. “A Model for Lithium Diffusion and Stress Generation in an Intercalation Storage Particle with Phase Change”. en. In: *J. Electrochem. Soc.* 160.10 (2013), A1638–A1652. DOI: 10.1149/2.011310jes.

[18] Chris Gritton et al. “Using the material point method to model chemical/mechanical coupling in the deformation of a silicon anode”. en. In: *Modelling Simul. Mater. Sci. Eng.* 25.4 (June 2017), p. 045005. DOI: 10.1088/1361-651X/aa6830.

[19] Bin Wu and Wei Lu. “A consistently coupled multiscale mechanical–electrochemical battery model with particle interaction and its validation”. en. In: *Journal of the Mechanics and Physics of Solids* 125 (Apr. 2019), pp. 89–111. DOI: 10.1016/j.jmps.2018.12.005.

[20] Gabriel N. Gatica, Bryan Gomez-Vargas and Ricardo Ruiz-Baier. “Formulation and analysis of fully-mixed methods for stress-assisted diffusion problems”. en. In: *Computers & Mathematics with Applications* 77.5 (Mar. 2019), pp. 1312–1330. DOI: 10.1016/j.camwa.2018.11.008.

[21] Marc Doyle and John Newman. “The use of mathematical modeling in the design of lithium/polymer battery systems”. en. In: *Electrochimica Acta* 40.13-14 (Oct. 1995), pp. 2191–2196. DOI: 10.1016/0013-4686(95)00162-8.

[22] Sean R. Bishop et al., eds. *Electro-Chemo-Mechanics of Solids*. en. Electronic Materials: Science & Technology. Cham: Springer International Publishing, 2017. ISBN: 978-3-319-51405-5 978-3-319-51407-9. DOI: 10.1007/978-3-319-51407-9.

[23] Feng Hao, Wenxiu Wang and Partha P. Mukherjee. “Electrochemical-Reaction-Driven Interfacial Stress in a Solid-Solid Layered Architecture”. en. In: *Phys. Rev. Applied* 11.3 (Mar. 2019), p. 034038. DOI: 10.1103/PhysRevApplied.11.034038.

[24] Xu Song et al. “A coupled electro-chemo-mechanical model for all-solid-state thin film Li-ion batteries: The effects of bending on battery performances”. en. In: *Journal of Power Sources* 452 (Mar. 2020), p. 227803. DOI: 10.1016/j.jpowsour.2020.227803.

[25] Yu-qiang Shao et al. “A Fully Coupled Mechano-Electrochemical Model for All-Solid-State Thin-Film Li-Ion Batteries with Non-Porous Electrodes: Effects of Chemo-Mechanical Expansions on Battery Performance and Optimization Strategies for Stress Evolution”. en. In: *J. Electrochem. Soc.* 169.8 (Aug. 2022), p. 080529. DOI: 10.1149/1945-7111/ac8b3a.

[26] Yu-qiang Shao et al. “A fully coupled mechano-electrochemical model for all-solid-state Li-ion batteries: An optimal strategy for controlling interfacial contact using internal stress generated by electrode expansion”. en. In: *Electrochimica Acta* 443 (Mar. 2023), p. 141958. DOI: 10.1016/j.electacta.2023.141958.

[27] Pooja Vadhva et al. “Silicon-Based Solid-State Batteries: Electrochemistry and Mechanics to Guide Design and Operation”. en. In: *ACS Appl. Mater. Interfaces* (Aug. 2023), acsami.3c06615. DOI: 10.1021/acsami.3c06615.

[28] S.D. Fabre et al. “Charge/Discharge Simulation of an All-Solid-State Thin-Film Battery Using a One-Dimensional Model”. en. In: *J. Electrochem. Soc.* 159.2 (2011), A104–A115. DOI: 10.1149/2.041202jes.

[29] Namdar Kazemi et al. “Modeling of all-solid-state thin-film Li-ion batteries: Accuracy improvement”. en. In: *Solid State Ionics* 334 (June 2019), pp. 111–116. DOI: 10.1016/j.ssi.2019.02.003.

[30] E Bruce Nauman and David Qiwei He. “Nonlinear di usion and phase separation”. en. In: *Chemical Engineering Science* (2001), p. 20.

[31] Gregory H. Teichert et al. “A comparison of Redlich-Kister polynomial and cubic spline representations of the chemical potential in phase field computations”. en. In: *Computational Materials Science* 128 (Feb. 2017), pp. 127–139. DOI: 10.1016/j.commatsci.2016.11.024.

[32] Yi Zeng and Martin Z. Bazant. “Cahn-Hilliard Reaction Model for Isotropic Li-ion Battery Particles”. en. In: *MRS Proc.* 1542 (2013), mrss13–1542–g02–01. DOI: 10.1557/opl.2013.740.

[33] Tobias Hofmann et al. “Numerical simulation of phase separation in cathode materials of lithium ion batteries”. en. In: *International Journal of Solids and Structures* 100-101 (Dec. 2016), pp. 456–469. DOI: 10.1016/j.ijsolstr.2016.09.018.

[34] R Painter, L Sharpe and S K Hargrove. “A Phase Field Model for Lithium Ion Battery Particles”. en. In: (2017), p. 5.

[35] Neel Nadkarni et al. “Modeling the Metal–Insulator Phase Transition in $Li_x CoO_2$ for Energy and Information Storage”. en. In: *Adv. Funct. Mater.* 29.40 (Oct. 2019), p. 1902821. DOI: 10.1002/adfm.201902821.

[36] Simon Daubner et al. “Multiphase-field modeling of spinodal decomposition during intercalation in an Allen-Cahn framework”. en. In: *Phys. Rev. Materials* 5.3 (Mar. 2021), p. 035406. DOI: 10.1103/PhysRevMaterials.5.035406.

[37] Mustafa Sabri Kilic, Martin Z. Bazant and Armand Ajdari. “Steric effects in the dynamics of electrolytes at large applied voltages. II. Modified Poisson-Nernst-Planck equations”. en. In: *Phys. Rev. E* 75.2 (Feb. 2007), p. 021503. DOI: 10.1103/PhysRevE.75.021503.

Butler-Volmer Equation for All-solid-state Batteries

[2] John O’M. Bockris, Amulya K. N. Reddy and Maria Gamboa-Aldeco. *Modern Electrochemistry 2A, Fundamentals of Electrodics*. 2nd ed. New York: Kluwer Academic Publishers, 2000.

[8] Robert Pierret. *Semiconductor Device Fundamentals*. Second Edition. Addison Wesley, 1996. ISBN: 978-0-201-54393-3.

[10] D. Danilov, R. A. H. Niessen and P. H. L. Notten. “Modeling All-Solid-State Li-Ion Batteries”. en. In: *J. Electrochem. Soc.* 158.3 (2011), A215. DOI: 10.1149/1.3521414.

[11] L.H.J. Raijmakers et al. “An advanced all-solid-state Li-ion battery model”. en. In: *Electrochimica Acta* 330 (Jan. 2020), p. 135147. DOI: 10.1016/j.electacta.2019.135147.

[12] L. Cabras, V. Oancea and A. Salvadori. “A novel two-mechanism full battery model for solid state Li-ion batteries: review and comparisons”. en. In: *arXiv:2104.05424 [cond-mat]* (May 2021).

[17] Esther Bohn et al. “A Model for Lithium Diffusion and Stress Generation in an Intercalation Storage Particle with Phase Change”. en. In: *J. Electrochem. Soc.* 160.10 (2013), A1638–A1652. DOI: 10.1149/2.011310jes.

[19] Bin Wu and Wei Lu. “A consistently coupled multiscale mechanical–electrochemical battery model with particle interaction and its validation”. en. In: *Journal of the Mechanics and Physics of Solids* 125 (Apr. 2019), pp. 89–111. DOI: 10.1016/j.jmps.2018.12.005.

[28] S.D. Fabre et al. “Charge/Discharge Simulation of an All-Solid-State Thin-Film Battery Using a One-Dimensional Model”. en. In: *J. Electrochem. Soc.* 159.2 (2011), A104–A115. DOI: 10.1149/2.041202jes.

[29] Namdar Kazemi et al. “Modeling of all-solid-state thin-film Li-ion batteries: Accuracy improvement”. en. In: *Solid State Ionics* 334 (June 2019), pp. 111–116. DOI: 10.1016/j.ssi.2019.02.003.

[38] H. H. Girault. *Analytical and physical electrochemistry*. en. Fundamental sciences. Lausanne, Switzerland : New York: EPFL ; Marcel Dekker, 2004. ISBN: 978-2-940222-03-2 978-0-8247-5357-3.

[39] Wolfgang Schmickler. *Interfacial electrochemistry*. en. New York: Oxford University Press, 1996. ISBN: 978-0-19-508932-5.

[40] Manuel Landstorfer, Stefan Funken and Timo Jacob. “An advanced model framework for solid electrolyte intercalation batteries”. en. In: *Phys. Chem. Chem. Phys.* 13.28 (2011), p. 12817. DOI: 10.1039/c0cp02473b.

[41] Qi Zhang, Qingzhi Guo and Ralph E. White. “A New Kinetic Equation for Intercalation Electrodes”. en. In: *J. Electrochem. Soc.* 153.2 (2006), A301. DOI: 10.1149/1.2142287.

[42] Arnulf Latz and Jochen Zausch. “Thermodynamic derivation of a Butler–Volmer model for intercalation in Li-ion batteries”. en. In: *Electrochimica Acta* 110 (Nov. 2013), pp. 358–362. DOI: 10.1016/j.electacta.2013.06.043.

[43] A. M. Ramos and C. P. Please. *Some comments on the Butler-Volmer equation for modeling Lithium-ion batteries*. en. Tech. rep. arXiv:1503.05912. arXiv, Mar. 2015.

[44] Markus Ganser et al. “An Extended Formulation of Butler-Volmer Electrochemical Reaction Kinetics Including the Influence of Mechanics”. en. In: *J. Electrochem. Soc.* 166.4 (2019), H167–H176. DOI: 10.1149/2.1111904jes.

[45] L. Cabras et al. “A two-mechanism and multiscale compatible approach for solid state electrolytes of (Li-ion) batteries”. en. In: *Journal of Energy Storage* 48 (Apr. 2022), p. 103842. DOI: 10.1016/j.est.2021.103842.

PDE model and parameters extraction

[1] John O’M. Bockris and Amulya K. N. Reddy. *Modern Electrochemistry 1, Ionics*. 2nd ed. New York: Kluwer Academic Publishers, June 1998.

[9] W Ross Mckinnon. “Physical Mechanisms of Intercalation Batteries”. en. PhD thesis. University of British Columbia, 1980.

[38] H. H. Girault. *Analytical and physical electrochemistry*. en. Fundamental sciences. Lausanne, Switzerland : New York: EPFL ; Marcel Dekker, 2004. ISBN: 978-2-940222-03-2 978-0-8247-5357-3.

[46] Thomas Nann and Jürgen Heinze. “Simulation in electrochemistry using the finite element methodPart 1: The algorithm”. en. In: *Electrochemistry Communications* 1.7 (July 1999), pp. 289–294. DOI: 10.1016/S1388-2481(99)00055-7.

[47] Lucie Le Van-Jodin et al. “Dielectric properties, conductivity and Li+ ion motion in LiPON thin films”. en. In: *Solid State Ionics* 253 (Dec. 2013), pp. 151–156. DOI: 10.1016/j.ssi.2013.09.031.

[48] I. Braems, S. Franger and F. Berthier. “Reliable Discrimination of Models Based on EIS Data”. en. In: *J. Electrochem. Soc.* 156.5 (2009), J81. DOI: 10.1149/1.3082127.

[49] H. R. Thirsk, W. I. Archer and R. D. Armstrong. “The application of A. C. impedance methods to solid electrolytes”. en. In: *Electrochemistry*. Ed. by H R Thirsk. 1st ed. The Royal Society of Chemistry, Jan. 1980, pp. 157–202. ISBN: 978-0-85186-870-7 978-1-84973-263-5. DOI: 10.1039/9781849732635-00157.

[50] R. D. Armstrong and R. A. Burnham. “The effect of roughness on the impedance of the interface between a solid electrolyte and a blocking electrode”. In: *Journal of Electroanalytical Chemistry and Interfacial Electrochemistry* 72.3 (Sept. 1976), pp. 257–266. DOI: 10.1016/S0022-0728(76)80312-9.

[51] R. De Levie. “The influence of surface roughness of solid electrodes on electrochemical measurements”. en. In: *Electrochimica Acta* 10.2 (Feb. 1965), pp. 113–130. DOI: 10.1016/0013-4686(65)87012-8.

[52] B. Fleutot et al. “Investigation of the local structure of LiPON thin films to better understand the role of nitrogen on their performance”. en. In: *Solid State Ionics* 186.1 (Mar. 2011), pp. 29–36. DOI: 10.1016/j.ssi.2011.01.006.

[53] Brecht Put, Philippe M. Vereecken and Andre Stesmans. “On the chemistry and electrochemistry of LiPON breakdown”. en. In: *J. Mater. Chem. A* 6.11 (Mar. 2018), pp. 4848–4859. DOI: 10.1039/C7TA07928A.

[54] W. Weppner and R. A. Huggins. “Determination of the Kinetic Parameters of Mixed-Conducting Electrodes and Application to the System Li3Sb”. en. In: *J. Electrochem. Soc.* 124.10 (Oct. 1977), p. 1569. DOI: 10.1149/1.2133112.

[55] C. John Wen et al. “Thermodynamic and Mass Transport Properties of “ LiAl ””. en. In: *J. Electrochem. Soc.* 126.12 (Dec. 1979), pp. 2258–2266. DOI: 10.1149/1.2128939.

"[...] τό φῶς ἐν τῇ σκοτίᾳ φαίνει, καὶ ἡ σκοτία αὐτὸ οὐ κατέλαβεν.*"*

from ΚΑΤΑ ΥΩΑΝΝΗΝ

"[...] the light reveals in the dark, and the darkness has not grasped it."

trad. from the *Gospel of John*

CHAPTER IV

Thick Cathode Dynamics and Optimization

ABSTRACT

This chapter is dedicated to the core experimental results of the present thesis. In particular, by means of electrical testing and operando synchrotron X-ray diffraction, the physical model predictions about rate performances and lithium distribution in the cathode are validated. For the first time, the phase transition dynamic inside a thin-film LCO cathode was imaged together with the interface accumulation at the end of the discharge, confirming the simulation prediction.

The first section is dedicated to the electrical testing of electrochemical cells with variable cathode thickness. The evolution of the available capacity and the rate performance as a function of the quantity of active material are evaluated.

The second section reports on the synchrotron X-ray diffraction experiment. After a review of the available literature, experimental data are presented and the results are discussed and compared with the simulated lithium profile.

The third and closing section is a critical evaluation of the accumulation process at the end of discharge in the thin-film configuration. The literature is reviewed starting from the experimental results of the present work in order to better understand the underlying physics.

Contents

1. Electrical Characterization of Thick Cathodes

This last chapter is dedicated to the electrical and physical characterization of electrochemical cells, as described in the second chapter. The comparison between the charge/discharge data of the cell and the simulated prediction permits a first coarse verification of the model. Of particular relevance is the variation of the available capacity during charge and discharge as a function of the cathode thickness and the current density. As the physical model predicts an asymmetric behavior between charge and discharge, this is a perfect starting point to test it. The second section focuses on the detailed observation of the lithium profile inside the cathode by means of X-ray diffraction. During this analysis, the predicted phase transition dynamic and the modeling assumptions are challenged, and a finer verification of the model is accomplished.
The electrical measurements have been performed on four different devices, with cathode thickness ranging from 5 to 30 µm, while the X-ray diffraction was restricted to the thicker stacks. Electrolyte thickness is either 4 or 6 µm. Total active area of the cell is $0.5\,\mathrm{mm}^2$.

1.1 Electrical testing protocols

The electrical testing has been performed with a consistent protocol on all devices under test. The measurements were conducted in dry air at $37\,^\circ$C. The devices are charged by applying a constant voltage until a cut-off current is reached. This way, the maximum possible current is drawn, and the charge time is minimized. The discharge is performed with a constant current (CC) down to $3\,$V. Relaxations and impedance spectroscopy measurements are included in order to monitor the evolution of the cell's internal status.

Charge

The complete charge process comprises five steps, in the following order:

1. $10\,$s OCV measurement
2. EIS spectrum from 1×10^6 to 0.1 Hz at $30\,$mV input amplitude
3. Charge at a constant $4.3\,$V until a current of $0.5\,\mu\mathrm{A\,cm}^{-2}$ is reached
4. $10\,$s OCV measurement
5. EIS spectrum from 1×10^6 to 0.1 Hz at $30\,$mV input amplitude

The measurement of the OCV before and after the charge has two main purposes. First, it permits monitoring the actual state-of-charge of the cell once the relaxed cell voltage is known. Second, it guarantees proper relaxation of the cell before performing the impedance spectroscopy. As already pointed out, the impedance is a steady-state, small-signal analysis and should not be performed while the cell voltage is varying. An example of the current and capacity profiles during the $4.3\,$V step is reported in Figure 4.1a. At any time step, the actual overpotential η is the difference between the OCV and the imposed constant voltage. At the beginning, the LCO is fully discharged, with an OCV of around $3.9\,$V. The $400\,$mV overpotential is almost completely absorbed by the LiPON. In fact, the maximum current is easily derived by Ohm's law:

$$I_{bat} = \frac{\eta}{R_{ely}} = \frac{4.3\,\mathrm{V} - OCV(c)}{R_{ely}} = \frac{400\,\mathrm{mV}}{35\,\mathrm{k\Omega}} \sim 11\,\mu\mathrm{A} \tag{4.1}$$

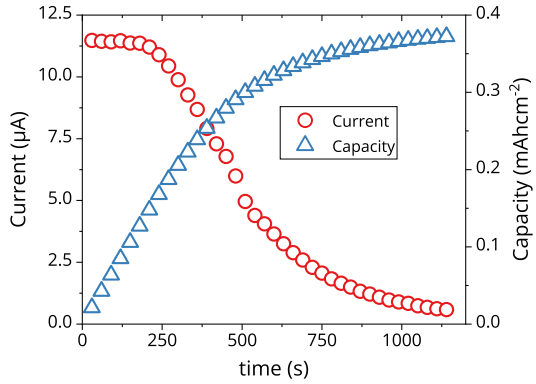

(a) Example of charge profile for a 5 µm thick cathode cell. Charge condition: imposed 4.3 V until 0.5 µA current is reached.

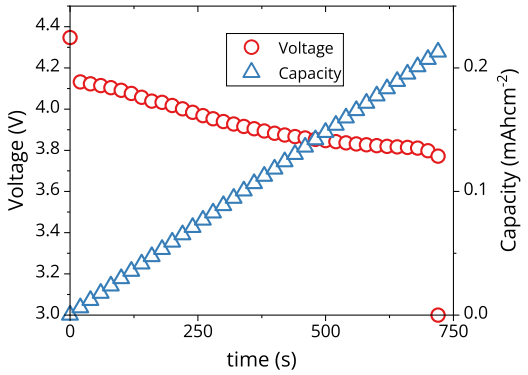

(b) Example of discharge profile for a 5 µm thick cathode cell. Discharge condition: imposed 5 µA until 3 V voltage is reached.

Figure 4.1: Charge and discharge protocol

Where R_{ely} is the resistance associated with the ion drift inside the electrolyte. While the cell is charging, the OCV increases and the overpotential decreases. As a result, the shape of the current has the same feature as the negative $-OCV(c)$ function: first a plateau and then a steady decrease. The differences between the two come from the variable speed at which the $OCV(c(t))$ function is traversed since the discharge is not at constant current. At the initial plateau, the current is at its maximum, and, in proportion, it is compressed with respect to the following slope. Another important consequence is the different charge times for different portions of the capacity. While the first 60 % is charged linearly and accounts for less than half of the total charge time, the final part is characterized by a decay in the current and a much longer charge time per unit of capacity. Even so, the protocol is the fastest possible at iso-charged-capacity, as long as the maximum voltage is fixed. In fact, in order to charge the same amount of capacity, by imposing a constant current without crossing the 4.3 V threshold, a current as low as the current cut-off should be imposed. Put differently, by plotting the capacity versus the current from Figure 4.1a it is possible to read the maximum applicable current in order to charge a certain capacity once the threshold voltage is fixed. This is a convenient way to deduce the rate performance of a cell without explicitly charging the cell at a different current, as is usually the case in the literature.

Discharge

As for the charge, the discharge is composed of several measurement steps. In order to properly measure the EIS and the OCV of the cell, in particular, the same structure has been implemented:

1. 10 s OCV measurement
2. EIS spectrum from 1×10^6 to 0.1 Hz at 30 mV input amplitude
3. Discharge at constant current 5 µA until 3 V are reached
4. 10 s OCV measurement
5. EIS spectrum from 1×10^6 to 0.1 Hz at 30 mV input amplitude

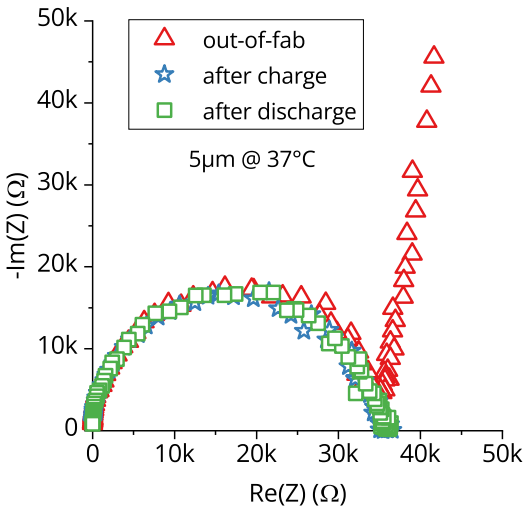

Figure 4.2: Evolution of the impedance spectrum during the first charge and discharge cycle.

When the cell is cycled, the OCV and EIS steps are shared between each charge and the previous and following discharges. In Figure 4.1b, an example of the voltage and capacity evolution during discharge is reported. As for the charge, it is possible to link the voltage profile (V_{cell}) and the overpotential. In particular, as long as there is no dynamic limitation inside the cathode, the overpotential is a function of the ion drift only:

$$V_{cell} = OCV(c) - \eta = OCV(c) - I_{cell}R_{ely} \sim OCV(c) - 175\,\text{mV} \tag{4.2}$$

The formula is expected to be valid until the onset of the phase transition, where the lithium dynamics in the LCO dominates the general behavior. In fact, as the potential reaches the plateau voltage, the discharge is suddenly stopped. It must be noted that, assuming a constant plateau voltage at around $3.9\,$V, the drop in V_{cell} can be associated with an increase in the overpotential: the reaction at the interface is drastically reduced by a shortage of insertion sites, and the electrons spend a lot of time waiting at the electrode/electrolyte interface, increasing the accumulated charge.

Impedance spectroscopy evolution

The measurement of cell impedance at each step makes it straightforward to follow the cell's evolution and eventual degradation, in particular during cycling. While the cycling will be addressed only in the concluding section, the evolution of the impedance spectrum during the first charge and discharge is reported in Figure 4.2. The first curve refers to the cell in the anode-free configuration before the first charge. In this case, the anode current collect acts as a blocking electrode, and the signature is identical to a MIM structure. The semicircle corresponds to the bulk LiPON impedance linked to ion drift (around $35\,\text{k}\Omega$ of diameter). After the first charge, the lithium is able to cross both the anode and cathode interfaces, and the increase in impedance linked to the blocking capacitor disappears. The interface reaction contribution is too small to be distinguished from the bulk LiPON and a single semicircle is identified in both the charged and discharged states. The discharge is not complete, and a lithium layer is always present at the anode, as a result, the initial signature is not recovered.

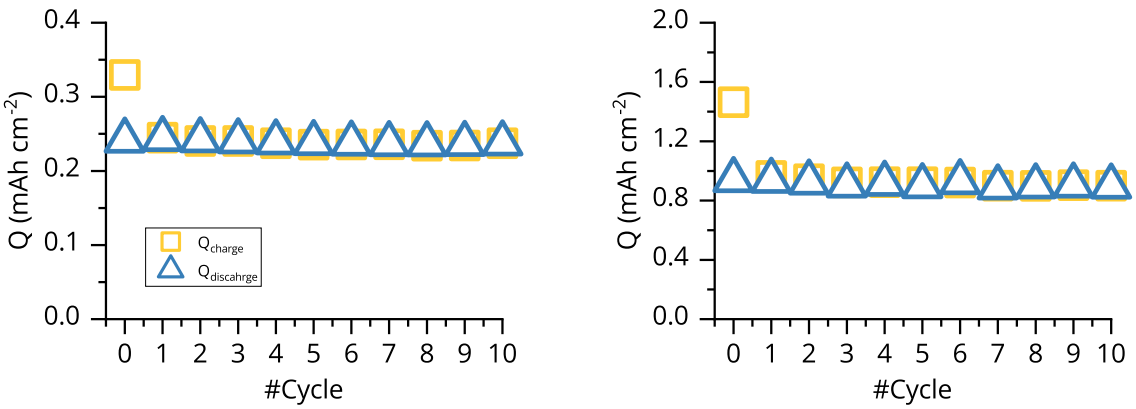

(a) 5 µm thick cathode.

(b) 30 µm thick cathode.

Figure 4.3: Charge and discharge capacity evolution during cycling.

1.2 First cycle loss as a function of cathode thickness

From the simulation, we expect an intrinsic loss of capacity during the very first discharge. In order to validate this prediction, it is possible to compare the capacity between the first charge and the first discharge for different cathode thickness. According to the model, the loss is associated to a certain percentage of the lithium, and should increase with the cathode thickness: the Li_xCoO_2 cannot be replenished above $x = 0.8$, and considering a charged state at around $x = 0.5$ a loss of 40 % of the first charge capacity is estimated. On the other hand, if a loss is associated to other phenomena, like interface degradation and SEI formation, it should not depend on the thickness.

Experimental results

In Figure 4.3a and 4.3b, the charge and discharge capacities are reported for cells with a cathode thickness of 5 and 30 µm. In both cases, the capacity loss is limited to the first cycle. All subsequent cycles show excellent reversibility of the charged capacity. This is, in fact, as expected for a loss associated with dynamic limitation. Interface degradation usually shows an effect that is diluted over multiple cycles, unless a very stable interface is formed. Moreover, even at this level of detail, it is possible to appreciate the stable nature of the loss, whose absolute value seems to scale linearly with the cathode thickness. In order to better appreciate this effect, the first cycle loss alone is reported in Figure 4.4 for all cathode thicknesses. Both charge and discharge capacities increase linearly with the cathode dimension. This is an important aspect, showing that increasing the active material quantity is actually beneficial to the total cell capacity, even if the loss relative value is increased as well. The ratio between the two capacities is slightly higher than expected for the 5 µm cell, while it is closely aligned to the model prediction for all other tested devices. The former is small enough for the interface accumulation zone at the end of the discharge to be comparable to the total cathode thickness. From the precedent chapter, the accumulation zone was estimated around 2 µm.

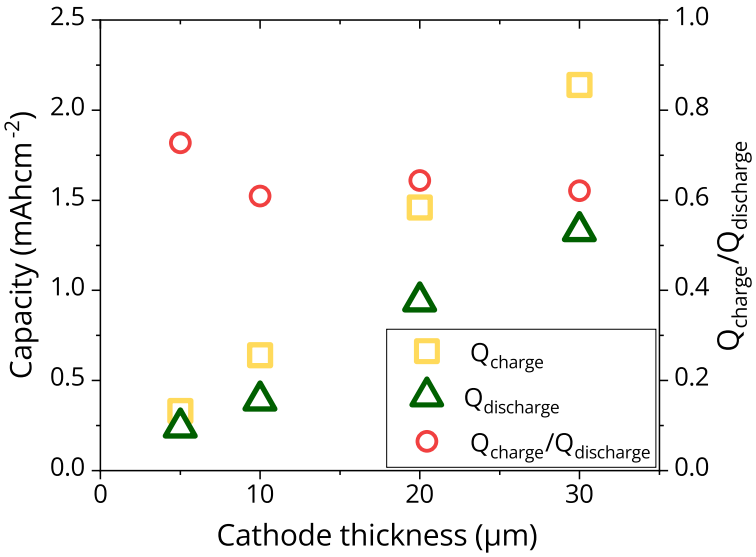

Figure 4.4: capacity loss as a function of the cathode thickness.

Comparison with simulation

The validation of the model prediction can be performed not only from a qualitative point of view but also by direct comparison of the simulated charge and discharge curves with the measured profiles. In Figure 4.5a and 4.5b the results are reported for all cathode thicknesses during both charge and discharge. The general predicted behavior is undoubtedly quite close to the measured one. An interesting difference is the voltage curvature during the phase transition. While in the measured profile the polarization smoothly increases in the early phase of accumulation and then shoots down to the voltage threshold, in the simulated profile the transition is far more abrupt. This is particularly evident in the case of thicker cathodes. The discrepancy can be traced back to two main factors. First, the diffusion coefficient extraction near the phase transition is intrinsically a difficult operation. It is not hard to imagine an increase in the error near this region between the extracted value and the actual value. Second, in the model definition, the interface reaction speed was set high enough to be negligible during normal operation of the cell. As long as the overpotential is linked to the drift current, this hypothesis holds, and an error in the reaction rate estimation does not impact the simulation. Unfortunately, during phase transition, the current and the overpotential, are limited by the interface reaction and the availability of arrival sites. In this case, the actual value of the interface kinetics impacts the simulation, and a proper optimization is required. At this stage, it is not possible to distinguish between the two causes, and correcting in one direction or the other would just be an over-interpretation of the simulation results. In the second part of this chapter, a refinement of the diffusion coefficient by means of X-ray diffraction measurement will enable a more thoughtful analysis of the problem.

1.3 Rate performance as a function of cathode thickness

In the simulation section, the LCO was anticipated to be a slow-discharge material. As a consequence, it is of particular interest to study the evolution of the available capacity during discharge under different currents while keeping the charge process constant to ensure to begin

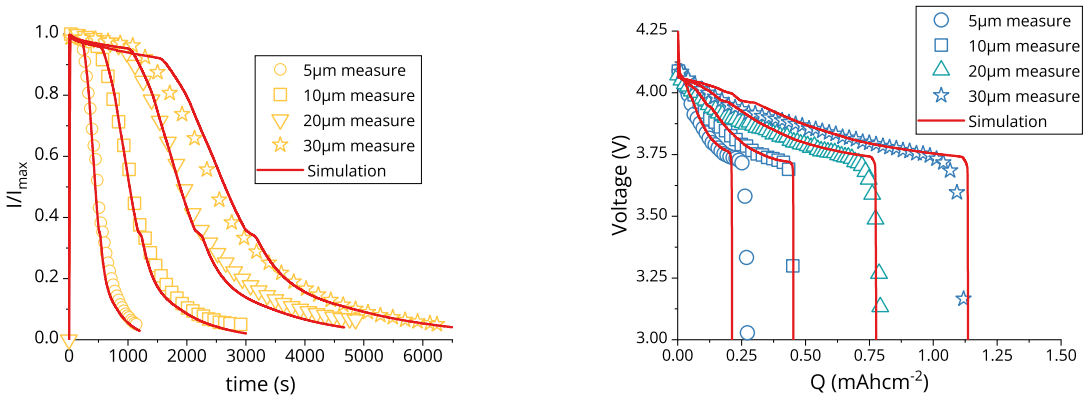

(a) Charge profiles at constant potential (4.3 V).

(b) Discharge profiles at constant current (1 mA cm^{-2}).

Figure 4.5: Charge and discharge simulation and measurement for different LCO thicknesses

from the same starting line.

Discharge rate performances

The first analysis proposed in Figure 4.6a concerns the discharge capacity evolution for a 20 µm thick cathode for discharge current from 0.1 to 4 µA cm^{-2}. The red line refers to the simulated results, which faithfully reproduce the experimental behavior. The curve can be divided into three zones. The first (in green), characterized by a fast capacity loss, and the relatively flat second zone (in blue), are the two already identified during the analysis of the physical model results. In both cases, the limiting factor is lithium diffusion inside the bulk cathode. The third zone (in red) was not previously reported and is associated with the ion drift in the bulk electrolyte. As the current increases, the battery voltage will decrease according to equation 4.2. In particular, at around 3.5 mA cm^{-2} (17 µA), the voltage drop associated with the ion drift is around 0.9 V ($R_{int} = 50$ kΩ for 6 µm LiPON). As a consequence, the voltage plateau associated with phase transition is situated close to the 3 V threshold voltage. Compared to Figure 4.5b, where a large margin is available between the start of the interface accumulation and the cut-off voltage, at higher current, the discharge is stopped before the interface accumulation is actually reached. For high enough current, the cell starts its discharge below the threshold, and zero capacity is available at the imposed conditions. The increase in the error bar in this region is due to experimental variation in the LiPON thickness.

Measurement and simulation results as a function of cathode thickness

Extending the analysis, the model is able to correctly predict the rate performances at all measured thicknesses, as reported in Figure 4.6b. The increase in the slope of the second zone, with increasing LCO thickness, can be understood in terms of the lithium profile inside the bulk cathode. Even if, at iso-current, the slope of the accumulation profile is the same, the value at the interface increases, leading to a larger capacity loss. Considering the simulated profile in Figure 3.10b, the interface concentration for a 20 µm thick cathode at $t = 1000$ s is the same as in a 30 µm cathode, but 10 µm deep into the bulk ($x = 0.7$ instead of $x = 1$). This observation is of interest in order to complete the picture sketch by figure 4.4. Even if, in general, increasing the

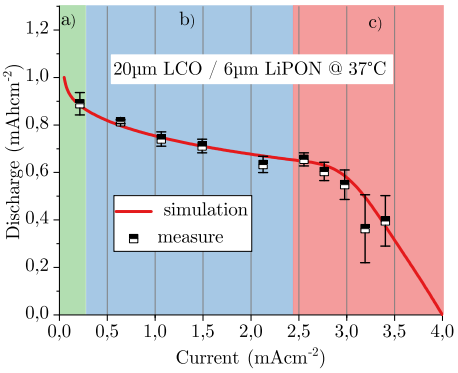

(a) Evolution of the discharge capacity for a 20 µm LCO cell. Zone a): capacity limited by the lithium diffusion in LCO; zone b) flat region associated to high diffusion coefficient in LCO; zone c) capacity is limited by the lithium drift in the electrolyte (IR-drop).

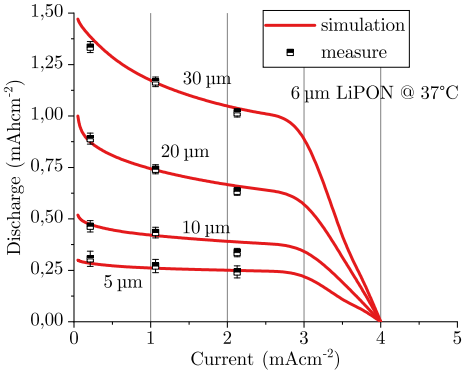

(b) Simulation and measurement of the rate performance for different LCO thicknesses.

Figure 4.6

cathode thickness is beneficial, the actual effect is strongly dependent on the discharge current. For a prescribed current, there is a limit to the maximal cathode thickness, after that, no gain or a loss of volumetric capacity is expected [1].

2. Probing lithium concentration by operando XRD

To really understand the electric behavior of an electrochemical cell, it is necessary to probe some other physical quantities to be coupled with the electrical data. Usually, by accessing the crystal structure or the chemical environment of the electrodes, it is possible to study in detail the evolution of the materials during intercalation and de-intercalation of lithium ions. In the following, I will first present a brief review of operando technique, and in particular XRD operando, and the main results already shared in the literature. One of the main novelties of the results reported in this section, compared to the literature, is the objective of the measurement. In particular, this is the first time, to my knowledge, that the lithium variation along the diffusion axis has been observed for a thin-film, all-solid-state battery with a cathode side above few micrometers in a volume probing configuration. In particular, for the first time, we clearly imaged the phase transition boundary displacement during the operation of a thin-film, all-solid-state LCO cathode. Although composite cathodes have been previously imaged, the actual lithium dynamics is radically different.

2.1 Review of Operando techniques for batteries

Operando measurement are reported for a large set of techniques, including Raman spectroscopy [2, 3], atomic force microscopy [4], optical microscopy [5], electron microscopy, ion beam analysis [6], and various X-ray related techniques (XANES,HAXPES,XRD,XAS,XRF) [7–13]. Even if the technique may differ, the principles of operando measurement are shared, and some general considerations can be drawn for the entire portfolio of available characterization. This is

a particularly important operation in order to choose the right technique and configuration according to the question to be answered.

Setup geometry and probed zone

The first aspect to consider in an operando measurement is the setup, and in particular the cell geometry. The first choice is the orientation of the cell with respect to the impinging probing ray. Considering planar cell geometry, the ray can either be parallel or perpendicular to the cell normal axis (see Figure 4.7). In general, the perpendicular geometry is the most flexible configuration because it permits the probe of any material, no matter the order of the stack. The only problem may be the resolution. In fact, for a technique to be used with this geometry, the lateral resolution has to be smaller than the thickness of each layer, or the signal will be averaged over different materials.
As a second point, we can broadly divide the characterization techniques into surface and volume techniques. The signal for a surface technique, such as optical microscopy, atomic force microscopy or Raman spectroscopy, comes from the first nanometres or micrometers (for Raman) of the cell. In the case of a perpendicular configuration, these techniques permit only the topmost layer to be probed. The main advantage is the high level of precision and details (single particles probing [3, 13]) achievable. In fact, the volume technique's signal comes from the whole volume of the sample and is usually an average over several tens of micrometers. Single particle dynamics is much harder to obtain in this configuration, usually requires complex post-processing, and is prone to artifacts like in the case of X-ray tomography [14–16]. A general aspect to be considered is the representativeness of the measurement with respect to the overall behavior of the cell. Surface techniques, even if they tend to give access to more details, are sometimes far from being representative of bulk behavior. Because at the edge of the cell the parallel plane capacitor hypothesis is no longer valid and the electric field bends, the ions drift may be different with respect to the center of the cell. Moreover, mechanical constraints are much weaker, and ion diffusion also differs due to the blocking interface at the edge of the domain. On the other hand, a volume measurement is sure to be representative of the average behavior of the cell, but depending on the geometrical configuration, a great deal of information may be lost. In fact, in volume measurement, it is much harder to get information about the spatial variation of probed quantities [17].

Probed quantities and dimensionality

Each technique provides access to a unique set of physical information about the cell, but since the setup geometry is fixed, the information provided by each is limited, and a holistic discussion may be of interest to better understand the strengths and weaknesses of each one. A first possible distinction is, in fact, between measurements with or without spatial resolution. Just as an example, a typical powder X-ray diffraction setup will provide zero spatial information; the signal is the average of the whole volume. By decreasing the size of the impinging beam and enabling the sample to be displaced during the measurement, 1D, 2D or 3D spatial information can be added. Because, up to 2D resolution, it is just a matter of displacing the sample on the plane perpendicular to the impinging beam, any technique can virtually be used to acquire a 2D map of the sample. To include the third dimension, which extends in the same direction as the impinging beam, two main strategies are possible. First, in the case of surface probing, it may be possible, by displacing the sample in the third direction, to alter the signal. For example, in Raman spectroscopy, the signal comes from the region around the focus point of the laser beam.

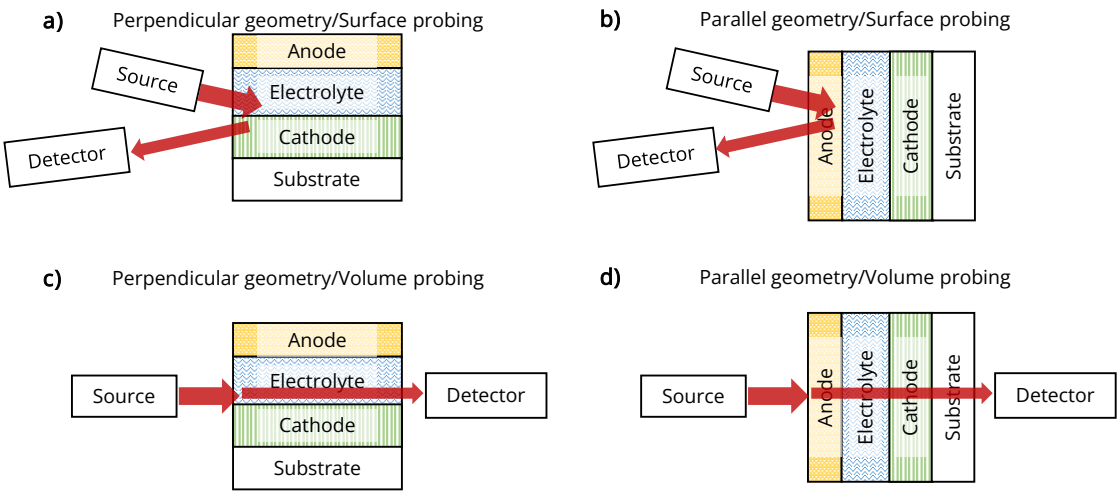

Figure 4.7: Setup orientation for Operando probing of an electrochemical cell.

If the sample is displaced, and as long as the attenuation is not too high, it is possible to produce a 3D image of the analyzed device [18]. The second option, used in the case of volume probing, is to rotate the sample. For each rotation angle, the impinging ray crosses a different portion of the stack. The signal is still averaged, but each time the average is obtained by combining different parts of the full device. It is possible, as in the case of X-ray tomography, to recover the 3D image all at once with proper post-processing of the data. While the first approach can be used to obtain a local 3D image of a region of interest, the second technique can only produce complete images because all rotation angles are needed. This usually results in much longer probing times, even for low-resolution images. 3D probing is in general slow and is rarely used for operando measurement due to the temporal constraint: the cell must be imaged multiple times between the charge and the discharge to follow its temporal evolution.
Depending on the spatial resolution, a different set of questions can be addressed. For example, if we are interested in determining which phases are present in an electrode during charge, a 0D measurement may be enough to obtain a broad answer. On the other hand, to study the dynamics of phase transitions, a minimum of one dimension is needed to follow the phase boundary displacement. We may split the bibliography between the ”what”-is-going-on class [8, 10] and ”where”-it-is-going-on one [3, 12]. Given that the nature of operando techniques automatically includes ”when”. Of course, the higher dimension analysis can always be reduced, and answering to the ”where” question automatically provides information about ”what”.
Focusing on cobalt oxide alone, multiple papers are available in the literature that try to describe both what happens from a physical and chemical point of view and where it happens. In the majority of the work, the analyzed cell is based on composite electrodes, which are commercially available. Before presenting my own results, I will review both the composite and the thin-film bibliographies.

Latest results on LCO

During the intercalation and de-intercalation of lithium ions, LCO withstands various modifications of its crystal structure, including modifications of both the bond length and the crystal symmetry. These phenomena have been extensively studied with more or less all the available operando techniques, at least at the 0D scale. In particular, Raman spectroscopy and X-ray-

based techniques have been used to map the evolution of the crystal structure all along the cycling of the cell [8, 10, 11, 19–22]. This information is particularly important to understand the degradation mechanisms linked to the formation of irreversible phases or to phase-transition-induced mechanical stress.
A second group of papers can be identified, focusing on the spatial description of the lithium intercalation [2, 3, 5, 12, 23–25]. The majority of works of this group is based on surface probing configurations. Some X-ray absorption measurements are actually used for volume probing, but the information obtained is quite limited [7, 26, 27]. In fact, no works have been published on operando X-ray diffraction with a 2D resolution on a pure $LiCoO_2$ cathode. Moreover, the totality of the works are either realized with a composite cathode or with sub-micrometer thin film. Combining the surface analysis with a composite electrode, the probed dynamic is expected to be completely different from that of a $20\,\mu m$ thin-film LCO. As an example, the dynamic that is observed with a surface measurement is linked to the reaction rate and the interface resistance, which determine where and how fast the material is lithiated, but no information about the internal lithium distribution is provided. For example, in the work of Pandya et al. [25], they refer to optical imaging as a "3D" technique. This is in fact not totally correct, because the technique used (reflection confocal microscopy) is in fact capable of imaging 3D surfaces, meaning that the surface is not lying on a plane, but the measurement is restricted to the surface of the particles. This is, of course, almost a philosophical question whether this kind of measurement should be considered 3D, but in any case, no information is provided concerning the internal state of each imaged particle. In the same work, the phase boundary displacement on the surface of the particle is imaged and the phase front velocity extracted. Notwithstanding, the imaged dynamics have nothing in common with the actual phase transition. The front velocity is not only linked with the lithium diffusion inside the particles but is mainly impacted by the surface reaction speed. To describe this case with a simile, it is like trying to calculate the diffusion of coffee into a biscuit by dipping it into a mug and measuring the wetting of the external part. Of course, the wetting speed at the exterior will be determined by the speed at which we are dipping the biscuit and not by the coffee diffusion coefficient. If only the tip of the biscuit is plunged, the situation is indeed different, but in our situation, this can be accomplished only with a non-porous electrode, where the electrolyte contact with the electrode is limited to the top interface. A thin-film, all-solid-state configuration is the best option to ensure proper experimental conditions.
Back to the bibliography, it is true that surface work on thin-film should still be representative of the overall lithium diffusion (as in [24]), but from the simulation chapter we already expect the diffusion to be a limiting factor for cathodes thicker than a few hundreds of nanometers. The available papers are limited to very thin cathodes, and the results are not sufficient to study the LCO limitation linked to lithium diffusion and phase transition.

2.2 Synchrotron X-ray diffraction measurement setup

For the probing of the lithium distribution inside a thin-film cathode, synchrotron radiation is necessary for both its power and resolution. Because the adopted geometry, as described below, is the perpendicular one coupled with volume probing, it is necessary for the impinging beam to be powerful enough to cross the full thickness of the cell without the attenuation to suppress it. In particular, the cell under test has a total thickness around $300\,\mu m$. With a standard, lab-scale copper X-ray source, it would be impossible to cross such a distance. Moreover, the needed resolution to map the lithium concentration along the substrate axis is around $1\,\mu m$, according to the simulation results. The resolution is determined by the beam dimension, and once again,

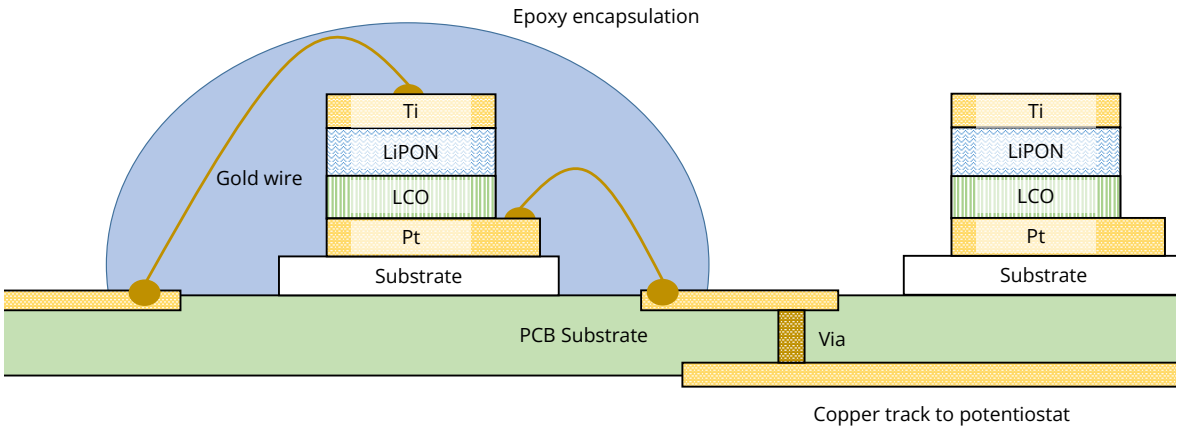

Figure 4.8: Custom PCB used for operando synchrotron X-ray diffraction measurement.

only synchrotron sources can achieve such a beam size. In our case, the beam size was slightly lower than 1 µm and the radiation wavelength was 0.6881 Å (energy around 18 keV).

Setup and geometry

A custom setup has been developed in order to probe multiple cells at the same time without any manual intervention or recalibration. The cells are attached to a printed circuit board (PCB), and the contact between the cell and the board is realized by means of wire bonding, as reported in Figure 4.8. The cells are encapsulated with epoxy to both protect the golden wires and prevent lithium oxidation during battery operation. Up to 10 batteries can be connected to the same PCB. Because the X-ray beam is aligned with respect to the board, it is possible to test any of the cells without recalibration of the measurement system. This is particularly important considering the fragility of the bonding, which may break during transport, and the possibility of cell failure during operation. With a fair number of cells, it is possible to minimize the risk of failing the analysis and the need to change the PCB and realign the whole setup. The PCB is connected directly to a potentiostat. Each cell has its own testing channel, and parallel charge and discharge are possible. The remaining part of the setup (Figure 4.9) is a standard synchrotron X-ray configuration, with a collimator and beam stopper before and after the cell, in order to reduce the beam size and divergence and block the X-ray source beam from impinging the detector. A screen detector is placed around 10 cm from the probed device. In order to map the X-ray signal for both the y and z-axis, the sample holdercan be displaced in both directions during the measurement. For each acquisition time, an image of 50 x 50 pixels is recorded, with a step of 30 µm along the y-axis and 1 µm along the z-axis.

Probed quantities

Measurement output is composed of two types of data. The first is the measurement of X-ray absorption by each material. In Figure 4.10, the absorption map of a 30 µm thick LCO cell is reported. The signal is mostly attenuated by the cathode, which contains heavy cobalt atoms. Gold wire and titanium contacts are still visible, even if the absorption is much lower. LiPON, polymer passivation layer, and the epoxy encapsulation are almost invisible. The absorption data is particularly useful during the preprocessing of the diffraction spectra in order to correct the intensity, as described in the next section.

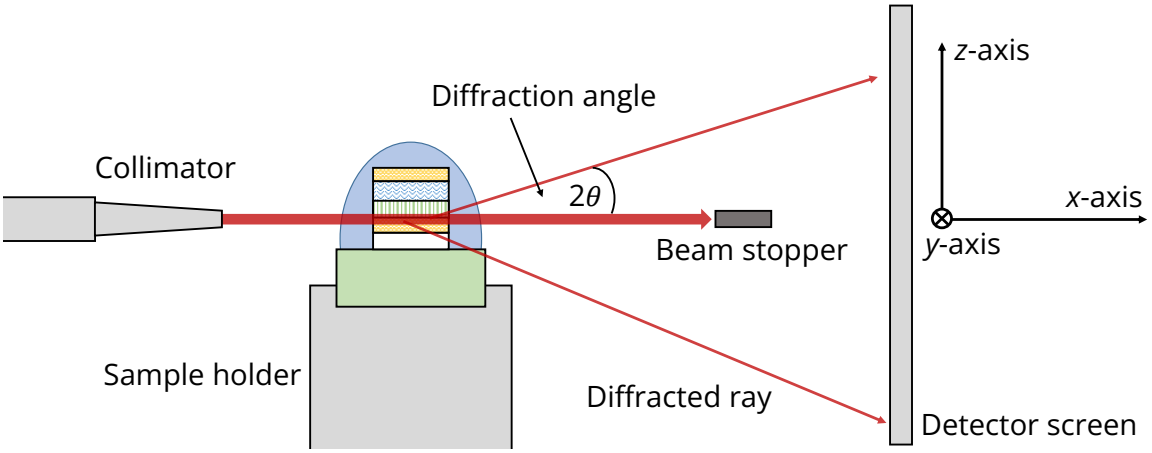

Figure 4.9: Complete setup for operando synchrotron X-ray diffraction measurement.

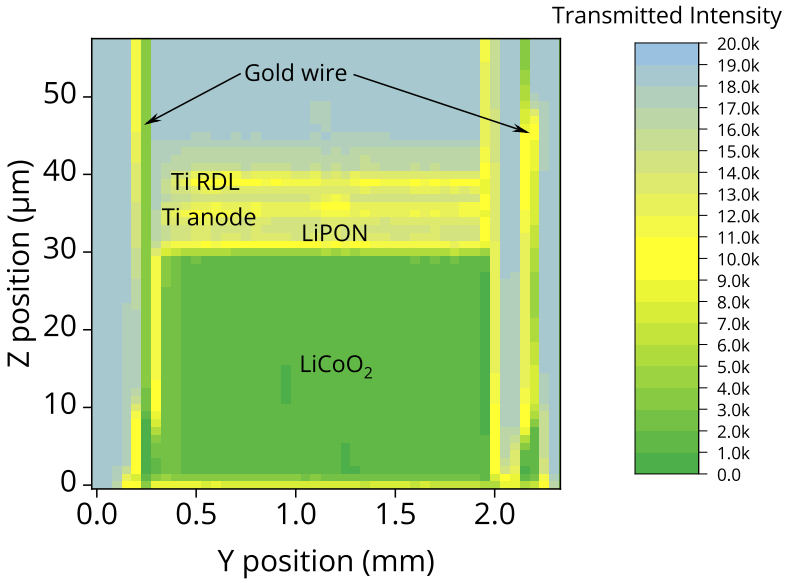

Figure 4.10: Xray absorption 2D mapping of a cell with $30\,\mu$m-thick cathode.

Much richer information comes from the diffraction pattern acquired for each pixel of the absorption image. At each (z, y)-position, diffraction rings, such as the ones shown in Figure 4.11a, are registered. The pattern is projected on a screen detector, and the raw format is an image on the z-y plane. In the same image, it is possible to notice how the signal in the top half of the screen is more intense with respect to the bottom half. This is a partial shadowing effect of the PCB substrate and sample holder; only diffraction rays pointing downward are attenuated by the substrate. The data are reported in polar coordinates, with r the distance from the beam center and ψ the angle on the z-y plane. Knowing the distance d between the sample and the screen, it is possible to convert the radius into the angle θ (see Figure 4.9):

$$2\theta = \tan^{-1}\left(\frac{r}{d}\right) \tag{4.3}$$

In the new coordinates, the same diffraction pattern looks like the one reported in Figure 4.11b. Each crystal plane pattern is projected on a circle in the natural coordinates and along a line in the $\theta - \psi$ coordinates. The angle θ is the usual angle used in the indexation of XRD patterns, as

reported in the second chapter. The angle ψ offers additional information that is not accessible by a standard power diffraction experiment. In fact, while the θ angle is used to identify which crystal plane is being observed, the ψ angle describes the rotation of the normal vector of the plane around the x-axis. For example, the spot at around $2\theta = 8°$ refers to the (003) plane. From Figure 4.11b it is possible to read the relative rotation of the vector normal to the (003) plane, for example, $\psi = 90$ indicates a normal vector pointing upwards with respect to the cell substrate. From such an analysis, it is possible to study the texture of the thin film along the diffusion axis and reinforce the homogeneity hypothesis used in the physical modeling.
As briefly discussed in the second chapter and in the previous section of the literature review, the expansion of the cathode matrix during cycling results in a movement of the peaks' θ-position. In particular, an increase in the atomic plane distance along a certain direction induces an increase in the diffraction angle. In general, the ψ position is not expected to change unless the mechanical stress is such as to physically displace the LCO crystals, which is not the case considering the low volume expansion of the cathode during cycling. Notwithstanding, the relative ψ-position of each spot is valuable information. We already pointed out that the diffusion inside 2D material is influenced by the relative orientation between the diffusion direction and the diffusion planes. Certain orientations will be more favorable, and a different lithiation velocity may be observed by following each spot individually. Before delving into the static and dynamic analysis of the XRD patterns, I will spend one last section discussing the pre-processing used on the raw data in order to correct various artifacts.

2.3 Data preprocessing

The preprocessing of the raw data consists of two main steps. First, any misalignment of the relative position between the detector and the diffraction should be corrected. This procedure aims to correct the θ-position of each diffraction spot. Then, in order to correct the relative intensity, it is necessary to compensate for the different absorption as a function of the ψ and θ angles.

Detector position correction

In Figure 4.12 the ideal and skewed detector geometry are reported. In ideal geometry, the X-ray beam source is normal to the detector plane. In this configuration, each (nhk) diffraction plane , is mapped onto a circle on the screen detector with center O and radius r. In reality, the detector screen may be skewed by an angle α along a certain direction. In this case, the circle is projected on the skewed plane as an ellipse with a center O'. The presence of a skew in the detector position is easily spotted if the raw diffraction pattern is zoomed in the ψ-θ representation. As an example, in Figure 4.13a it is possible to observe the sinusoidal shape of the diffraction spots distribution. The artifacts appear during the conversion from the raw data to the ψ-θ representation: the center is considered equal to the position of the beam stopper, which is the correct assumption in ideal geometry, and the distance r calculated accordingly. Coming back to the raw data, it is possible to fit different ellipses for each diffraction ring and trace the variation of the center position as a function of the mean distance from the beam center. In Figure 4.13b the center position for three rings is reported, and a linear drift is observed. In particular, the drift is concentrated on the z-axis of the detector. The skew angle α can be calculated with trigonometry, along with its direction, which, in this case, is assumed to be parallel to the z-axis to simplify the problem. The first step is to find the "real" center by extrapolating the center position for $r' \to 0$. In general, it should coincide with the point of incidence of the main beam, but

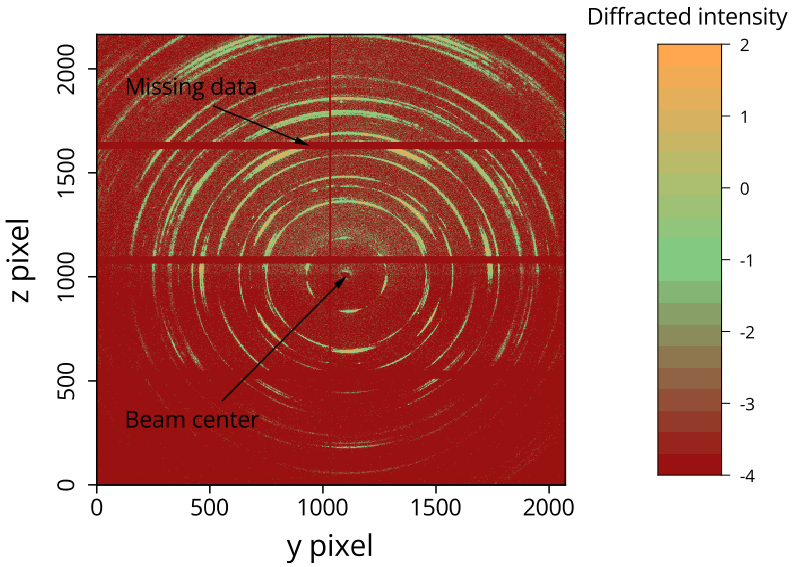

(a) Diffraction rings on the detector

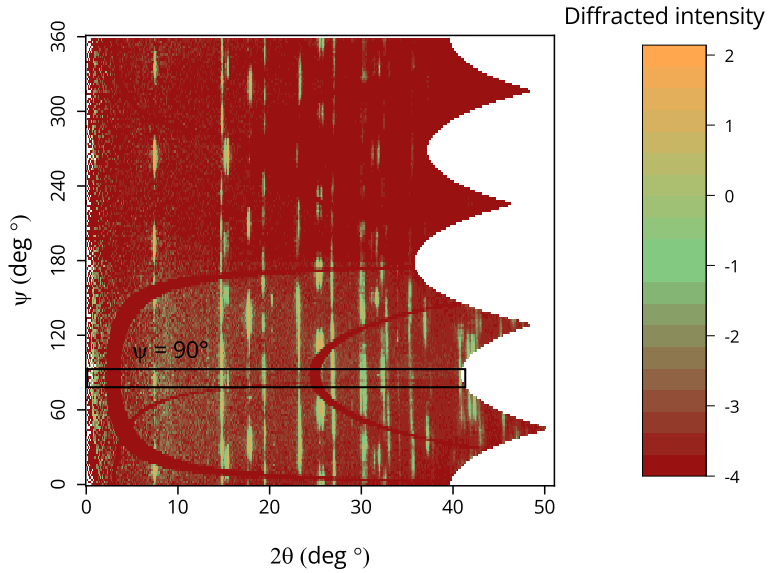

(b) Example of diffraction pattern for a pixel in the cathode domain in the $2\theta - \psi$ representation.

Figure 4.11

with this procedure, its position can be further refined. Once the center is known, it is possible to obtain the "ideal" r by simply considering the direction of the skew plane perpendicular to the skew direction. Along this direction, r and r' are coincident. Knowing the center, the distance $\overline{AO}$ can be calculated altogether with the angle $2\theta = \tan\left(\frac{r}{d}\right)$. Then, by focusing on the scalene AOA' along the skew direction and by knowing two sides and one angle, it is possible to solve it. In particular, $\angle AAO' = \frac{\pi}{2} + 2\theta$ and α is found by solving the following system of equations in

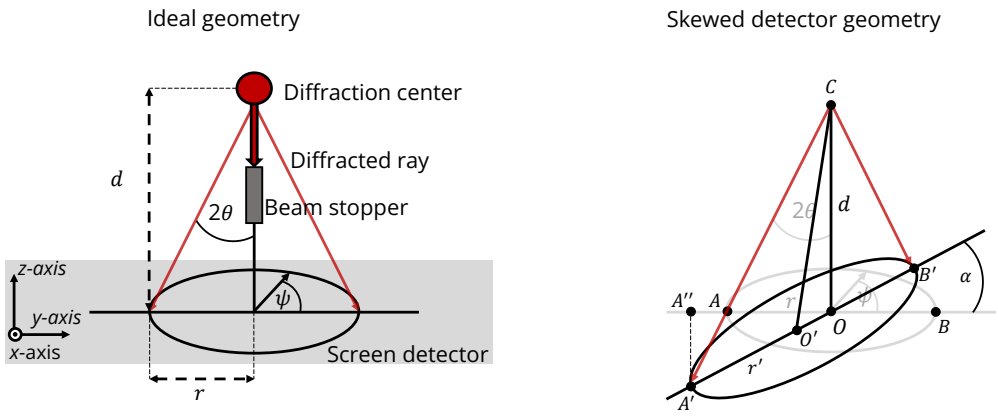

Figure 4.12: Effect of an α skew on the measurement geometry.

$\overline{AA'}$:

$$\begin{cases} r'^2 = \overline{AA'}^2 + r^2 - 2\overline{AA'}r\cos\left(\frac{\pi}{2} + 2\theta\right) \\ \overline{AA'} = r^2 + r'^2 - 2rr'\cos\alpha \end{cases} \tag{4.4}$$

Once α is known ($\alpha_0 = 6°$ in the present case), in order to get the "real" angle 2θ at any position,

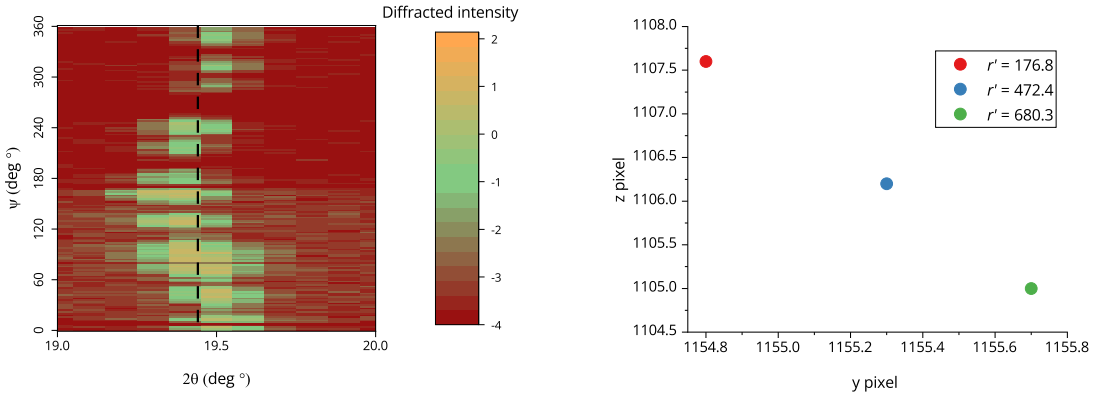

(a) Sinusoidal shape of the diffraction ring due to detector skew.

(b) Center position of the fitted ellipsis for different distance from the beam center.

Figure 4.13

it is necessary first to solve the scalene COA'. This is indeed a trivial task since we know two sides ($\overline{A'O} = r'$ and $\overline{CO} = d$) and the angle in between ($\angle COA' = \frac{\pi}{2} \pm \alpha$). The sign depends on the relative direction with respect to the skew vector: positive for the r' z-component in the same direction as the skew vector and vice versa. According to the rule of cosines:

$$\overline{A'C} = \sqrt{r'^2 + d^2 - 2r'd\cos(\frac{\pi}{2} \pm \alpha)} \tag{4.5}$$

At this point, the 2θ angle is calculated by inverting the same formula applied to r':

$$\cos(2\theta) = \frac{d^2 + \overline{A'C}^2 - r'^2}{2d\overline{A'C}} \tag{4.6}$$

and the radius on the ideal plane is:

$$r = d\tan(2\theta) \tag{4.7}$$

The only tricky point is the actual value of α with respect to the ψ position: The angle is $\alpha = \alpha_0$ only along the skew direction (i.e., the z-axis), while in general the skew goes from α_0 to zero (along the y-axis). To solve this second problem, it is enough to consider the unitary circle on the skew plane and its orthogonal projection to the ideal plane. It must be noticed that the orthogonal projection differs from the stereographic projection considered for the diffracted ray. In particular, in Figure 4.12, the points A and A' are one the stereographic projection of each other, while the orthogonal projection of A' on the ideal plane is A''. In Cartesian coordinates, the relation between the two points is:

$$\begin{cases} y'' = y' = r' \sin\psi \\ z'' = z' \cos\alpha = r' \cos\psi \cos\alpha \end{cases} \tag{4.8}$$

The right triangle $A'A''O$ formed by the two vectors can be easily solved, and the angle $\angle A''OA'$ obtained as:

$$\angle A''OA' = \alpha(\psi) = \cos^{-1}\left(\frac{\overline{OA''}}{\overline{OA'}}\right) = \cos^{-1}\left(\frac{\sqrt{\sin^2(\psi) + \cos^2(\psi)\cos^2(\alpha_0)}}{1}\right) \tag{4.9}$$

Where r' is the unit by construction and $\alpha(\psi)$ is the skew angle as a function of the psi angle. Back to equation 4.6 and with a bit of trigonometry, the final expression for 2θ reads:

$$\cos(2\theta) = \frac{d^2 \pm 2r'd(\pm^*1)\cos\psi\sqrt{1-\cos^2\alpha_0}}{2d\sqrt{r'^2 + d^2 \pm 2r'd(\pm^*1)\cos\psi\sqrt{1-\cos^2\alpha_0}}} \tag{4.10}$$

Where the second plus-minus sign ($\pm^*$) refers to the conversion from sine to cosine and depends on the quadrant of ψ: positive for $0 < \psi < \pi$. The total sign, $\pm \cdot \pm^*$ is negative in the first and third quadrants and positive otherwise.
I will conclude with a final remark on the distance d. So far, the distance between the diffraction center and the incident point of the beam on the screen was supposed to be known. In general, when the distance is measured or provided by the instrument, it may refer to another point of the detector, the base of the displacement motor, for example. In this case, the distance should be considered a variable, and the problem cannot be solved analytically. Notwithstanding, if a known diffraction pattern is used for the calibration, the distance and the skew angle can be optimized by the mean square algorithm in order to fit the calibration signal.

Absorption correction

The second artifact to be considered is linked to the attenuation as a function of the ψ and $theta$ angles. In Figure 4.14a the schematic optical path for different diffraction directions is reported. Depending on both angles, the diffracted beam crosses different materials and different thicknesses of the same material. For example, the uppermost beam exits from the $LiCoO_2$ after a short path and gets into the LiPON. For the same angle θ, but at opposite ψ, the same signal is entirely attenuated by LCO, and the total attenuation is greater. The same consideration is valid for the last shown path, with a higher diffraction angle. It is attenuated by cobalt oxide alone, but the optical path and the resulting attenuation are larger. This is the very same principle as the shadowing of the bottom part of the detector screen, as already observed in Figure 4.13a. In this case, the difference in attenuation is so high that the bottom part of the detector is barely exploitable for $\theta > 25°$. In order to avoid additional bias, I restricted the analysis to the top part of the detector only ($0° < \psi < 180°$) or low diffraction angle ($2\theta < 15°$) .

To calculate the effective attenuation at each (r, ψ) position on the screen, it is necessary to use the absorption matrix ($\mu(r, \psi)$) as reported in Figure 4.10. At this point, it is important to consider the finite thickness of the sample. In fact, the diffraction will take place along the whole thickness l of the cell. That means that at each spatial element $dV(x, r, \psi)$ diffracts but the impinging power is attenuated for spatial elements closer to the detector. Vice versa, the elements closer to the source are hit by a more energetic beam, but they have to cross a longer optical path in order to reach the detector. In summary, for each spatial element, it is necessary to calculate the attenuation before and after the diffraction takes place. The total attenuation for a volume element at position (x, r, ψ) can be expressed as:

$$I(x, r, \psi) = I_0 \exp\left(-\mu(r, \psi)x\right) \exp\left(-\int_{r=0}^{r=(l-x)\tan(2\theta)} dr\, \frac{\mu(r, \psi)}{\sin(2\theta)}\right) \tag{4.11}$$

Where I_0 is the output power of the source, the first exponential is the attenuation before diffraction, and the second one is the sum of the attenuation in each volume element crossed after diffraction. It should be considered that the diffraction at different x-positions results in a broadening of the diffraction spot because the effective distance d is different for each volume element. The total intensity on each pixel is given by summing the intensity impinging on the same pixel of the screen from different volume elements. As a matter of example, I reported the evolution of the calculated attenuation as a function of the ψ position for the peak (003) of LCO in Figure 4.14b. As expected, the maximum of attenuation is attained for $\psi = 0$ and $\psi = 180$. The relative intensity of peaks on the same diffraction rings (same θ-value), once corrected for absorption, can be directly compared in order to establish the presence of each ψ orientation. For example, in Figure 4.11b, the diffraction plane (003) ($2\theta \sim 8°$) exhibits six evenly spaced peaks at $\psi = 20° + n60°$. By comparing the relative intensities of each, the texture of the film as a function of the z-position can be estimated. There is also another possibility, in order to evaluate the preferential orientation of the film, that exploits the principle proposed in the second chapter by comparing the measured pattern with a reference signature from powder diffraction. In the case under analysis, this second approach, presented in the next subsection, is of particular interest due to some missing data, as visible in Figure 4.11a and 4.11b. The detector is composed of multiple smaller screen detectors, and at the junction point between each subunit, the data is not registered. By chance, the peaks (003) at $\psi = 20°$ and $\psi = 140°$ are partially lost, and the direct comparison of diffraction peak intensity would result in a biased estimation. Moreover, the (003) peak is the only one not strongly attenuated by the PCB horizon and was the best candidate for texture analysis.

Dimension reduction and powder comparison

In the second chapter, in order to assess the texture orientation and its distribution along the z-axis of the LCO, the diffraction pattern relative intensities were compared with the powder reference, for which the orientation is completely random. The powder reference pattern is a 1D spectrum without any resolution with respect to the ψ angle. In fact, in a standard powder diffraction experiment, the detector and the impinging ray are always at $\psi = 90°$. With respect to the full signal of Figure 4.11b, a powder diffraction spectrum is limited to the area of the black rectangle. In order to be able to analyze the texture of the thin film LCO starting from the synchrotron signal, it is enough to extract and integrate along the ψ axis the signal inside the rectangle and reduce the dataset dimension to θ only:

$$I_{powder}(2\theta) = \int_{\psi=85°}^{\psi=95°} d\psi\, I_{synchrotron}(\psi, 2\theta) \tag{4.12}$$

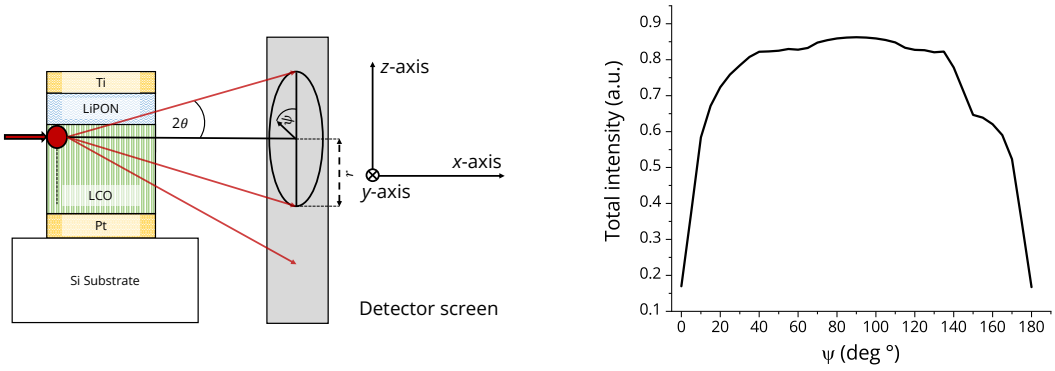

(a) Effect of θ and ψ position on the optical path and the resulting attenuation.

(b) Calculated attenuation as a function of the ψ angle for $2\theta = 10°$.

Figure 4.14

Where the integration limits are chosen in order to mimic the finite dimension of the powder diffraction detector.
All results are presented in the next section.

2.4 Diffraction pattern analysis

All data reported in the followings refer to a $20\,\mu$m thick LCO cell. First, I will present the initial state 2D mapping in order to extend the texture results already introduced in the second chapter. Then, I will focus on the temporal evolution of the crystal structure and, in particular, the distance between the (003) planes (c-axis). The distance correlates with lithium content, and the lithium profile can be extracted from it in order to be compared with the simulation results. Phase transition dynamics during charge and discharge is analyzed, and differences between the model and the measures are discussed.

XRD spectra indexing

In order to index of the diffraction peaks, the starting point is the integration of the signal from the detector in the range $0 < \psi < 180$. The resulting spectra and their indexation have already been reported in Chapter 2 (see Figure 2.9). Once the different diffraction planes are defined, it is possible to focus on the intensity and position of single peaks in order to study the cathode texture and behavior during cycling.

Out-of-fab 2D mapping

In order to analyze the texture, the synchrotron spectrum was further restricted to the $\psi = 90°$ zone to be comparable with the GIXRD reference as discussed in the previous section, and only the predominant 003 ($2\theta \sim 8°$) and 012 ($2\theta \sim 17°$) orientations were considered. As already discussed in Section 2.2, it is possible to map the relative abundance of each orientation by comparing the measured intensity and the powder reference intensity. The following formula was employed:

$$\frac{(003)}{(012)} = \log_{10}\left(\frac{I_{003\_measured}}{I_{003\_reference}}\frac{I_{012\_reference}}{I_{012\_measured}}\right) \tag{4.13}$$

If the ratios between the measured and the reference intensity for the two orientations are equal, the relative abundance is $1:1$ and $\frac{(003)}{(012)} = 0$. If the texture is preferentially (003), let's say $10:1$, $\frac{(003)}{(012)} = 1$ while it will be $\frac{(003)}{(012)} = -1$ in the opposite case ($1:10$). The resulting 2D texture map is reported in Figure 4.16a for the first time step. In particular, as already anticipated in the second chapter, the top part of the cathode tends to be slightly (003) oriented: $\frac{(003)}{(012)} = 0.2$ corresponds to a less than $1.6:1$ texture distribution. While near the current collector and in bulk, the film is strongly oriented along the (012) axis.
Another important point is the homogeneity along the y-axis of the crystalline orientation. This observation permits reducing the analysis to the z-axis only. In particular, by averaging the signal along the y-position which largely increases the quality of the data.

The second approach to map the relative orientation abundance is by direct comparison of

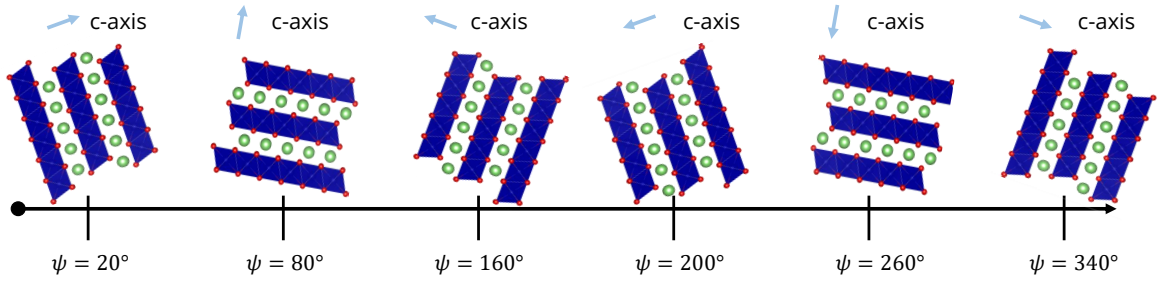

Figure 4.15: Position of the c-axis of the LCO crystal for different ψ angle position of the 003 peak.

different diffraction spot along the ψ direction of a certain diffraction plane. As anticipated, the (003) diffraction is of particular interest because it is the only one not attenuated by the substrate. It exhibit, as anticipated in figure 4.11b, six diffraction peaks along the $\psi axis$. Each peak correspond to a different orientation of the 003 vector with respect to the deposition substrate. In particular, the vector normal to the (003) diffraction plane is called c-axis. In Figure 4.15 the relative position of the c-axis with respect to the diffraction angle ψ is reported. It can be observed that with respect to the orientation of the diffusion channel the xis peaks correspond to only 2 different channel orientation. For $\psi = 80°, 260°$ the channel are parallel to the deposition substrate and diffusion in hindered. Any other ψ angle correspond to a favourable orientation with almost perpendicular channels (equivalent to a (012) orientation). In order to avoid the missing data zone, only the three peaks at $\psi > 180$ are considered. Because the two peaks at $\psi \sim 200°$ and $\psi \sim 340°$ correspond to the same (012) orientation of the film, it is enough to compare the central peak ($\psi \sim 260°$) corresponding to the (003) unfavourable orientation with the sum of the other two in order to reproduce the result of the previous analysis. In Figure 4.16b the logarithm of the ratio of the intensity is reported, and the same conclusion is reached: partial (003) texture on the top of the film and a majority of (012) in the central/bottom part.

Operando 2D mapping: charge

To study the evolution of the crystal structure during charge and discharge processes, I focused on the same three (003) peaks used for the texture mapping. By following the displacement of the diffraction peaks, it is possible to follow the lithium diffusion process inside the cathode. The peak profile is analyzed by means of skewed Gaussian fitting in order to extract the exact peak position. The c-axis dimension is then calculated from the diffraction angle with the formula:

$$d = \frac{n\lambda}{2\sin\theta} \tag{4.14}$$

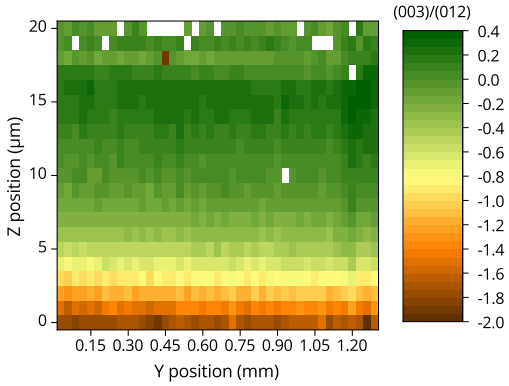

(a) Texture mapping inside the LCO cathode obtained with GIXRD-like method analysis.

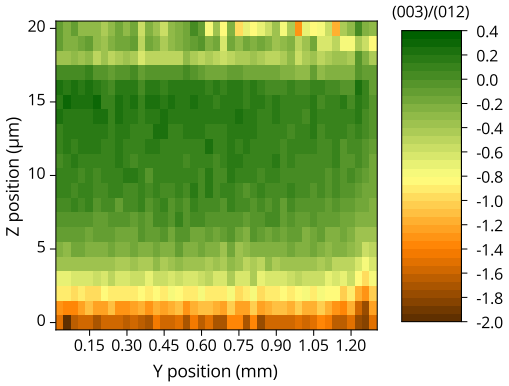

(b) Texture mapping inside the LCO cathode obtained by direct comparison of (003) peaks intensity.

Figure 4.16: Cathode texture distribution at initial time step.

Where λ is the X-ray wavelength and n is the Miller plane index ($n = 3$ for the (003) plane).
In Figure 4.17a-4.17f I reported the 2D mapping of the c-axis dimension for the $\psi = 200°$ peak at six different time steps. The first three images correspond to the inset and propagation of the phase transition boundary from the electrode/electrolyte interface to the current collector interface. The yellow zone corresponds to the $Li_{0.75}CoO_2$ phase, while the dark orange one is stoichiometric LCO. The following three images are taken from the second part of the charge, when lithium intercalates homogeneously through the entire thickness thanks to a high diffusion coefficient. In fact, the images do not show a gradient, and the color is homogeneous at each time step. The total variation of the c-axis dimension is around 0.3 Å. As for the texture mapping, the cathode behavior is homogeneous along the y-axis. In order to facilitate the reading and for a more qualitative assessment of the data, in Figure 4.17g, the average c-axis dimension is plotted as a function of the z-position. This second plot is nothing but the average of the 2D mapping. The same six time steps are reported as for the 2D mapping graphs. In this case, the phase boundary profile can be fully appreciated. The profile shape is stable, and the displacement velocity can be calculated by taking the middle point (in red in the plot) and tracing its z-position as a function of the time step. As a quick estimation, considering an average acquisition time of 180 s the phase front displacement is about $35\,\mathrm{nm\,s^{-1}}$.
In Figure 4.17h the average c-axis dimension is plotted for the topmost, central and last pixel as a function of time. Apart from a delay, displacement of the diffraction peak is constant along the whole cathode thickness, and the total displacement is in good agreement with literature results [10, 19]. The initial absolute value (14.25 Å) is higher than previously reported in the literature (14.05 Å). This discrepancy may be linked to the distance between the sample and the screen detector, as described in the artifacts correction section.
In Figure 4.17i the c-axis dimension variation along the z-position is reported for the diffraction peak at $\psi = 260°$. This orientation corresponds to a diffusion channel oriented parallel to the substrate. Which is a particularly unfavorable situation for lithium diffusion, as confirmed by the measured crystal axis variation. In fact, the total c-axis variation is much lower than for the other two orientations, signaling a smaller lithium de-intercalation for crystals with the (003) orientation. Luckily, from the texture mapping, the relative fraction of (003) orientation was confirmed to be overall negligible, and no impact on the available capacity has been measured. An import-

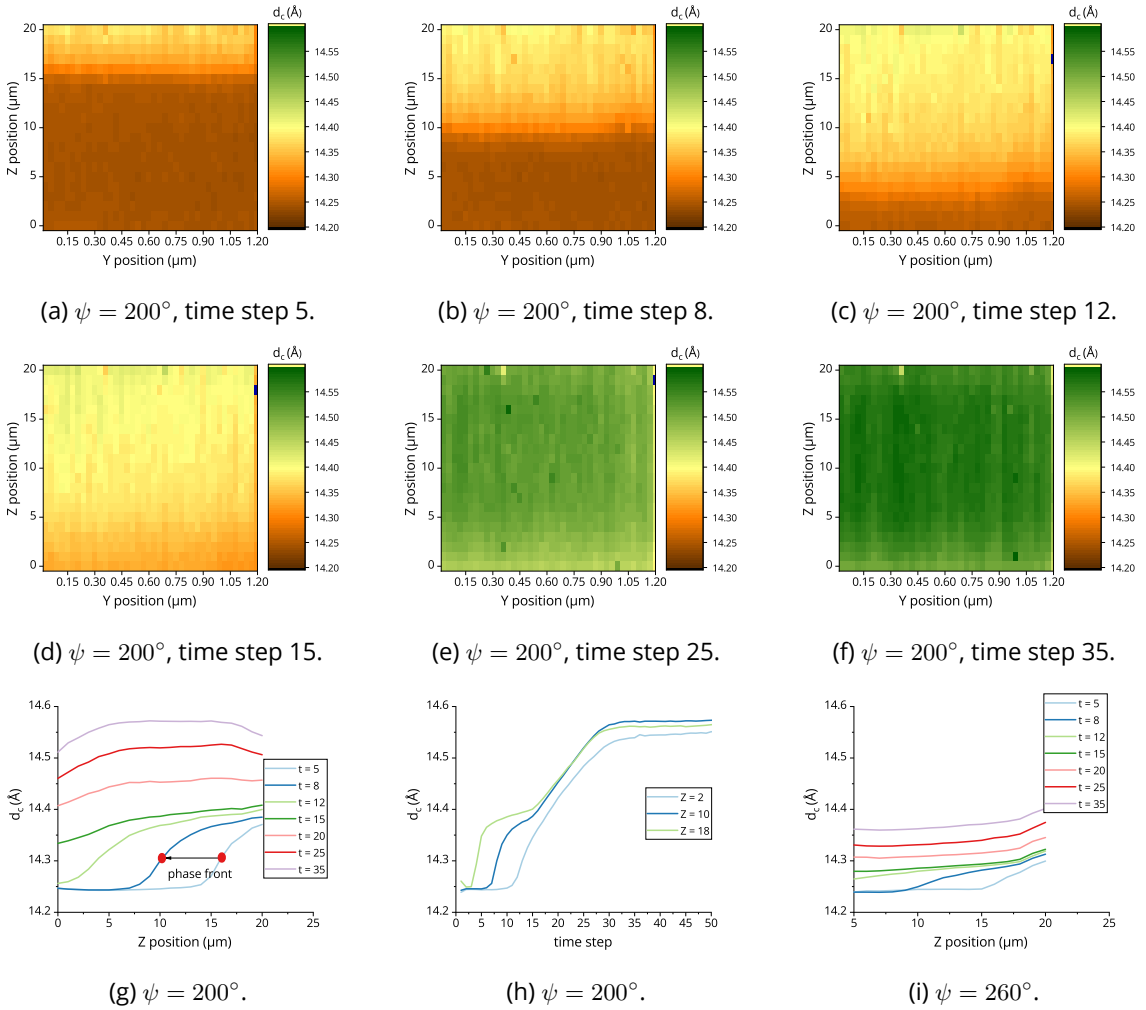

(a) $\psi = 200°$, time step 5. (b) $\psi = 200°$, time step 8. (c) $\psi = 200°$, time step 12.

(d) $\psi = 200°$, time step 15. (e) $\psi = 200°$, time step 25. (f) $\psi = 200°$, time step 35.

(g) $\psi = 200°$. (h) $\psi = 200°$. (i) $\psi = 260°$.

Figure 4.17: 2D mapping of the (003) diffraction plane c-axis dimension during charge.

ant aspect is the presence of the same two-phase regions as for the other crystal orientation. The phase boundary is still visible, but the gap between the lithium poor and lithium rich phases is less than half compared to the (012) orientation. In order to explain this phenomenon, it should be considered that the total ion current splits unevenly between the two orientations. We may expect only a small fraction of the total current to be accounted for by the (003) orientation. The difference is linked to the difficult intercalation, but inside the two domains, no difference in lithium diffusion is expected. Put differently, the (003) orientation should just charge much slower than the (012), but with identical dynamics. Notwithstanding, the observed phase transition profile differs. In the "hard" phase transition picture, as predicted by the Cahn-Hilliard model, the phase formation is linked to interface energy balance, and its onset is linked exclusively to the local stoichiometry of LCO. On the other hand, in the diffusion-limited picture, as adopted in the present work, the phase separation is a dynamic phenomenon induced by the current density. In this second framework, it is much easier to interpret the different behavior of the (003) orientation. Recalling the extracted diffusion coefficient as reported in Chapter 3, its minimum is around $x = 0.95$, and a monotonic increasing is observed for lower lithium fractions. The two-phase distance is determined by the current, in the sense that the accumulation spans the lithium fraction with a diffusion coefficient too low to redistribute the incoming lithium flux. Let's try to picture the situation with a water pipe analogy. The water flux represents the ions

diffusing through the cathode, and the diffusion coefficient is a measure of the size of the pipe. The intercalation fraction can be interpreted as the pressure inside the pipe. If the pipe is flexible, we can imagine that an increase in the water pressure (intercalation fraction) leads to a stretch of the pipe and an increase in its section. If the initially imposed input flux is higher than the flux the pipe can sustain, the pressure rises. That is the beginning of the charge, when the interface concentration of lithium quickly drops because the diffusion is too slow to replenish it. The increase in pressure (lithium depletion) leads to an increase in the pipe diameter, and more water can cross per unit time. In equilibrium, the pressure is such that the pipe diameter is a perfect fit for the input flux. That is also the case for the cobalt oxide: the value of the interface accumulation is such that the diffusion coefficient is high enough to sustain the input current. That means that it is the input current that fixes the stoichiometry of the lithium-poor phase. As a matter of example, if the (012) orientation current density needs at least a diffusion coefficient of $1 \times 10^{-14}\,\mathrm{m^2\,s^{-1}}$, the phase separation region will span between $x = 1$ and $x = 0.75$, when the diffusion coefficient reaches the minimum redistribution value. On the other hand, in the (003) orientation, the current density is much lower, and a diffusion coefficient of, let's say, $1 \times 10^{-15}\,\mathrm{m^2\,s^{-1}}$ is enough. In that second case, the phase transition zone will end at around $x = 0.8$ (See Figure 3.9b).

Operando 2D mapping: discharge

The same analysis is proposed for the discharge step in the sequence of Figures 4.18a- 4.18f. The picture is inverse with respect to the charge. In the first part (Figure 4.18a-4.18c), the c-axis is constant along the whole cathode thickness, and the discharge proceeds homogeneously. Near the end of the discharge, a sudden change is registered at the electrolyte/electrode interface. In Figure 4.18d and 4.18e the formation of an orange interface, linked to the high lithium content phase, is visible at the topmost pixels. As soon as the $3\,\mathrm{V}$ threshold is crossed and the discharge is stopped, the cell switches to the relaxation step. The lithium-rich interface disappears (Figure 4.18f) at this stage, signaling an unstable phase boundary. By analyzing the average profile along the z-axis in Figure 4.18g the discharge dynamics can be appreciated from a quantitative point of view. The interface formation results in a sudden decrease in the fitted peak position. The same decrease is clearly visible when the time evolution of the topmost pixel is plotted (Figure 4.18g). As expected from the 2D map, the lithium-rich phase is formed only at the top interface. By analyzing the raw data reported in Figure 4.18h during the final time steps of the discharge, it is possible to distinguish two peaks. The first one at around $c = 14.3\,\text{Å}$, corresponding to the lithium-rich phase observed in the initial state (see Figure 4.17h), and a second one at $c = 14.45\,\text{Å}$. During the end of the discharge, the two phases $LiCoO_2$ and $Li_{0.8}CoO_2$ are then both present at the interface. The actual coexistence of the two phases cannot be discussed due to the measurement setup: each pixel is the average over $300\,\mu\text{m}$ and it is not possible to determine whether the cathode presents multiple single-phase domains or a single solid-solution domain with both phases coexisting.
In any case, the lithium-rich phase relaxes as the discharge ends. This is a second important clue to support the hypothesis of a dynamics-induced phase transition, as proposed in the modeling section. Hard phase transition mechanism, such as the one modeled by the Cahn-Hilliards equation, would result in a stable interface without any relaxation between the two phases.

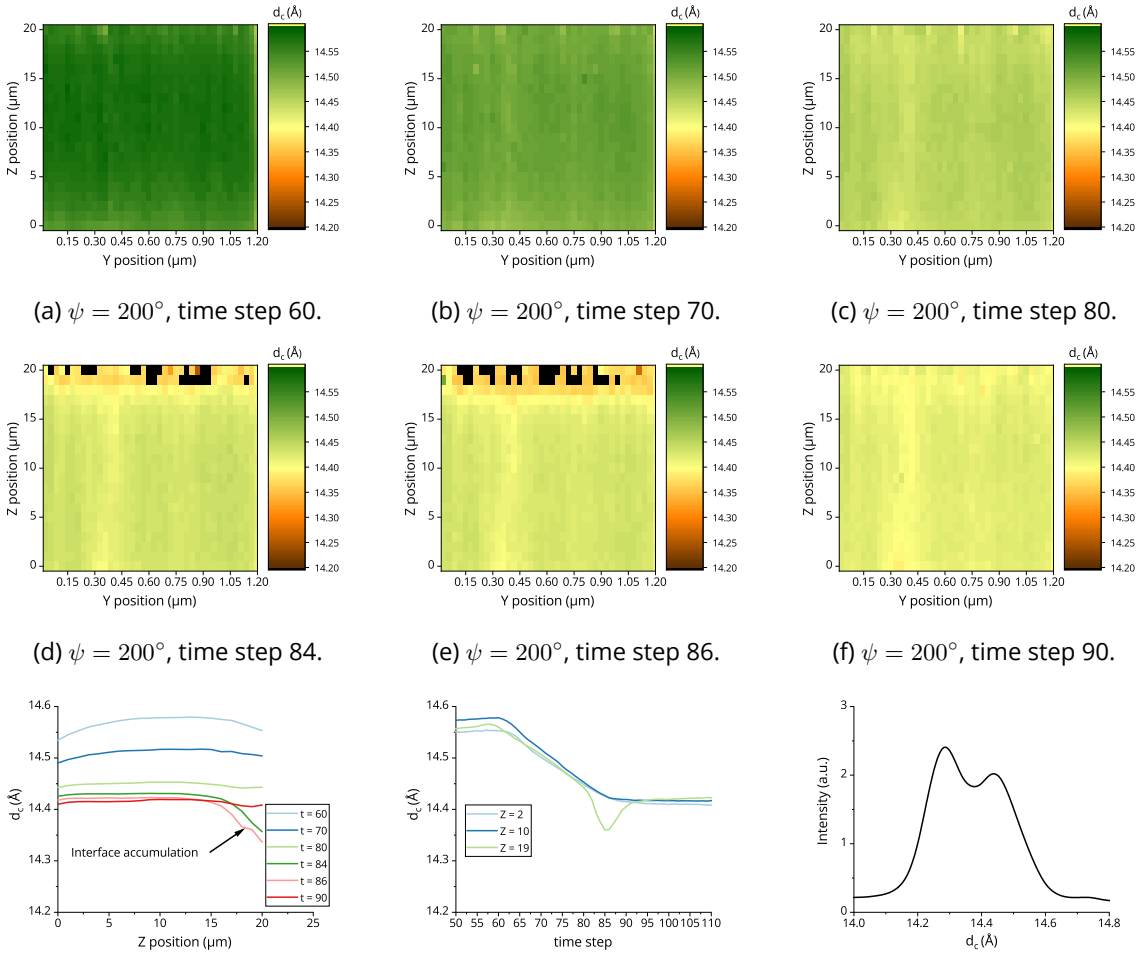

(a) $\psi = 200°$, time step 60.

(b) $\psi = 200°$, time step 70.

(c) $\psi = 200°$, time step 80.

(d) $\psi = 200°$, time step 84.

(e) $\psi = 200°$, time step 86.

(f) $\psi = 200°$, time step 90.

(g) $\psi = 200°$.

(h) $\psi = 200°$.

(i) Peak splitting during interface accumulation (Zpos 20, time step 84).

Figure 4.18: 2D mapping of the (003) diffraction plane c-axis dimension during discharge.

2.5 Comparison with model results

In order to compare the measured profiles with the simulation results, it is first necessary to convert the variation of the crystal axis to lithium concentration. I assumed a linear variation of the plane distance with respect to the lithium concentration, as previously reported in the literature [19]. The total distance variation is 0.33 Å at the $Li_{0.47}CoO_2$ end phase. The end of charge stoichiometry is determined by measuring the OCV after charge (around 4.2 V) and using the GITT measurement as a calibration curve. The linear conversion equation between the plane distance and the intercalation fraction is then:

$$x_{Li} = (d_c - min(d_c)) * \frac{0.53}{0.33} \tag{4.15}$$

The converted profiles at different time steps are reported in Figure 4.19a for the two-phase regime of the charge. The second-phase stoichiometry is around $Li_{0.8}CoO_2$. The distance between the two hexagonal phases (~ 0.15 Å) is in agreement with the most recent literature [10].
Altogether with the profile variation along the Z-axis, it is of interest to evaluate the model prediction against the interface concentration variation as the redox reaction is impacted by the

interface concentration only (see Figure 4.19b as an example). Starting from the observed behavior, it is possible to improve the simulation quality near the end of the discharge: if the simulated and measured lithium profiles are in good agreement, the error in the predicted cell voltage will most probably be linked with the reaction rate coefficient; on the other end, if the lithium profiles are too far apart, the cause should be found in an error in the extraction of the diffusion coefficient.
As the conversion to lithium concentration seems to be satisfactory and in line with the literature, it is possible to proceed with a direct comparison between the measured and the simulated lithium profiles.

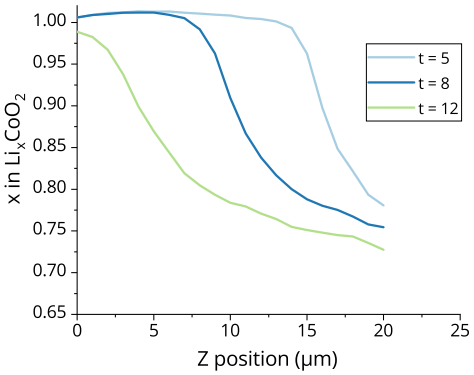

(a) Lithium concentration profile along the cathode thickness during the charge phase transition derived according to equation 4.15.

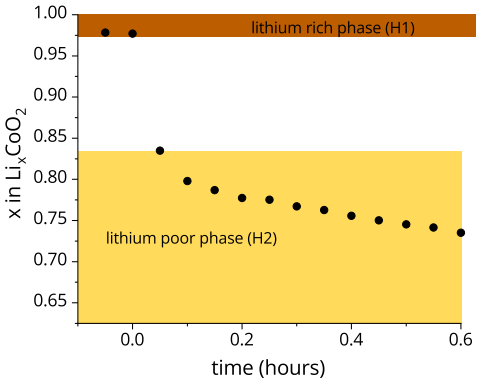

(b) Lithium concentration at the electrode/electrolyte interface during the charge phase transition.

Figure 4.19

Phase transition dynamics

The first point of interest is phase transition dynamics. In particular, the shape of the phase front and the lithium profile in the lithium poor region can be easily compared for the simulated and measured profiles, as reported in Figure 4.20a. The phase front displacement is correctly modeled from the point of view of the speed, but the shape itself is much steeper for the simulated profile. This means that the GITT diffusion coefficient variation is faster in the lithium-rich phase compared to the real one. In particular, in order to obtain a more flat phase boundary, it would be necessary to increase the diffusion coefficient in the region $0.9 < x < 0.8$. Concerning the slope in the lithium-poor region, the model and the measurement are in good agreement (see the slope near the electrode/electrolyte interface for $t = 12$). As a more detailed verification, the concentration profile is reported in Figure 4.20b. While the bulk profile is not completely satisfactory, the interface concentration is properly reproduced. That means that the extracted diffusion coefficient is close to the real one for lower lithium content, and the extraction error is limited to the phase transition region.

Interface accumulation

The second important feature to benchmark in the physical model is the interface accumulation at the end of the discharge. In Figure 4.21a, the simulated and measured lithium profiles during

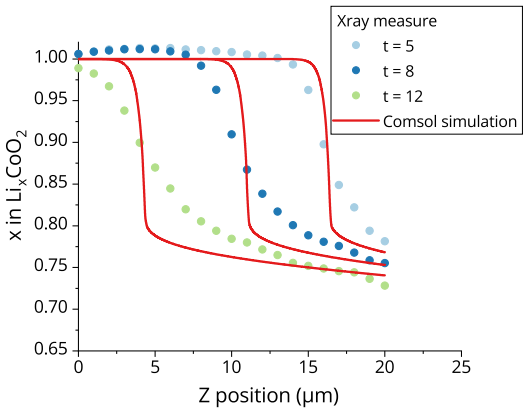

(a) Simulated and measured lithium concentration profile along the cathode thickness during charge.

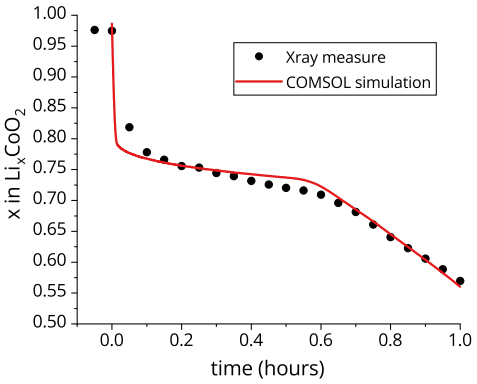

(b) Simulated and measured interface lithium concentration evolution during charge.

Figure 4.20

discharge are reported. Before the onset of the interface accumulation, the model is able to follow the measured profile, except for the zone near the current collector. The measured profile shows a positive curvature, while the simulation is (relatively) flat. The difference is due to the initial condition imposed in the simulation. The starting profile is fixed to $x = 0.5$ everywhere in the cathode domain, considering a perfect relaxation after charge. In reality, the discharge is started immediately after the charge, and the curvature, which is a residue of the first phase transition, does not have time to relax. As a matter of fact, it relaxes during the discharge itself, and by step $t = 80$, the accumulation near the current collector has almost completely disappeared.

As the final accumulation starts, some major differences are visible. While the general trend (accumulation and relaxation) is confirmed, the simulated cathode provides more capacity than measured. In fact, as clearly reported in Figure 4.21b, the concentration profile monotonically increase up to $x = 0.75$, before a sudden upswing, while in the measure the same accumulation starts at around $x = 0.7$. Moreover, the measured profile presents a smoother transition, with a lithium accumulation reaching deeper inside the cathode. This observation combines with the one already discussed during the analysis of electrical results. The simulation presents an abrupt transition in the voltage profile while the measured voltage slowly increases before shooting to $3\,\mathrm{V}$ (see Figure 4.5b). From the analysis of the charge profile, an error in the value of the diffusion coefficient for higher intercalation fraction has already been spotted. It is possible to explain the difference in the discharge profile with the very same argument. In particular, the real diffusion coefficient is expected to be smoother with respect to the one from the GITT measurement. A smoother profile guarantees a more flat shape during both charge and discharge, as well as a faster accumulation during discharge and an early crossing of the $3\,\mathrm{V}$ threshold.

At the same time, some information can also be obtained regarding the diffusion coefficient far from the accumulation region $x < 0.7$. Comparing the simulated and measured slopes near the current collector, the simulation shows a larger gradient (see $t = 84$) with respect to the measured profile. We can hypothesize a diffusion coefficient higher than the measured one in this region.

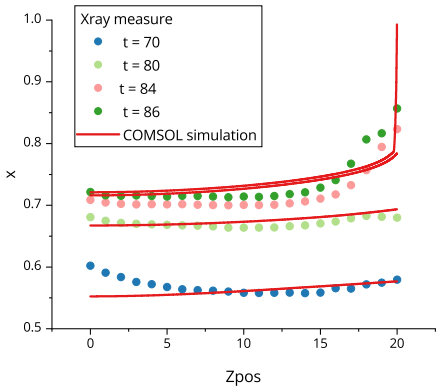

(a) Simulated and measured lithium concentration profile along the cathode thickness during discharge.

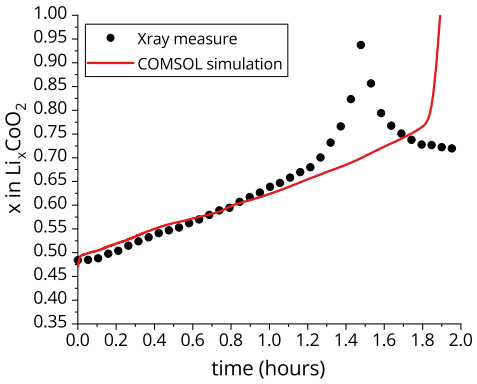

(b) Simulated and measured interface lithium concentration evolution during discharge.

Figure 4.21

Acknowledgements

The synchrotron experiments were conducted on the ID13 beamline at the European Radiation Synchrotron Facility (ESRF, Grenoble France). We acknowledge the beamline scientist M. Burghammer and our local contact A. Medjahed for their help and support. Beamtime at the ESRF was granted within the Battery Pilot Hub MA4929 "Multi-scale Multi-techniques investigations of Li-ion batteries: towards a European Battery Hub" coordinated by CEA-IRIG. Moreover We thanks Sandrine Lyonnard, Samuel Tardif, and Quentin Jacquet from the CEA-IRIG STEP laboratory for the opportunity to collaborate, for the organisation of the experiment and the help they provided with the data analysis and interpretation and the fruitful discussions.

3. Understanding LCO Limitations

The concluding section of this chapter aims to summarize the results obtained for thick cathodes from both electrical and physical point of view. The purpose is then to propose a deeper and novel interpretation of the physical mechanisms limiting the discharge capability of $LiCoO_2$.

3.1 Review of $LiCoO_2$ performances

Starting from the physical model, it is possible to predict the performance of a cell based on the LCO cathode for different current densities and cathode thicknesses. It is of interest, first, to compare the predictions with the thin-film literature, disregarding composite and porous cathodes. Then, in order to assess if some of the limitations here observed are specific to this configuration, extend the analysis to any type of cathode based on the same material.

Thin-film rate performance and projections

In Figure 4.22, I reported the projected discharge volume energy density for a cell composed of a $100\,\%$ active cathode in a thin-film configuration with variable thickness and an overhead of

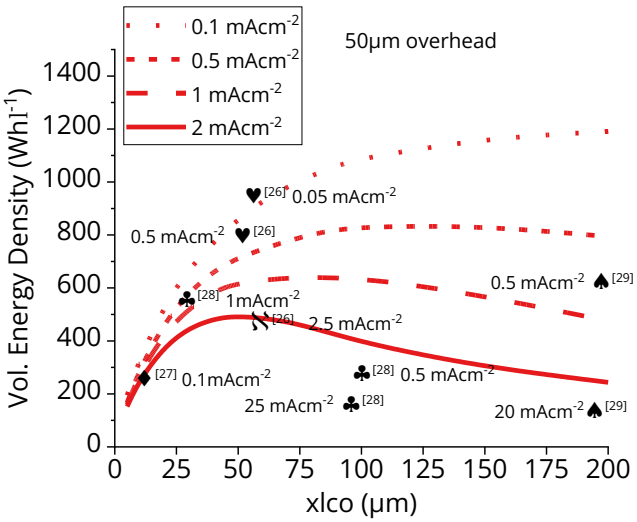

Figure 4.22: Reported [28–31] and projected discharge performances for a thin-film cell based on LCO cathode with 50 µm overhead (non active material) as a function of the cathode thickness and the discharge current density.

50 µm. The overhead refers to the other components of a cell, such as the substrate, the electrolyte and the encapsulation. In order to compare results from the literature, the same overhead was added to any cell before calculating the volumetric energy density. Sources from the literature [28–31] are in good agreement with the model projection from the qualitative point of view, with some divergence in the absolute value for a few of them. That confirms the generality of the first cycle loss and the dynamic limitation described in the present work in the field of thin-film LCO cathode.
Concerning the shape of the curve reported, at lower current density, the increase of the cathode size is always beneficial up to 200 µm; as the current is increased, after a first raising of the gain, eventually, an increase in the size results in a loss of volumetric capacity. That means that for a given application, as the discharge current density is fixed, it is possible to define an optimal cathode thickness that maximizes the energy density. The choice of the value of overhead impact affects not only the absolute value of the volumetric energy density, but also the relative gain when the cathode is increased. Considering that an increase in cathode is also an increase in cost, depending on the overhead, it may or may not be economically of interest to increase the thickness up to the optimal point.

Porous and composite LCO cathode performance

When enlarging the field of view to any type of cathode based on LCO, it is easy to be persuaded that the first cycle loss is not a universal phenomenon. Even if some studies report the same loss in the slurry or composite cathodes [32–35], other works reported a good reversibility of the first cycle [5, 36, 37]. Concerning the composite cathode, the loss is often associated with a low electronic conductivity due to the grain-to-grain contact and is not exclusively related to ion diffusion and phase transition.

3.2 Interface accumulation: ions perspective and electrons perspective

The diffusion framework in a composite or slurry cathode is completely different from that in a thin-film cell, and the direct comparison of the dynamic performance between the two structures is a complex task. In particular, even if the single particles of a composite cathode are the same size as the thickness of a thin-film cathode, the total thickness of the composite electrode is around tens of micrometers. The dynamic of the single particle is hence comparable with that of a thin-film cell, but the overall performance is expected to differ. Before trying to explain the different behavior of LCO in the various cathode configurations, I will recap the main result obtained so far.

Summary of experimental data

From the experimental results collected in the present work, a few central facts can be listed concerning the capacity loss and the dynamic limitation of the LCO thin-film cathode. First, the first cycle loss is shown to be proportional to the cathode thickness; hence, it is linked with bulk phenomena. Second, from the X-ray diffraction experiment, it is confirmed that, before reaching the end of the discharge, lithium accumulates at the electrode/electrolyte interface. This same accumulation is shown to be unstable, and after a few minutes of relaxation, it disappears. Third, the same phenomenon is present during the charge process, but it has no effect on the rate performance of the cathode, which can be easily charged at high current density.
From the literature, the lithium-rich phase is known to be electrically insulating. As a consequence, at high lithium intercalation fractions, the motion of electrons and ions cannot be considered independent because the metallic conductor hypothesis is no longer valid. The LCO in the low-conductive state is closer to an electrolyte than to an electrode. As a consequence, the lithium motion is subject to both drift and diffusion, while the electrons are not able to cross the lithium-rich region.

Ion and electron path analysis

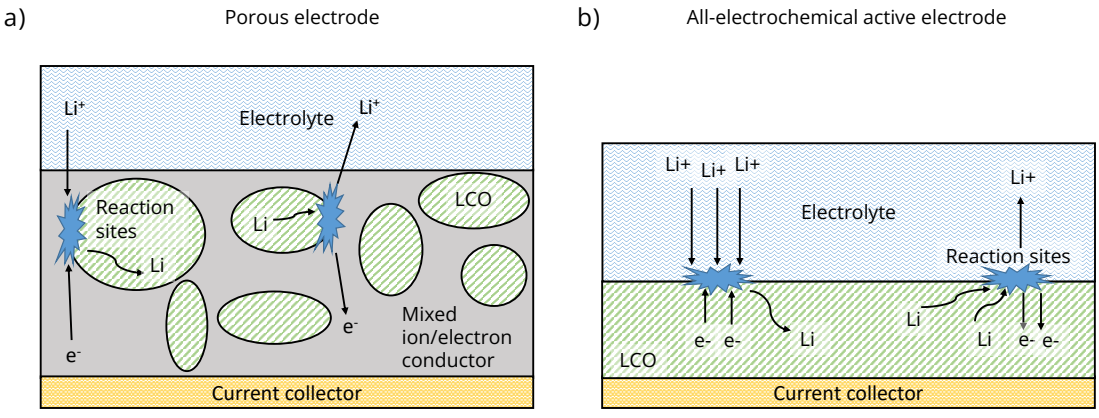

Figure 4.23: Lithium and electron path during intercalation and de-intercalation in porous electrode and thin-film electrode.

If we consider at the same time the electrons and the ions, by comparing the relative paths of the two species in the all-electrochemical active configuration and in the composite electrode

configuration, it may be possible to get some sense out of the literature results.
Let's consider two cathodes realized starting from the same amount of active material, i.e., LCO. In the first one, the LCO powder is embedded in a carbon matrix, forming a porous composite electrode, while in the second one, it is composed of active material alone (all-electrochemically active electrode). In Figure 4.23a, the intercalation and de-intercalation of lithium in the composite cathode are schematically depicted. During the charge of the cell, the lithium diffuses to the interface of a particle before being split into a lithium ion and an electron. Both species have to cross the matrix in which the particles are encapsulated. This matrix is usually highly electronically conductive and porous. The porosity of the matrix permits the electrolyte to permeate the matrix, increasing its ions' conductivity. During the discharge, the lithium from the electrolyte is recombined with electrons from the current collector. Both ions and electrons do not interact with the LCO particles until the recombination takes place.
In the case of all-electrochemically active electrode, the situation is quite different, as reported in Figure 4.23b. While the ions' path is the same during charge and discharge with respect to the composite electrode, that is not the case with electrons. In order to reach or leave the reaction site at the electrode/electrolyte interface, electrons have to cross the LCO itself. During the charge process, the cathode is initially insulating, meaning that the valence band is fully occupied, and the conduction band is empty. As soon as the lithium reacts and a free electron is generated, the latter will fill a place in the conduction band. We already discussed this point, saying that in an intercalation cathode, the electronic carrier concentration is imposed by the intercalation fraction, as in a doped semiconductor. That means that any additional lithium atom removed from the cathode will act as an additional doping atom. As a result, the electrons will be easily able to cross the cathode and reach the current collector. Even if the lithium is not able to diffuse from the lithium rich phase to the lithium poor phase, it will be possible to extract more lithium and sustain the interface reaction.
In the opposite situation, when the lithium is intercalated, at the interface the conduction sites are depleted as the discharge proceeds. During charge, the electrons from the reaction are created at the interface, in this case, they come from the current collector. The increase in the resistance near the reaction interface will make it harder to bring electrons to the interface in order for the reaction to happen. At the same time, the depletion of the conduction band near the interface results in sluggish lithium diffusion due to the reduction in electric field screening. The increase in interface lithium concentration results in higher resistance, and this positive feedback leads to a fast end of the discharge. The main difference between charge and discharge is the physical location of the lithium accumulation. In the former, the accumulation takes place in bulk, away from the reaction zone. In the latter, the accumulation limits the concentration of electrons at the reaction interface, resulting in an increase in overpotential. With respect to all-electrochemically active, in a composite electrode, the electrons do not cross the LCO, but are distributed by means of the conductive matrix. As a matter of fact, the resistance experienced by the current going from the current collector to the reaction site is constant at any state of charge. The increase in the overpotential is limited to the accumulation of ions at the interface and does not have to account for an increase in the electron resistance as well. That means that in any case, the situation is more favorable in the composite and slurry cathodes.
In order to improve the dynamic performance of a all-electrochemically active cell, it would be necessary to design an alternative path for electrons from the current collector to the reaction interface, avoiding the crossing of the LCO itself. Further investigation into this possibility is needed to verify the proposed interpretation.

Bibliography

Electrical Characterization of Thick Cathodes

[1] Jacopo Celè et al. “Minimal Architecture Lithium Batteries: Toward High Energy Density Storage Solutions”. en. In: *Small* 19.16 (Apr. 2023), p. 2207657. DOI: 10.1002/smll.202207657.

Probing Lithium Concentration by Operando XRD

[2] Toshio Nishi, Hideki Nakai and Akinori Kita. “Visualization of the State-of-Charge Distribution in a LiCoO $_2$ Cathode by In Situ Raman Imaging”. en. In: *J. Electrochem. Soc.* 160.10 (2013), A1785–A1788. DOI: 10.1149/2.061310jes.

[3] Hitoshi Fukumitsu et al. “Development of In Situ Cross-Sectional Raman Imaging of $LiCoO_2$ Cathode for Li-ion Battery”. en. In: *Electrochemistry* 83.11 (2015), pp. 993–996. DOI: 10.5796/electrochemistry.83.993.

[4] Jing Zhu, Li Lu and Kaiyang Zeng. “Nanoscale Mapping of Lithium-Ion Diffusion in a Cathode within an All-Solid-State Lithium-Ion Battery by Advanced Scanning Probe Microscopy Techniques”. en. In: *ACS Nano* 7.2 (Feb. 2013), pp. 1666–1675. DOI: 10.1021/nn305648j.

[5] Alice J. Merryweather et al. “Operando optical tracking of single-particle ion dynamics in batteries”. en. In: *Nature* 594.7864 (June 2021), pp. 522–528. DOI: 10.1038/s41586-021-03584-2.

[6] Sören Möller et al. “Absolute Local Quantification of Li as Function of State-of-Charge in All-Solid-State Li Batteries via 2D MeV Ion-Beam Analysis”. en. In: *Batteries* 7.2 (June 2021), p. 41. DOI: 10.3390/batteries7020041.

[7] Nozomu Ishiguro et al. “Comprehensive Operando Visualization of the Electrochemical Events in the Cathode/Anode Layers in Thin-Film-Type All-Solid-State Lithium-Ion Batteries”. en. In: *ACS Appl. Energy Mater.* 6.15 (Aug. 2023), pp. 8306–8315. DOI: 10.1021/acsaem.3c01441.

[8] Hisao Kiuchi et al. “Operando hard X-ray photoelectron spectroscopy of LiCoO2 thin film in an all-solid-state lithium ion battery”. en. In: *Electrochemistry Communications* 118 (Sept. 2020), p. 106790. DOI: 10.1016/j.elecom.2020.106790.

[9] Shuaifeng Lou et al. “Insights into interfacial effect and local lithium-ion transport in polycrystalline cathodes of solid-state batteries”. en. In: *Nat Commun* 11.1 (Nov. 2020), p. 5700. DOI: 10.1038/s41467-020-19528-9.

[10] Kazuhiko Mukai, Takeshi Uyama and Takamasa Nonaka. “Revisiting LiCoO $_2$ Using a State-of-the-Art *In Operando* Technique”. en. In: *Inorg. Chem.* 59.15 (Aug. 2020), pp. 11113–11121. DOI: 10.1021/acs.inorgchem.0c01598.

[11] Tsuyoshi Ohnishi, Kazutaka Mitsuishi and Kazunori Takada. “In Situ X-ray Diffraction of $LiCoO_2$ in Thin-Film Batteries under High-Voltage Charging”. en. In: *ACS Appl. Energy Mater.* 4.12 (Dec. 2021), pp. 14372–14379. DOI: 10.1021/acsaem.1c03046.

[12] Wenxiong Zhang et al. “Chemical-state distributions in charged LiCoO2 cathode particles visualized by soft X-ray spectromicroscopy”. en. In: *Sci Rep* 13.1 (Mar. 2023), p. 4639. DOI: 10.1038/s41598-023-30673-1.

[13] Joshua W. Gallaway et al. “An Operando Study of the Initial Discharge of Bi and Bi/Cu Modified MnO_2”. en. In: *J. Electrochem. Soc.* 165.13 (2018), A2935–A2947. DOI: 10.1149/2.0221813jes.

[14] G. R. Davis and J. C. Elliott. “Artefacts in X-ray microtomography of materials”. en. In: *Materials Science and Technology* 22.9 (Sept. 2006), pp. 1011–1018. DOI: 10.1179/174328406X114117.

[15] S. Bruns, S.L.S. Stipp and H.O. Sørensen. “Looking for the Signal: A guide to iterative noise and artefact removal in X-ray tomographic reconstructions of porous geomaterials”. en. In: *Advances in Water Resources* 105 (July 2017), pp. 96–107. DOI: 10.1016/j.advwatres.2017.04.020.

[16] Andrew Maurice Kingston et al. “X-Ray Ghost-Tomography: Artefacts, Dose Distribution, and Mask Considerations”. en. In: *IEEE Trans. Comput. Imaging* 5.1 (Mar. 2019), pp. 136–149. DOI: 10.1109/TCI.2018.2880337.

[17] Joseph I. Goldstein et al. *Scanning Electron Microscopy and X-Ray Microanalysis*. en. New York, NY: Springer New York, 2018. ISBN: 978-1-4939-6674-5 978-1-4939-6676-9. DOI: 10.1007/978-1-4939-6676-9.

[18] Neil Everall. “Optimising image quality in 2D and 3D confocal Raman mapping: 2D and 3D Raman imaging”. en. In: *J. Raman Spectrosc.* 45.1 (Jan. 2014), pp. 133–138. DOI: 10.1002/jrs.4430.

[19] Jan N. Reimers and J. R. Dahn. “Electrochemical and In Situ X-Ray Diffraction Studies of Lithium Intercalation in Li_xCoO_2”. en. In: *J. Electrochem. Soc.* 139.8 (Aug. 1992), pp. 2091–2097. DOI: 10.1149/1.2221184.

[20] Lucie Le Van-Jodin et al. “Ex situ and operando study of $LiCoO_2$ thin films by Raman spectroscopy: Thermal and electrochemical properties”. en. In: *J Raman Spectrosc* 50.10 (Oct. 2019), pp. 1594–1601. DOI: 10.1002/jrs.5669.

[21] Eibar Flores et al. “Operando Monitoring the Insulator–Metal Transition of $LiCoO_2$”. en. In: *ACS Appl. Mater. Interfaces* 13.19 (May 2021), pp. 22540–22548. DOI: 10.1021/acsami.1c04383.

[22] Akira Yano et al. “Capability and Reversibility of $LiCoO_2$ during Charge/Discharge with O3/H1−3 Layered Structure Change”. en. In: *J. Electrochem. Soc.* 168.5 (May 2021), p. 050517. DOI: 10.1149/1945-7111/abfc9d.

[23] Ziying Wang et al. “In Situ STEM-EELS Observation of Nanoscale Interfacial Phenomena in All-Solid-State Batteries”. en. In: *Nano Lett.* 16.6 (June 2016), pp. 3760–3767. DOI: 10.1021/acs.nanolett.6b01119.

[24] Yuki Nomura et al. “Dynamic imaging of lithium in solid-state batteries by operando electron energy-loss spectroscopy with sparse coding”. en. In: *Nat Commun* 11.1 (June 2020), p. 2824. DOI: 10.1038/s41467-020-16622-w.

[25] Raj Pandya et al. “Three-dimensional operando optical imaging of particle and electrolyte heterogeneities inside Li-ion batteries”. en. In: *Nat. Nanotechnol.* (Aug. 2023). DOI: 10.1038/s41565-023-01466-4.

[26] Laisuo Su et al. “Multiscale operando X-ray investigations provide insights into electro-chemo-mechanical behavior of lithium intercalation cathodes”. en. In: *Applied Energy* 299 (Oct. 2021), p. 117315. DOI: 10.1016/j.apenergy.2021.117315.

[27] Johanna Nelson Weker et al. “Operando Spectroscopic Microscopy of LiCoO2 Cathodes Outside Standard Operating Potentials”. en. In: *Electrochimica Acta* 247 (Sept. 2017), pp. 977–982. DOI: 10.1016/j.electacta.2017.06.173.

Understanding $LiCoO_2$ Limitations

[5] Alice J. Merryweather et al. “Operando optical tracking of single-particle ion dynamics in batteries”. en. In: *Nature* 594.7864 (June 2021), pp. 522–528. DOI: 10.1038/s41586-021-03584-2.

[28] Jaecheol Choi et al. “Effect of LiCoO2 Cathode Density and Thickness on Electrochemical Performance of Lithium-Ion Batteries”. en. In: *J. Electrochem. Sci. Technol* 4.1 (Mar. 2013), pp. 27–33. DOI: 10.33961/JECST.2013.4.1.27.

[29] Jason Trask et al. “Optimization of 10-µm, sputtered, LiCoO 2 cathodes to enable higher energy density solid state batteries”. en. In: *Journal of Power Sources* 350 (May 2017), pp. 56–64. DOI: 10.1016/j.jpowsour.2017.03.017.

[30] Huigang Zhang et al. “Electroplating lithium transition metal oxides”. In: *Science Advances* 3.5 (2017), pp. 2–10. DOI: 10.1126/sciadv.1602427.

[31] Renjie He et al. “Enhancing the Reversibility of Lithium Cobalt Oxide Phase Transition in Thick Electrode via Low Tortuosity Design”. In: *Nano Letters* 22 (2022), pp. 2429–2436. DOI: 10.1021/acs.nanolett.2c00123.

[32] M. Ménétrier et al. “On “Really” Stoichiometric LiCoO[sub 2]”. en. In: *Electrochem. Solid-State Lett.* 11.11 (2008), A179. DOI: 10.1149/1.2968953.

[33] Jay Hyok Song et al. “Suppression of irreversible capacity loss in Li-rich layered oxide by fluorine doping”. en. In: *Journal of Power Sources* 313 (May 2016), pp. 65–72. DOI: 10.1016/j.jpowsour.2016.02.058.

[34] Wen Jing Li et al. “Fabrication and electrochemical properties of a LiCoO2 and Li10GeP2S12 composite electrode for use in all-solid-state batteries”. en. In: *Solid State Ionics* 285 (Feb. 2016), pp. 136–142. DOI: 10.1016/j.ssi.2015.05.007.

[35] Yingchun Lyu et al. “An Overview on the Advances of LiCoO2 Cathodes for Lithium-Ion Batteries”. en. In: *Advanced Energy Materials* 11.2 (2021), p. 2000982. DOI: 10.1002/aenm.202000982.

[36] Jin K Hong, Jong H Lee and Seung M Oh. “Effect of carbon additive on electrochemical performance of LiCoO2 composite cathodes”. en. In: *Journal of Power Sources* 111.1 (Sept. 2002), pp. 90–96. DOI: 10.1016/S0378-7753(02)00264-1.

[37] Nam Hee Kwon et al. “Impact of composite structure and morphology on electronic and ionic conductivity of carbon contained LiCoO2 cathode”. en. In: *Electrochimica Acta* 134 (July 2014), pp. 215–221. DOI: 10.1016/j.electacta.2014.04.121.

「人は自分のためには再生できないということなの。
他の誰かのためにしかできない」

from *1Q84 Book 3*, **Murakami Haruki**

”People aren’t reborn for their own sakes. They can only do it for someone else.”
trad. from *1Q84 Boook 3*, **Murakami Haruki**

CONCLUSION AND PERSPECTIVE

Table of Contents

1. Conclusions on the present work

In the four chapters of this thesis, I tried to answer some of the many questions linked to all-electrochemical-active electrodes and, in particular, provide a physical framework to understand the general behavior of intercalation cathodes.
After the first bibliographical chapter, the physical characterization of the device under test is proposed in the second chapter. The anode-free stack is composed of a $LiCoO_2$ cathode, a LiPON electrolyte and a titanium current collector, where the lithium anode is plated during the first charge. Scanning electron microscopy, Raman spectroscopy, X-ray diffraction and confocal microscopy were employed to analyze the chemical, crystallographic and morphological homogeneity of the different layers composing the thin-film cell. The main objective of this analysis is the validation of the modeling hypothesis exploited in the third chapter. In particular, the possibility of reducing the lithium diffusion inside the cathode to a 1D problem.
In the third chapter, after the mathematical derivation of all main equations, a physical model is presented in order to study the dynamic and static performances of $LiCoO_2$-based thin-film cells. The lithium profile during charge and discharge is simulated and commented on. The effects of constant and variable diffusion coefficients and phase transition dynamics are analyzed from a theoretical point of view.
The first part of the fourth chapter is dedicated to the electrical characterization of the cell and the validation of the results against the model predictions for different thicknesses of the cathode electrode. Particular attention is devoted to the assessment of the dependency of charge and discharge capacity as a function of the drawn current.
After the first cycle loss, in common with all architectures, cycling stability is demonstrated, and no impact of the cathode thickness is visible in the early cycling phase. The study of the first cycle loss in thin-film cathode and its analysis by means of a variable diffusion coefficient model were successful, and a comprehensive explanation was proposed on the basis of a dynamically induced phase transition. The asymmetry between charge and discharge rating performance of $LiCoO_2$ was explained by the same model and correlated linearly with the thickness of the cathode. From the modeling results, an optimal design for a thin-film-based cell has been proposed in order to maximize the available energy density once the discharge current is known.
The second part of the same chapter is dedicated to synchrotron radiation X-ray diffraction operando 2D mapping. The variation in (003) diffraction plane peak position is followed during charge and discharge of the cell and mapped along the cathode thickness with a 1 µm resolution. The diffraction experiment permitted the imaging of the lithium profile along the cathode and confirmed the dynamic origin of the phase transition. The phase transition stoichiometry and accumulation were shown to be a function of the drawn current and to relax as the discharge stopped. Experimental and simulated lithium profiles are compared, and the main divergences discussed.
As a conclusion, the differences between composite electrodes and thin-film electrodes were partially addressed, and a first hypothesis was proposed. In particular, the root cause of the variation in discharge capacity density is explained in terms of ion and electron path differences between the two configurations. In the composite electrodes, the electrons are transported by means of the conductive matrix, while in the thin-film configuration, they are transported by the cathode material itself. Changes in the electron conductivity of LCO strongly impact only the latter.
Even if all analyses are conducted on a specific cathode material, the limitations induced by the thin-film configuration are shown to be independent of the material itself and linked to the na-

ture of the electrode. It should be possible to extend the same considerations to any material, as long as it is in an all-electrochemically-active electrode configuration. The model itself can be easily adapted by measuring the input physical parameters for a different cell, without any modification of the equations.

2. Perspectives for future research

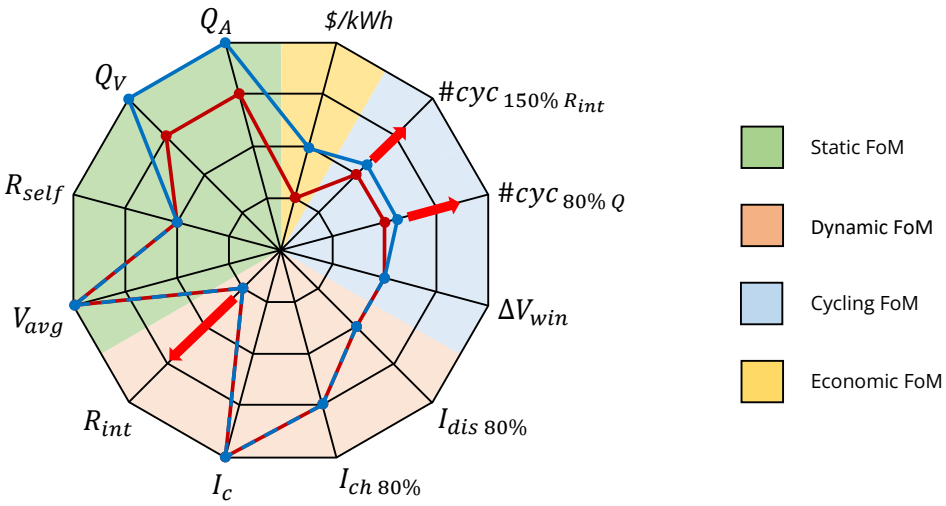

Figure 5.1: Performance summary for the thin-film cell developed in the present work. The reported indicator are: Q_A the areal capacity; Q_V the volumetric capacity; R_{self} the electron resistance; V_{avg} the average OCV value; R_{int} the ion resistance; I_C the critical current for dendrite formation; $I_{ch80\,\%}$ the charge current corresponding to $80\,\%$ loss on the nominal capacity; $I_{dis80\,\%}$ the discharge current corresponding to $80\,\%$ loss on the nominal capacity; ΔV_{win} the stability windows; $\#cyc_{80\,\%Q}$ the number of cycles before $80\,\%$ loss on the nominal capacity; $\#cyc_{150\,\%R_{int}}$ the number of cycles before $+50\,\%$ increase on the nominal internal resistance; *$/kWh* is the production cost of the cell.

To fully understand the performance of an all-electrochemically-active electrode, many questions still need to be answered. During my work, I have not addressed the loss of capacity during cycling for thin-film batteries. In the context of my thesis, the main point hindering the study of such a problem was the difficulty in producing reliable results. In particular, the anode-free configuration is very sensitive to moisture and oxygen. As the quantity of lithium in the anode is exactly the amount needed for a full discharge, if the device is not properly sealed, a fast capacity decay is experienced. A first run of tests was conducted in an argon-filled glove box, with some preliminary results on the effect of cycling parameters on the capacity decay. Notwithstanding, the limited number of channels and the long measurement time resulted in an insufficient number of samples. Multiple failure modes and process variability were shown to add lots of variance to the cycling performances, and further investigation was delayed until a more robust production and a larger number of test channels would be available.
Other research paths were explored that are worth pursuing. Preliminary work on battery management systems suggested the possibility of exploiting the full capacity of the cathode by leveraging the intrinsic current variation during operation in most IoT devices. In fact, these devices are in an idle state for long periods, and only occasionally is data collected and transmitted.

While the latter operation requires a large power output, the idle state current is so small that the phase transition is almost completely suppressed, and the whole capacity can be exploited. Also, model-wise, various improvements are possible to make the prediction much more reliable. A first step would be a thorough study of the redox reaction dynamics. So far, the electrolyte of the devices under test is quite thick, and the overall dynamics is controlled by the ohmic drop. By thinning the electrolyte down to a few tens of nanometers, it should be possible to switch to reaction-limited dynamics and properly extract the reaction coefficient. In general, the upgrade of the device to a three-electrode system would also be beneficial to split anode and cathode contributions and produce a more meaningful model.
More generally, we can recall the different figures of merit (FoMs), described for batteries at the beginning of the first chapter, in the form of a spider chart. In Figure 5.1 twelve FoMs are reported, concerning the various aspects of an electrochemical cell. The status before the beginning of the present work is reported in red, while in blue is the performance for the optimized cell. The red arrows indicate the critical improvements for the next generation of microbatteries. Some parameters were already at the optimal point, as the average voltage and the critical current, thanks to the intrinsic properties of $LiCoO_2$ and LiPON.
The main output of the present work has been an optimization of the total available capacity by increasing the cathode size. The obtained value reached the state-of-the-art for volumetric and areal capacity in the context of thin-film technology. At the same time, the increase in capacity resulted in a decrease in the total cost of the cell. Moreover, an initial study on cycling showed the possibility of improving cycling performance by tuning the charge and discharge protocols. This is probably one of the most important axis of improvement for the next generation. Cycling limitations are, in fact, a major gap between standard technologies and thin-film batteries.
Related to the particular stack under investigation, the large internal resistance results from the thickness of the electrolyte that was not optimized. This point is, of course, a mandatory improvement for the next generation of cells to both increase the output power density and improve the characterization, as already pointed out.
Rating performances ($I_{ch80\,\%}$, $I_{dis80\,\%}$), stability windows and the self-discharge are strongly related to the choice of materials, which are not expected to be modified in the short period.

"This page intentionally left blank."

anonymous

"This page intentionally left blank."

anonymous

RÉSUMÉ EN FRANÇAIS

Introduction

En 2013 a été publié le premier rapport sur les technologies de rupture (Mckinsey) . Douze technologies ont identifiées en raison du potentiel économique de leur commercialisation. L'une d'entre elle est l'internet des Objet (IdO).
Au fil des ans, le concept de disruption et les technologies listées observent un regain d'intérêt. Les rapports périodiques du comité européen sur les technologies de rupture (en 2017 et 2021) ont suivi les travaux précurseurs de Mckinsey. Le même concept de perturbation a mérité son propre document en 2020. Dans un document de l'UE de 2021, la liste des technologies de rupture a été réduite (de 12 à 6) et revue (deux nouvelles technologies et trois changements de marque). La seule qui ait gardé un nom intact depuis son premier baptême en 1999 est l'Internet des objets .
Les changements qui résultent d'une rupture ont souvent associés à une croissance du marché et à des opportunités. Alors que la part de marché de l'IdO commence à croître, divers problèmes doivent être résolus pour que son plein potentiel se développe. La gestion de l'alimentation est l'un des aspects les plus importants de l'IdO. La gestion de l'énergie est un des principaux thèmes de la conception de capteurs pour l'IdO. Même si un seul appareil consomme peu d'énergie, le déploiement de milliards d'entre eux entraîne une consommation agrégée énorme (effet rebond). L'impact économique et environnemental de la consommation d'énergie des appareils IdO est une des premières préoccupations du développement en raison des estimations d'unités déployées. La principale stratégie d'optimisation et de réduction de la consommation d'énergie consiste à équiper le nœud de détection d'une alimentation autonome. Il est également nécessaire de maximiser l'autonomie de l'alimentation afin d'éviter les remplacements fréquents ou les temps d'arrêt, ce qui augmenterait le coût et diminuerait la qualité du service. Les systèmes d'alimentation s'articulent autour de trois technologies principales : les batteries, les supercondensateurs et la récolte d'énergie.
Dans ce contexte, les batteries à couches minces à l'état solide se présentent comme une solution potentielle. Néanmoins, cette technologie n'a pas encore atteint sa maturité, et des problèmes intrinsèques la hantent encore. Par exemple, les batteries à couche mince présentent une capacité surfacique plus faible, une densité de puissance plus faible et une pertede la capacité plus importante par rapport aux batteries standard, même lorsque les mêmes matériaux de cathode sont utilisés. La recherche de l'origine physique des différences entre les cathodes commerciales et les cathodes à couches minces à l'état solide est l'objet du présent travail.

Chapitre 1

Le premier chapitre est principalement consacré à une vaste revue bibliographique des batteries à couches minces, tant du point de vue des matériaux que de la conception.
Après une brève introduction historique sur les raisons du développement des batteries à l'état solide, les différences entre les batteries à couche mince et les batteries classiques sont mises en évidence. Le processus de production étant l'un des points les plus critiques mais des plus innovants de la technologie proposée, une brève revuedes méthodes de production des couches minces est également proposé. Toutes les principales techniques de dépôt de couches minces sont présentées, et les principaux avantages et limites sont signalés.
Avant de passer à l'inventaire bibliographique des matériaux disponibles pour réaliser une batterie à couches minces, les principes physiques et les principaux indicateurs de performance sont révisés. En particulier, la caractérisation par microscopie électronique de la diffusion des atomes de lithium dans les milieux solides et l'évolution des quantités thermodynamiques en

fonction de la fraction de lithium à l'intérieur du matériau d'électrode sont exposées. Les matériaux d'électrodes positives, les matériaux d'électrodes négatives et les matériaux d'électrolytes solides sont ensuite étudiés. Pour chaque matériau, une brève analyse est proposée, en mettant l'accent sur la littérature relative à la configuration des couches minces. La diffusion ionique, la conductivité électronique, la densité de capacité disponible, l'expansion de volume et d'autres paramètres significatifs sont rapportés pour chaque matériau et résumés dans des tableaux synthétiques. Le $LiCoO_2$ est identifié comme l'un des matériaux cathodiques les plus prometteurs pour la réalisation à court terme de batteries à couches minces en raison du processus de dépôt mature, de la densité d'énergie et de puissance élevée, et de la stabilité du cycle. L'électrolyte solide LiPON est considéré comme un matériau prometteur en raison de sa résistance à la formation de dendrites et de sa stabilité électrochimique par rapport au lithium et au $LiCoO_2$. La configuration sans anode est ensuite choisie comme solution d'anode afin de maximiser la densité d'énergie volumétrique du dispositif, même si la littérature fait état de diverses limitations ; à savoir, une faible stabilité au cyclage et une extrême sensibilité à l'humidité. L'étude met également en évidence le nombre réduit d'études expérimentales concernant la configuration des batteries à couches minces. En particulier, divers matériaux n'ont jamais été testés dans une configuration à couche mince à l'état solide en raison des faibles performances de la conception classique de la batterie.

Chapitre 2

Le deuxième chapitre est consacré au processus de fabrication des batteries à couches minces utilisées pour produire le dispositif qui a été analysé dans le cadre du présent travail.
Après une brève introduction du processus de dépôt par pulvérisation cathodique, une revue bibliographique est proposée pour les matériaux $LiCoO_2$ et LiPON concernant l'effet des paramètres de dépôt sur les propriétés physiques du film. L'effet de la puissance de dépôt, de l'atmosphère, des propriétés de la cible, et de la température de l'air sur les propriétés physiques du film a été étudié. Pour le matériau de la cathode, l'effet de la puissance de dépôt, de l'atmosphère, des propriétés de la cible et des traitements thermiques sur la vitesse de dépôt et la densité du matériau est analysé. En raison de la grande dispersion des données expérimentales, aucune conclusion claire ne peut être tirée sur l'effet global des paramètres de dépôt. La pulvérisation de l'électrolyte solide LiPON est également examinée. Alors que l'effet des paramètres de dépôt sur la vitesse de dépôt peut être évalué, les autres propriétés physiques, telles que la diffusion des ions et la composition chimique, ne peuvent pas être clairement corrélées avec les conditions de dépôt.
La deuxième partie du chapitre est consacrée à la caractérisation physique et chimique des films déposés, et en particulier à l'évaluation de l'homogénéité morphologique et chimique des films de cathode et d'électrolyte. L'objectif est non seulement d'étudier la qualité des films déposés, mais aussi d'établir une base expérimentale solide pour les hypothèses de modélisation qui sont exploitées dans le troisième chapitre. En particulier, afin de réduire la charge de calcul, la géométrie du dispositif est réduite à 1D, grâce à la bonne homogénéité de la cellule le long des dimensions latérales. Des résultats d'imagerie MEB sont rapportés, confirmant la bonne morphologie de la cellule et la densité de la couche cathodique. La qualité de l'interface entre chaque composant de la cellule est également évaluée. La diffraction des rayons X et la spectroscopie Raman sont utilisées pour étudier la composition chimique et cristalline de la cathode. Hormis un léger gradient de texture le long de la direction verticale, la cartographie chimique et cristallographique de la cathode valide l'hypothèse de la modélisation 1D et la haute qualité des films déposés.

La dernière caractérisation proposée dans ce chapitre est l'observation optique du placage de lithium sur le collecteur de courant de l'anode au cours du processus de charge et de décharge du dispositif. La morphologie et l'homogénéité du lithium sont confirmées. De plus, la densité de lithium est estimée, et les résultats expérimentaux montrent une valeur proche de la valeur théorique, indiquant un placage très dense et continu.

Chapitre 3

Afin d'étudier et de comprendre la différence de performance entre la configuration à couche mince et la conception classique de la cellule, le troisième chapitre est consacré au développement d'un modèle physique 1D d'une cellule à couche mince. La modélisation physique des systèmes électrochimiques est un sujet très vaste en termes de littérature disponible, et de nombreux modèles différents ont été proposés dans le temps pour modéliser n'importe quel aspect d'une batterie. La plupart des publications se concentrent sur la configuration de l'électrolyte liquide, et la plupart des équations utilisées ont été développées pour ce cas particulier.
Le chapitre est divisé en deux sections afin de discuter séparément de la physique de la diffusion des ions et de la réaction électrochimique à l'interface électrode/électrolyte. Dans les deux cas, la théorie des dispositifs à l'état solide est développée à partir de l'hypothèse thermodynamique de base pour mettre en évidence les principales modifications nécessaires, par rapport à l'équation la plus courante utilisée dans la littérature, afin de modéliser correctement le dispositif dans le présent travail. À la fin de chaque chapitre, un bref examen du modèle populaire est proposé, ainsi qu'une comparaison avec l'équation choisie pour la modélisation de l'état solide en couche mince. La théorie des dispositifs à l'état solide est développée à partir de l'hypothèse thermodynamique de base.
La deuxième partie de ce chapitre traite de l'implémentation réelle dans COMSOL du modèle physique et de sa solution pour le cas d'une batterie à couche mince $LiCoO_2$/LiPON. Pour que le modèle reproduise le comportement du dispositif, divers paramètres physiques doivent être déterminés expérimentalement pour le dispositif choisi. En particulier, une cellule $LiCoO_2$ de 5 µm d'épaisseur est utilisée comme référence. Le coefficient de diffusion du lithium est déterminé à la fois pour la cathode (au moyen du GITT) et pour l'électrolyte (au moyen d'une mesure EIS). La variation du coefficient de diffusion en fonction de la fraction d'intercalation du matériau de la cathode est discutée et mise en œuvre dans l'équation physique de la diffusion.
La dernière partie du chapitre est consacrée à l'analyse des résultats de la simulation. Une attention particulière est accordée à la description de l'effet de l'épaisseur de la cathode et de la densité du courant de décharge sur le courant de décharge disponible, qui s'avère expérimentalement beaucoup plus faible que celui attendu pour la même quantité de matériau de cathode dans une cellule commerciale. La cause principale de la perte de la capacité pendant la décharge est la limitation de la diffusion du lithium à l'intérieur de la cathode. Les résultats des modèles de diffusion constante et de diffusion variable sont comparés pour mettre en évidence la nature intrinsèque de la perte lors de la première décharge.
En conclusion, la supériorité du modèle de diffusion variable est également discutée dans le cadre d'une correcte modélisation du comportement de la cellule à différentes vitesses de décharge, ainsi qu'une brève analyse du profil du lithium à l'intérieur de la cathode et de l'électrolyte.

Chapitre 4

Le dernier chapitre du manuscrit est entièrement consacré à la caractérisation expérimentale du dispositif d'un point de vue fonctionnel et à la validation de la prédiction du modèle au moyen

de mesures électriques et physiques.
Dans la première section, la capacité fournie prédite en fonction de l'épaisseur de la cathode et de la densité de courant est validée. Des dispositifs avec des $LiCoO_2$ allant de 5 µm à 30 µm sont caractérisés et un bon accord avec les résultats de simulation est rapporté à la fois pour la capacité délivrée et la forme de la courbe de décharge de charge. Comme prévu par le modèle, une augmentation linéaire de la capacité de décharge disponible en fonction de l'épaisseur de la cathode est rapportée, confirmant l'effet bénéfique de la conception d'une cathode épaisse. Les limitations associées à la chute ohmique et à la diffusion de l'électrolyte sont également discutées.
Dans la deuxième partie du chapitre, la validation du profil de lithium simulé au moyen de la diffraction synchrotron des rayons X est abordée. Cette technique exploite la taille fine du faisceau du rayonnement synchrotron pour permettre une cartographie 2D de la section transversale de la cellule du point de vue de la structure cristalline. Étant donné que la structure cristalline du $LiCoO_2$ est modifiée au cours des processus de charge et de décharge, l'analyse de l'évolution de la position des pics de diffraction permet une cartographie directe de la teneur en lithium par rapport aux coordonnées spatiales. Une installation dédiée a été réalisée pour effectuer cette mesure, permettant de sonder simultanément jusqu'à 10 cellules en même temps.
L'analyse des données et les procédures de correction des artefacts ont été réalisées à l'aide d'un logiciel d'analyse de données. Les procédures d'analyse des données et de correction des artefacts sont décrites en détails. Les données corrigées sont ensuite analysées et le profil de lithium imagé est comparé au profil simulé. La charge et la décharge sont correctement modélisées d'un point de vue qualitatif par le modèle développé dans le troisième chapitre. Les divergences qualitatives sont discutées en détail et sont principalement liées à une extraction imparfaite du coefficient de diffusion pendant la transition de phase du $LiCoO_2$.
L'un des résultats les plus intéressants est l'imagerie de l'accumulation de lithium à l'interface $LiCoO_2$/LiPON à la fin du processus de décharge. Comme prévu par le modèle, il s'agit de la principale cause de réduction de la capacité à une densité de courant élevée. Elle est intrinsèquement liée aux propriétés physiques de la couche cathodique et non à la configuration en couche mince.
En conclusion de ce chapitre, une hypothèse sur la différence de comportement entre la configuration à couche mince et la configuration classique est fournie. En particulier, la disponibilité d'un chemin alternatif pour les électrons dans l'électrode composite est soulignée comme une raison possible de la suppression de la perte de capacité.

Conclusions et perspectives

Dans la conclusion, après un bref résumé de la thèse, les perspectives de recherche futures sont discutées. En particulier, il reste encore beaucoup à faire pour étudier les performances de cyclage du dispositif à couche mince, ce qui n'a pas été abordé dans le présent travail. L'impact des paramètres de cyclage sur la perte de capacité devrait être soigneusement analysé afin d'estimer le potentiel de la technologie à couche mince. Des solutions circulaires ciblant des applications précises peuvent également être imaginées pour faire face et récupérer la perte de capacité associée à la diffusion limitée du lithium et pour augmenter la densité de capacité. Le dopage de la cathode et l'amincissement de l'électrolyte sont d'autres moyens de maximiser la densité énergétique. D'une manière générale, les performances des différents matériaux devraient être réévaluées dans la configuration de la couche mince, car le présent travail montre que le comportement dépend de la configuration dans laquelle le même matériau est exploité.